THE UNIVERSITY *of* EDINBURGH

The behaviour of beam-column substructures with typical steel joints in progressive collapse scenarios

Thesis submitted for the degree of
Doctor of Philosophy

Xiaobo Cheng

Institute for Infrastructure and Environment

School of Engineering

The University of Edinburgh

July 2018

Table of Contents

Figures and Tables

Declaration

I hereby declare that,

This thesis was composed by me and the work contained therein was solely the work of the author except otherwise acknowledged in the text.

No part of this thesis has been submitted for any other degree or professional qualification.

Signed:

Xiaobo Cheng

The University of Edinburgh

Date submitted: 31/07/2018

Lay Summary

Progressive collapse of a building structure is often triggered by accidental actions, which typically can cause the loss of a load−carrying members such as a column in a framed building structure. The structural capacity to withstand such a partial failure largely depends on the capacity of the immediately affected substructure to redistribute the loads to the remaining structural system. In the past years, much research attention has been focused on the resistance behaviour of a double-span beam assembly due to the removal of a middle column, which plays a critical role in determining whether the remaining structural system would be able to avoid a catastrophic progressive collapse.

This thesis aims to investigate and quantify the full-range response of such double beam assemblies with typical joint details. To demonstrate the plastic deformation concentration and how it affects the ability of a beam assembly in developing an effective catenary action, a generic beam is first analysed using classical beam analytical methods, to establish the relationship between the material strain and the global deflection, thus a quantified limiting criterion. Experimental tests are carried out to supplement existing experimental literature concerning local failure events and the structural ability to develop catenary actions. Extending the conventional component-based method for modelling the plastic behaviour of steel connections, an analytical framework is proposed to analyse the double beam assembly with realistic behaviour of steel joints, focusing particularly on the large deformation regime. Furthermore, a comprehensive component model is developed for fin-plate steel connections, which is then applied in the proposed analytical framework so that the collapse behaviour of beam assembles involving fin-plate connections, as well as other typical joints types, can be evaluated analytically.

The analytical methods can be applied for more a realistic, and yet also economical in terms of the analysis effort, evaluation of the progressive collapse behaviour of steel framed structures.

Acknowledgements

I would like to express my sincere gratitude to my supervisor Professor Yong Lu for his valuable support during my PhD study. His extensive experience and vision have inspired my work in every aspect possible and make my study on the right track. He has been incredibly generous to spend countless time discussing with me and providing suggestions on the research details. His guidance means a lot to me and I will always appreciate that.

The research reported in the thesis is partly funded by the Chinese Scholarship Council and the University of Edinburgh through a joint scholarship for my PhD study. The financial support from them are gratefully acknowledged.

I would like to thank the Structural Laboratory technicians, Mark Parddington and Jim Hutcheson for the help in experimental tests.

I also much appreciate and treasure the unforgettable time with all my colleagues and friends in Edinburgh, Harry, Lige, Rongxin, Jiaming, Chuanchuan, Xizhong, to name but a few. They are not only close friends, but also role models for me in life and work.

I would like to give special thanks to my wife Dr. Wenjie Ding and my parents. Their sacrifice for me and the long-lasting support always mean a lot to me.

Abstract

In a progressive collapse scenario, the immediate effect due to a local triggering failure, i.e. the loss of a column as considered in the present study, is exerted on the beams bridging over the lost column. The behaviour of such double beam assembly plays a critical role in determining whether a progressive collapse would occur or not.

This study focuses on the realistic behaviour of such beam assemblies, particularly the plastic deformation concentration, the associated degradations in the connection regions, and how these in turn affect the overall resistance behaviour and the ultimate strength of the beam assemblies.

To start with, a generic axially-constrained beam is analytically examined in order to better understand the full range response including the large deflection regime, the development of the plastic deformation, and how this in turn affects the overall resistance and the deformability. The load-deflection relationship and the associated plastic deformation are first analytically derived for a bending scenario, and then the effect of the catenary action is introduced. The analytical solution provides some quantitative insight, although under idealised conditions, into the limiting local criterion (material strain in this case) and the global deflection and deformability.

A laboratory experimental study is then carried out on six reduced scale double beam assemblies. The purpose-designed connection details allow different local plastic mechanisms and local failure modes to develop, with an intention to represent relative weak connections so as to supplement the existing experimental literature in the coverage of relationship between connection failure limits and the overall resistance capacities. The test results have revealed that the specimens went through elastic and plastic bending stages; however, the catenary actions could not be developed sufficiently in most of the specimens whenever a premature local failure, such as material/weld fracture, bolt shear and concrete cracking, became dominant. The outcome highlighted the crucial importance of enabling the plastic deformation to “spread” in order to ensure a total plastic deformation capacity in the plastic zones as well as the importance of the axial capacities of the joint connections. In

conjunction with the existing studies, the experimental exploration provided further evidences for the future experimental and numerical studies to focus on the design details in typical connection types and how these could transpire into the actual development of the plastic regions and effective catenary action.

With representation of the realistic connection behaviour in mind and for practical applications, a new analytical framework is proposed in this study on the basis of component-based connection modelling, for the solution of the resistance function and the ultimate deformation limits. An analytical framework is realized by an in-house program written in MATLAB. In order to apply the analytical framework to double beam assemblies, the existing quantitative formulations for typical joint components of common steel joints are scrutinized. Examples of double beam assemblies with web-cleat and TSWA connection are carried out to verify the analytical solutions and demonstrate the key characteristics of the resistance functions involving these types of joints. Analytical results show good agreement with the corresponding test data.

A dedicated study is then devoted to the development of a complete component model for a widely used connection in steel gravity frames, namely the fin-plate connection, which is however relatively less investigated in terms of the component modelling into the large deformation regime. Subsequently the overall behaviour of double beam assemblies involving such joints is examined using the analytical framework. In the development of the component model for the fin-plate joints, existing models and formulations to describe general plate bearing and bolt shearing behaviour are incorporated to establish the basic constitutive properties of the bolted lap-plate component set. Upon the initial verification, improvement of the constitutive descriptions is found to be necessary. To this end, high-fidelity finite element analysis is conducted, and on this basis, modifications to the plate bearing and bolt shearing behaviour are proposed. The analytical solutions with the modified lap-plate component properties are found to be in good agreement with the experimental results.

The outcome of this thesis has provided new insight and evidence on the realistic behaviour of beam assemblies, and pointed out the directions for more robust design

for improved progressive collapse resistance of the steel framed structures. The analytical framework and the associated solution provide a useful tool for the analysis of the resistance functions for the critical beam assemblies for practical applications.

With this approach, the key to the reliability and soundness in the analysis of the resistance function lies upon the adequacy and accuracy of the description of the joint components. In this respect, the future work should focus on more comprehensive quantification of the properties and deformation limits of joint components for a variety of joint types and design details.

1 Introduction

1.1 Background of structural progressive collapse

Failures of civil engineering structures are often caused by abnormal events beyond the normal design considerations. Examples of such events include malicious attack, accidental hazards (e.g. fire or blast) or undetected component deterioration (e.g. fatigue fracture of steel connections). A lack in awareness of the effects of abnormal loading on modern buildings would make them structurally vulnerable to accidental exposures.

Figure 1.1 shows the widely known 1968 collapse incident of the Ronan Point apartment, where the loss of support on the 18th floor set off a chain reaction of collapse all the way to the ground. After 27 years, history repeated in the Murrah building, in which three badly damaged columns led to failure of a transfer girder, and then the collapse of columns and floor areas supported by the transfer girder. When it comes to 21st century, a catastrophic collapse due to terrorist attack took place in USA. The World Trade Towers were crashed by high speed jetliners. Subsequently, the impact zone lost its capacity to support the upper structure due to collision and fire damage, and then gravity and debris impact caused the collapse extending downward. It is a prime example of severe impact and fire affected buildings in ways not anticipated by those who built it.

Ronan Point building, 1968

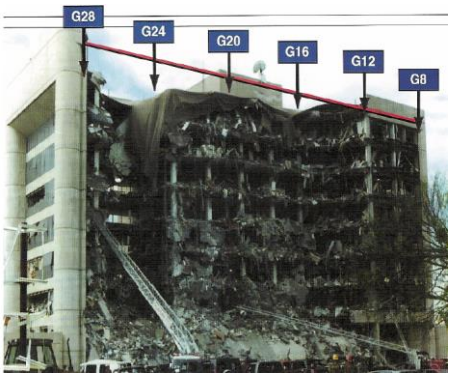

Alfred P. Murrah building in OKC, 1995

World Trade Centre, 2001

Figure 1.1 Collapse incidents in history (https://bsbgroup.com/blog/progressive-collapse-of-structures/)

So far, some terrorist attacks and collapse incidents have highlighted the need for research on enhancing structural robustness to mitigate the consequences of abnormal exposures. Actually, the concept of structural robustness under abnormal loading has evolved as a scholastic hotspot for quite some time, but there has been no commonly accepted method for its quantitative assessment (Brett and Lu 2013), and essential data regarding the structural behaviour under excessive deformations is still limited.

1.2 Rationale of investigation into double beam assembles and joint behaviour

In the event when a multi-story framed building structure is subjected to a sudden column loss, various levels of substructures may be used for the analysis of the dynamic responses, as Figure 1.1 summarizes. It can be seen that in the hierarchy of a framed structure, each level of structural idealisation incorporates basic assumptions and conditions. A model reduction will make the evaluation process more affordable and even more reliable.

Structural Level	Schematic illustration	Assumptions
Level 1, Global multi-story frame structure	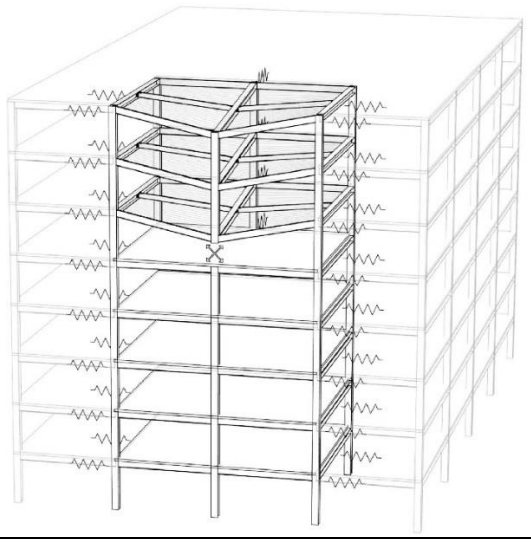	Sudden column removal scenario, which is event-independent.

Level 2, Substructure of multiple affected bays and stories	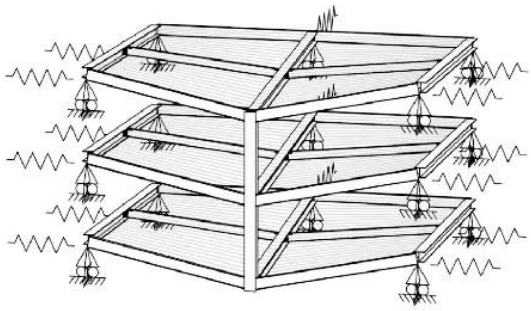	Assumptions made to the boundary conditions of the affected substructures.
Level 3, Single story beam-column-slab assembly	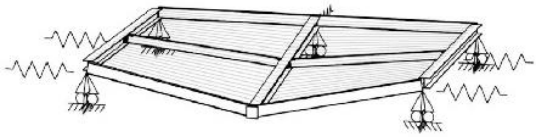	The responses of affected floors over the damaged column are identical.
Level 4, Beam-column subassembly, without floor slabs	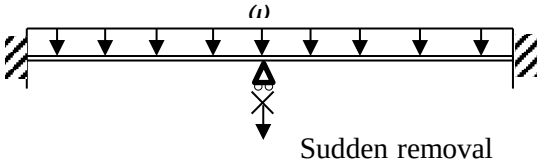	The floor slab effect is ignored.
Level 5, Equivalent SDOF system	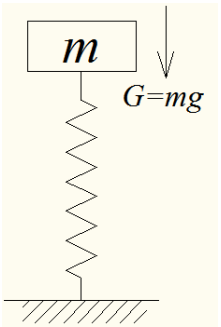	Damping is ignored; Only the history of displacement is considered.

Figure 1.2 Model simplification levels to evaluate the dynamic response to sudden column removal (first three graphs from Stylianidis et al. (2016))

Each level of structures is further explained in detail below.

Level 1:

The global structure can be used directly for the analysis of structural response to a sudden column loss. However, this could be extremely complicated and time-consuming. What is more, it is actually not necessary because the affected area is limited and the surrounding structures may have very little effect on the global structural performance. An adequate model reduction is therefore essential in terms of practical applications.

Level 2:

The substructure which is significantly affected by the sudden column removal can be extracted from the global structure. However, the boundary conditions of the substructure needs to be defined properly in order to represent the realistic interaction between the substructure and its surrounding structural components.

Level 3:

On the single story beam-column subassembly with floor slabs included (level 3), the contribution of floor slabs is accounted for. The membrane action of the slabs, similar to the beam catenary action, could enhance the substructure ability to resist progressive collapse. However, on the other hand, it will also add to the demand of adjacent structures as the slabs can pull on and damage the structure components adjacent to the affected area. The modelling analysis including the floor slabs are more complicated. For instance, for typical steel composite floor slabs, the metal deck, concrete slab and the shear stud connection are all required to be properly considered.

Level 4:

In the general situation where the affected floors are more or less identical to each other, a single floor beam-column subassembly can be used for the evaluation of the critical response. On the level of the beam-column subassembly, the response is characterised by significant geometric and material nonlinearity, especially when the response enters into large deformation regime and beam catenary action is mobilised to resist the vertical load. The survivability of the subassembly is largely dependent on the deformation capacity and ductility of the connections.

Level 5:

Since the structural behaviour under a sudden column loss is usually dominated by a single deformation mode, the dynamic effects in progressive collapse of column-removed structure can be evaluated using a simplified single-degree-of-freedom (SDOF) system. More specifically, once the nonlinear quasi-static behaviour is realistically represented for the double span beam subjected to the central column removal, it can be expected that the overall dynamic response can be obtained quite

accurately using the SDOF model, by fitting the quasi-static behaviour as a constitutive description of the spring force-displacement relationship in the SDOF system.

The SDOF modelling method makes an effective and efficient way for evaluating the dynamic effects in a progressive collapse scenario. The SDOF model equivalency is shown in Figure 1.3.

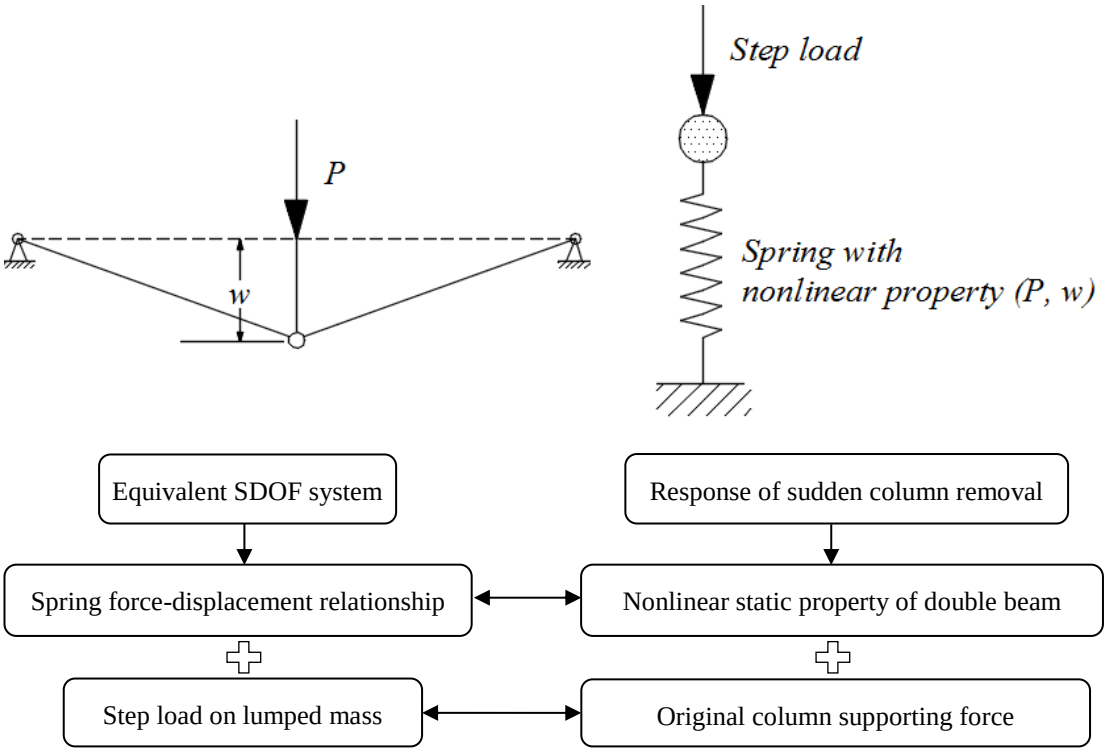

Figure 1.3 The equivalency relationships between SDOF system and the sudden column loss scenario

From the above analysis, it can be concluded that the determination of a realistic resistance function (i.e. the spring-displacement relationship in an SDOF model) of the critical double beam assembly under a column removal is central to the evaluation of the progressive collapse of a framed structure. Figure 1.4 shows a typical double beam assembly extracted from a frame structure which is subjected to an internal column loss, which is a further reduction taken between two contra-flexure locations.

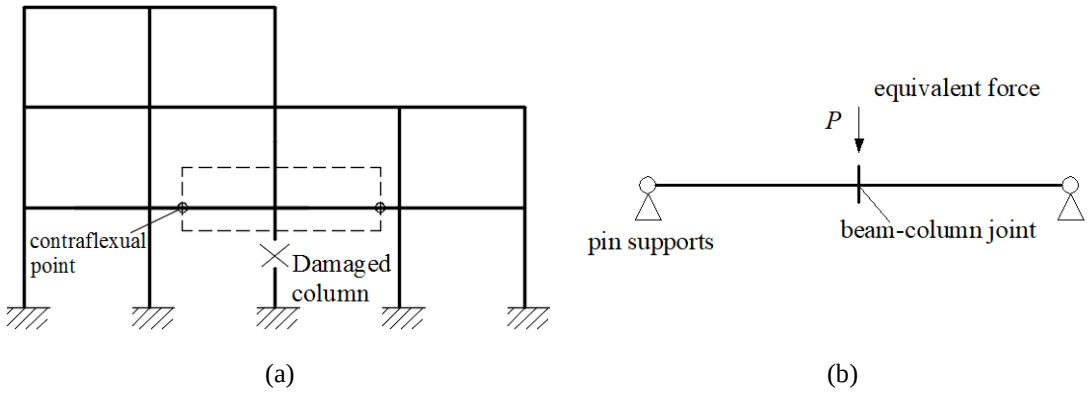

Figure 1.4 A reduced double beam assembly extracted from a column loss scenario with pin supports

A typical resistance function of the double-beam assembly is schematically illustrated in Figure 1.5. Four distinctive stages can be identified: I) elastic, II) plastic-hardening (arching), III) transitionary, and IV) catenary (tension). In the beginning, the flexural bending is predominant. When the vertical deflection is sufficiently large, plastic deformation will develop, typically at the connection locations (including beam plastic zones). In the meantime, the axial force developed would have an increasing influence on the vertical load resistance. As the deflection further increases, the axial force contribution to the vertical load resistance will gradually become predominant. The assembly will eventually collapse when the critical region, i.e. the middle connection region, completely fails.

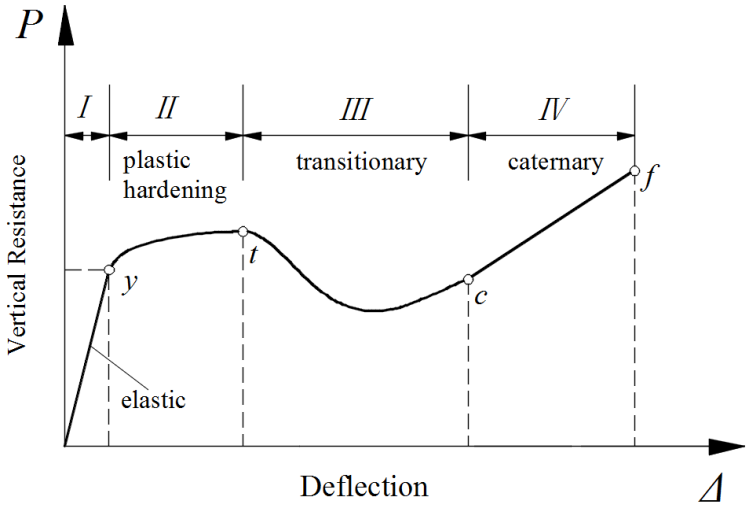

Figure 1.5 Typical resistance function of a beam-column subassembly

In the whole assembly response, of particular interest are the plastic hardening stage II and the catenary stage IV. Information on the magnitude of these effects, as well as the ultimate deformation capacity which would dictate the extent to which the catenary action could actually develop, is not covered in classical beam-column and connection studies.

In the steel framed structures, a beam-to-column joint acts as a medium through which forces and moments are transferred between the connecting members. Joints are usually the weakest links in a steel frame structure system. When it comes to the progressive collapse scenario under extreme loading, the joint region over the damaged or removed column tend to be the most crucial parts for the affected substructure to survive against catastrophic collapse. More specifically, the integrity of the connection region and its deformation limit will play determinative roles in the structural ability to develop effective catenary action.

As illustrated in Figure 1.6, the middle connection will be subjected to considerable axial tension force as well as bending moment. Therefore, the beam-to-column joint behaviour under a support column loss is critical to the establishment of load resistance function and failure criteria for the full-range response.

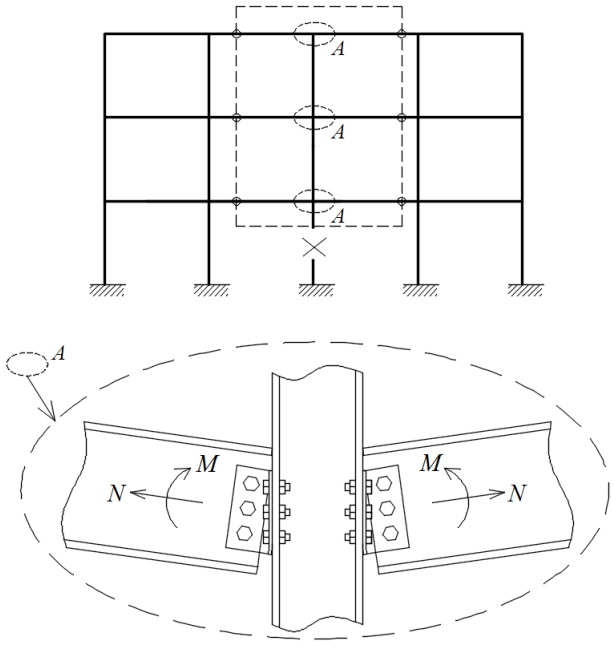

Figure 1.6 Schematic illustration of the joint deformation under internal column loss

1.3 Research objectives

This thesis is aimed to enhance the evaluation of realistic, full-range resistance functions and ultimate failure criteria of the double beam assemblies under a column loss scenario. The realistic behaviour of beam-column steel joints and the associated double beam assemblies are particularly investigated.

Firstly, in order to explore how the large deformation limit is related to the local fracture limit, the load-deflection characteristics of a generic beam subjected to axial constraints and mid-span loading are analysed using conventional mechanics theories. The predominant role of plastic concentration in the critical region is quantitatively established. The analytical solutions show that in an idealised situation where the plastic deformation is governed by the material failure, enlarging the size of the plastic zone is an effective way to improve the global deformation capacity and hence the ability of a beam assembly in developing an effective catenary action.

Secondly, a laboratory experimental study is then conducted with a particular intention to observe local failure modes within typical beam-column steel joints, possible premature failure happening in the connection regions, and how these failure events affect the global resistance functions.

On top of the generic beam exploration and laboratory tests, the thesis proceeds to develop an analytical framework, in order to enable a realistic analysis of the behaviour of the double-beam steel assemblies with typical joint types. The framework is established on the basis of a component-based joint modelling approach and can cover a wide range of joint types

To successfully apply the analytical framework, the constitutive properties of typical joint components are comprehensively investigated. In particular, a complete component model for the fin-plate connections is developed and it is subsequently applied in the analytical framework.

1.4 Outline of the thesis

The main chapters of the thesis are briefly described below.

Chapter 2:

The state-of-the-art researches on the performances of the double beam assembly with typical steel joints in the progressive collapse scenario are reviewed. This includes relevant experimental studies, numerical modelling studies by using finite element analysis and the conventional component-based methods. The suitability and potential issues when applying the component method to analyse the joint behaviour and the overall resistance of beam assemblies in a progressive collapse scenario are discussed.

Chapter 3:

A generic axially-constrained beam is theoretically examined in order to better understand the full range response including the large deflection regime, the development of the plastic deformation, and how this in turn affects the overall resistance and the deformability. The load-deflection relationship and the associated plastic deformation are first analytically derived for a bending scenario, and then the effect of the catenary action is introduced. The analytical solution provides some quantitative insight, although under idealised conditions, into the limiting local criterion (material strain in this case) and the global deflection and deformability.

Chapter 4:

In this chapter, a laboratory experimental study is then carried out on six reduced scale double beam assemblies. The purpose-designed connection details allow different local plastic mechanisms and local failure modes to develop, with an intention to represent relative weak connections so as to supplement the existing experimental literature in the coverage of relationship between connection failure limits and the overall resistance capacities. Test results have revealed that the specimens went through elastic and plastic bending stages; however, an effective

catenary action could not be developed in most of the specimens whenever a premature local failure, such as material/weld fracture, bolt shear and concrete cracking, became dominant. The outcome highlighted the crucial importance of enabling plastic deformation to "spread" in order to ensure a total plastic deformation capacity in the plastic zones. In conjunction with the existing studies, the experimental exploration provided further evidences for the future experimental and numerical studies to focus on the design details in typical connection types and how these could transpire into the actual development of the plastic regions and effective catenary action.

Chapter 5:

With representation of the realistic connection behaviour in mind and for practical applications, a new analytical framework is proposed in this chapter on the basis of the component-based connection modelling, for the solution of the resistance function and the ultimate deformation limits. An analytical framework is realized by an in-house program written in MATLAB. In order to apply the analytical framework to double beam assemblies, the existing quantitative formulations for typical joint components of common steel joints are scrutinized. Examples of double beam assemblies with web-cleat and TSWA connection are carried out to verify the analytical solutions and demonstrate the key characteristics of the resistance functions involving these types of joints. Analytical results show good agreement with the corresponding test data.

Chapter 6:

In this chapter, a dedicated study is devoted to the development of a complete component model for a widely used connection in steel gravity frames, namely the fin-plate connection, which is however relatively less investigated in terms of the component modelling into the large deformation regime. Subsequently the overall behaviour of double beam assemblies involving such joints is examined using the analytical framework. In the development of the component model for the fin-plate

joints, existing models and formulations to describe general plate bearing and bolt shearing behaviour are incorporated to establish the basic constitutive properties of the bolted lap-plate component set. Upon initial verification, improvement of the constitutive descriptions is found to be necessary. To this end, high-fidelity finite element analysis is conducted, and on this basis, modifications to the plate bearing and bolt shearing behaviour are proposed. The analytical solutions with the modified lap-plate component properties are found to be in good agreement with the experimental results.

2 State-of-the-art research on double beam assembly and performance of steel joints in the progressive collapse scenario

2.1 The classification and representative types of joints in steel-framed structures

2.1.1 Steel joint classification and analysis procedures

In the conventional analysis of steel frames, joints in a moment resisting frame are often modelled as being "perfectly rigid", and simple joints in a gravity frame are often modelled as being "perfectly pinned". This simplifies the force transmissions and the analysis procedures. Nowadays, it has been widely accepted that it is essential to consider the realistic partial strength and rigidity of the joints in both design and analysis. In particular, when large deformation is developed under extreme loading, the joints may undergo considerable local damages in some of the key constituent components. Under this circumstance, the effects of residual strength and stiffness are important for determining the global structural behaviour at large deflection.

According to the current Eurocode 3 Part 1-8 (BSI 2005) guidance, steel joints are generally classified into three categories based on their initial rotational stiffness (S_j), namely nominally pinned, rigid and semi-rigid connections. The initial rotational stiffness is evaluated at a bending moment not exceeding 2/3 of the joint design moment capacity. In Figure 2.1, L_b and I_b are the length and second moment area of the connected beam, respectively.

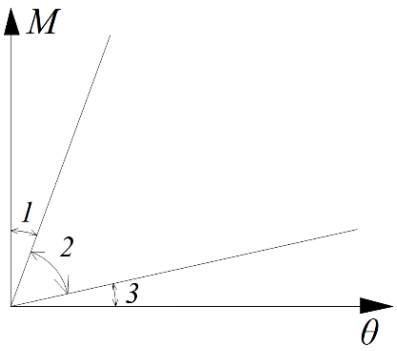

Zone 1 (rigid)	$S_j \geq k_b EI_b/L_b$
Zone 2 (semi-rigid)	All other joints
Zone 3 (nominally pinned)	$S_j \leq 0.5EI_b/L_b$

Note: correction coefficient k_b=8 or 25, depending on the frame conditions.

Figure 2.1 Classification of steel joints by rotational stiffness (Eurocode 3 2005)

As shown in Figure 2.2, the steel joints are usually simplified into rotation springs in the frame structural analysis. The moment-curvature property is defined as shown in Figure 2.3, according to Eurocode 3 (BSI 2005).

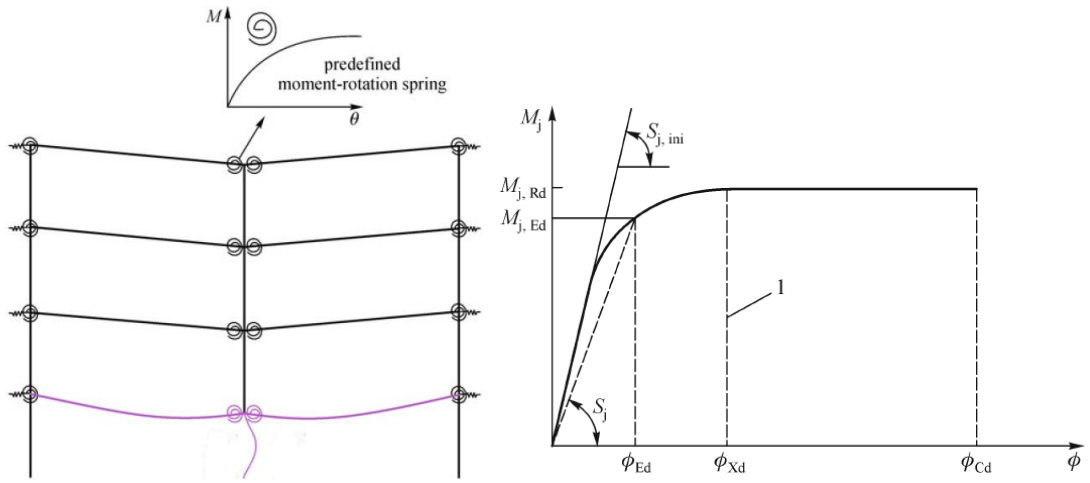

Figure 2.2 Design moment-rotation curve (Eurocode 3, BSI 2005)

As a further simplification, a bi-linear simplification of the moment-rotation relationship may be used, and the rotational stiffness is taken as $S_{j,ini}/\eta$. For beam-to-column joints, the stiffness modification coefficient η is specified to be 2.0.

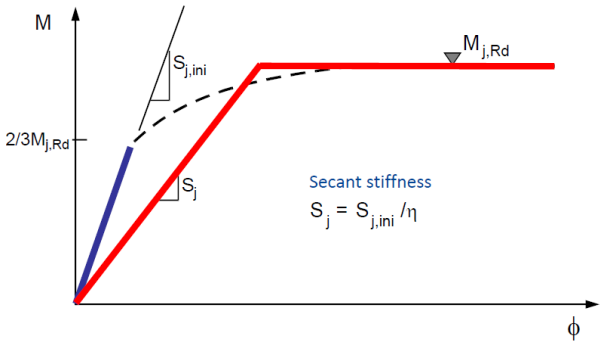

Figure 2.3 The simplified bi-linear design *M*-ϕ curve (Red line)

2.1.2 Representative connection types and features

Compared to the welded connections, bolted connections behave in more complicated manners, simply because more elements such as bolts, angles, plates are introduced into the congested connection zone. However, the bolted connections, if designed properly, can provide much higher deformability as well as ductility. As has already been observed in experiments, such by Li et al. (2013) and the tests in this study (Chapter 4), welded connections fail in a quite brittle way and have adverse effects on the global deformation ductility. Therefore, in this chapter, the selection of typical steel joints is mostly limited to bolted connections.

(1) Pinned joints

The pinned connections are also termed as simple connections. Usually in these connections, the beam web is connected, while there is no connection for the flanges. In design, they are supposed to transmit only axial and shear forces. However, it may be transformed to moment connection through prying action developed between the beam flanges and supporting column when the beam rotation is sufficient (Stylianidis and Nethercot 2015). Some typical examples of simple connections include web cleat connection and fin plate connection. The web cleat connection utilized double angles, each leg of which is bolted to the beam web or column flange (Fig. 2.4).

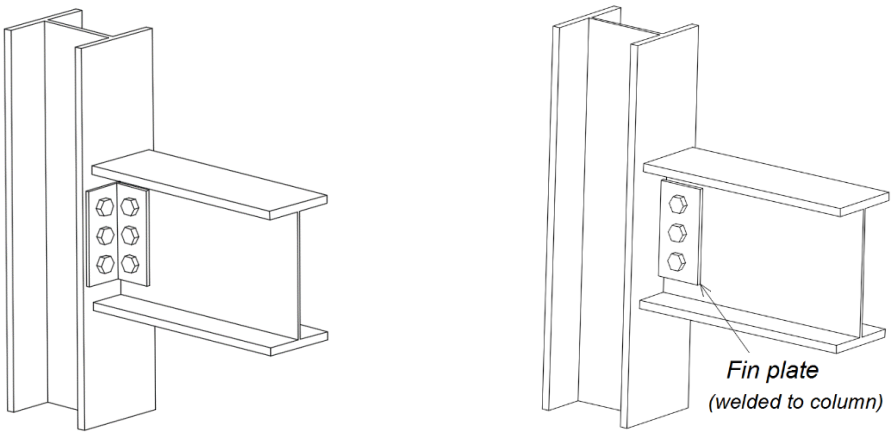

(a) Web cleat connection **(b) Fin plate connection**

Figure 2.4 Representative simple (pinned) connections

(2) Rigid joints

Rigid joints have sufficiently large rotational stiffness to maintain the angle between the beam and column. The most rigid type is where the beam is fully welded to the column on site, but this is expensive and it is difficult to control the weld quality (Martin and Purkiss 1992).

(3) Semi-rigid joints

Joints classified as semi-rigid have finite stiffness and allow for predictable degrees of rotation between the beam and column. Some typical joints deemed as semi-rigid includes flush end-plate connections, extended end-plate connection, top and seated angle connection, top and seated angle and web angle (TSWA) connections are shown in Fig. 2.5. (Trahair et al. 2008)

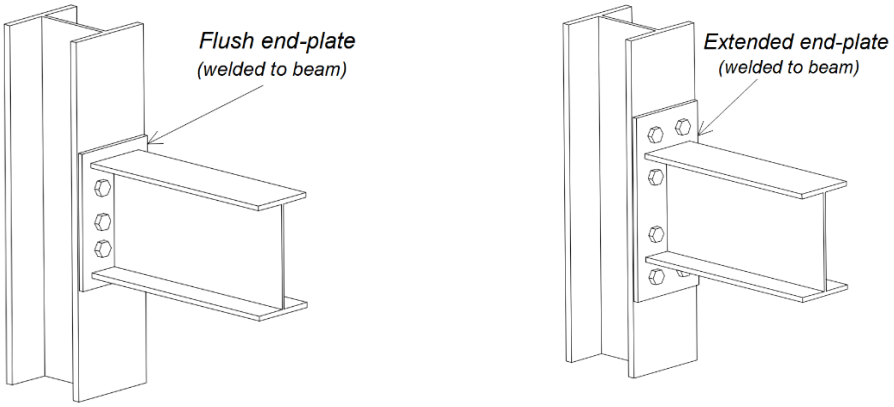

(a) Flush end-plate connection (b) Extended end-plate connection

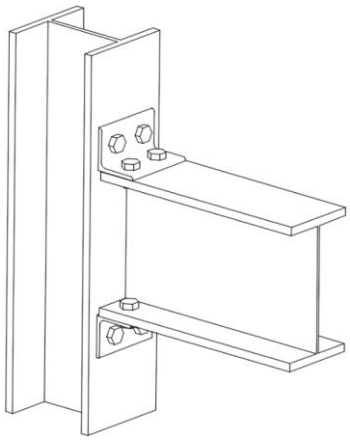

(c) Top and seated angle connection

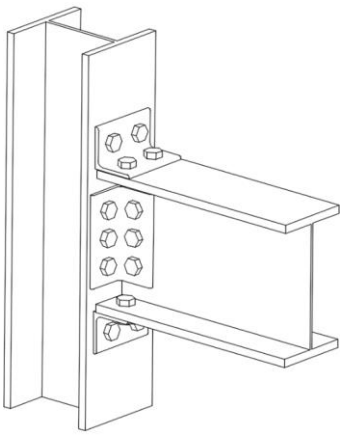

(d) Top and seated and web angle (TSWA) connection

Figure 2.5 Representative semi-rigid bolted connections

In the steel beam-to-column joints, stiffener plates are usually installed to 'shore up' the column flanges and web against the forces transmitted by the beam flanges, as shown in Fig. 2.6. The conventional stiffeners are parallel with beam flanges. They may be full length or extending only part of the column web depth. Some other stiffening possibilities are also shown in the figure.

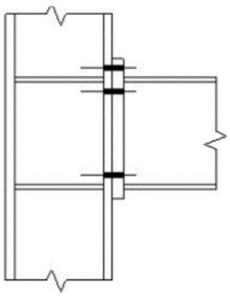

(a) Conventional horizontal stiffener

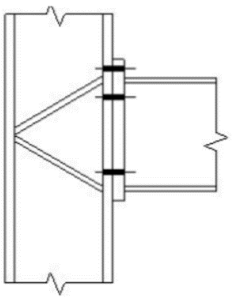

(b) K type stiffener

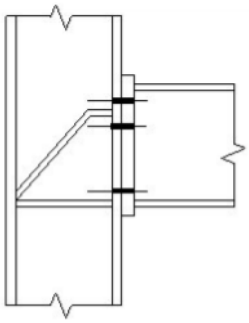

(c) 'Morris' stiffener

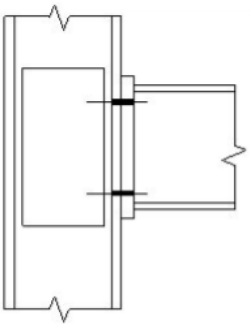

(d) Supplementary web plate

Figure 2.6 Stiffening possibilities of column (Davison and Owens 2011)

Stiffeners have certain effects on the joint response, especially in the large deformation regime. The column web could be protected from local buckling, and the column flanges can be protected from excessive deformation under out-of-plane tension. Overall, the stiffeners could enhance the stiffness of the joint zone outside the connection zone.

Therefore, the various deformations within the column panel can be neglected at large deflection, to allow the mechanical modelling to be simplified, and focused on the connection zone. This idea is used in the analytical modelling study in Chapter 5.

2.2 Experimental studies on double beam assembly with typical steel joints under column removal

Experimental tests, though costly to conduct, are reliable in gathering convincible evidences of joint failure modes, and the global load-deflection patterns. As by-products of the experimental data, some empirical formulations generated by the curve-fitting technique may be useful for further analytical studies. By assembling and synthesising the test results, the findings can form a basis of more realistic description of the joints, both numerically and theoretically.

2.2.1 Existing experimental studies

Various research efforts have been devoted in recent years to the understanding of the damage processes and the mechanisms governing the development of the arching action and the catenary effects.

Sadek et al. (2011) experimentally tested two full-scale steel beam assemblies. One was with a Welded Unreinforced Flange-Bolted web (WUF-B) connection used in intermediate moment frames (IMFs). Another one was the reduced beam section (RBS) connection used in special moment frames (SMFs). Each assembly comprise two beam spans and three columns, and downward displacements of the centre column are imposed until failure (Fig. 2.7).

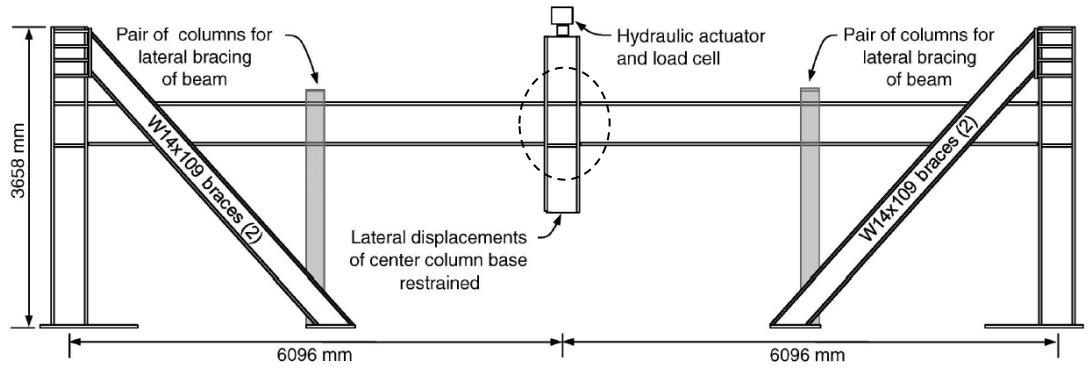

(a) The test set-up

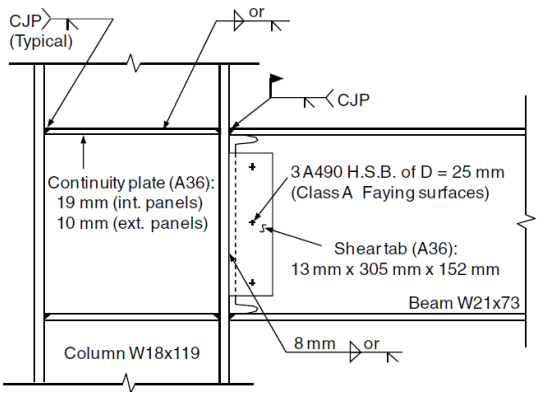

(b) The WUF-B connection details

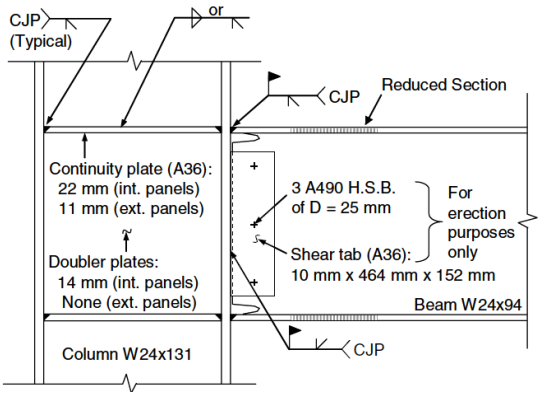

(c) the RBS connection details

Figure 2.7 Test setup and for the double beam assemblies details (Sadek et al. 2011)

The assembly with the WUF-B connection experienced large deflections and rotations prior to failure. The connection sequentially experienced local buckling of the top flanges of the beams at the centre column, successive shear fractures of the bolts, and finally fracture of the bottom flange near the weld access hole, see Fig. 2.8 .

The assembly with RBS connection has large load resistance and deflection at failure, which is characterized by fracture of the bottom flange in the middle of the reduced section. The fracture propagated through the web until load resistance was depleted.

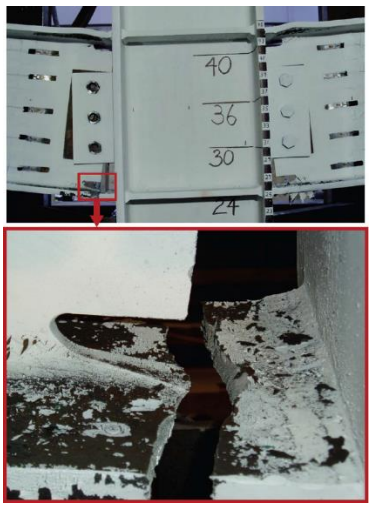

(a) Tested failure mode of WUF-B connection

(b) Tested failure mode of RBS connection

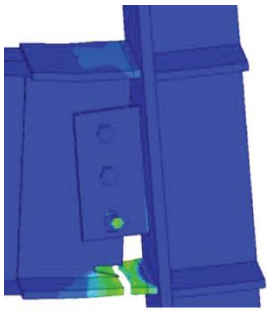

(c) Simulated failure mode of WUF-B connection

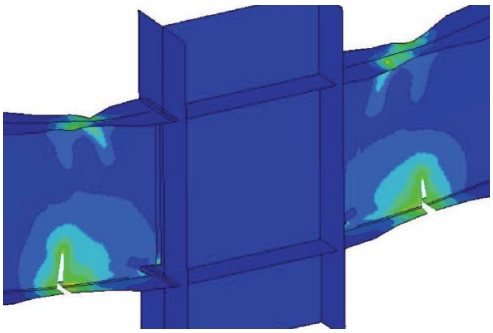

(d) Simulated failure mode of RBS connection

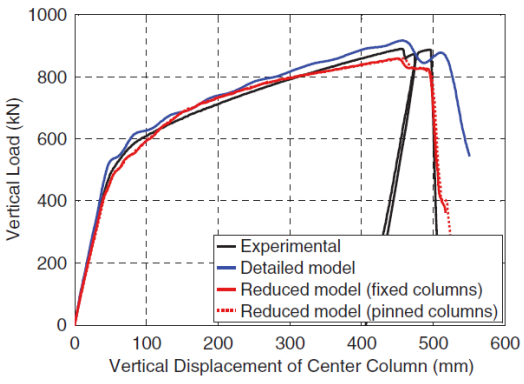

(e) Resistance function of WUF-B connection

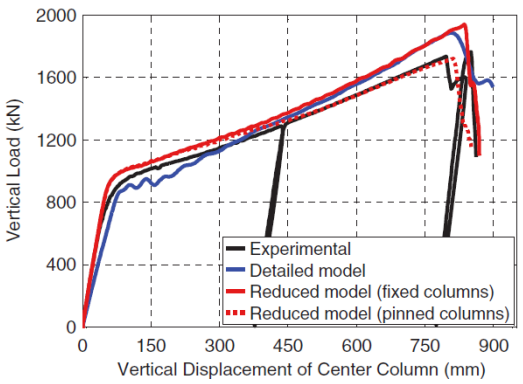

(f) Resistance function of RBS connection

Figure 2.8 Failure modes and resistance function curves of the WUF-B connection and RBS connection (Sadek et al. 2011)

From the comparison between the two assemblies, the more stringent seismic design and detailing of the RBS connection increased the failure displacement by a factor of 1.72 and the ultimate load by a factor of 2.00 relative to the assembly with the WUF-

B connection. Both assembly exhibited initial linear stage, and hardening behaviour associated with the development of catenary action.

Yang and Tan (2013) tested the performance of seven bolted joints under central column removal, at Nanyang Technological University, and discussed the general response features of the typical joints. The joint types included web cleat, top and seat angle, top and seat with web angle (TSWA) (8 mm angle), fin plate, flush end plate, extended end plate and TSWA (12 mm angle). The overall test set-up is shown in Fig. 2.9.

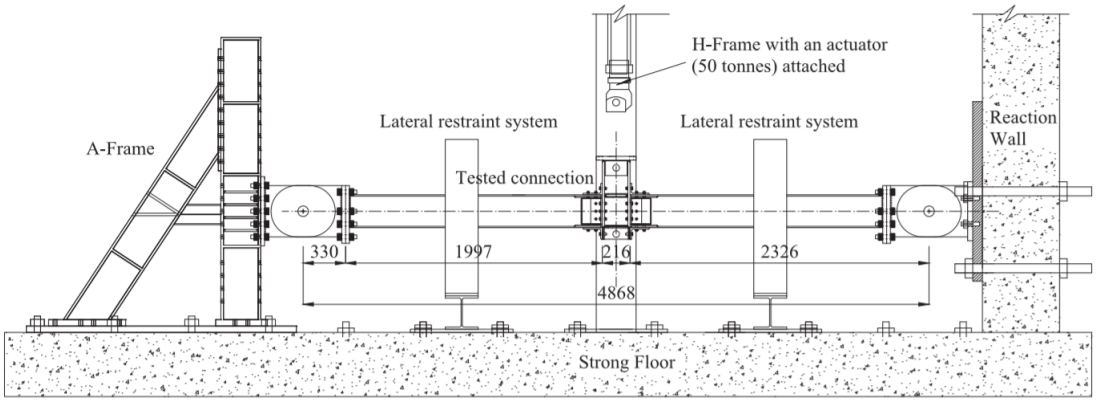

Figure 2.9 Test setup for all the specimens by Yang and Tan (2013)

The configurations of bolted joints are in line with the summarised representative joint types in Section 2.1.2 of this chapter. The behaviour and failure modes of these seven types of connections are presented. As an example, the load resistance function of the assembly featuring top and seated angle is shown in Fig. 2.10, with the angle fracture point indicated in the curve.

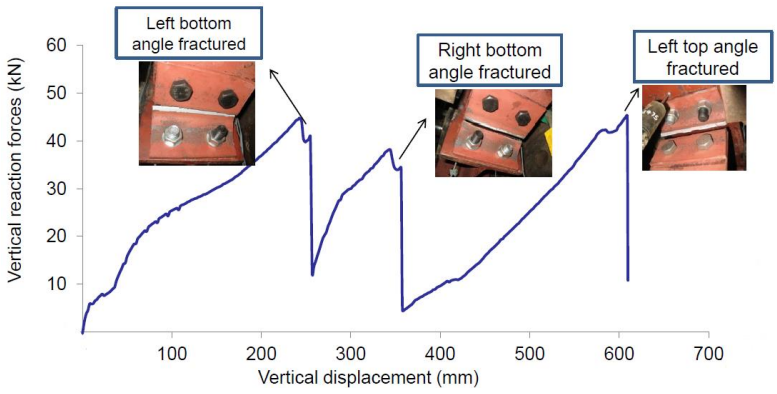

Figure 2.10 The resistance function of a double beam assembly with top and seated angle connections (Yang and Tan 2013)

A comparison between the resistance functions of assemblies with TSWA connection and end-plate connections is plotted in Figure 2.11. The test results indicate that the web cleat connection has the best performance in the development of catenary action. The flush end plate, fin plate and TSWA connections could also deform in a ductile manner and develop catenary action. The test results also demonstrate that the rotation capacities of typical steel joints based on the experimental results are much higher than the recommended values by DoD (2009).

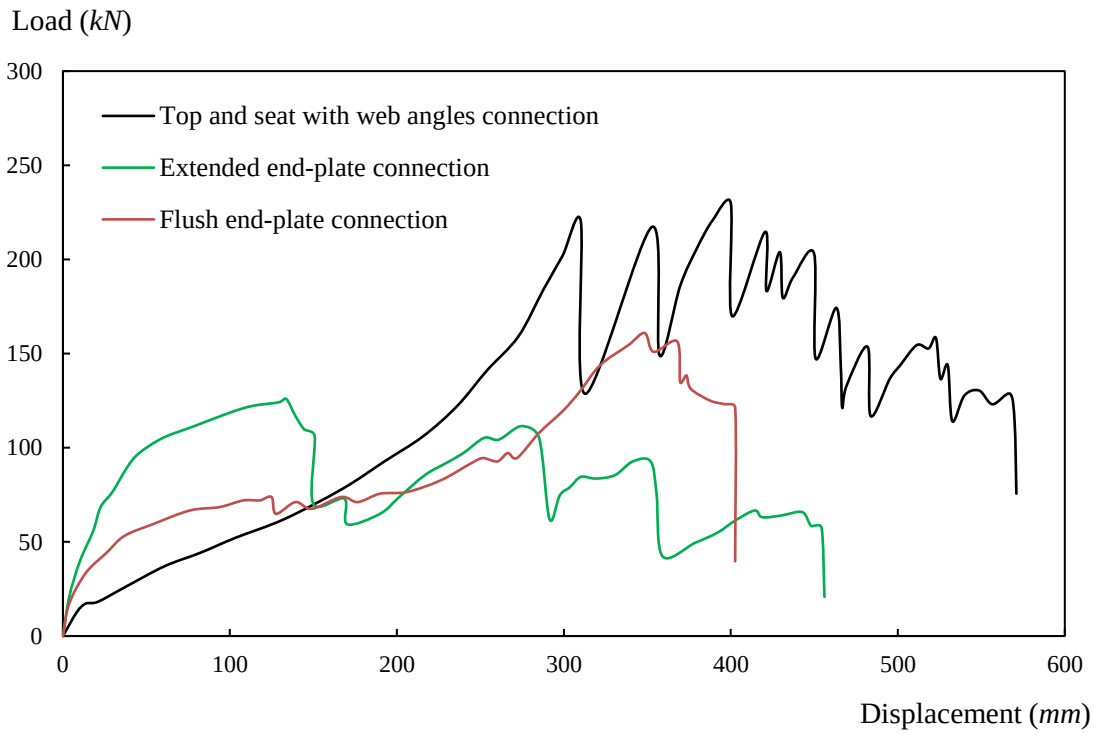

Figure 2.11 The load-deflection responses of typical semi-rigid connection (Yang and Tan 2013)

Li et al. (2013) tested two full-scale double beam assemblies, featuring beam-to-tubular column connections with an outer-diaphragm connector. One assembly was with full weld connections, and another had flange-welded web-bolted connections, see Figs 2.12 and 2.13.

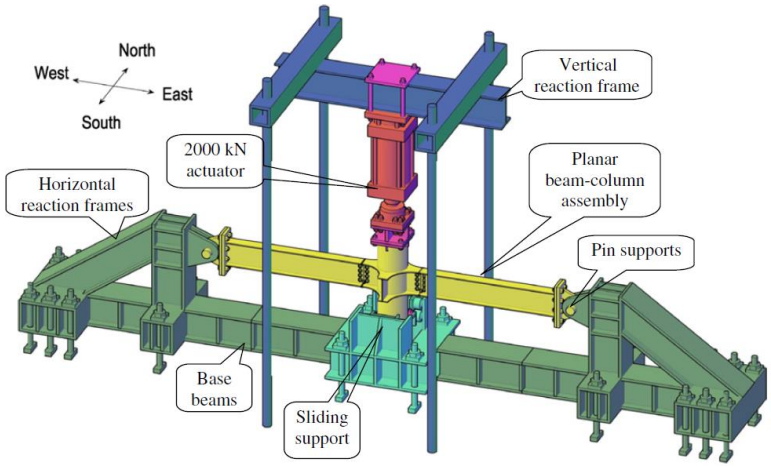

Figure 2.12 Test set-up of double beam assemblies with beam-to-tubular column connections (Li et al. 2013)

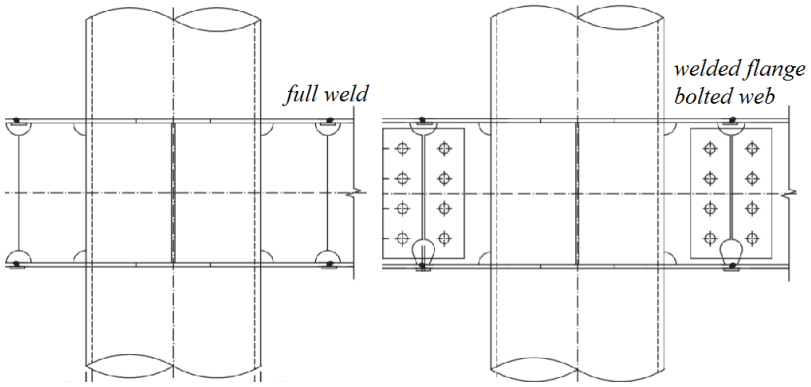

Figure 2.13 The configurations of full weld and welded flange-welded web connections (Li et al. 2013)

The tests found that the full weld connection experienced local buckling of top flanges, and then weld cracking from the bottom flange towards the top. The welded flange-welded web connection also experienced local buckling of top flanges, and the weld fracture at the bottom flange. Then the lowest bolts sheared web plates to result in significant bearing deformations. The details are given in Fig. 2.14.

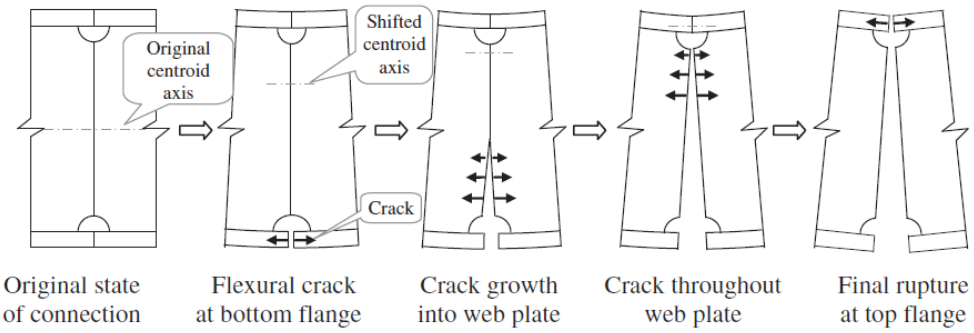

(a) The failure process of full weld connection

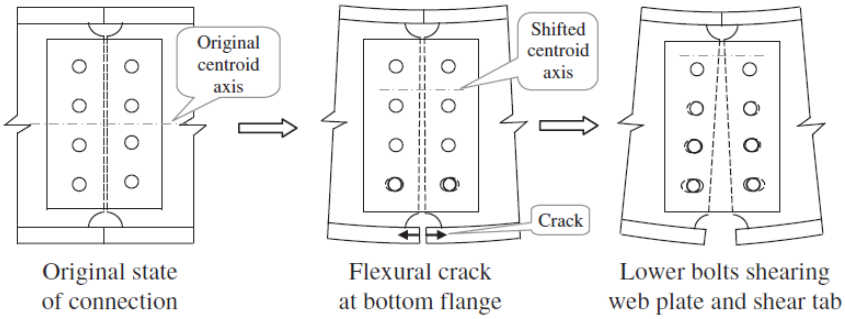

(b) The failure process of welded flange-bolted web connection

Figure 2.14 The failure processes of the full weld connection and welded flange-bolted web connections (Li et al. 2013)

It was concluded that welded web connection could not develop catenary action with a continuous failure, while bolted web connections performed in a more robust manner than the welded web connection.

Li et al. (2015) carried out additional tests for comparative study on web bolted connection behaviours with two different bolt layouts. When all (four) bolts were arranged in one row, the lowest bolt bearing area on the beam web tends to be compressed to fracture before bolt tear-out occurs near the weld access hole. When the bolts were arranged in two rows, however, the shear tab cracked at the section across the bolt holes. The former failure mode was deemed to be more robust than the latter under a column removal scenario.

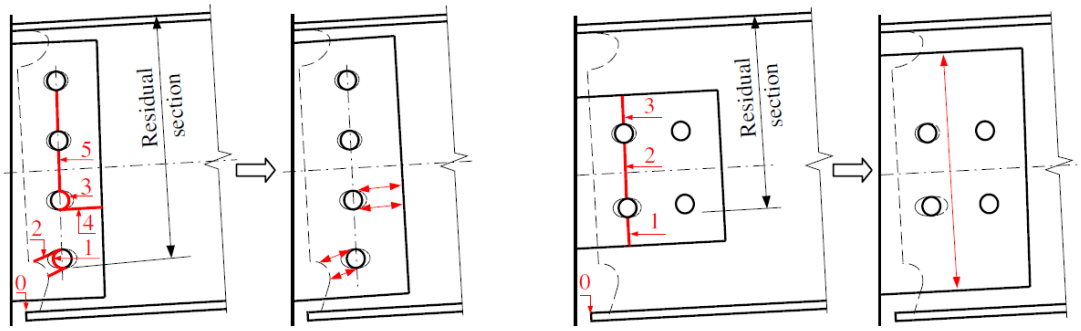

(a) Single-row bolts layout (a) Double-row bolts layout

Figure 2.15 Failure modes of web bolted connections for different layouts (Li et al. 2015)

Taking into account the effect of the concrete slab, Guo et al. (2013) carried out a test on a one-way 4-bay composite floor system under a column-missing scenario. The beam-column joints were made rigid by full weld (Fig. 2.16). The test results showed that the response of the composite assembly consisted of 6 stages: elastic stage, elastic–plastic stage, arch stage, plastic stage, transient stage and catenary stage. Beam flange buckling, weld fracture, buckling of reinforcement in slab and concrete cracking were observed during the test.

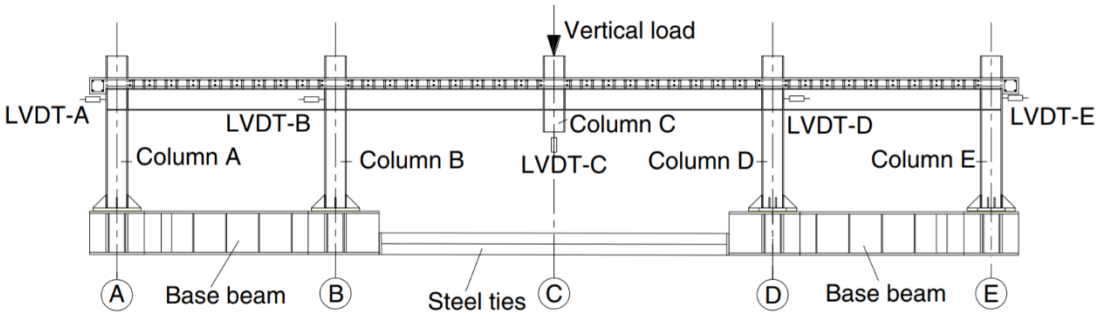

Figure 2.16 Test set-up for a beam-slab composite assembly (Guo et al. 2013)

It was concluded that the assembly showed a good resistance to progressive collapse. It was also found that horizontal restraining stiffness of the frame exerted great influence on the resistance in catenary stage.

2.2.2 Summary of the experimental studies

The existing experimental studies have highlighted the failure modes and the capability of the assembly to develop catenary action. Most of these studies investigated bare steel beam-to-column joints without considering the effect of floor slabs.

Generally speaking, the existing experimental studies and the associated numerical verifications have been limited to the response characteristics and potential failure modes. Examinations on the damage processes governing the patterns of the resistance functions and the ultimate limit on catenary action have been largely qualitative. Quantifications of the limit states of deformation defining the resistance function and methods for their calculations are still lacked.

2.3 An overview of the finite element modelling for steel joints at large deformation

In the experimental studies, finite element simulations were also performed to verify against test results. They are actually individual case-specific studies, but the commonly-used approaches can be summarised.

The models in the finite element analysis of the steel joints mainly include three-dimensional high fidelity modelling and reduced-scale modelling. The former approach usually employs solid/shell elements for all joint parts, as has been done in most verifying experimental studies; while the latter utilizes simpler elements like springs and connectors to model the detailed joint, and uses beam-column elements for connecting members.

2.3.1 High fidelity finite element modelling

Yang and Tan (2012) used general-purpose finite element package ABAQUS to model the behaviour of steel beam-to-column joints they tested (Yang and Tan 2013). As shown in Figure 2.17, their model is a quarter model due to symmetry in both directions. More importantly, the column web panel is not modelled, as it is assumed to be rigid. This is justified as the in-plane stiffness of the column web is much

higher than that of the bolted connections. To reduce the number of elements, the joint zone is modelled with solid elements, and the remaining part is modelled using general beam elements.

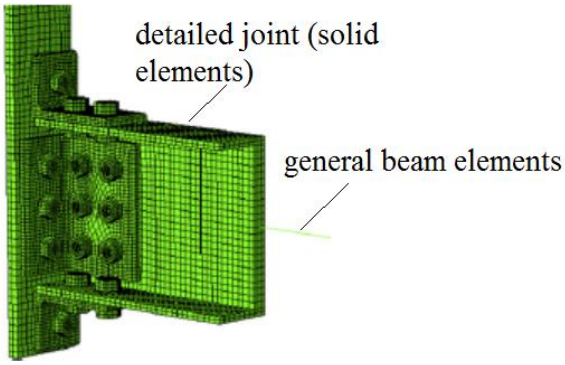

Figure 2.17 FE model of bolted joint (Yang and Tan 2012)

Li et al. (2015) created similar high fidelity models to verify against the test results carried out by the authors. The welds between beam flanges and column are not modelled, while the bolted connections are simulated in detail, as shown in Fig. 2.18.

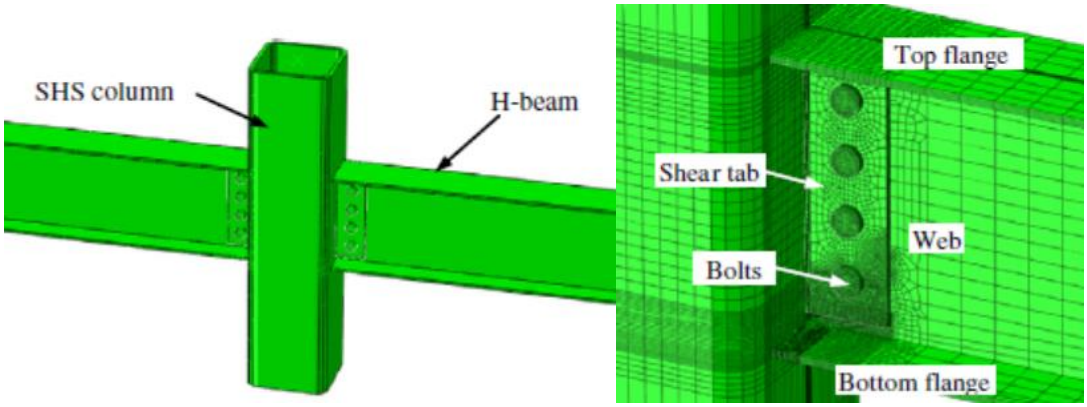

Figure 2.18 The detailed FE model of beam-tubular column (Li et al. 2015)

In the high fidelity modelling, the primary modelling challenge is the simulation of material cracking at large deflection. The ductile damage model in ABAQUS has been used in both of the studies mentioned above. It is a phenomenological model for predicting the onset of damage due to nucleation, growth and coalescence of voids.

The ductile damage model assumes the damage starts when the specified equivalent plastic strain at the onset of damage is reached. The damage evolution, which is characterised by the progressive degradation of the material stiffness, was also defined. Once the fracture strain is reached, the damaged elements will be deleted from the mesh. It is worth mentioning that the fracture criterion is dependent on mesh size. Therefore, for the degrading response, the fracture energy or a stress-displacement relationship is usually defined, instead of a stress-strain relationship.

Due to the existence of multi-surface contacts and the material fracture phenomenon, it is quite difficult to overcome the convergence problem with static solver. Therefore, the explicit dynamic solver is used to for the solution process. During the solution process, the dynamic effects can be ignored if the kinetic energy of the deformed structure is only a fraction (typically 5% and 10%) of its internal energy throughout the structural response (ABAQUS Manual version 6.12). In order to control this, the loading history is displacement-controlled, similar to the method used in the experimental tests. The appropriate time step size has to be chosen. In this way, quasi-static solution can be achieved to reasonably represent the static structural response.

In the 3D detailed models, “surface-to-surface” contact interactions are usually employed. The frictional condition is represented by the isotropic Coulomb friction model.

Khandelwal and El-Tawil (2007) used shell elements to model the steel frame joints, using the parallel explicit finite element code MPP-DYNA. In the shear connections, shear tabs are connected to columns by complete joint penetration welds, and to the beams through fillet welds. All welds are modelled using rigid point to surface constraints, see Fig. 2.19.

Within the connection region, material fracture is characterized by a micromechanical constitutive model proposed by Gurdon (1977) and its modified version. Other regions are modelled with a computationally less expensive piecewise linear J_2 plasticity model. According to the Gurdon model, the elements would be removed when the effective void volume fraction reaches a pre-defined threshold

value. This study also devoted efforts to carrying out calibration of model parameters against existing test results of plate specimens under tensile loading.

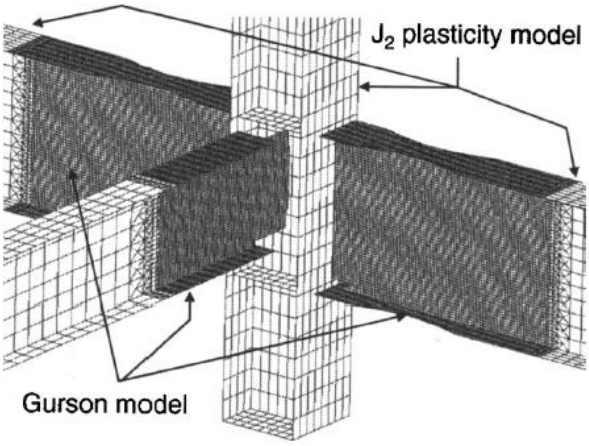

Figure 2.19 The shell element model and material definition (Khandelwal and El-Tawil 2007)

One important limitation of this finite element model is that the Gurdon model being used with shell elements means tri-axial effects are not taken into accounted. Because of the limitations, the simulation is believed by the authors to be more qualitative rather than quantitative.

2.3.2 Reduced scale finite element modelling

To reduce the computational cost and mitigate the modelling challenges, reduced scale finite element modelling is of great significance to develop. One typical example is described as follows.

Khandelwal et al. (2008) developed two-dimensional macro-based models, which utilized a combination of beam-column and spring elements, in an attempt to model the behaviour of steel frame structures. The model was implemented in commercial code LS-DYNA, and explicit dynamic analyses are conducted.

The model for commonly-used shear tab connections consists of a spring representing binding effect between the bottom beam flange and the column flange, a beam element to model bolt/shear tab interaction, and a spring which represents represent the concrete slab (Fig. 2.20). The beam element has integration points that correspond to individual bolts in the simple connection. The size of the force transfer region, l_t, is taken as the distance between the column flange and bolt line.

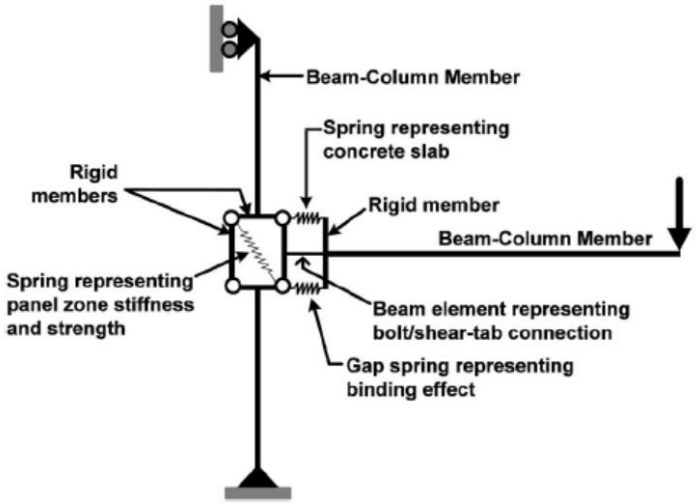

(a) The overall model

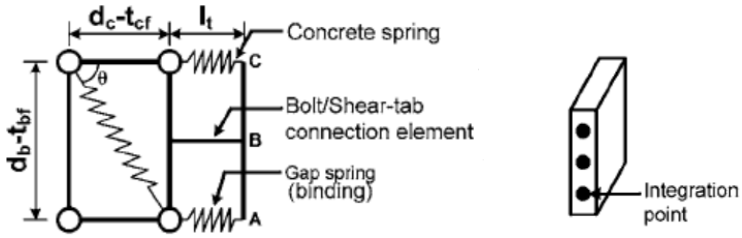

(b) The connection zone details (c) The integration points in shear connection element

Figure 2.20 The model for shear tap connections (Khandelwal et al. 2008)

The model for moment connections is simpler, as the panel zone and beam are rigidly connected (Fig. 2.21). The panel zone in both shear and moment connections is modelled by four rigid bars and a diagonal spring to enable pure shear deformation, which has been observed in past tests.

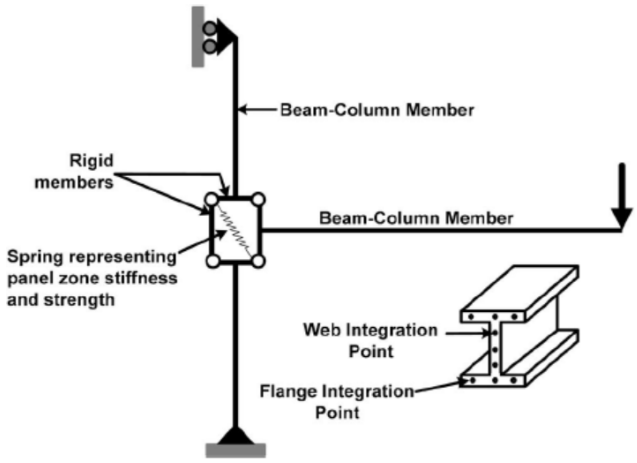

Figure 2.21 The model for moment connections (Khandelwal et al. 2008)

The spring properties and stress-strain properties at integration points of beam-column elements are specified in Fig. 2.22. For the panel zone spring, the formulations of shear stiffness and strength codified by AISC (2006) are directly used. For the beam elements, piecewise linear stress-strain curves for both tension and compression are used.

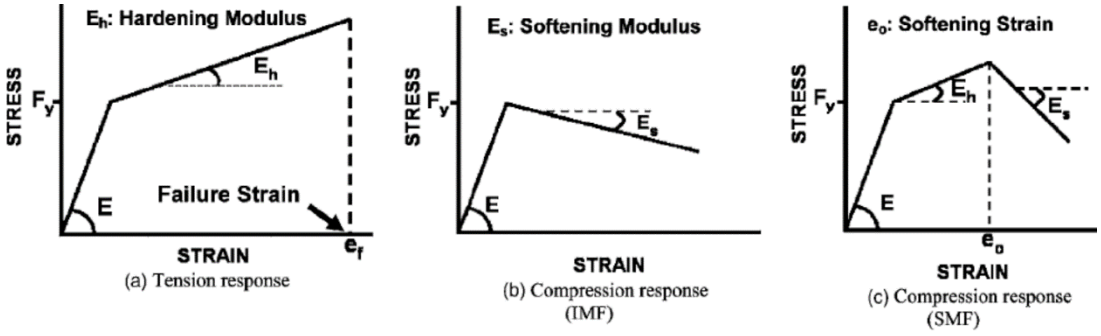

Figure 2.22 Stress-strain responses for integration points of beam elements (Khandelwal et al. 2008)

By carefully tailoring the stress-strain response at each integration point, the proposed macro-model is able to represent local behaviour such as local buckling and fracture, as described in the study. It can also capture moment-axial force interaction, which is a major concern in progressive collapse analysis.

2.4 Component-based mechanical modelling for typical joints in progressive collapse analysis

2.4.1 Component method: a classical theory

The component-based modelling method for codified use was initially proposed in the Annex J of Eurocode 3 (1998), and then was improved with modifications in Eurocode 3 (BSI 2005). It has been widely accepted for analytical modelling of various steel connections, as the method is both explicit in concept and cost-effective for application.

Basically, the component method involves a step-by-step solution procedure:

(1) The joint is properly decomposed into constituent components, according to the loading condition;

(2) The constitutive laws (force-displacement relationship), including failure criteria of each individual component should be quantitatively established;
(3) The separate components are assembled into a spring model, which is used to quantify the mechanical properties of the joint.

The component method is effectively a semi-analytical approach. The force-displacement (F-δ) relationship of each component is expressed as the follow equation, in which k_i is stiffness coefficient of the component i:

$$F_i = (k_i \cdot E) \cdot \delta_i \tag{2-1}$$

As has been illustrated before, the moment capacity and initial rotational stiffness are the two basic parameters to determine a simplified nonlinear moment-rotation (M-θ) curve. The moment capacity is determined by the minimum capacity of the components as:

$$M_{j,Rd} = (h_b - t_{fb}) \cdot \min\{F_1; F_2; \dots F_i\} \tag{2-2}$$

The force in each spring is equal to F, and the moment acting in the assembly model is equal to $F \cdot z$, where z is the lever arm or the distance between the centres of tension and compression. The initial rotational stiffness S_j is determined from the stiffness of constituent components as

$$S_j = \frac{M_j}{\varphi_j} = \frac{Fz}{(\sum \delta_i)/z} = \frac{Fz^2}{\frac{F}{E}\sum \frac{1}{k_i}} = \frac{Ez^2}{\sum \frac{1}{k_i}} \tag{2-3}$$

where k_i is the initial stiffness for joint component and z is the lever arm.

2.4.2 Standard spring assembly models

Annex J of Eurocode 3 lists the guidance of basic components that are decomposed from common joint configurations (double- and single-sided joints, beam splices) and different joint types (welded, end-plate, top and seated angle, etc.). Some of them are presented in Table 2.1.

Table 2.1 Representative basic components defined by Eurocode 3

Component number	Component feature
(1)	column web panel in shear
(2)	column web in compression
(3)	column web in tension
(4)	column flange in bending
(5)	endplate in bending
(7)	beam flange and web in compression
(8)	beam web in tension
(10)	bolts in tension

In Eurocode 3, the procedures of assembling basic components into a spring model are also proposed for typical joints. The examples of typical full-weld and end-plate connection are shown in Figures 2.23 and 2.24.

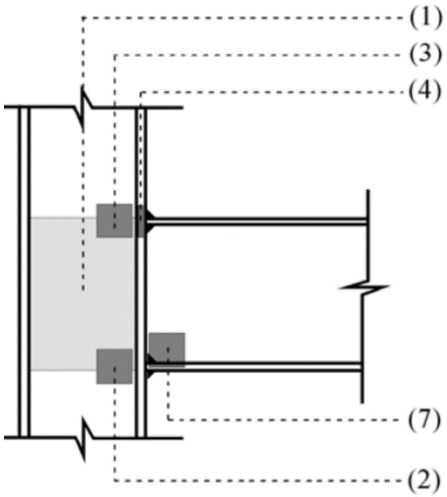

Figure 2.23 Components of full weld connections (Eurocode 3)

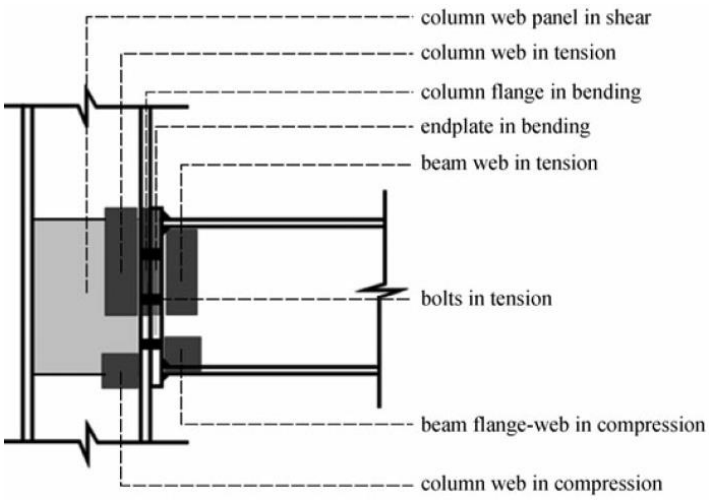

Figure 2.24 Joint components for end-plate connections

Lemonis and Gantes (2009) introduced a series of modified models to establish the complete moment-rotation relationship of typical end-plate joints and top and seated angle joints. The associated basic joints containing two types of joints are listed in Table 2.2:

Table 2.2 A list of basic components (Lemonis and Gantes 2009)

Components	**Abv.**	**Components**	**Abv.**
Column web panel in shear	cws	Bolts in shear	bs
Column web in compression	cwc	Angle leg in bearing	ab
Beam flange/web in compression	bfwc	Beam flange in bearing	bfb
Column web in tension	cwt	Seat angle in compression	sac
Column flange in bending	cfb	Top angle in bending	tab
Bolts in tension	bt	Top angle in tension	tat
End plate in bearing	epb	Web angle in bending	wab
Beam web in tension	bwt	Beam web in bearing	bwb

For the case of end-plate connections, the EC3 model is shown in Fig 2.25, and it can be extended for the prediction of the complete moment-rotation curve. The difference between the two models lies in the absence of individual “bolts in tension” components from the second model, since the tensile deformability of the bolts has

been incorporated to the adjacent “column flange in bending” and “end-plate in bending” T-stub components.

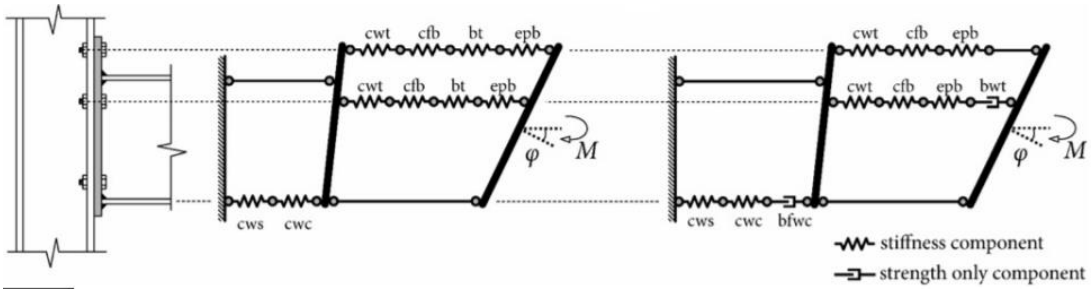

(a) The EC3 model for end plate connection (b) The extension model

Figure 2.25 The EC3 model for end-plate connection and its extension for the estimation of the complete M–ϕ curve (Lemonis and Gantes 2009)

Besides the Eurocode 3 model, other alternative mechanical models are also available. Huber and Tschemmernegg (1998) proposed a model for end-plate connections (referred to as the Innsbruck model). In this model, an additional rigid element that separates the components of the column panel from the connection components is introduced. Thus it becomes possible to measure separately the part of the total joint rotation originating from each of them. The fact that the column panel components both in the tension and the compression zone are grouped separately and operate independently from the respective connection components reflects more closely the real joint behaviour. The disadvantage of this model compared with the Eurocode 3 one lies in that it’s more complex solution that does not allow simple analytical expressions to be realized.

Taib and Burgess (2013) proposed another model (referred to as the Coimbra model), in which the components are aligned. In their model, the interactions between tensile and compressive components and between column panel and connection components are allowed. This model does not reflect closely the actual joint behaviour but on the other hand it facilitates easier computer programming of the model. Figure 2.26 illustrates the comparison of the two models.

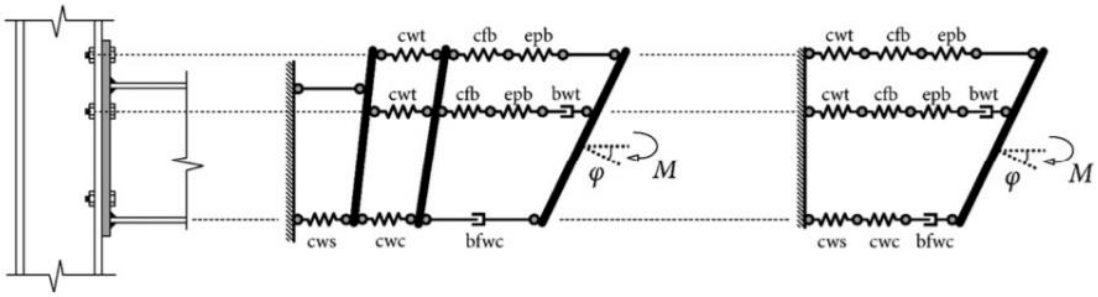

(a) The Innsbruck model (b) The Coimbra model

Figure 2.26 The Innsbruck model and Coimbra model for end-plate connections

For the top and seated angle joint, the EC3 models are shown in Fig. 2.27.

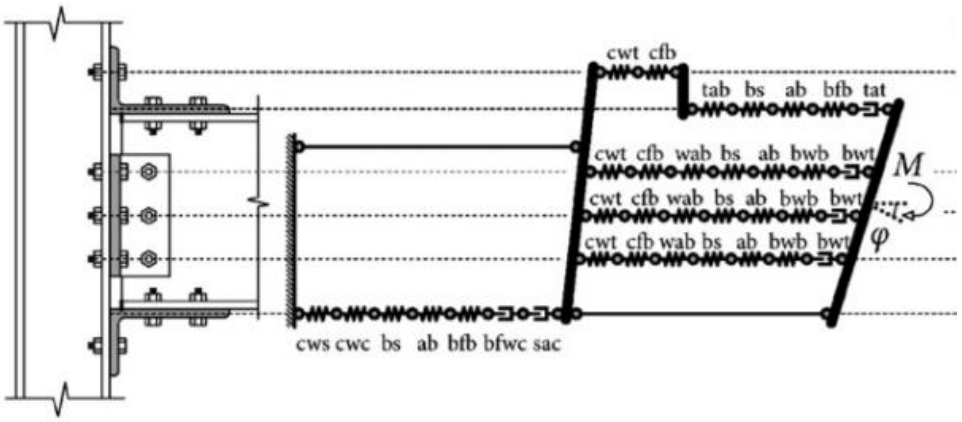

(a) The non-aligned EC3 model for top and seated angle joint

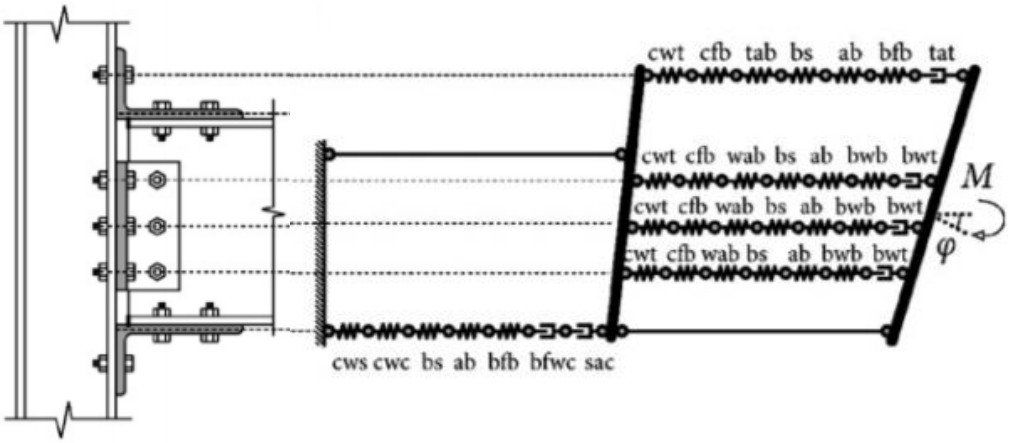

(b) The non-aligned EC3 model for top and seated angle joint

Figure 2.27 The EC3 model for top and seated angle joint: non-aligned and aligned.

The respective Innsbruck model for the top and seated angle connections is depicted inFigure 2.28, and it is characterized by the additional rigid element that separates the column panel components from the connection components. Likewise, the respective Coimbra model for angle connections is shown in Figure 2.29.

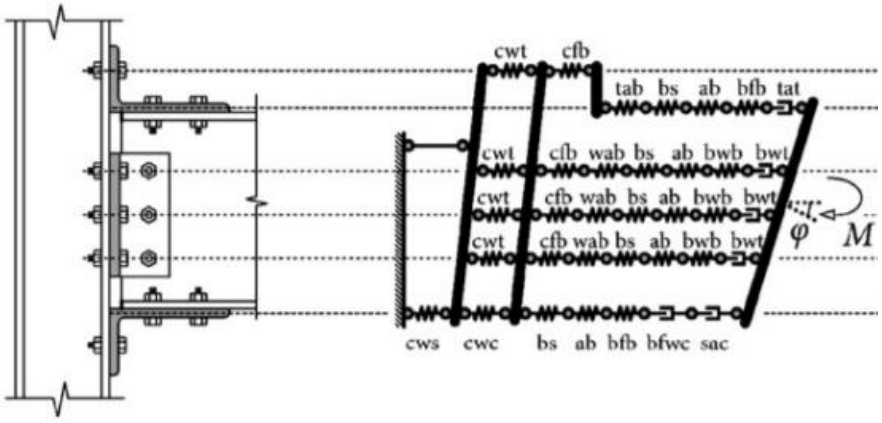

Figure 2.28 The Innsbruck model for top and seated angle joint

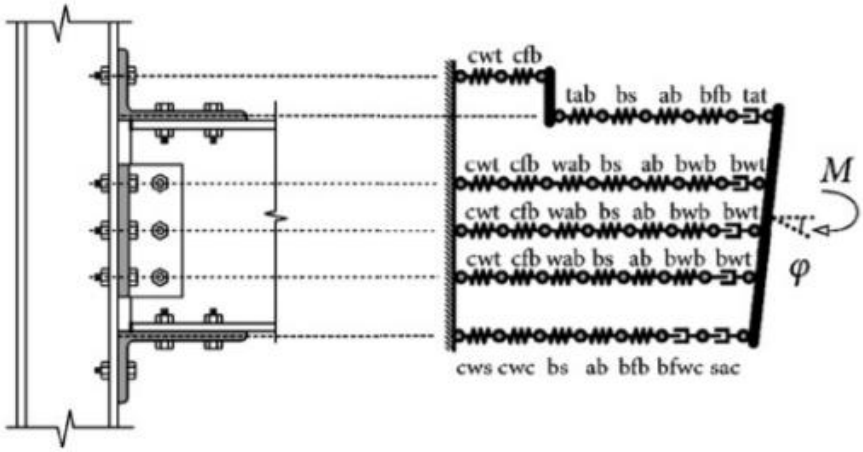

Figure 2.29 The Coimbra model for top and seated angle joint

The general layout of the spring assembly of the above model can be concluded as follows:

1) Eurocode 3 model: the tensile and compressive springs are separated;
2) Innsbruck model: the springs of the column panel and the connection are separated;
3) Coimbra model: all springs interact without any rigid element between them.

Regarding the alignment of the springs in the first row in extended end plate connections and angle connections, the following types are distinguished:

1) Aligned model: all the springs of the first row are aligned with the bolt axis;
2) Non-aligned model: the springs corresponding to components of the column panel are aligned with the bolt axis while the springs corresponding to components of the connection are aligned with the beam flange or the horizontal leg of the angle.

2.4.3 Simplified component models by using assembled components

As can be seen, the standard component-based models involved many basic components, thus making the analysis complicated. Actually, the model can be simplified by using equivalent components, which are assembled by several basic components. These are called critical components herein, which does represent the loading mechanism in particular local regions of the joint.

Generally, there are one or several critical components that provide the dominant contribution to the ultimate global deformation at large deflection. With regard to the other components, their deformation engagement is surely distinct within the normal range of plastic deformation. However, when the joint response enters large deflection regime under extreme loading, the deformation of secondary components becomes almost negligible compared to that of the critical components.

One example is the component representing the joint panel zone in shear, which is essential to be considered in conventional design and analysis. When the double-sided joint is subjected to large deflection, the shear deformation will be relatively limited due to the following two reasons:

(1) The shear deformation of the panel zone is, by its nature, caused by the compression near the beam top flange and the tension near the bottom flange. With the increase of post-yield deflection and upwards shifting of the neutral axis, the bending moment will degrade, and the catenary axial force will increase. Consequently, the gap between the compression and tension will be greatly reduced, thereby making the joint panel zone subjected to much less shear force.

(2) At large deflection, the expected local damages in the connection zone naturally mitigate bending moment capacity as compared to conventional analysis which doesn't involve these failures. Thus, the shear deformation is accordingly less crucial when considered.

(3) The column web is usually reinforced by transverse stiffeners or supplementary web plates. Hence, the shear stiffness of the panel zone will be significantly enhanced. This will further reduce the shear deformation.

Based on the above reasons, the shear deformation of the joint panel zone can be reasonably neglected under large deflection (Fig. 2.30). It is justified to exclude this particular component from the joint mechanical model.

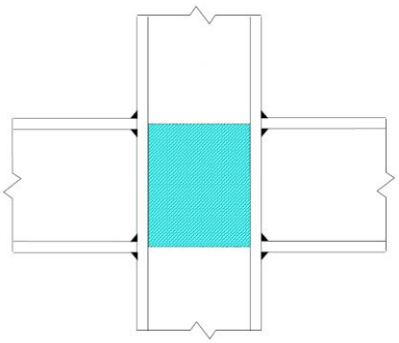

Figure 2.30 Joint panel zone in shear

On the other hand, the critical components are often the weakest parts within the joints. As a result, they are actually governing the overall deformation capacity and limiting the load resistance. Therefore, it is of great importance to identify and investigate the constitutive properties of these critical components, so as to facilitate the modelling of the global joint behaviour at large deflection.

The aforementioned critical components of a particular joint could be a combination of some basic components, such as bolt in tension, angle plate in bending, beam web in tension, etc. The constitutive laws of the basic components under axial action are simple and straightforward. They have been well understood and defined in the existing studies or codified guidance. However, the assembled critical components can exhibit complicated behaviour, with several different potential failure mechanisms. Various material and geometrical parameters could influence the failure

modes, and then the resistance and deformability. This necessitates detailed modelling and analysis of the assembled critical components.

The existing studies have seen efforts devoted to investigating the assembled components, by means of mechanical modelling and experimental studies to successfully establish their force-displacement relationships. The following sections are presenting the review of the studies, and extracting useful findings which may be further utilised for the joint analysis at large deflection.

For instance, regarding a standard end-plate connection subjected to pure negative bending, the components that contribute to the flexural capacity include column web in compression, column web in tension, column web in shear, column flange in bending and end-plate in bending. As shown in Fig. 2.31, the last two are usually analysed using T-stub analogy.

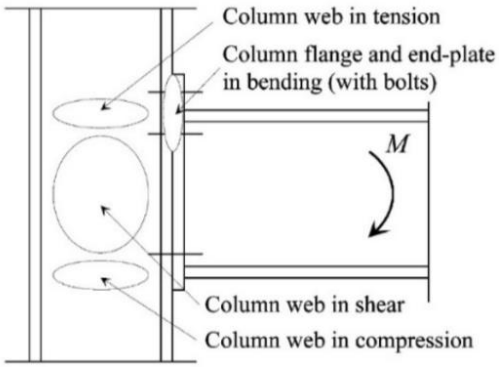

Figure 2.31 Simplified component model of end-plate connections

As an example, Shi and Chen (2017) analysed the moment-rotation behaviour of the ultra-large capacity end-plate joint, a new joint form used in steel frames with large spans or heavy loads (Fig. 2.32). The basic components such as beam flange in compression (bfc), column web in shear (cws) and column web in compression (cwc) are three basic components which have been investigated and specified in Eurocode 3. To investigate the complicated components of end plate in tension (ept) and column flange in tension (cft), they are made equivalent to a new cruciform-stub, of which the force-displacement behaviour was studied (Fig. 2.33).

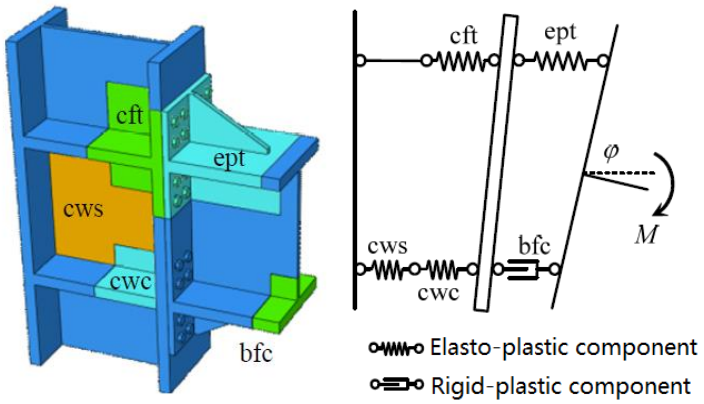

Figure 2.32 Components model for ultra-large capacity end-plate connections (Shi and Chen 2017)

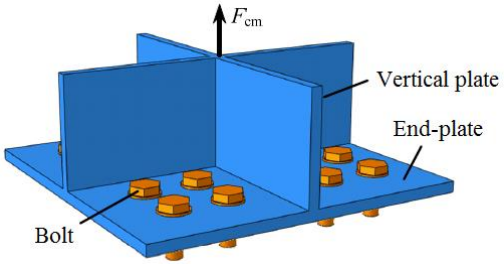

Figure 2.33 The equivalent cruciform stub (Shi and Chen 2017)

Yang et al. (2015) developed simplified component-based models to establish force-displacement curves for composite beam-column joints, see Fig. 2.34.

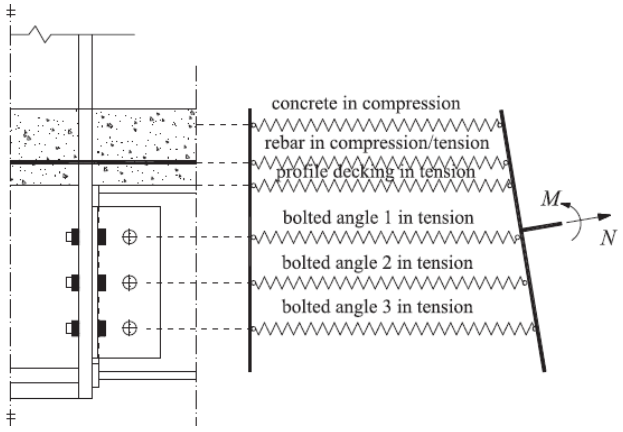

(a) The component model for web cleat composite middle joint

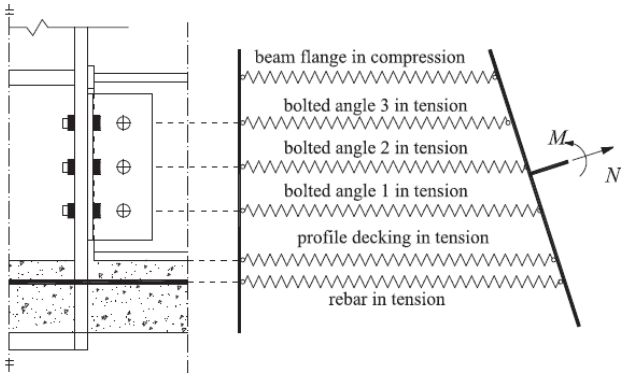

(b) The component model for web cleat composite side joint

Figure 2.34 Simplified component models for composite joints (Yang et al. 2015)

Different from the complicated standard component model, the simplified component models by the authors only involved the following critical components:

1) Bolted angles in tension (bt);
2) T-stub in tension (tst);
3) Beam flange and web in compression (bfwc);
4) Concrete in compression (cc);
5) Rebar in compression/tension (bct);
6) Profile decking in tension (pdt).

These critical components are investigated separately, before being assembled together for further analysis.

2.4.4 Application of component method modelling to the progressive collapse analysis

It is worth noting that there exist some important characteristics while applying the conventional component method to the progressive collapse problem. Firstly, due to the large deflection involved in the progressive collapse situation, the damage limits of individual components should be well defined, before they can be put into a useable assembly. Secondly, different from normal joint analysis which mainly considers pure bending, the axial force will be so considerable at large deflection and must be accounted for. Thus, the corresponding mechanical model should also be devised to incorporate the interaction between the axial force and bending moment.

2.5 Existing analytical frameworks for the resistance functions of the double beam assembly with a middle joint

The establishment of the resistance function can contribute to engineering design practice or further analysis. One straightforward and useful application is to fit into the single-degree-of-freedom (SDOF) model which is subjected to dynamic loading. Thus, it will pave an effective and efficient way to investigate the effects of load resistance patterns on the dynamic resistance and hence any dynamic increase factor (DIF) could be incorporated.

In order to achieve the resistance functions of the double beam assembly with a middle joint, the existing solutions can be divided into two categories, namely the direct solution and the indirect solution. Here two case studies are reviewed in detail to illustrate how the existing analytical frameworks are performed.

2.5.1 Direction solution example

The simplified model proposed by Hou and Yang (2014) concerned the critical points, and made use of conventional RC structure theories and a series of simplifications to quantify the points. They used conventional RC structural analysis to quantify the characteristic points, and produced the multi-linear load-deflection relation.

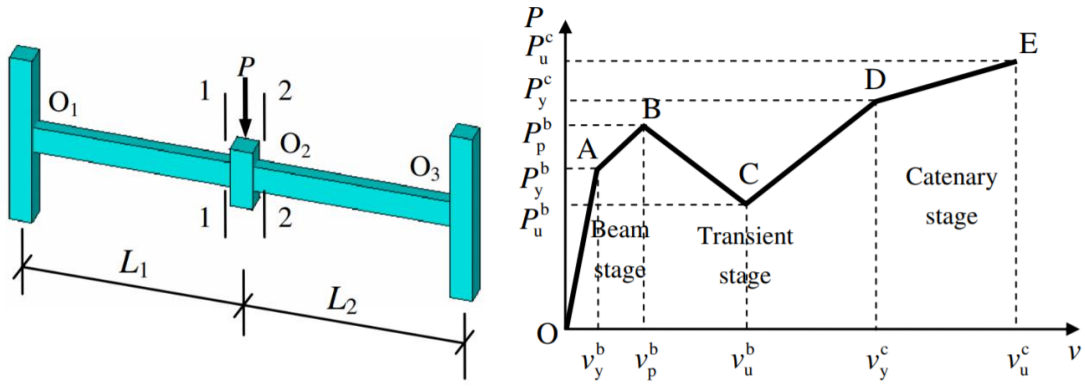

(a) The RC double beam assembly (b) The multi-linear load-deflection response

Figure 2.35 Simplified resistance function curve of the substructure (Hou and Yang 2014)

The beam stage (Line O-A-B)

The first yield (point A) is reached when the longitudinal reinforcement yields on both sides of the removed column. Based on strain compatibility and moment equilibrium, the first yield moment M_{y2} is obtained as follows, where ξ is the relative depth of the compressive zone.

$$M_{y2} = \frac{\xi^2 h_0^2}{2\alpha_E(1-\xi)} f_y b \left(1 - \frac{\xi}{3}\right) + \frac{\xi h_0 - a_s'}{h_0(1-\xi)} f_y A_s'(h_0 - a_s') \tag{2-4}$$

According to elastic theory, the vertical load at Point A is:

$$P_y^b = \frac{(L_1 + L_2)^3}{2L_1^2 L_2^2} \cdot M_{y2} \tag{2-5}$$

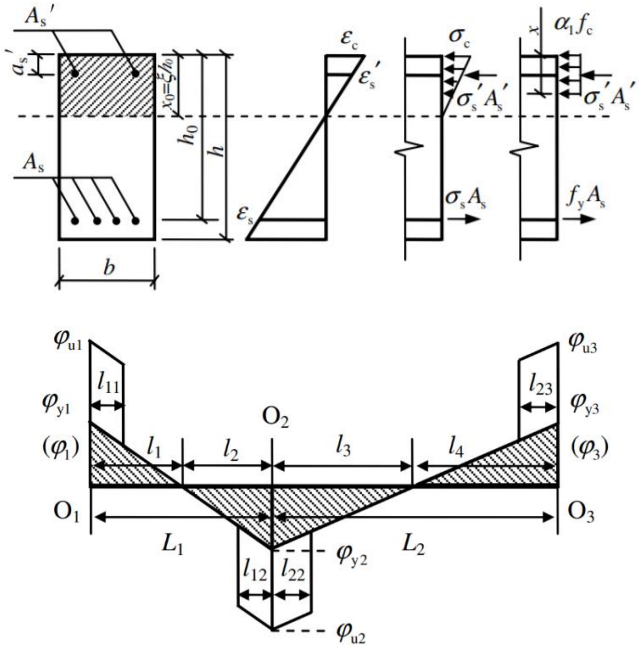

Figure 2.36 The section analysis and curvature distribution along the RC beam (Hou and Yang 2014)

Assume that the distribution of the sectional curvatures is linear at Point A. By further calculating moments of sections on the sides of two edge columns, the associated curvatures $\varphi_{1(3)}$ can be obtained (Fig. 2.36). Therefore, the deflection can be obtained by integration of the curvature along either beam.

$$v_y^b = \frac{\varphi_{1(3)} l_{1(4)}}{2} \left[L_{1(2)} - \frac{l_{1(4)}}{3} \right] + \frac{\varphi_{y2} l_{2(3)}^2}{6} \tag{2-6}$$

At point B, the depth of compressive zone is approximated to be $2a_s'$. This simplifies the calculation of bending moments at mid-span (M_{p2}) and support ends (M_{p1} and M_{p3}). The corresponding load can be obtained from:

$$P_p^b = \frac{M_{p1} + M_{p1}}{L_1} + \frac{M_{p2} + M_{p3}}{L_2} \tag{2-7}$$

By calculating the curvatures along the beam, the deflection at Point B can be obtained as

$$\begin{aligned} v_p^b = {} & \frac{\varphi_{1(3)} l_{1(4)}}{2}\left[L_{1(2)} - \frac{l_{1(4)}}{3}\right] + \frac{\varphi_{y2} l_{2(3)}^2}{6} \\ & + \left[\varphi_{p1(3)} - \varphi_{y1(3)}\right] l_{11(23)}\left[L_{1(2)} - \frac{l_{11(23)}}{2}\right] \\ & + \frac{\left(\varphi_{p2} - \varphi_{y2}\right) l_{12(22)}^2}{2} \end{aligned} \tag{2-8}$$

For the equivalent plastic hinge lengths involved in the equation, the empirical formulation given by Corley (1966) is adopted as:

$$l \ = 0.5h_0 + 0.2\sqrt{h_0}(z/h_0) \tag{2-9}$$

where h_0 is the effective beam depth and z is the distance from the critical section to the contraflexure point.

The transient stage (Line B-C-D)

The load and deflection at point C is simplified as $P_u^b = 0.85P_p^b$, $v_u^b = 10v_y^b$ with reference to previous studies.

Point D represents the ultimate state of the transient stage. Assume $L_1 \leq L_2$, the deflection and load at this point are obtained as

$$v_y^c = L_1 \cdot \sqrt{\left(\varepsilon_y'\right)^2 + 2\varepsilon_y'}, \qquad P_y^c = \frac{(L_1 + L_2)v_y^c}{L_1 L_2} \cdot f_y(A_s + A_s') \tag{2-10}$$

Catenary stage (Line D-E)

Point E represents the ultimate state of the catenary stage. At Point E, the steel rebars in the plastic hinge zone all reach f_u, so the resistance is simply expressed as follows, where A_{th} is the rebars area of the whole section.

$$P_u^c = \frac{(L_1 + L_2)v_u^c}{L_1 L_2} \cdot f_u A_{th} \tag{2-11}$$

The stress and strain of steel rebars outside the plastic hinge zone are assumed to be the yield stress and the strain at onset of strain hardening (ε_y'). The ultimate deflection v_u^c can be determined from the following geometric equation as:

$$(v_u^c)^2 + L_1^2 = L_1 + (L_1 - l_{11} - l_{12})\varepsilon_y' + (l_{11} + l_{12})\varepsilon_{rup} \tag{2-12}$$

2.5.2 The indirect solution example

Del Savio et al. (2009) proposed a generalized component-based model for the joint subjected to bending moment and axial force. The model contains three rigid bars representing the column centreline (support bar), the column flange centreline (b_2) and the beam end (b_1). These rigid bars are connected by a series of springs that model the joint components (Fig. 2.37).

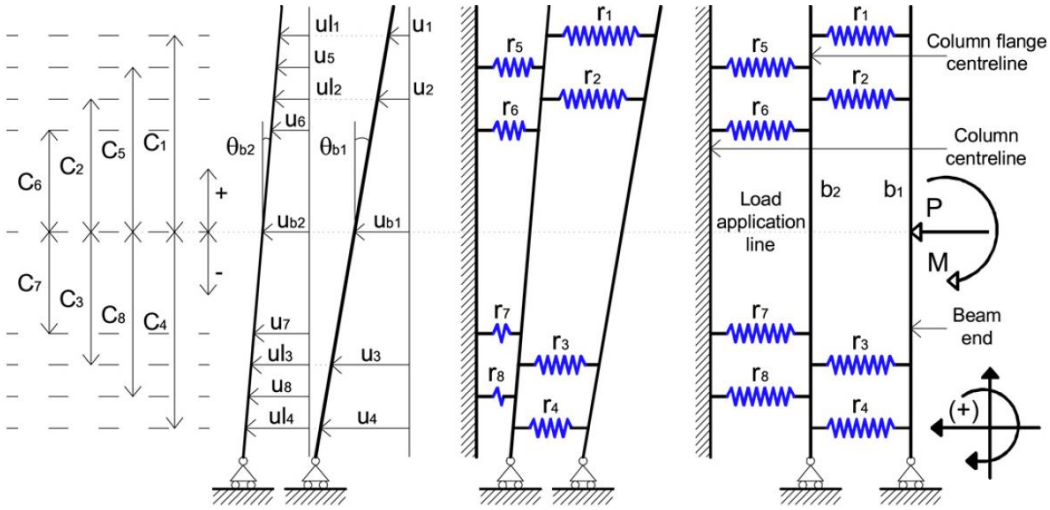

(a) Coordinates (b) deformed configuration (c) Original configuration

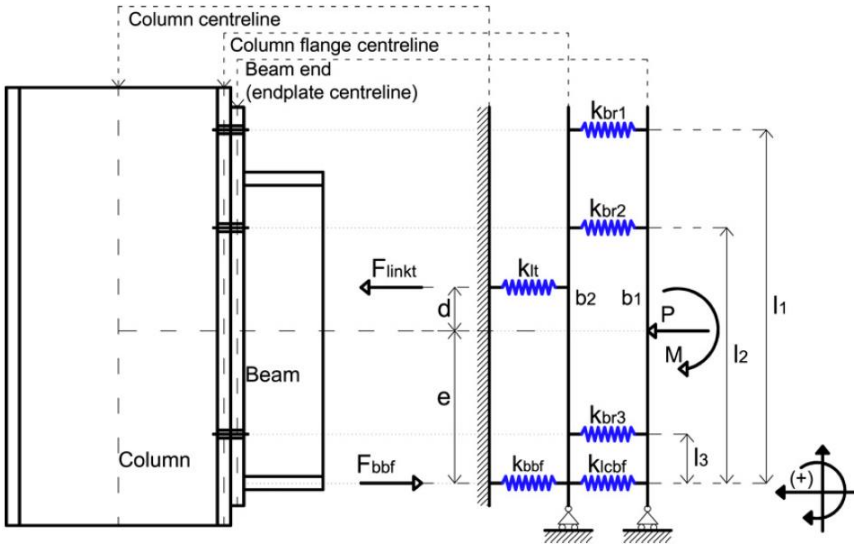

(d) End-plate connection example

Figure 2.37 The generalised model under *M-N*, proposed by Del Savio et al. (2009) and an example of end-plate connection example

With all the component behaviour properly defined, the rotation and displacement can be analytically solved. The main goal is to generate solutions using equilibrium and deformation compatibility equations, without executing numerical simulation of the proposed model.

The energy principle was used to formulate the model stiffness matrix and the equilibrium equations. The total energy Π is equal to the system strain energy U subtracting the total load potential W:

$$\Pi = U - W = \left[\sum_{i=1}^{ns} \frac{1}{2} k_i \delta_i^2\right] - [P(u_{b1} - u_{b2}) + M\theta_{b1}] \tag{2-13}$$

Then, the equilibrium equations can be derived from the functional stationary condition:

$$\frac{\partial \Pi}{\partial d_i} = 0; d_i = u_{b1}, \theta_{b1}, u_{b2}, \theta_{b2} \tag{2-14}$$

The stiffness matrix and internal load vector can also be derived as:

$$K_{ij} = \frac{\partial^2 U}{\partial d_i \, \partial d_j}, F_i = \frac{\partial U}{\partial d_i};\ d_i = u_{b1}, \theta_{b1}, u_{b2}, \theta_{b2} \tag{2-15}$$

Therefore, the equilibrium equations can be expressed based on the symmetric stiffness matrix. Thus, the moment-rotation curve can be predicted, for any axial force level.

Based on the work by Del Savio et al. (2009), Stylianidis and Nethercot (2015) developed a 2-rigid bar spring model, and derived a closed-formed solution of the connection rotation and axial deformation (*M-N-φ* and *M-N-u* relationships). The component-based model by Stylianidis and Nethercot (2015) consists of the following elements (Fig. 2.38):

1) Rigid bars 1 and 2, which separate the tension and compression zones;
2) Rigid links K_R^T and K_R^C that transform the compression and total tensile internal forces;
3) Component springs in tension $K_{t,i}$;
4) Component spring in compression K_R^T, located at the centre of tension.

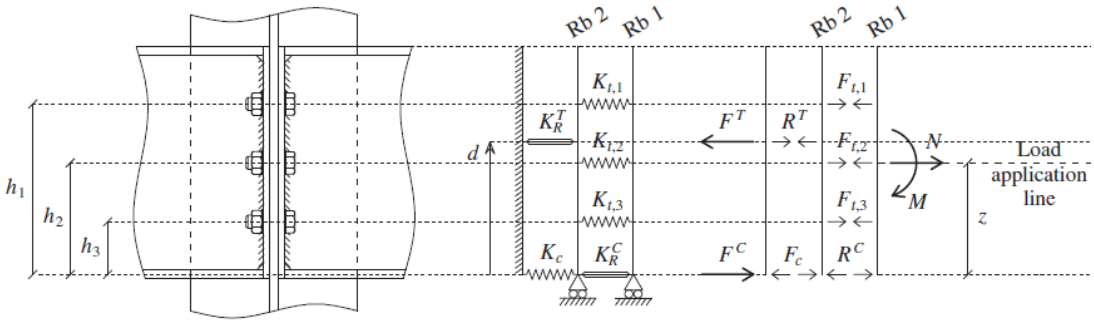

(a) Connection geometry (b) spring model (c) load distribution

Figure 2.38 The component model under *M-N*, proposed by Stylianidis and Nethercot (2015)

Global equilibrium equations

Equilibrium of rigid bars 1 and 2 leads to the following relations:

$$M + N \cdot z = R^T \cdot d = \sum F_{t,i} h_i$$
$$R^C + N = R^T + R^C - F_c = \sum F_{t,i} \quad (2\text{-}16)$$

From the above relations, the support reactions and connection equivalent lever-arm can be defined as:

$$F_c = \frac{M + Nz}{d} - N$$
$$d = \sum F_{t,i} h_i \Big/ \sum F_{t,i} \tag{2-17}$$

Deformation modes

Four deformation modes are shown as below. Mode (I) defines the activation of compressive components only, which is unlikely to happen in progressive collapse scenarios. Mode (II) represents the typical situation when both the tension and compression zones are activated, which is mostly occurring during the post-yield response stage. In mode (IV) the compressive force is zero, which represents the situation in catenary stage. In mode (III), the compressive internal force and the axial translation are both zero. It is the limit between modes (II) and (IV). Fig. 2.39 illustrates the four deformation modes.

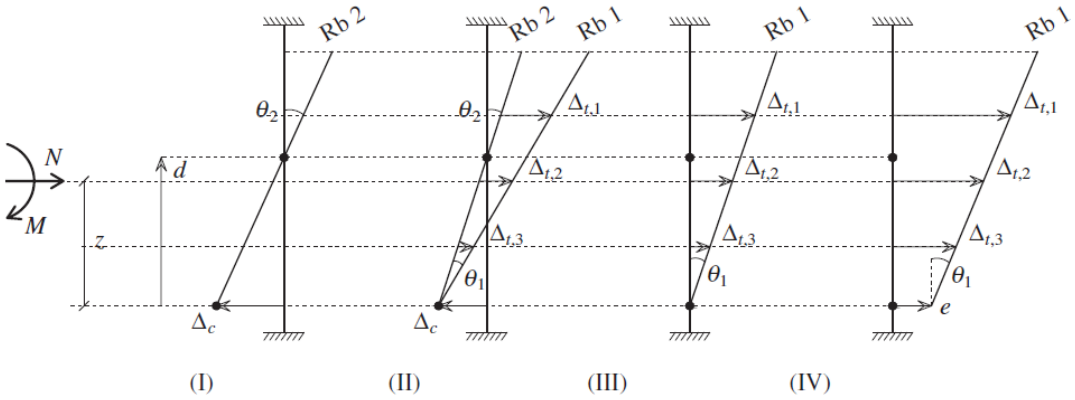

Figure 2.39 Connection deformation modes (I) - (IV) (Stylianidis and Nethercot 2015)

From the deformation configuration, the following deformation equations can be obtained:

$$\theta_1 = \frac{\Delta_{t,i} - e}{h_i};\ \theta_2 = \frac{\Delta_c}{d} \tag{2-18}$$

Definition of component behaviour

As a crude treatment, all of the component properties are approximately bi-linear (Fig. 2.39). And the unloading behaviour is considered for the potential deformation

reversal of some components. A generalized load-deflection (*F*-*Δ*) equation is proposed as follows:

$$\Delta = \frac{F - F_{Rd}}{K} + \frac{F_{Rd}}{K^e} + \Delta^{pl} \leq \Delta^f \tag{2-19}$$

In the above equation, K^e is the elastic stiffness, F_{Rd} is the design resistance and $\Delta^{pl}$is the plastic residual deflection. When $F \leq F_{Rd}, K = K^e$; if $F > F_{Rd}, K = K^p$, where K^p is the plastic stiffness. For the incremental loading, $\Delta^{pl} = 0$; for the unloading at the intersection point, $\Delta^{pl} = \Delta^{int} - F^{int}/K^e$. The deformation limit Δ^f is sourced from relavant studies.

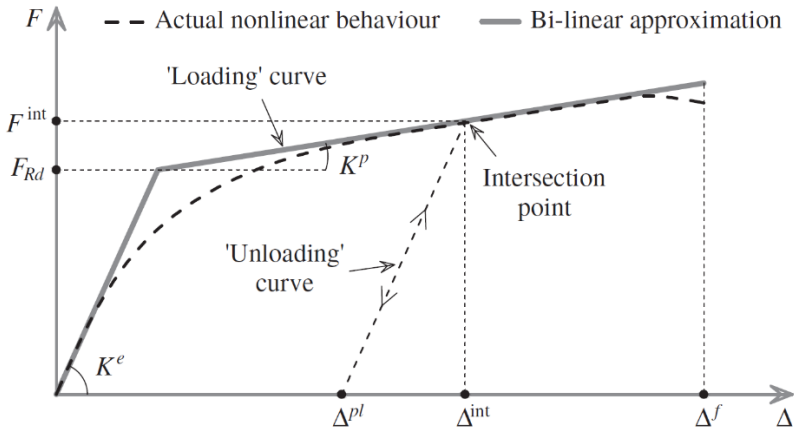

Figure 2.40 Bilinear approximation of component behaviour (Stylianidis and Nethercot 2015)

Components assembly and solution

Combing all the equilibrium and deformation compatibility equations, and the component behaviour functions, the rotations $\theta_1, \theta_2, \theta_3$ can be solved, and expressed as functions of the known parameters.

The overall connection rotation (φ) is the sum of relative rotations of the rigid bars:

$$\varphi = \theta_1 + \theta_2 + \theta_3 = M\alpha_1 + Nz\beta_1 - \gamma_1 \tag{2-20}$$

where α_1, β_1 and γ_1 are parameters related to the connection configurations.

The connection axial deformation may be approximated by considering only the deformations of the tension and compression regions as:

$$u = \theta_1 z_1 - \theta_2 (d - z_1) + e \tag{2-21}$$

By substituting the previous solutions of θ_1, θ_2 and e, the *M-N-u* relationship can be obtained as:

$$u = M\alpha_2 + Nz\beta_2 - \gamma_2 \tag{2-22}$$

The above *M-N-φ* formulations can be applied to any combination of bending moment and axial force. The full range joint behaviour can be traced by an iterative step-by-step procedure (e.g. the spreadsheet method). In each step, the component deformations are compared to the associated deformation limit. In this way, the overall deformation limit of the connection may be determined.

Using the above joint modelling results, Stylianidis et al. (2015) further developed a calculation method to formulate the complete behaviour of double beam substructure under column loss. In their analytical beam model, the joint responses are represented by rotational springs and a horizontal axial spring, as shown in Fig. 2.41.

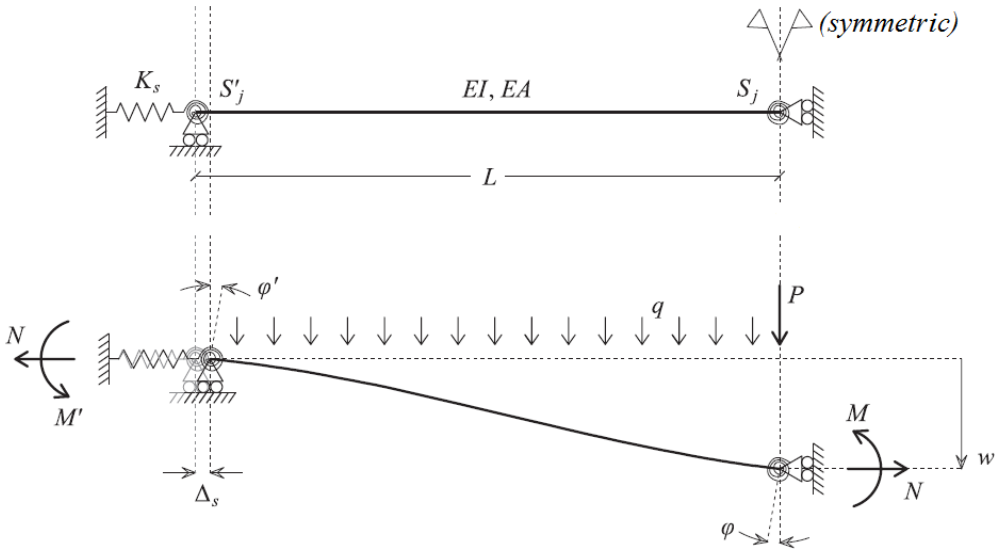

Figure 2.41 The simplified structural representation (Stylianidis et al. 2015)

Considering a composite beam exhibits different behaviours under sagging and hogging moments (Fig. 2.42), it is divided into two sections with different stiffnesses. The uncracked stiffness is considered in the sagging moment region, while the reduced cracked stiffness is considered in the hogging moment region.

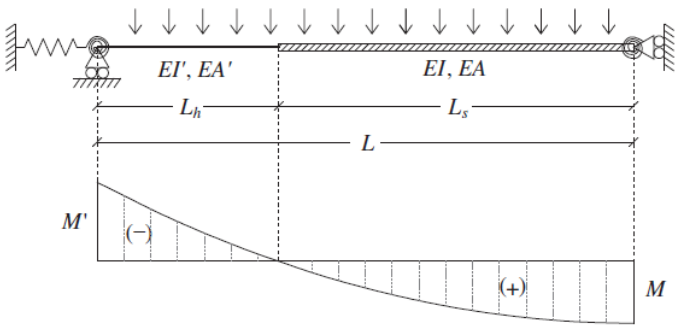

Figure 2.42 Modelling of composite beam with non-uniform stiffness (Stylianidis et al. 2015)

Using traditional stiffness method and the concept of releasing clamped structures, the nodal forces are obtained in a matrix form. For simplicity, the inflection point is assumed to be at the mid-span ($L_h = L_s = L/2$). Thus, the following equations can be established:

$$\begin{bmatrix} -M' \\ -M^0 \\ Q^0 \end{bmatrix} = \begin{bmatrix} \frac{4EI'}{L_h} & \frac{2EI'}{L_h} & \frac{-6EI'}{L_h^2} \\ \frac{2EI'}{L_h} & \frac{4EI'}{L_h} & \frac{-6EI'}{L_h^2} \\ \frac{-6EI'}{L_h^2} & \frac{-6EI'}{L_h^2} & \frac{12EI'}{L_h^3} \end{bmatrix} \begin{bmatrix} \varphi' \\ \varphi^0 \\ w^0 \end{bmatrix} + \begin{bmatrix} -\frac{qL_h^2}{12} \\ \frac{qL_h^2}{12} \\ -\frac{qL_h}{2} \end{bmatrix} \tag{2-23}$$

$$\begin{bmatrix} M^0 \\ -M \\ -Q^0 \\ Q \end{bmatrix} = \begin{bmatrix} \frac{4EI}{L_s} & \frac{2EI}{L_s} & \frac{6EI}{L_s^2} & -\frac{6EI}{L_s^2} \\ \frac{2EI}{L_s} & \frac{4EI}{L_s} & \frac{6EI}{L_s^2} & -\frac{6EI}{L_s^2} \\ \frac{6EI}{L_s^2} & \frac{6EI}{L_s^2} & \frac{12EI}{L_s^3} & -\frac{12EI}{L_s^3} \\ -\frac{6EI}{L_s^2} & -\frac{6EI}{L_s^2} & -\frac{12EI}{L_s^3} & \frac{12EI}{L_s^3} \end{bmatrix} \begin{bmatrix} \varphi^0 \\ \varphi \\ w^0 \\ w \end{bmatrix} + \begin{bmatrix} -\frac{qL_s^2}{12} \\ \frac{qL_s^2}{12} \\ -\frac{qL_s}{2} \\ -\frac{qL_s}{2} \end{bmatrix} \tag{2-24}$$

The effects of axial force are considered by introducing the equilibrium conditions, as shown in Fig. 2.43, where Z represents the distance between the centroids of the two cross-sections in the hogging and sagging moment regions.

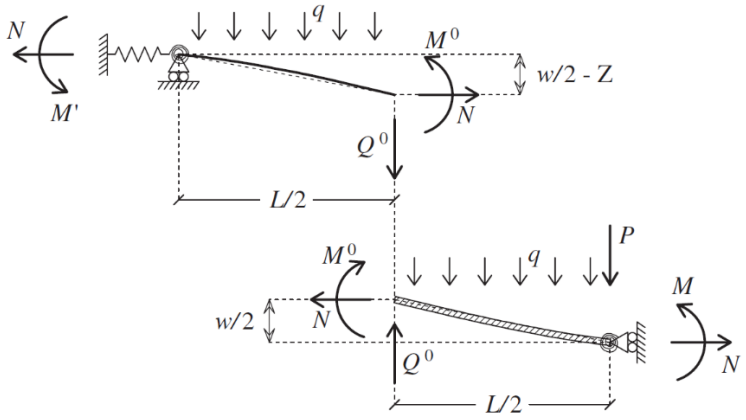

Figure 2.43 The equilibrium diagram of the single span beam at large deflection (Stylianidis et al. 2015)

The equilibrium equations are expressed as:

$$M' = qL^2/8 + Q^0\frac{L}{2} - M^0 - N(\frac{w}{2} - Z)$$

$$M = -qL^2/8 + Q^0\frac{L}{2} + M^0 - \frac{Nw}{2} \tag{2-25}$$

$$Q^0 = \frac{qL}{2} + P$$

Combining the above equations with the following formulae of the connection deformations obtained from previous study (Stylianidis and Nethercot 2015), the bending moment and axial force can be solved. They are expressed as functions of gravity loading (q, P) and the beam deflection (w) as:

$$\varphi' = M'\alpha_1' + Nz'\beta_1' - \gamma_1'$$

$$\varphi = M\alpha_1 + Nz\beta_1 - \gamma_1$$

$$u' = M'\alpha_2' + Nz'\beta_2' - \gamma_2' \tag{2-26}$$

$$u = M\alpha_2 + Nz\beta_2 - \gamma_2$$

Due to geometric changes, the total axial deformation may be approximated with respect to the vertical deflection $\Delta = w^2/2L$. The total axial deformation can be further expressed as:

$$\frac{w^2}{2L} = u' + u + \Delta_a + \Delta_b \tag{2-27}$$

Here, u' and u represent the horizontal deformations of the support. Δ_a denotes the axial deformations of the beam section, and it can be obtained using an equivalent axial stiffness as:

$$\Delta_a = \frac{N}{K^a} = \frac{N}{\frac{1}{K^s} + \frac{L}{EA}} \tag{2-28}$$

where K^s is stiffness of the axial support and Δ_b is an additional deformation due to bending of the beam. Provided the reference line coincides with the hogging neutral axis, only the deformation due to sagging moment is considered as:

$$\Delta_b = \frac{Z}{EI}\int_0^{L_s} M_x dx \tag{2-29}$$

Having obtained each of the deformation components, the total axial deformation can be finally achieved and expressed in terms of external loading *M* and *N*. Thus, the vertical load resistance can be easily calculated from the equilibrium equations, with known deflection and internal forces.

2.6 Concluding remarks

In this chapter, the current researches on the performances of the double beam assembly with typical steel joints in the progressive collapse scenario are reviewed. This includes relevant experimental studies, numerical modelling studies by using finite element analysis and the conventional component-based methods. The suitability and potential issues when applying the component method to analyse the joint behaviour and the overall resistance of beam assemblies in a progressive collapse scenario are discussed.

The existing experimental studies highlighted the local failure characteristics in the critical joint connection zone, and their effects on the global double beam assembly response. However, the experimental studies are generally lacking in attempts for the

quantification of joint behaviour and assembly resistance function, especially concerning the joint deformation limits and the associated effects on overall response.

The current analytical frameworks to establish the full-range resistance function of a double beam assembly under column loss are reviewed in detail. The direct solution example shows a sophisticated process of calculating critical points in the response curve; while the indirect solution example attempts to solve the joint behaviour under axial force and bending moment, and then use simplified spring model to work out the global resistance function. Both of them are complicated and time-consuming to carry out. Therefore, it is necessary to develop an explicit and accurate model and analytical solutions for the double beam assembly with realistic middle joint.

3 Analytical solutions of resistance function and failure criteria for a generic axially-constrained beam assembly at large deflection

3.1 Introduction

The plastic deformation capability at critical connections is a key factor for most beam-column substructures to resist disproportionate collapse under a column loss scenario. More specifically, the plastic rotation and axial deformation capacities are governing the effective participation of the catenary force during the plastic response stage. So far, a host of experimental and numerical studies have collectively revealed various local failures in beam-column substructures subjected to large deflection (Khandelwal and El-Tawil 2007, Sadek et al. 2011, Guo et al. 2013, etc.). These failure events would significantly alter the overall resistance function of the substructure, and ultimately limit the extent to which the catenary effect could develop upon complete failure. Therefore, it is reasonable to state that the ultimate collapse resistance and deformation capacity are virtually governed by the limits of failure mechanisms in critical plastic zones.

To date, the majority of past research efforts have been devoted to examining the failure mechanisms for typical beam-column assemblies, either with numerical or experimental approaches, as shown in the review in Chapter 2. Although these studies have demonstrated the characteristics of typical local failure processes and the corresponding impact on the resistance function curves, quantification of the deformation limits at the major failure events and the termination of the resistance function have been largely empirical and individual case-dependent. Generalized quantification of the deformation limits, and how the local failures governs the deformation limit and load resistance, are still lacking.

On the analytical research side, theoretical formulation has been developed for the construction of the global resistance functions for the beam-assemblies, based largely on idealised bending and axial strength properties at the sectional and plastic-hinge level (e.g. Izzuddin 2005). However, there has been a disconnect between such

formulation and the reality as whether the beam-column substructures have the ability to develop into large deflection regime, where catenary action can take considerable effect, without being terminated pre-mature due to local failure.

Therefore, there is an appealing need to establish a more systematic and generalised approach to determining the deformation capacities of beam assemblies in the development towards a catenary mechanism. Of particular importance is the establishment of the ultimate deformation capacity in the critical plastic region, which would effectively terminate the catenary action even though significant residual axial strength capacity remains.

In this chapter, an analytical exploration into the relationship between the global deflection and the local plastic deformation in a generic beam assembly is conducted, with a specific objective to highlight the plastic concentration and how such concentration would limit the capacity of a beam assembly to develop into large deflection regime and hence an effective catenary stage.

For the completeness of the discussion, the general characteristics of the resistance function of a beam assembly under a progressive collapse scenario are briefly explained. This is followed by summarizing the existing analytical modelling of an axially restrained beam, which is assumed to exhibit a mid-span plastic hinge mechanism. The scope and limitation of the existing models are also discussed. Subsequently, the chapter proceeds with the derivation of an analytical solution for a beam assembly relating the deflection to a critical local deformation.

For simplicity in the derivation of an analytical solution, while still being representative of a generic beam, a solid rectangular section is assumed with the material being elastic-perfectively plastic, and the local failure is assumed to be governed by the maximum strain at the critical section. The failure deflection corresponding to steel rupture is obtained from the solution. This solution is then further improved by introducing a characteristic length for more realistic representation of the physical rupture strain. Accordingly, the deflection-strain relationship is updated, based on the modified nominal strain over the characteristic length. By use of the analytical solution, the correlation between the global deflection and a limiting failure criterion, in this case defined by a rupture strain, can

be examined from the viewpoint of the catenary action development in resisting the progressive collapse.

The interpretation of the analytical findings is firstly focused on potential development of catenary action. The results suggest that it would be practically impossible for a solid beam to develop into catenary phase. Worse still, it has been demonstrated that the beam would prematurely fail even within the bending stage.

The discussions in this chapter pave a way for a quantitative investigation into the local failure criteria, the limiting deformations, and the subsequent establishment of the resistance functions for beam assemblies with realistic beam-column joint scenarios in the following two chapters.

3.2 Background and existing theoretical studies on resistance functions of beam assemblies

3.2.1 General characteristics of response of beam assemblies under a progressive collapse scenario

As introduced before, a commonly assumed progressive collapse scenario for typical frame structures involves the removal of a column, thus creating the so-called "double-span" beams above the lost column. The ability of such a double-span beam in bridging over the lost column and transferring the gravity loads to adjacent spans plays a pivotal role in the structure regaining a balanced state and avoiding a progressive collapse.

A simplified version of a double-span beam is the inflection-to-inflection portion, and assuming a total axial restraint, it is equivalent to a beam assembly pinned at the two ends. The actual representation of this portion of the double-span beam would include a middle joint. For the analysis in this chapter and assuming the joint remains in an intact condition, the beam can be further simplified by omitting the middle joint. Therefore the analysis model becomes a classical pinned beam with a point load applied in the middle, as shown in Fig 3.1. The plastic deformation primarily concentrates in the mid-span region.

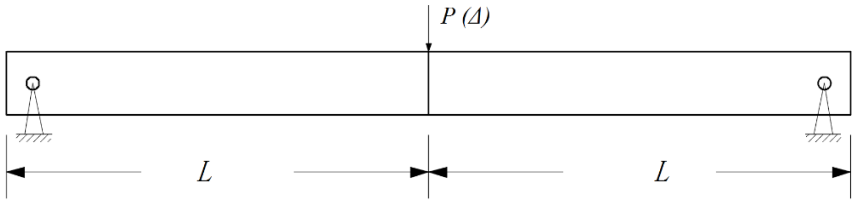

Figure 3.1 Simplified beam under lateral loading

The typical resistance function of such an axially restrained beam (or beam assembly) in terms of vertical load-deflection (*P*-*Δ*) relationship is schematically illustrated in Fig. 3.2.

After the typical elastic-plastic response within normal flection regime, the assembly will develop into a transitionary stage. In this stage, the axial force starts to participate, and the axial-flexural (N-M) interaction on the plastic section has a significant effect on the incremental plastic deformation. The axial force will make more and more contribution to the overall resistance, while the bending moment will fade away. In the meantime, any possibility of local material fracture within the critical connection zone will lead to potential degradation of the global resistance.

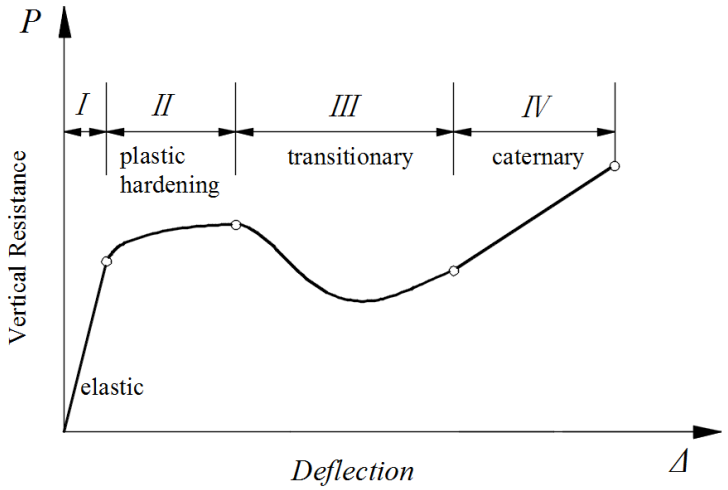

Figure 3.2 General resistance function and deformation stages

With the gradual deterioration of bending capacity in the transitionary phase, the axial tension force begins to contribute almost solely to the vertical resistance. This is indicating the start of the final catenary stage. The structure will behave in catenary action, which becomes the dominating load-carrying mechanism. As the rotation of plastic zone and axial elongation continue to increase, both the deflection and load resistance will increase steadily until the ultimate failure happens.

3.2.2 The existing theoretical modelling studies

In practical design against progressive collapse, it is very desirable for engineers to have a simple and effective analytical model, which can reflect all essential features of large deflection response. However, so far, this has been seldom covered in the past research efforts.

Yin and Wang (2005) incorporated the effect of catenary action into the beam response at elevated temperature, by considering the interaction between the axial force and bending moment of the critical beam section. Their assumption that the axial force is purely elastic and changes in isolation leads to overestimation of catenary forces.

Also by employing the plastic interaction relation between axial force and bending moment, Izzuddin (2005) proposed a more reliable formulation process and resistance function model for a generic axially restraint beam. As depicted in Figure 3.3, the formulations are established based on the rigid-plastic mechanism with a single-point plastic hinge at mid-span. The cross-sectional bending behaviour is assumed to be elastic-perfectly plastic. Under the rigid-plastic mechanism, and according to geometrical kinematics, the increments of the axial deformation, Δ_N, and the plastic rotation, θ_p, can both be obtained from incremental mid-span displacement ω as:

$$\delta\Delta_N = \delta(\omega \cdot \theta) = \delta\left(\omega \cdot \frac{\omega}{L/2}\right) = 4\omega\frac{\delta\omega}{L} \qquad (3\text{-}1)$$

$$\delta\theta_p = \delta(2\theta) = \delta\left(2\frac{\omega}{L/2}\right) = 4\frac{\delta\omega}{L}$$

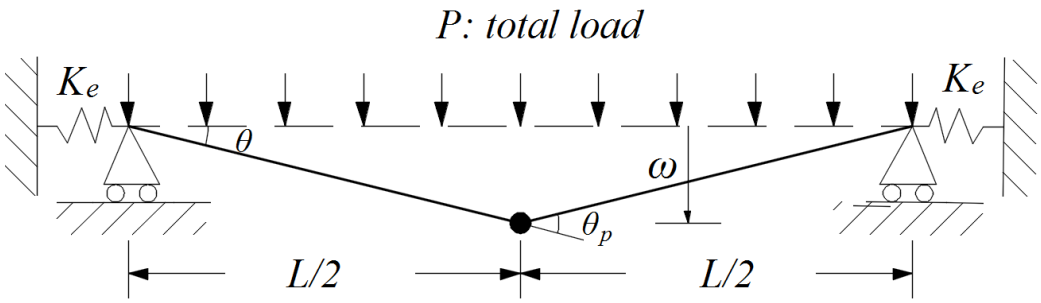

Figure 3.3 Axially restraint beam with mid-span plastic hinge at large deflection (Izzuddin 2005)

For simplification, in this model the plastic interaction between the axial force and bending moment is idealized to be linear, as schematically shown in the normalized N-M curve (Figure 3.4). It should be noted that a realistic N-M interaction (also shown in the same graph) would generally be nonlinear, and the linear assumption will lead to underestimation of the axial capacity under at a certain level of bending moment. However, the linear simplification is advantageous in facilitating straightforward formulations of plastic response during the transitionary stage.

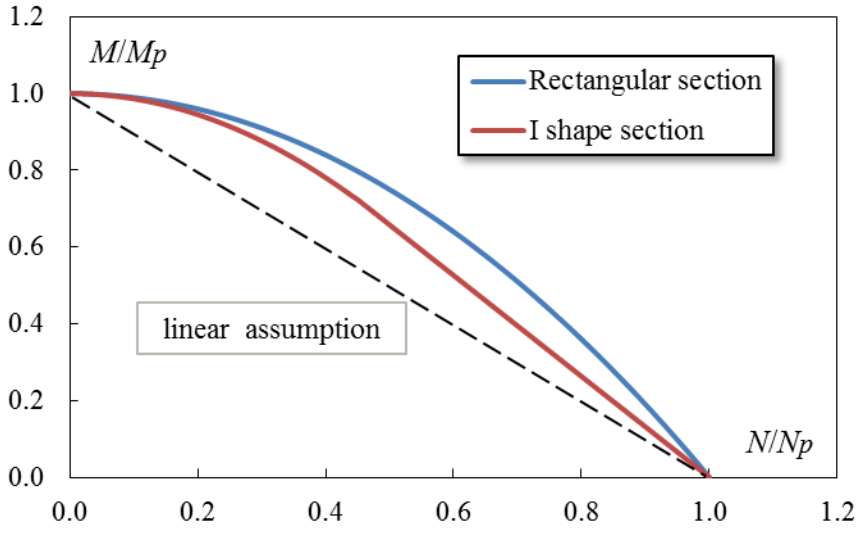

Figure 3.4 The actual and idealized N-M interaction curves

The participation of catenary force in the post-bending stages requires the derivation of both axial deflection and hinge rotation. They are combined as an incremental plastic deformation vector noted as $\delta = (\delta\Delta_p, \delta\theta p)$. According to the associated plasticity flow rule, the incremental vector and the surface normal of the yielding function share the same direction, as illustrated in Figure 3.5. Therefore, under the linear N-M interaction assumption, the plastic increment of axial deformation and rotation angle will have the follow simple correlation, where the constant M_p/N_p was referred to as plastic interaction radius r_p.

$$\frac{\delta\Delta_p}{\delta\theta_p} = \frac{M_p}{N_p} \tag{3-2}$$

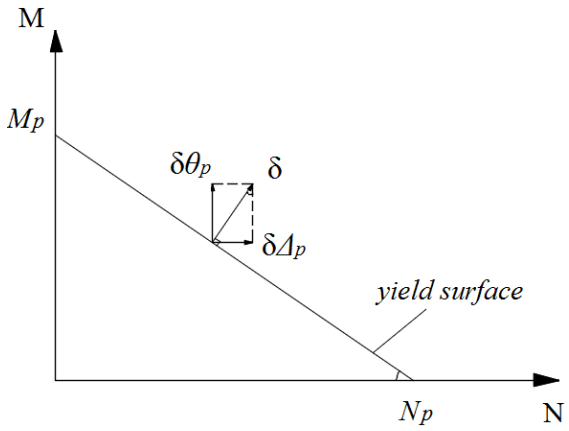

Figure 3.5 The plastic deformation flow direction

Based on the aforementioned assumptions, a four-stage resistance function model was established (Figure 3.6). Especially for the transient stage, which commences when the axial force increases from zero and terminates when it reaches the maximum plastic capacity N_p, the response is formulated to account for plastic axial-flexural interaction.

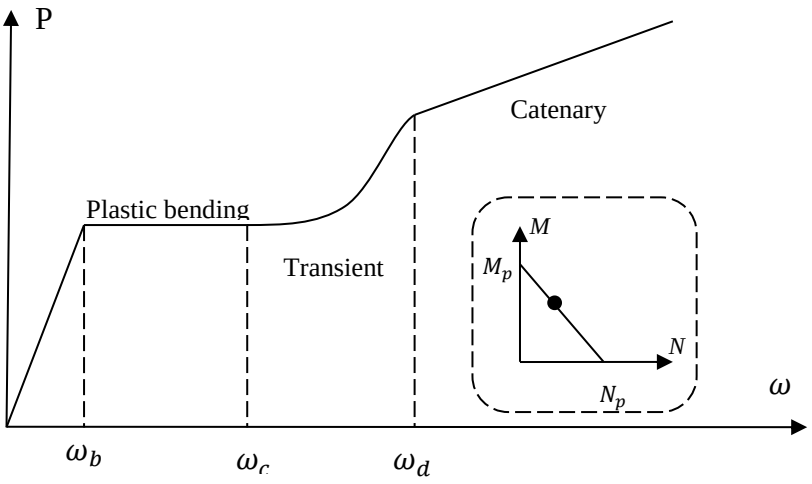

Figure 3.6 Four stage resistance model proposed by Izzuddin (2005)

As an direct extension of the study by Izzuddin (2005), Li et al. (2012) improved the formulations of transition stage, by employing a more realistic N-M interaction curve for the standard I-shape section. The improved solution still used the same rigid-plastic mechanism and applied the same assumptions. However, the extended study did not either address the quantification of the ultimate failure.

The model by Izzuddin (2005) is explicit and flexible for practical application, as it brings out the essential information of catenary action effect. Nevertheless, some of the underlying assumptions and the consequent limitations need to be discussed.

First and foremost, the ultimate failure criteria have not been not addressed. The load resistance in the final catenary stage was a linear function of deflection, given by

$$P = 4\frac{N_p}{L}\omega \tag{3-3}$$

Obviously, the deformation limit cannot be concluded or sourced from this formulation. The model does not deal with how the final failure could actually develop, nor does it cover any formulation that could lead to reasonable failure criteria and the governing factors.

In numerous studies by Paulay and Priestly (1992) and Dat et al. (2015), the plastic hinge length l_p has been an important parameter in relating section-level behaviour into member-level response.

However, most researchers relied on experimental testing to obtain empirical results for the equivalent plastic hinge length (Zhao et al. 2011). In all, it is necessary to use a simplified model to investigate the plastic distribution in the curvature localization zone.

In this way, the plastic rotation and plastic stretching could be related to local failure criteria in the critical zone, and the failure criteria could be reasonably established.

To address the above limitations in the past studies, this chapter will provide more physical substance to the existing hypothetical formulations, and show the influence of plastic zone performance on the effective development of catenary action.

3.3 Theoretical formulation of deformation limits on the resistance function curve for a generic beam assembly

As discussed before, for a realistic substructure with detailed beam-column connections, the ultimate capacity is closely dependent on limits and ductility of local failure mechanisms, especially when large deflection comes into being. However, when a simplified generic beam assembly is considered, the ultimate failure is governed by the material strain (rupture limit) and it is possible to formulate theoretically a relationship between the local strain and the global deflection. From there we can establish an idea about how the evolution of the plastic deformation in the critical zone affects the ability of the beam assembly in developing the catenary action in some quantitative terms. This will provide a good basis for the subsequent investigation into beam assemblies involving more realistic connection details.

We shall begin with a beam in pure bending under a mid-span load, and assuming elastic-perfectly plastic material stress-strain behaviour, to formulate a theoretical relationship between the critical strain in the beam and the global deflection, with a

focus especially on the evolution of the plastic zone in the large deformation regime until material rupture.

We shall then extend the formulation to include the developing tension in the catenary stage and incorporate the axial force – bending moment interaction in the sectional yield criterion. With an assumption on the distribution of the tensile plastic strain, the total critical plastic strain in the catenary stage can also be evaluated. This will then determine the rupture of the material and therefore the termination of the catenary action, thus completing the entire resistance function.

3.3.1 Analysis procedure

In this section, the generic beam under pure bending is analysed first. A step-by-step analytical procedure is presented in order to derive a closed-form solution of the global displacement against critical strain.

To start with, the deflection shape, bending moment diagram, curvature distribution for a half of the generic beam under simple support at a post yield stage are depicted in Fig 3.7. The length of actual plastic zone is denoted as l_p, so the remaining elastic part for one-side beam has a length of $L_e=L-l_p/2$. The bending moment has a linear distribution due to the concentrated load at the mid-span. The distribution of the curvature in the plastic zone will depend upon the moment-curvature relationship, which in turn depends on the sectional geometry and the material stress-strain behaviour.

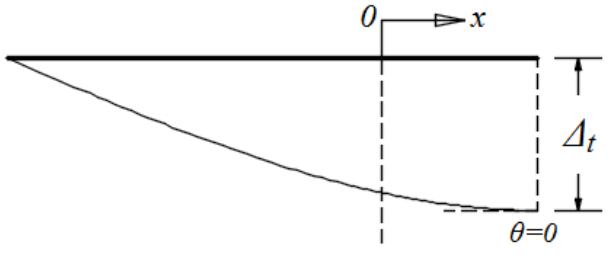

(a) The deflection shape

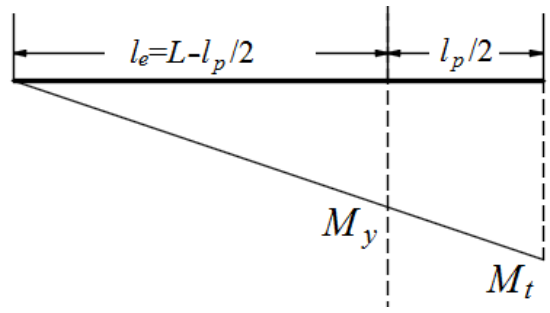

(b) The moment diagram

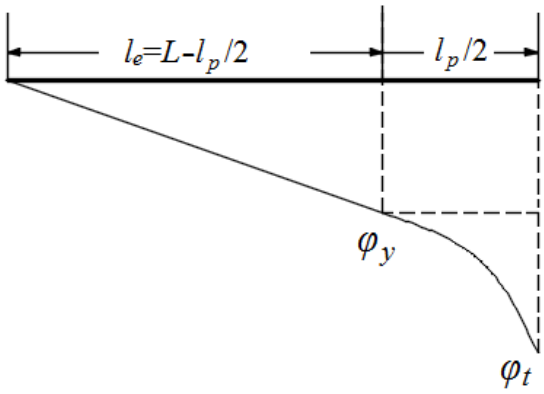

(c) The curvature diagram

Figure 3.7 Deflection, bending moment and curvature distribution (half beam is shown considering symmetry)

The procedure for the analysis of the load-deflection-curvature (strain) relationship is straightforward in the context of inelastic analysis of beams. For the sake of convenience, the key steps are listed as follows.

- **Step 1**: Assuming that plane section remains plane, use sectional stress analysis to obtain the moment-curvature (M-φ) relation of the beam section.
- **Step 2**: Before attaining apparent global yielding, the beam analysis may be carried out by a load controlled manner. Thus, for a load in a post-initial yield stage, use the bending moment diagram (BMD) and the initial yield moment to determine the actual length of plastic zone;
- **Step 3**: The bending moment along the plastic zone can be found by linear interpolation, and the corresponding curvature can be solved from the moment-curvature relation. In this way, the plastic curvature distribution along the plastic zone can be formulated.
- **Step 4**: Carry out the integration of the curvature distribution function twice along the practical plastic zone. Then the application of boundary conditions would allow the deflection shape to be finalised.

- **Step 5**: The deflection at the mid-span can be computed, as a function of the maximum strain on the mid-span section.
- **Step 6**: When the mid-span section reaches the rupture strain, the beam response will terminate immediately, and the ultimate deformation is obtained.

3.3.2 The strain or curvature distribution in the plastic zone

For simplicity, the generic beam is assumed to have uniform solid rectangle section (width = *b*, depth = *h*). It is subjected to a mid-span concentrated lateral load, which pushes the beam downwards continuously.

The material behaviour is elastic and perfectly plastic. Another important assumption is that the beam sections are assumed to remain plane under large deformation. Under this assumption, the stress and strain distributions at the first yield and a post-yield status are explained in Fig 3.8. After the first yield at the section edges is reached, the plastic strain near the section top or bottom will continue to increase, before the plasticity propagates to the whole section depth. In fact, the full plasticity of the section is an unattainable ideal situation. Therefore, it is implied that there is an asymptotic line to the moment-strain/curvature curve.

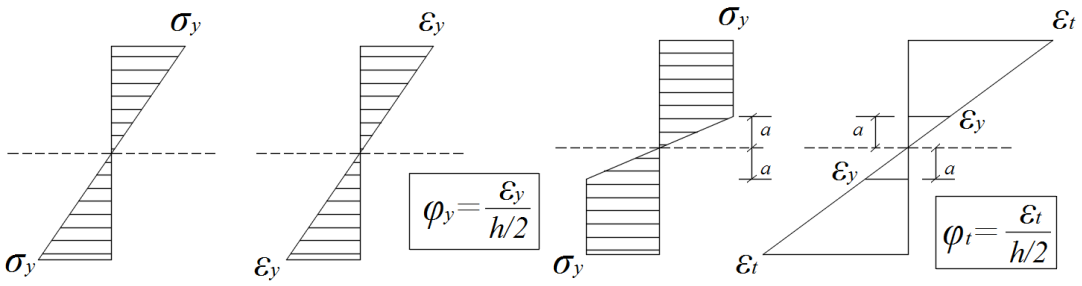

(a) Stress and strain at first yield (a) Stress and strain at a post-yield point

Figure 3.8 The stress and strain diagrams at first yield and a post-yield state

As can be obtained from the strain diagram at a post-yield state, for the maximum strain in the range of $\varepsilon_y < \varepsilon_t < \varepsilon_u$, there is a proportional relation as follows:

$$\frac{\varepsilon_y}{\varepsilon_t} = \frac{a}{h/2} \tag{3-4}$$

The plastic bending moment M_t in this case can then be integrated from the corresponding stress diagram as:

$$\begin{aligned} M_t(\varepsilon_t) &= \sigma_y b\left(\frac{h}{2} - a\right)\left[\frac{h}{2} - \left(\frac{h}{2} - a\right)\right] + \frac{1}{6}\sigma_y b(2a)^2 \\ &= \sigma_y b\left(\frac{h^2}{4} - \frac{a^2}{3}\right) = \frac{1}{4}\sigma_y b h^2\left[1 - \frac{1}{3}\left(\frac{\varepsilon_y}{\varepsilon_t}\right)^2\right] \end{aligned} \tag{3-5}$$

The bending moment at the first yield and ideal full plasticity for a rectangle section are simply obtained as:

$$M_y = \frac{1}{6}\sigma_y b h^2, M_p = \frac{1}{4}\sigma_y b h^2 \tag{3-6}$$

Hence, the bending moment can be explicitly expressed as the function of the maximum strain in the section below, and the normalized moment-strain/curvature relation is plotted in Figure 3.9.

$$\frac{M_t}{M_p} = 1 - \frac{1}{3}\left(\frac{\varepsilon_y}{\varepsilon_t}\right)^2 \text{ or } \frac{M_t}{M_y} = \frac{3}{2} - \frac{1}{2}\left(\frac{\varepsilon_y}{\varepsilon_t}\right)^2 \tag{3-7}$$

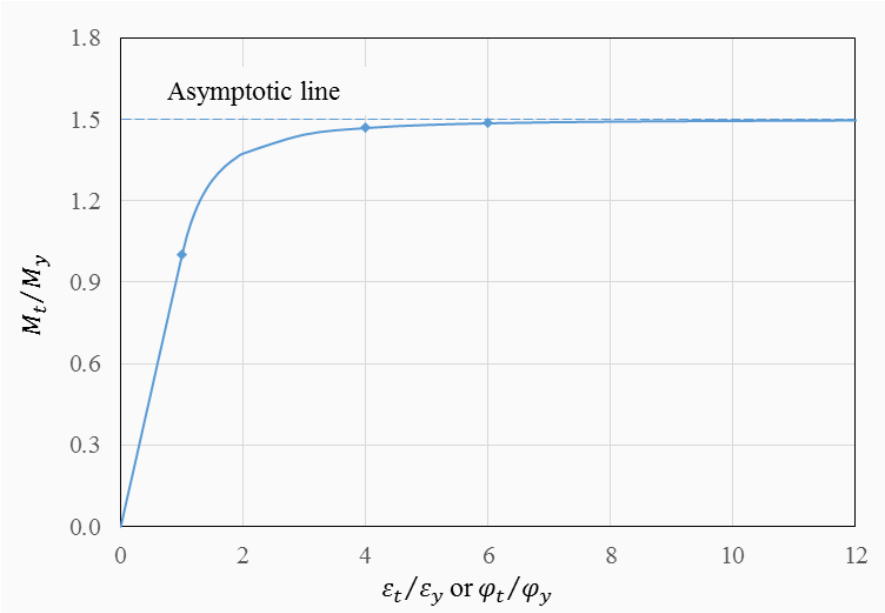

Figure 3.9 The normalized moment-curvature relation of a rectangle section under pure bending

The bending moment diagrams (BMD) at the two critical states are plotted in Figure 3.10. State I represents the first yield of the mid-span critical section, while state II refers to a random post-yield state, when the mid-span section has a certain level of the maximum strain ε_t or bending moment M_t.

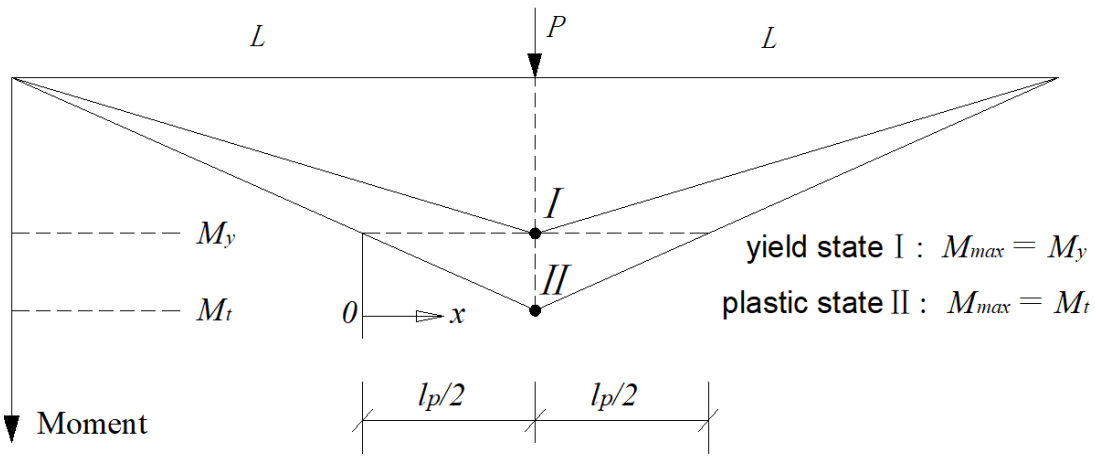

Figure 3.10 Bending moment diagrams at the first yield and post-yield states

According to the BMD, the length of actual plastic zone can be calculated through the following proportional equation:

$$\frac{l_p/2}{L} = \frac{M_t - M_y}{M_t} \tag{3-8}$$

The plastic zone length can be obtained as:

$$l_p = 2L\left(1 - \frac{M_y}{M_t}\right) \tag{3-9}$$

Substituting Equation (3-9) into Equation (3-7), we get the relationship between the plastic zone length and the maximum strain level as:

$$\frac{l_p}{2L} = \frac{1 - \left(\varepsilon_y/\varepsilon_t\right)^2}{3 - \left(\varepsilon_y/\varepsilon_t\right)^2} \tag{3-10}$$

As can see from the plotted curve in Fig 3.11, the actual hinge length increases drastically with the increase of the strain after first edge yield of the section. However, it will be approaching but not exceeding one third of the full span. This is because the bending moment is limited to its full plastic capacity.

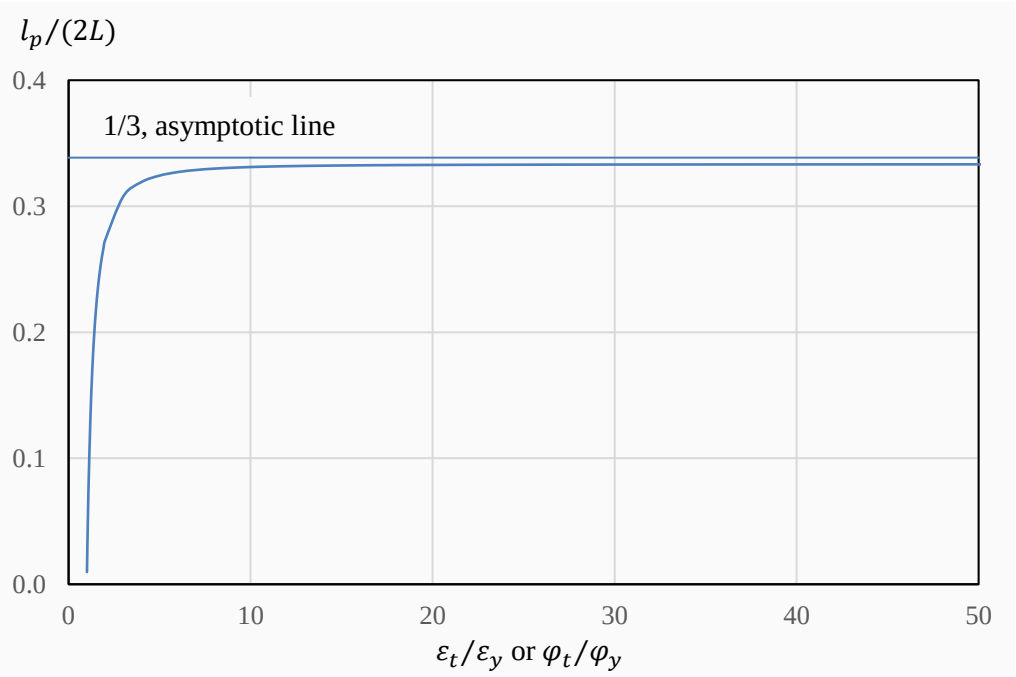

Figure 3.11 The actual plastic zone length vs. the maximum strain

For the particular interest to observe the global deformability given a failure criterion of rupture strain, it is necessary to relate the deflection to the maximum strain, and in the case here this can be achieved through the curvature. The curvature distribution along the beam is schematically shown in Figure 3.12.

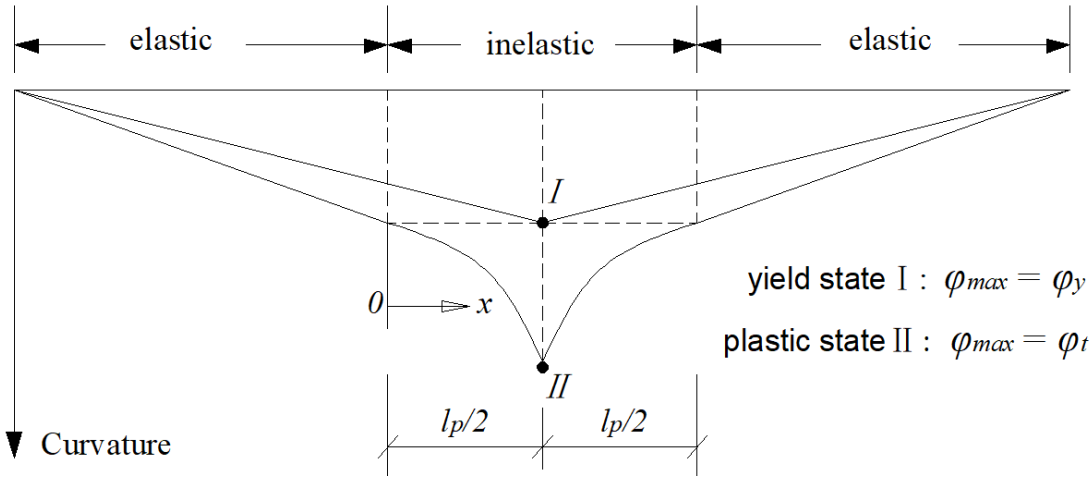

Figure 3.12 The curvature distribution along the whole beam set

Considering an ***x*** coordinate axis, originating from the boundary of plastic zone, the variation of sectional moment can be obtained by linear interpolation between first yield and maximum moments (M_y and M_t) as:

$$M(x) = M_y + \frac{x}{l_p/2}\left(M_t - M_y\right), 0 \le x \le l_p/2 \tag{3-11}$$

By substituting Equation (4-4) into Equation (4-8), the bending moment is further expressed as a function of the location *x* and the maximum strain ε_t as:

$$\begin{aligned} M(x) &= M_y + \frac{x}{l_p/2}\left(M_t - M_y\right) \\ &= M_y + \frac{x}{l_p/2}\left[\left(1 - \frac{1}{3}\left(\frac{\varepsilon_y}{\varepsilon_t}\right)^2\right)M_p - M_y\right] \\ &= \left(1 - \frac{x}{l_p/2}\right)M_y + \frac{x}{l_p/2}\left[\left(1 - \frac{1}{3}\left(\frac{\varepsilon_y}{\varepsilon_t}\right)^2\right)\right]M_p \end{aligned} \tag{3-12}$$

To find the strain and curvature variations along the plastic hinge zone ($0 \leq x \leq l_p/2$), the above bending moment is combined with Equation (3-7) to work out the corresponding sectional maximum strain $\varepsilon(x)$ as:

$$\left(1-\frac{x}{l_p/2}\right)M_y+\frac{x}{l_p/2}\left[\left(1-\frac{1}{3}\left(\frac{\varepsilon_y}{\varepsilon_t}\right)^2\right)\right]M_p = \left[1-\frac{1}{3}\left(\frac{\varepsilon_y}{\varepsilon(x)}\right)^2\right]M_p \tag{3-13}$$

The sectional maximum strain can eventually be solved, and is expressed as the function of *x* as:

$$\varepsilon(x)=\frac{\varepsilon_y}{\sqrt{1-\frac{x}{l_p/2}\left[1-\left(\frac{\varepsilon_y}{\varepsilon_t}\right)^2\right]}} \tag{3-14}$$

Accordingly, the curvature distribution along the plastic hinge zone can also be mathematically expressed as the function of the location *x* and the maximum strain ε_t as:

$$\varphi(x)=\frac{\varphi_y}{\sqrt{1-\frac{x}{l_p/2}\left[1-\left(\frac{\varepsilon_y}{\varepsilon_t}\right)^2\right]}} \tag{3-15}$$

Bases on Equation (3-15), we can plot Fig. 3.13, which shows the distribution (φ/φ_y) of normalized curvature along the plastic hinge zone, under different levels of maximum critical strain. As can be seen from the graph, the sectional curvature near the centre of plastic zone will be extremely large, if the maximum strain level at the mid-span critical section goes much beyond the material yielding strain. This phenomenon may lead to a singularity point in the distribution curve, but it cannot effectively represent the physical strain in the potential rupture area. This will be discussed and dealt with in the following section.

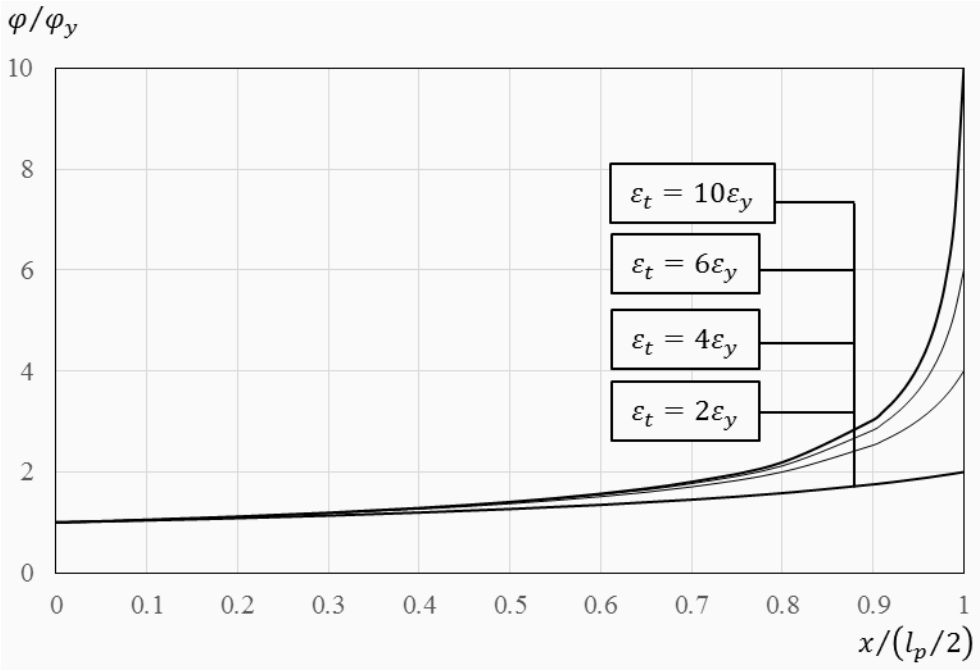

Figure 3.13 The curvature distribution in the plastic deformation zone at different strain levels

3.3.3 The theoretical relationship between the critical curvature/strain and global deflection

The plastic zone length l_p in the previous sections is the physical length of the plastic hinge region, over which actual plasticity spreads. An equivalent plastic hinge length, over which a given curvature is assumed to be uniform, may be more flexible for relating plastic rotation to the global deflection, and translating the deformation into sectional strains. The equivalent hinge length l_p^e is believed to have a certain intimate relationship with l_p. This relationship can be mathematically established through an intermediate parameter, namely the plastic rotation θ_p.

The total angle of plastic rotation can be computed from the integration of plastic curvature along the plastic zone as:

$$\theta_p = 2\int_0^{l_p/2} \varphi_p(x)dx \tag{3-16}$$

Through the following integration process in Equation (3-17), the resulting plastic rotation angle at a certain strain level can be obtained as:

$$\begin{aligned}
\theta_p &= 2\int_0^{l_p/2}\left[\varphi(x)-\varphi_y\right]dx \\
&= 2\int_0^{l_p/2}\frac{\varphi_y}{\sqrt{1-\frac{x}{l_p/2}\left[1-\left(\frac{\varepsilon_y}{\varepsilon_t}\right)^2\right]}}dx - 2\varphi_y\cdot\frac{l_p}{2} \\
&= 2\varphi_y\left(\frac{-l_p}{1-\left(\varepsilon_y/\varepsilon_t\right)^2}\sqrt{1-\frac{x}{l_p/2}\left[1-\left(\frac{\varepsilon_y}{\varepsilon_t}\right)^2\right]}\right)\Bigg|_0^{l_p/2} - \varphi_y l_p \\
&= -2\varphi_y l_p\frac{\varepsilon_y/\varepsilon_t-1}{1-\left(\varepsilon_y/\varepsilon_t\right)^2} - \varphi_y l_p = \frac{2\varphi_y l_p}{1+\varepsilon_y/\varepsilon_t} - \varphi_y l_p \\
&= \frac{1-\varepsilon_y/\varepsilon_t}{1+\varepsilon_y/\varepsilon_t}\varphi_y l_p
\end{aligned} \tag{3-17}$$

To achieve the equivalent plastic hinge length, the curvature over the equivalent plastic hinge length is assumed to be uniformly equal to the maximum curvature φ_t, as shown in Fig 3.14. More importantly, the total plastic rotation caused by equivalent plastic hinge zone has to be exactly equal to the total plastic rotation obtained by the integrated result in Equation (3-17).

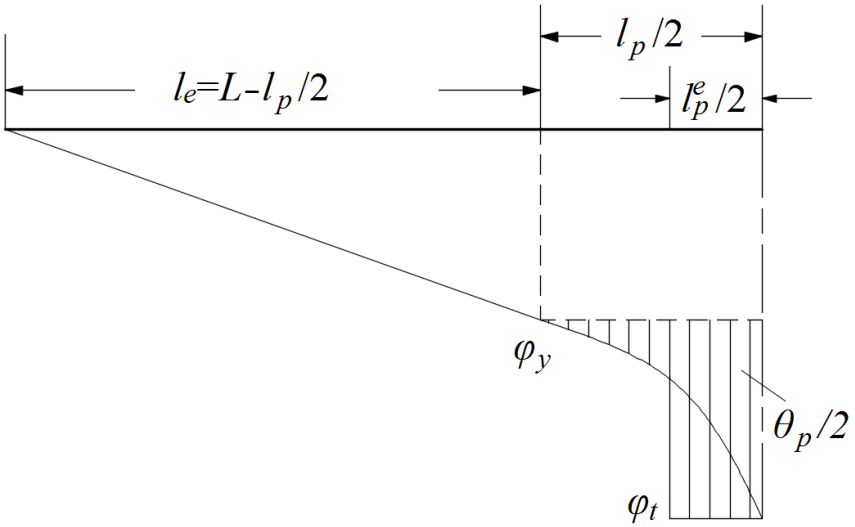

Figure 3.14 The equivalent plastic hinge length

Therefore, for $\varepsilon_t > \varepsilon_y$, the equivalent plastic hinge length can be calculated to be

$$l_p^e = \frac{\theta_p}{\varphi_t - \varphi_y} = \frac{1-\varepsilon_y/\varepsilon_t}{1+\varepsilon_y/\varepsilon_t} \cdot \frac{\varphi_y}{\varphi_t - \varphi_y} \cdot l_p$$
$$= \frac{1-\varepsilon_y/\varepsilon_t}{1+\varepsilon_y/\varepsilon_t} \cdot \frac{\varepsilon_y/\varepsilon_t}{1-\varepsilon_y/\varepsilon_t} \cdot l_p = \frac{\varepsilon_y/\varepsilon_t}{1+\varepsilon_y/\varepsilon_t} \cdot l_p \quad (3\text{-}18)$$

The ratio of the equivalent plastic hinge length to the plastic zone length is plotted against the normalized maximum strain level in Fig 3.15. As can be seen, the equivalent hinge length is getting less proportion of the actual plastic zone length, as the sectional strain develops further beyond the yielding strain.

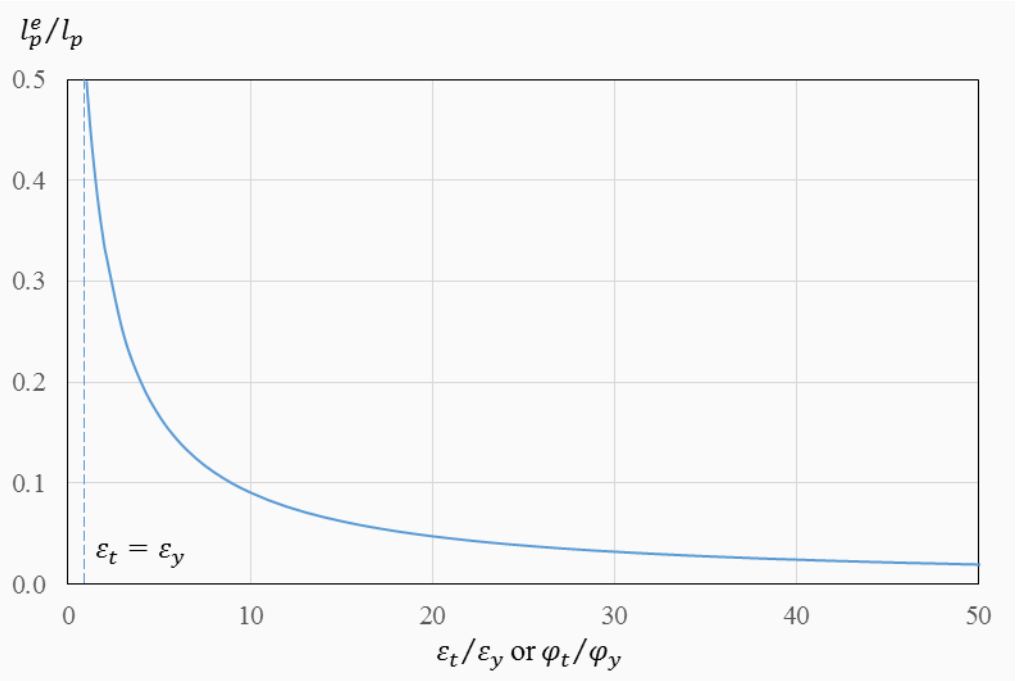

Figure 3.15 The ratio of the equivalent hinge length to the plastic zone length

By introducing a strain ratio parameter $\alpha = \varepsilon_y/\varepsilon_t$, then the equivalent plastic hinge length can be expressed as the function of α. By substituting Equation (3-9) into Equation (3-17), the formulation of the equivalent hinge length against the maximum strain level can be achieved as the following equation

$$l_p^e = \frac{\alpha}{1+\alpha} l_p = \frac{2\alpha}{1+\alpha} \cdot \frac{1-\alpha^2}{3-\alpha^2}(2L) = \frac{\alpha(1-\alpha)}{3-\alpha^2} \cdot (2L) \qquad (3\text{-}19)$$

This formulation is subsequently plotted into Figure 3.16 which shows that the maximum equivalent hinge length reaches the peak value, which is approximately 9% of the double span length, when the maximum strain is 1.8 times of the yielding strain. Afterwards, the equivalent length decreases gradually as the critical section develops larger strains.

When considering the commonly used structural steel, which usually has a strain ductility over 100, the equivalent length of plastic hinge will go below 1% of the double beam span, which is very small. This result implies that the rotational capacity is very limited for a solid beam, thereby making it less capable to develop

into catenary action. This will discussed later by presenting a case with real parameters and results.

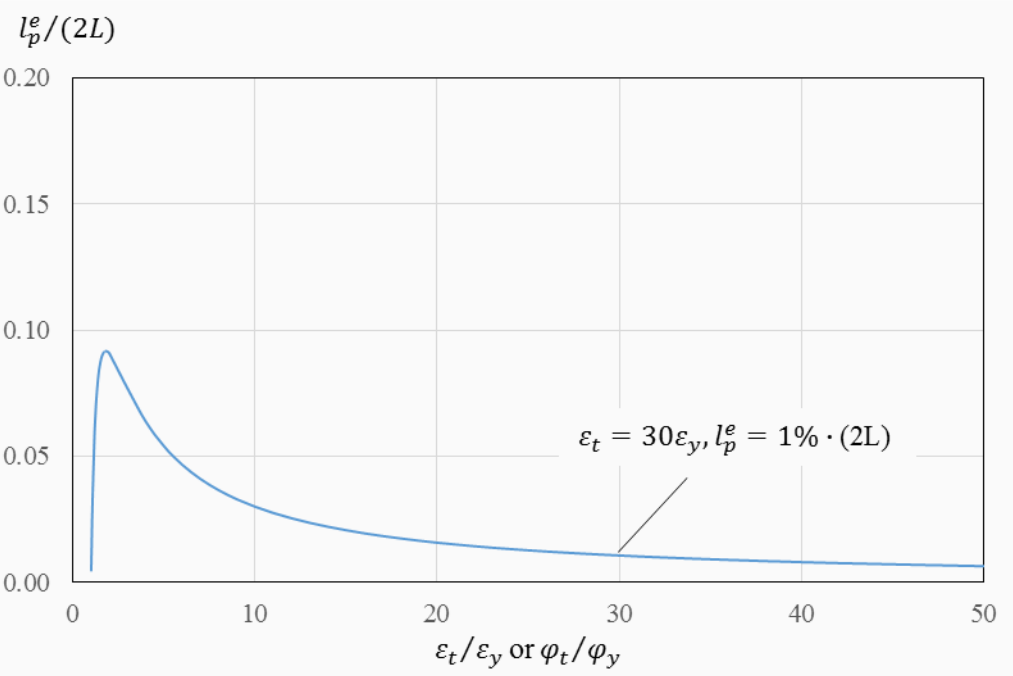

Figure 3.16 The ratio of equivalent plastic hinge length to double span length

As the curvature distribution along the whole double beam length has already been given, the deflection shape function can be worked out by integrating the curvature along the beam axis:

$$\omega(x) = \int \left(\int \varphi_x \, dx \right) dx + C_1 x + C_2 \tag{3-20}$$

The unknown constants C_1 and C_2 could be solved by applying the following three boundary conditions:

1) The deflection at the support is zero;
2) The slope angle ($d\omega/dx$) at the midspan is equal to zero;
3) The slope angle at the intersection of the elastic and plastic zones is smooth.

By omitting the derivation process, the beam deflection shape function along the full plastic zone ($0 \leq x \leq l_p/2$) can be finally achieved as:

$$\omega(x) = \frac{\varphi_y l_p^2}{3\left[1-\left(\varepsilon_y/\varepsilon_t\right)^2\right]^2}\left\{1-\frac{x}{l_p/2}\left[1-\left(\varepsilon_y/\varepsilon_t\right)^2\right]\right\}^{3/2} + \varphi_y l_p \frac{\varepsilon_y/\varepsilon_t}{1-\left(\varepsilon_y/\varepsilon_t\right)^2}\cdot x - \frac{\varphi_y l_p^2}{3\left[1-\left(\varepsilon_y/\varepsilon_t\right)^2\right]^2} - \frac{\varphi_y l_p l_e}{1+\varepsilon_y/\varepsilon_t} - \frac{\varphi_y l_e^2}{3} \quad (3\text{-}21)$$

By substituting $x = l_p/2$ into the above equation, we can now obtain the maximum global deflection at the middle of the double beam set as:

$$\omega_{max} = \omega\left(x = l_p/2\right) = \frac{\varphi_y l_p^2}{2\left[1-\left(\varepsilon_y/\varepsilon_t\right)^2\right]}\left(\frac{\varepsilon_y}{\varepsilon_t}\right) - \frac{\varphi_y l_p^2}{3\left[1-\left(\varepsilon_y/\varepsilon_t\right)^2\right]}\left[1-\left(\frac{\varepsilon_y}{\varepsilon_t}\right)^3\right] - \frac{\varphi_y l_e^2}{3} - \frac{\varphi_y l_p l_e}{1+\varepsilon_y/\varepsilon_t} \quad (3\text{-}22)$$

Because the lengths of elastic and plastic zones, l_e and l_p, are both directly dependent on the strain level, the global deflection is effectively a function of the maximum sectional strain (ε_t). This correlation points to the fact that the development of overall deflection is fundamentally governed by the maximum sectional strain along the double beam.

3.4 Modified relationship between critical strain and global deflection considering a characteristic length of rupture

3.4.1 The updated deflection using the modified nominal strain over the characteristic length

As has been pointed out in section 3.3.1, the strain and curvature near the central plastic zone could become exceptionally large. Figure 3.17 shows the curvature distribution at $\varepsilon_t = 50\varepsilon_y$, in comparison with the curves at lower strain levels.

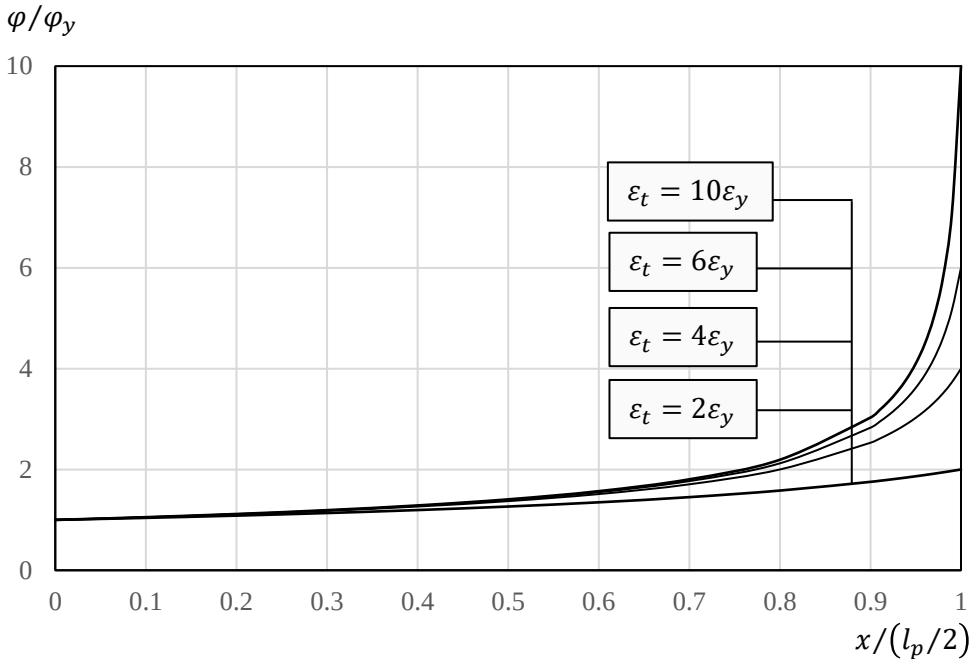

Figure 3.17 The curvature distribution along the plastic hinge zone

This phenomenon of strain localization is a ubiquitous feature in the deforming body of elastoplastic materials, especially those that are susceptible to cracking (Antolovich and Armstrong 2014). In modelling studies, the narrow zone of intense strains will cause much result sensitivity to the mesh sizes. To address this issue, a characteristic length is widely employed to allow for the modelling the cracked material in terms of stress-strain relations (Mosalam and Paulino 1997).

This concept can be extended to cope with the plastic strain concentration in the simplified beam modelling. A characteristic length is introduced for more realistic representation of the physical rupture zone. When the average curvature over the characteristic length reaches the rupture curvature, fracture failure is deemed to occur. This should identify more a reasonably ultimate deflection when the material rupture strain is finally reached.

Figure 3.18 introduces a characteristic length in the concentrated plastic zone. The quantification of the physical characteristic length for rupture of ductile materials is understandably a very complex subject and is beyond the scope of the present study. For an indicative purpose, a nominal characteristic length of 10 mm is assumed. The modified critical curvature over the characteristic length is denoted as φ_{avg}.

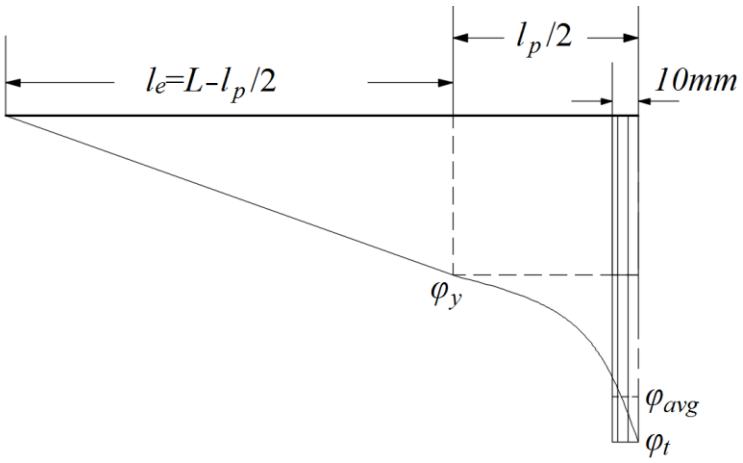

Figure 3.18 The characteristic length and the nominal curvature

Assuming that the total rotation accumulated from the distributed curvature is equal to that induced by the nominal curvature, the relation is expressed as

$$\varphi_{avg} \cdot L_{char} = \theta_{char} = \int_{l_p/2-10mm}^{l_p/2} \varphi(x)dx \tag{3-23}$$

The total rotation, accumulated from the distributed curvature along the characteristic length, is computed to be the integration of the curvature function (3-15) as:

$$\begin{aligned}
\theta_{char} &= \int_{l_p/2-10mm}^{l_p/2} \varphi(x)dx \\
&= \int_{l_p/2-10mm}^{l_p/2} \frac{\varphi_y}{\sqrt{1-\frac{x}{l_p/2}\left[1-\left(\frac{\varepsilon_y}{\varepsilon_t}\right)^2\right]}}dx \\
&= \varphi_y \left(\frac{-l_p}{1-\left(\varepsilon_y/\varepsilon_t\right)^2} \sqrt{1-\frac{x}{l_p/2}\left[1-\left(\frac{\varepsilon_y}{\varepsilon_t}\right)^2\right]} \right) \Bigg|_{l_p/2-10mm}^{l_p/2} \\
&= \frac{\varphi_y l_p}{1-\left(\varepsilon_y/\varepsilon_t\right)^2} \left\{ \sqrt{\left(\frac{\varepsilon_y}{\varepsilon_t}\right)^2 + \frac{10mm}{l_p/2}\left[1-\left(\frac{\varepsilon_y}{\varepsilon_t}\right)^2\right]} - \frac{\varepsilon_y}{\varepsilon_t} \right\}
\end{aligned} \tag{3-24}$$

Hence,

$$\varphi_{avg} = \frac{\theta_{char}}{L_{char}}$$

$$= \frac{\varphi_y l_p}{10mm\left[1-\left(\varepsilon_y/\varepsilon_t\right)^2\right]}\left\{\sqrt{\left(\frac{\varepsilon_y}{\varepsilon_t}\right)^2+\frac{10mm}{l_p/2}\left[1-\left(\frac{\varepsilon_y}{\varepsilon_t}\right)^2\right]}-\frac{\varepsilon_y}{\varepsilon_t}\right\} \quad (3\text{-}25)$$

The ratio of the nominal curvature to the theoretical maximum curvature φ_t can be expressed again as a function of the maximum strain as:

$$\frac{\varphi_{avg}}{\varphi_t} = \frac{l_p}{10mm}\frac{\varepsilon_y/\varepsilon_t}{1-\left(\varepsilon_y/\varepsilon_t\right)^2}\left\{\sqrt{\left(\frac{\varepsilon_y}{\varepsilon_t}\right)^2+\frac{10mm}{l_p/2}\left[1-\left(\frac{\varepsilon_y}{\varepsilon_t}\right)^2\right]}-\frac{\varepsilon_y}{\varepsilon_t}\right\} \quad (3\text{-}26)$$

By combining Equations (3-10) and (3-26), and bringing in some parameter values for the single-span length *L*, the ratio of the nominal to maximum curvature over the characteristic length can be plotted against the strain level. As shown in Figure 3.19, when the strain is sufficiently large, the modified critical strain in the characteristic length drops to around 20% of the maximum strain.

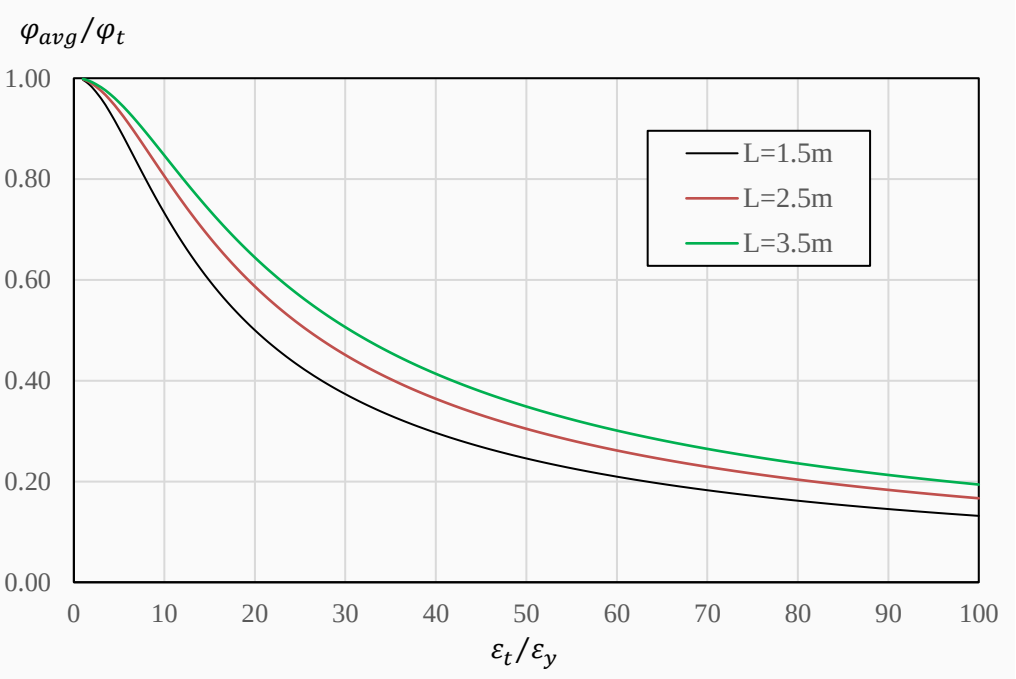

Figure 3.19 The ratio of nominal to maximum curvature/strain

With regard to the new deflection-strain relationship, the deflection could still be calculated from the previous formulation obtained as Equation (3-22). However, the strain ε_t will be substituted by the corresponding nominal strain ε_{nom}, which should be found using Equation (3-26). Thus, the updated solution of global deflection against the maximum strain is achieved.

3.4.2 Discussion of the generic beam under pure bending

In section 3.3, close-form mathematical formulation has been presented for the generic beam to relate a critical local deformation measure, in this case the critical curvature or strain, to the global deflection. The results have demonstrated clearly that the ability of a beam assembly to develop large global deflection, and hence an effective catenary stage, closely depends on the rotational capacity at the plastic region. Where the plastic concentration is severe, the plastic rotation capacity can be very limited even the material itself is very ductile (with a large rupture strain).

As in classical inelastic analysis of beams, it is not normally possible nor economical to derive closed-form relationship between a local deformation measure and the global deflection. Instead, an engineering approach is normally adopted, so that the two levels of relations, i.e. a) between the global deflection and the total plastic rotation, and b) between the total plastic rotation and a local failure criteria, are treated in an "uncoupled" manner.

Since the exact solution in a "coupled" system is already available, it makes sense to look at the analysis of the same beam using the above engineering approach, and compare the results with the exact solution, especially concerning the entire response including the large deformation stage.

3.4.3 Simplification of moment-curvature relationship

As was discussed in section 3.3.3, the full plastic section cannot be attained in practice, but the bending moment will tend to approach M_p when the maximum strain at the sectional edge exceeds the yield strain a few times. For a solid rectangular

section considered here as an example, when the maximum strain reaches about 6 times the yield strain, i.e. $\varepsilon_t = 6\varepsilon_y$, the sectional plastic moment already reaches $0.99M_p$. For simplification, the moment curvature relationship may therefore be simplified to have a full plastic stage starting from the above point.

The yield point may be assumed at the initial yield point when the first material yield is reached. In this way, the sectional moment-curvature relationship can be simplified into a tri-linear form, which is shown in Figure 3.20.

Under the tri-linear section behaviour assumption, the derivation of the modified global deflection can be seen in Appendix A of this chapter.

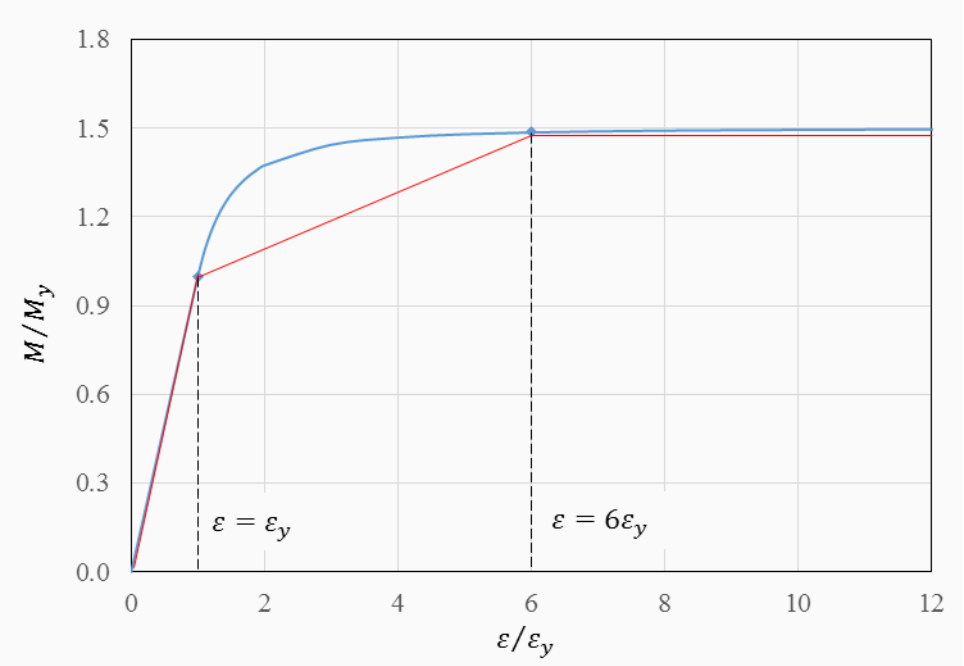

Figure 3.20 The simplified tri-linear moment-curvature relation

3.4.4 Example and discussion

In the previous sections, the analytical solutions for the relationship between the global deflection and the critical curvature or strain for a generic beam under pure bending have been obtained. Accordingly, the ultimate deflection limit can be identified assuming a material rupture strain limit ε_u for such an idealised beam situation

In this section, an example is given. The dimensions and material properties are listed in Table 3.1.

Table 3.1 Parameter values for a double beam example

Single span length	L	1500 mm
Section height	h	80 mm
Section width	b	50 mm
Material - Elastic stiffness	E	150 GPa
Material - Yielding strength	f_y	300 MPa
Material - Yielding strain	ε_y	0.002
Material – Rupture strain	ε_u	10%

Using formulation in Section 3.3.3, the relationship between the global mid-span deflection and the maximum sectional strain can be plotted in Figure 3.21,and the equivalent plastic hinge rotation is also plotted against strain level in Figure 3.22.

It can be seen that if the material rupture strain is set at 10%, the beam will fail at a deflection of 82 mm, which is less than 3% of the full beam length. It is obviously less than expected when a catenary stage is to take effect. Therefore, the result implies that a premature failure in the bending phase would occur before the substructure that is represented by the generic beam here can develop into catenary stage.

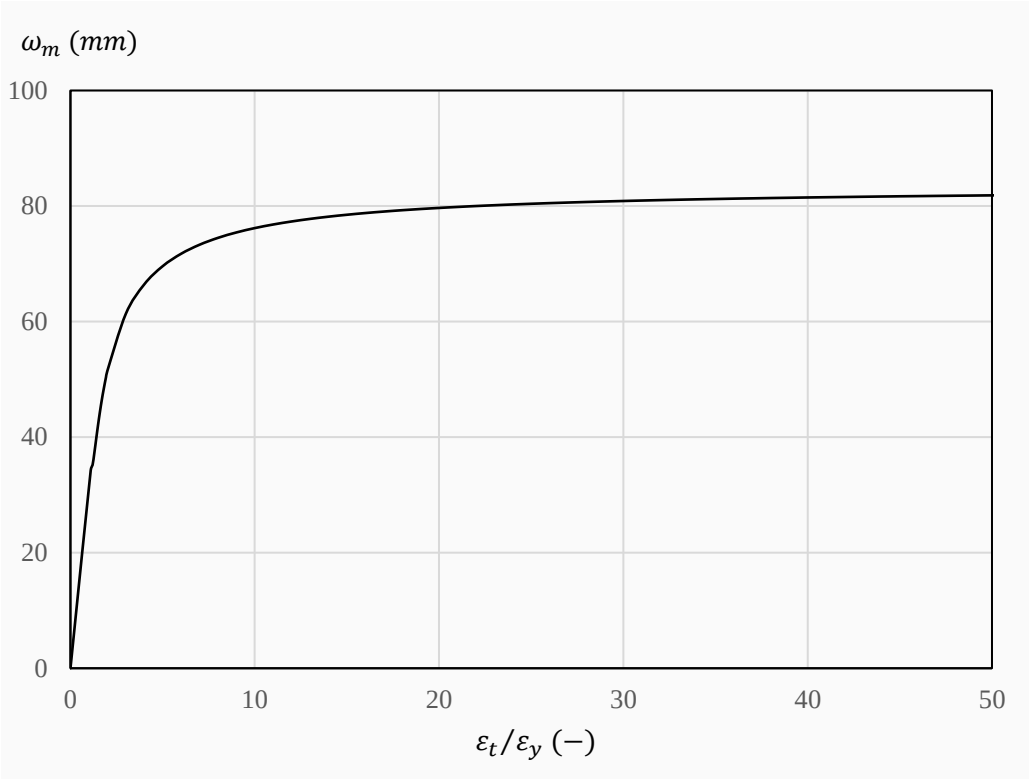

Figure 3.21 The original solution of vertical displacement against maximum strain level

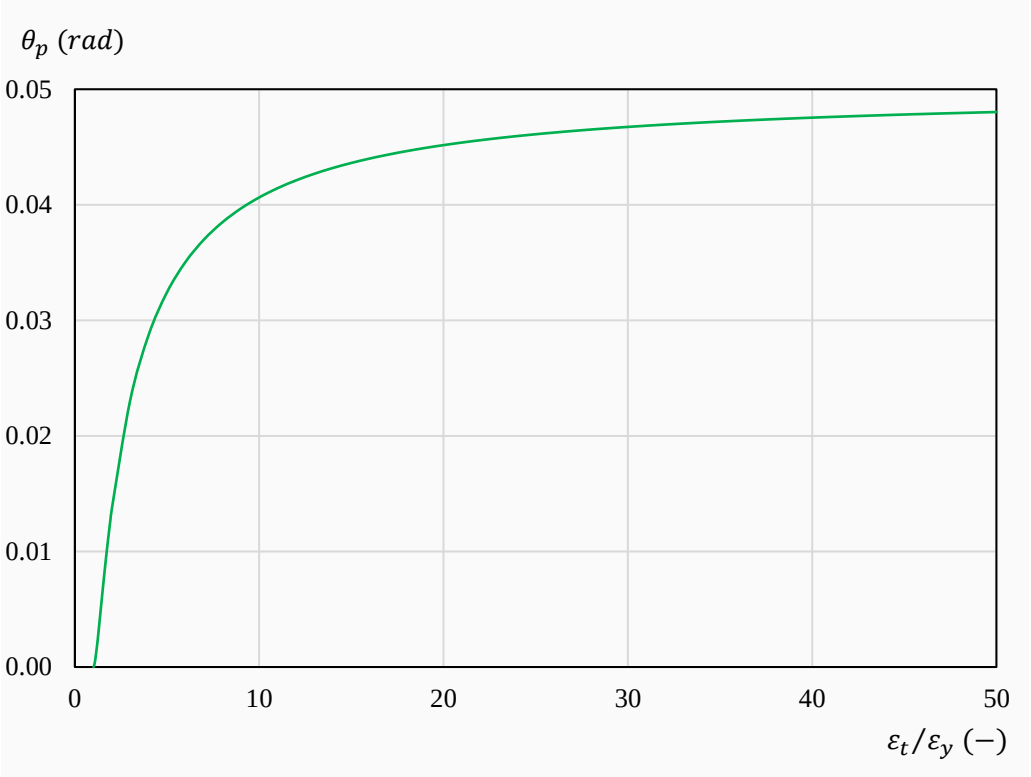

Figure 3.22 The development of plastic rotation angle

Figure 3.23 shows the difference after a characteristic length in the plastic concentration zone is introduced, and a nominal strain with more physical meaning is used. As can be seen, the modified strain does not have significant effect on the development of deflection-strain relation. This is due to the fact that the post-yield deflection is increasing at an incredibly low rate, as the strain continuously increases.

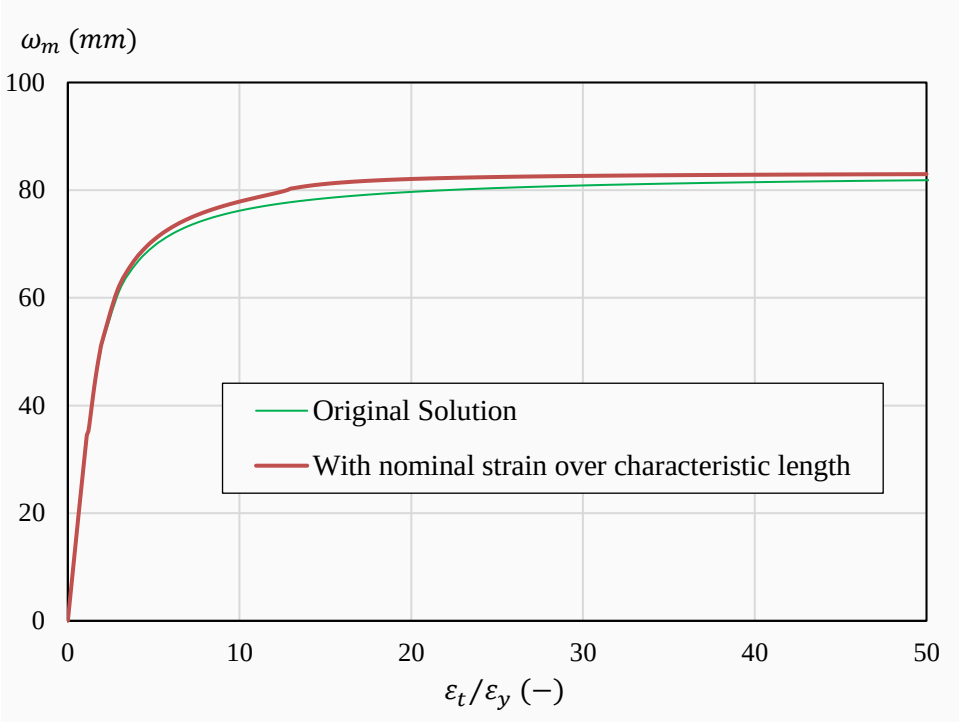

Figure 3.23 The new displacement-strain relation using nominal strain over the characteristic length

For a further analysis, the small discrepancy between the two solutions lies in the assumed deflection shape. The deflection is assumed to take a catenary curve shape, at the middle of which the rotation is always zero. This is not complying with the fact that plastic rotation increases after a small plastic zone or even a hinge point is formed.

As a matter of fact, during the plastic bending stage, it is acceptable to assume a catenary shape for the global deflection along the full length. However, once a concentrated plastic zone or a plastic hinge is formed, the global deflection is prone to take the shape of a triangle. This is consistent with the rigid-plastic mechanism, which has been widely used for large deflection analysis.

Therefore, it is reasonable to still use the original solution, but only before the full plastic moment is reached for the mid-span critical section. Fig. 3.24 depicts the deflection-strain curves, before the full plastic point.

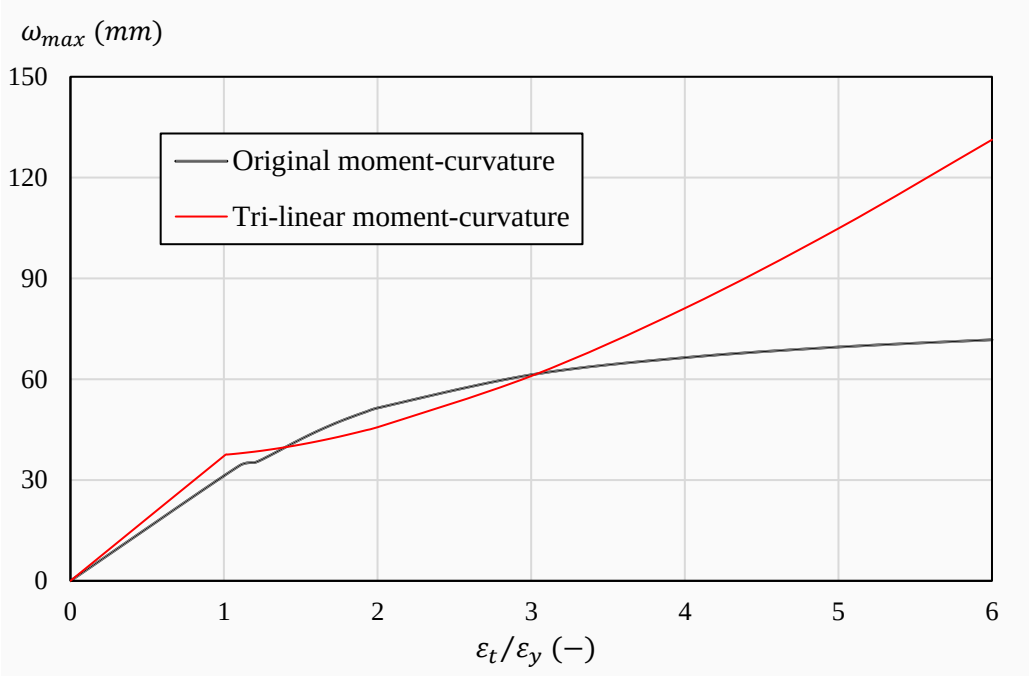

Figure 3.24 The deflection-strain relations before the full plastic point

At the first yield of the mid-span critical section, the standard solutions can be employed and listed below:

$$M_y = \frac{1}{4} P_y (2L) \tag{3-27}$$

$$\omega_y = \frac{1}{48EI} P_y (2L)^3 \tag{3-28}$$

$$\frac{M_y}{EI} = \varphi_y \tag{3-29}$$

Combining the above three equations to obtain the deflection at first yielding of the critical section, we get:

$$\omega_y = \frac{1}{3} \varphi_y L^2 \tag{3-30}$$

Thus, for the practical double beam set, the deflection at first yield is 37.5 mm, which verifies the accuracy of the solutions plotted in the figures.

It can also been from the above figure that the tri-linear simplification of the moment-curvature relation has caused considerable overestimation of the deflection, compared to the original solution. Therefore, a better solution is to establish the deflection-strain relation on the basis of the original solution, while formulating the catenary stage using the solution provided in section 3.4.3. The newly modified three-stage deflection-strain response is shown in Appendix B of this Chapter.

3.5 Analytical solution considering the effect of catenary tension force

3.5.1 Analytical solution of resistance function considering the catenary force effect

This section continues the discussion using the simplified generic beam on the global deformability (and hence the potential of developing effective catenary stage) in relation to the local failure, with explicit inclusion of the catenary tension force generated as the beam deforms.

The beam is assumed to be fully restrained axially at the supports. It should be mentioned that this can be easily extended to generalized support conditions by incorporating the rotational and axial stiffnesses of support ends into an equivalent beam stiffness (Yin and Wang 2005).

For the purpose of simplification, the catenary response stage is assumed to commence when the mid-span critical section reaches the full plastic bending moment. The deflection and critical strain at this particular point are accordingly denoted as ω_{p0} and ε_{p0}, respectively. These are the initial values for the subsequent increments to be added on.

The increments of deflection and plastic rotation are denoted as $\delta\omega_p$ and $\delta\theta_p$, respectively. From the geometric point of view, they have the linear correlation expressed in Equation (3-31), where L_1 is the distance from support end to the middle point (middle joint when there is a joint).

$$\delta\theta_p = 2\frac{\delta\omega}{L_1} = 2\frac{\omega - \omega_{p0}}{L_1} \tag{3-31}$$

Hence the total deflection is simply

$$\omega = \omega_{p0} + \delta\omega \tag{3-32}$$

As the effect of the catenary axial force is taken account for, the incremental axial deformation $\delta\Delta_N$ becomes an important variable in the formulation process of catenary stage. More specifically, it can be further decomposed into two components:

1) the elastic beam elongation over the length of L_1, denoted as $\delta\Delta_{Ne}$;
2) the plastic axial deformation at the plastic hinge, as by-product of plastic rotation under combined bending and tensile force denoted as $\delta\Delta_{Np}$.

Hence, the elastic axial elongation is the total axial deformation subtracting its plastic component. This may be expressed in the incremental formation as:

$$\delta\Delta_{Ne} = \delta\Delta_N - \delta\Delta_{Np} \tag{3-33}$$

The total incremental beam axial elongation, or length increase, could be found by the geometrical approximation as

$$\delta\Delta_N = \delta\left(\frac{\omega}{L_1}\cdot\omega\right) = \frac{2\omega\cdot\delta\omega}{L_1} \tag{3-34}$$

The axial deformation associated with the plastic rotation at the plastic hinge is understandably dependent on the details of the plastic zone including the contributing connection in actual beam assemblies. In an idealised condition this may be approximated by using the associated flow rule, and assuming a linear N-M yield surface (Izzuddin 2005), the plastic axial deformation may be found as:

$$\delta\Delta_{Np} = \frac{M_p}{N_p}\cdot\delta\theta_p \tag{3-35}$$

Substituting Equations (3-31), (3-34) and (3-35) into Equation (3-33), the increment of elastic axial deformation is obtained as

$$\delta\Delta_{Ne} = \frac{2\omega\cdot\delta\omega}{L_1} - \frac{M_p}{N_p}\cdot\left(2\frac{\delta\omega}{L_1}\right) \tag{3-36}$$

For further simplification as shown in Fig. 3.25, it is assumed that there is no beam axial stretching until the deflection rises to ω_{p0}. Under this assumption, the axial force developed in the beam can be calculated from the above result of elastic elongation of the critical section as:

$$N(\omega) = EA \cdot \frac{\delta\Delta_{Ne}}{L_1} = \frac{EA}{L_1}\left[\frac{2\omega \cdot \delta\omega}{L_1} - \frac{M_p}{N_p} \cdot \left(2\frac{\delta\omega}{L_1}\right)\right] = \frac{2EA}{L_1^2}(\omega - \frac{M_p}{N_p})\delta\omega \tag{3-37}$$

According to the N-M interaction relationship, the corresponding bending moment at the hinge location can be found as:

$$M(\omega) = M_p\left(1 - \frac{N}{N_p}\right) = M_p - \frac{M_p}{N_p} \cdot N = M_p - \frac{M_p}{N_p} \cdot \frac{2EA}{L_1^2} \cdot \left(\omega - \frac{M_p}{N_p}\right) \cdot \delta\omega \tag{3-38}$$

To eventually solve the load resistance, taking the beam over the length L_1 as a free body, of which the moment equilibrium equation is written as:

$$\sum M = M(\omega) + N(\omega) \cdot \omega - \frac{P}{2}L_1 = 0 \tag{3-39}$$

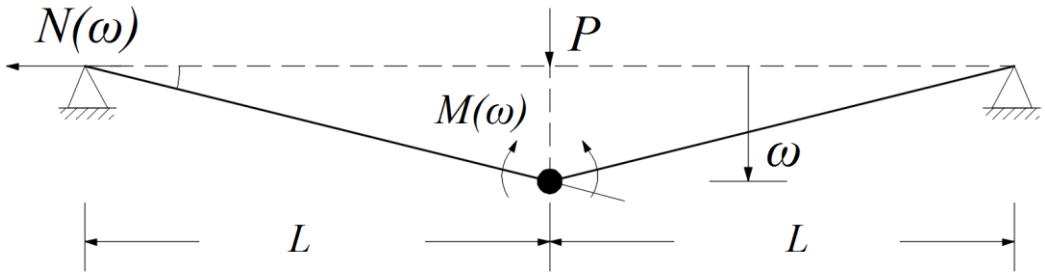

Figure 3.25 Equilibrium diagram of the double beam set

Substituting Equations (3-32), (3-37) and (3-38) into Equation (3-39) leads to the overall load resistance as:

$$P(\omega) = 2\frac{M(\omega) + M(\omega)\cdot\omega}{L_1} = \frac{2}{L_1}\left[M_p + N(\omega)\cdot\left(\omega - \frac{M_p}{N_p}\right)\right]$$
$$= \frac{2M_p}{L_1} + \frac{4EA}{L_1^3}\delta\omega\left(\omega - \frac{M_p}{N_p}\right)^2 \quad (3\text{-}40)$$

The above equation demonstrates that the overall post-yield load resistance is collectively contributed by the bending moment and axial force at the hinge section. Therefore, it will provide more understanding to investigate the separate load resistances contributed from flexural and axial mechanisms. Firstly, the bending moment results in the resistance by a value of

$$P_M(\omega) = \frac{2M}{L_1} = \frac{2M_p}{L_1} - \frac{4M_p}{N_p}\cdot\frac{EA}{L_1^3}\left(\omega - \frac{M_p}{N_p}\right)\delta\omega \quad (3\text{-}41)$$

and secondly, the load resistance attributed to catenary axial force is

$$P_N(\omega) = \frac{2N\omega}{L_1} = \frac{4EA\omega}{L_1^3}\left(\omega - \frac{M_p}{N_p}\right)\delta\omega \quad (3\text{-}42)$$

As given by Equation (3-32), the total deflection is the increment added on the initial value ω_{p0}, which has been recorded before. From these results, a load-deflection relationship similar to that by Izzuddin (2005) can be finally generated.

Using the generic beam example with the same parameter values in the previous section, the load-deflection relationship can be represented by the curve plotted as below. After the full plastic point, the separate contributions to the load resistance by bending moment and axial force have also been shown. With the increase of axial force and the deterioration of the flexural action, the majority contribution to the load

resistance is gradually shifting from bending moment to the catenary axial force, as shown in Fig. 3.26

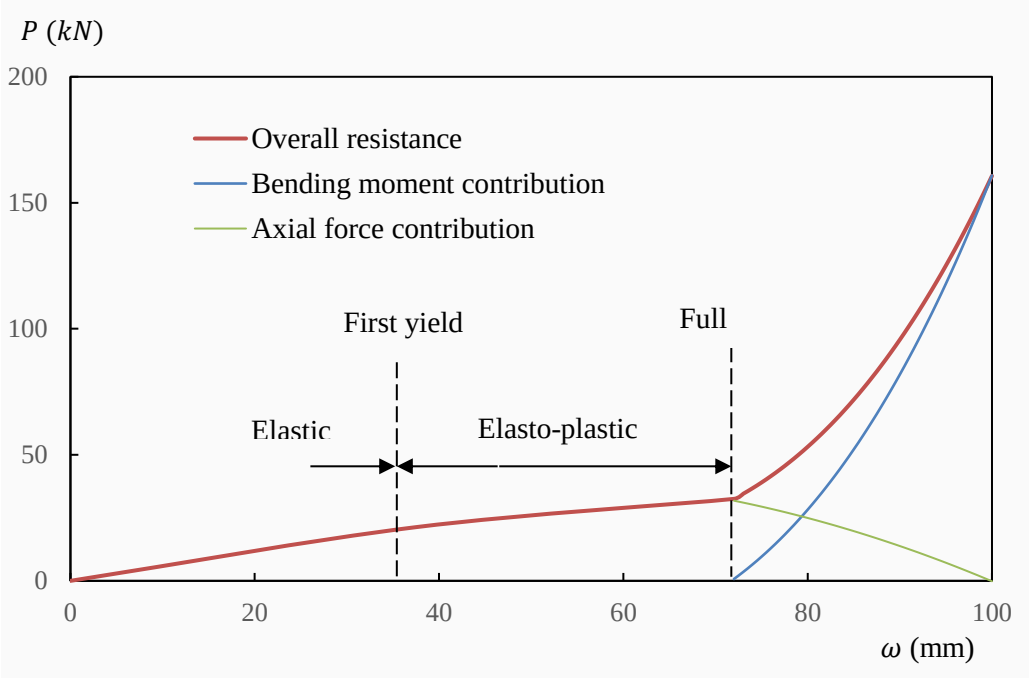

Figure 3.26 The load-deflection response of three stages

In the final catenary stage, the overall load resistance will be solely be sourced from the axial force, which is sustained at the full plastic capacity N_p. The load resistance will be a simple linear function of the overall deflection, given as

$$P = 2N_P \cdot \sin\theta = 2N_P \frac{\omega}{L} \tag{3-43}$$

The final catenary stage is not plotted here for the practical double beam example, as the failure criteria will be discussed in the following analysis.

3.5.2 The establishment of the ultimate failure criteria

As already discussed, the extent to which the catenary action can develop will be determined by the global deformability of the beam-assembly, which in turn depends on the total plastic deformation capacity in the plastic region. In simple terms, this is essentially about the rotational capacity of the plastic hinge.

For the generic beam considered herein, the inclusion of the tension force means there will be increase in the plastic strain on top of the strain due to bending, and as a result the ultimate deflection at material failure will reduce. Figure 3.28 schematically shows the full deflection-strain response, including three post-yield stages.

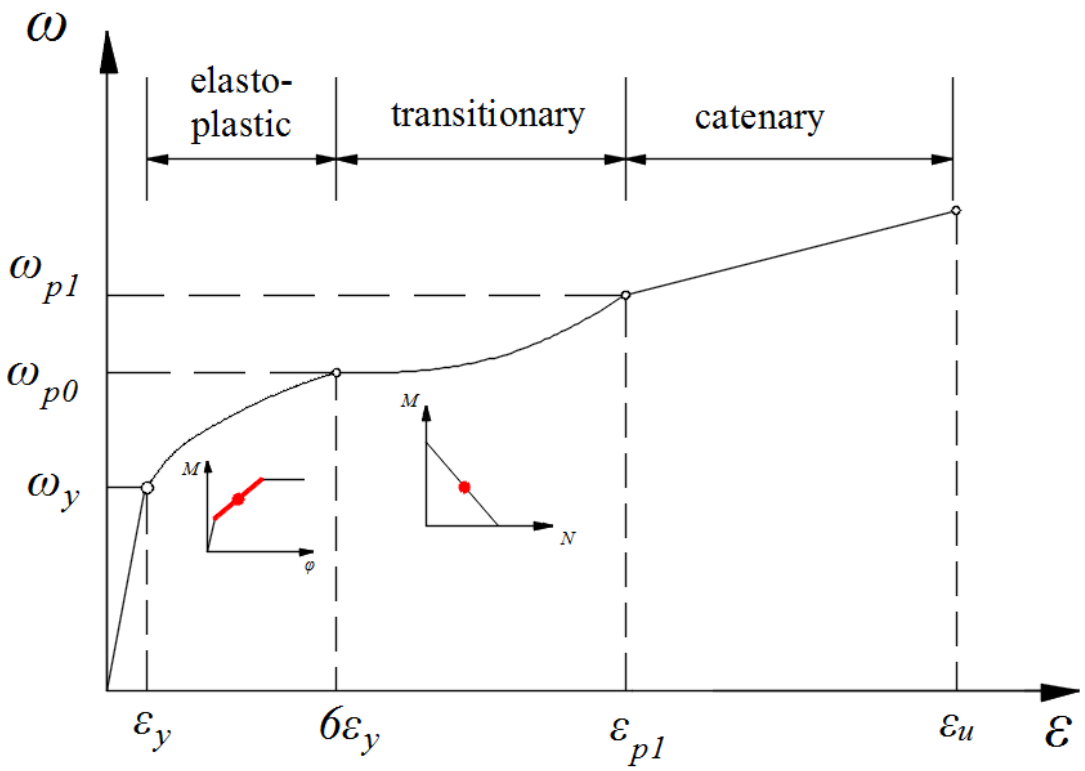

Figure 3.27 The full deflection-strain response up to failure

Three simplification assumptions are introduced here:

1) The plastic deformation is concentrated within a plastic hinge zone, which has the length equal to the equivalent plastic hinge length and all the plastic rotation will be concentrated in this hinge zone.
2) The axial deformation is decomposed into the elastic and plastic components. Likewise, the plastic axial extension is also concentrated in the designated hinge zone.
3) Elastic axial deformation occurs along the rest of the beam span length.

These assumptions will enable a correlation between the global deflection and local deformation (critical strain).

1) The deflection-strain response during the transitionary stage

As has been obtained in section 3.5.1, when the mid-span critical section reaches its full plastic moment, the strains are recorded as

$$\varepsilon_{M0} = 6\varepsilon_y, \quad \varepsilon_{N0} = 0 \tag{3-44}$$

and the overall deflection is noted as:

$$\omega = \omega_{p0} \tag{3-45}$$

This is regarded as the initial point, on which the subsequent strain increments are to be added. In this way, the maximum strain associated with each deflection point after ω_{p0} will be evaluated by the following equation

$$\varepsilon_{total} = \varepsilon_M + \varepsilon_N = (\varepsilon_{M0} + \delta\varepsilon_M) + (\varepsilon_{N0} + \delta\varepsilon_N) \tag{3-46}$$

Firstly, with regard to the flexural strain induced by the plastic bending moment, it can be associated with the plastic curvature, then with the total plastic rotation over the hinge zone. Their relationship is expressed as

$$\delta\theta_p = \delta\varphi_p \cdot l_p = \frac{\delta\varepsilon_M}{h/2} \cdot l_p \tag{3-47}$$

Combining the above formulation with Equation (3-31), the incremental plastic strain can be now directly related to the overall deflection

$$\delta\varepsilon_M = \frac{h}{L} \cdot \frac{\omega - \omega_{p0}}{l_p} \tag{3-48}$$

Secondly, the plastic component of the incremental axial strain is also concentrated within the hinge length l_p, so it can be estimated as

$$\delta\varepsilon_{Np} = \delta\Delta_{Np}/l_p \tag{3-49}$$

By making use of the N-M interaction flow rule, and combining with Equation (3-31), this plastic component is obtained as:

$$\delta\varepsilon_{Np} = \left(\frac{M_p}{N_p}\cdot\delta\theta_p\right)/l_p = 2\frac{M_p}{N_p}\cdot\frac{\omega-\omega_{p0}}{l_pL} \tag{3-50}$$

According to the third assumption made before, the elastic component of the incremental axial strain can be calculated from the elastic axial elongation achieved in Equation (3-36) as:

$$\delta\varepsilon_{Ne} = \frac{\delta\Delta_{Ne}}{L} = \frac{1}{L}\left[\frac{2\omega\cdot\delta\omega}{L} - \frac{M_p}{N_p}\cdot\left(2\frac{\delta\omega}{L}\right)\right] = \frac{2\delta\omega}{L^2}\left(\omega - \frac{M_p}{N_p}\right) \tag{3-51}$$

Finally, the incremental axial strain can be summed up as

$$\delta\varepsilon_N = 2\frac{M_p}{N_p}\cdot\frac{\omega-\omega_{p0}}{l_pL} + \frac{2\delta\omega}{L^2}\left(\omega - \frac{M_p}{N_p}\right) \tag{3-52}$$

Thus, the plastic strain increments have all been directly formulated base on the deflection. Then the deflection-strain relation can be established in the transitionary stage.

2) The deflection-strain response in the catenary stage

As stated before, the catenary response will come into play immediately when the axial force attains its full plastic capacity N_p. The deflection at this point can be calculated using the solution in the previous section, and it is denoted again as $\omega = \omega_{p1}$.

At this particular transition (end) point, the strain calculated from the transitionary stage solution is denoted as

$$\varepsilon = \varepsilon_{p1} \tag{3-53}$$

This has formed another reference point for subsequent strain increment to be added on during the final catenary stage.

The incremental strain due to the continued plastic rotation is calculated similarly by Equation (3-47). The new increment is expressed by

$$\delta\varepsilon_M = \frac{h}{L} \cdot \frac{\omega - \omega_{p1}}{l_p} \tag{3-54}$$

For the incremental axial strain, it is approximated by the incremental axial extension as:

$$\delta\varepsilon_N = \frac{\delta\Delta_N}{L} \tag{3-55}$$

By substituting the result of incremental axial, i.e. Equation (3-34), into the above equation, we get

$$\delta\varepsilon_N = 2\omega\left(\omega - \omega_{p1}\right)/L^2 \tag{3-56}$$

Therefore, the maximum total strain during the catenary response stage can be calculated as

$$\varepsilon = \varepsilon_{p1} + \delta\varepsilon_N + \delta\varepsilon_M = \varepsilon_{p1} + \frac{2\omega\left(\omega - \omega_{p1}\right)}{L^2} + \frac{h}{L} \cdot \frac{\omega - \omega_{p1}}{l_p} \tag{3-57}$$

Finally, the full deflection-strain relation accounting for the axial force effect can be readily established. More importantly, by simply introducing the material rupture strain, the final failure deflection can be found as the performance limit of the catenary stage.

Using the double beam example with the same parameter values in the previous section, the deflection-strain curve can be plotted in Fig. 3.28.

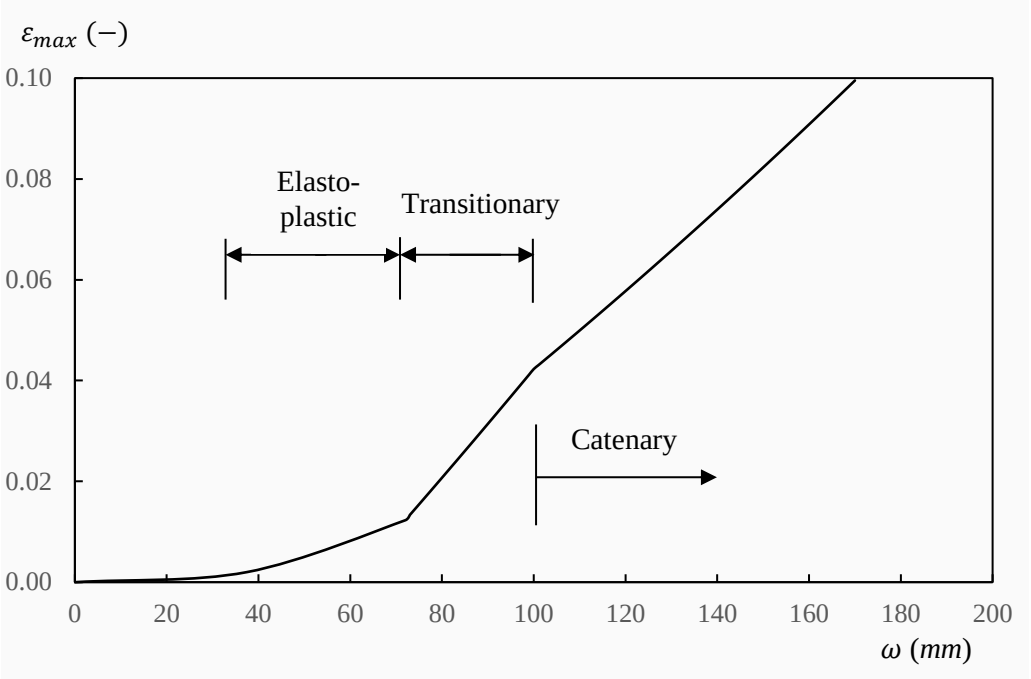

Figure 3.28 The full deflection-strain response for a practical double beam set

It can be clearly identified from the graph that when the maximum strain reached a prescribed rupture strain of 10%, the failure deflection is 170 mm. This ultimate deflection is 11.3% of the single span length (1500 mm).

3.6 Summary

In this chapter, a generic axially-constrained beam is analytically examined in order to better understand the full range response including the large deflection regime, the development of the plastic deformation, and how this in turn affects the overall resistance and the deformability. The load-deflection relationship and the associated plastic deformation are first analytically derived for a bending scenario, and then the effect of the catenary action is introduced. The analytical solution provides some quantitative insight, although under idealised conditions, into the limiting local criterion (material strain in this case) and the global deflection and deformability.

The theoretical formulations can be applied directly to similar beam assemblies where the local failure is governed by material rupture criterion.

The examination of the analytical results also suggests the importance to facilitate the "spread" of the plastic region in increasing the total plastic deformability, and hence the ability for a beam assembly to develop into an effective catenary action stage.

3.7 Appendix

The appendix explains the derivation of the resistance function, using the simplified tri-linear moment-curvature relationship for the beam section.

The moment-curvature relationship for a rectangular beam section can be simplified into a tri-linear form. The tri-linear *M*-φ curve includes the initial yielding point, the simplified "full plastic" point, and an inelastic stage in-between. The simplified *M*-φ relationship is schematically shown in Fig 3.29.

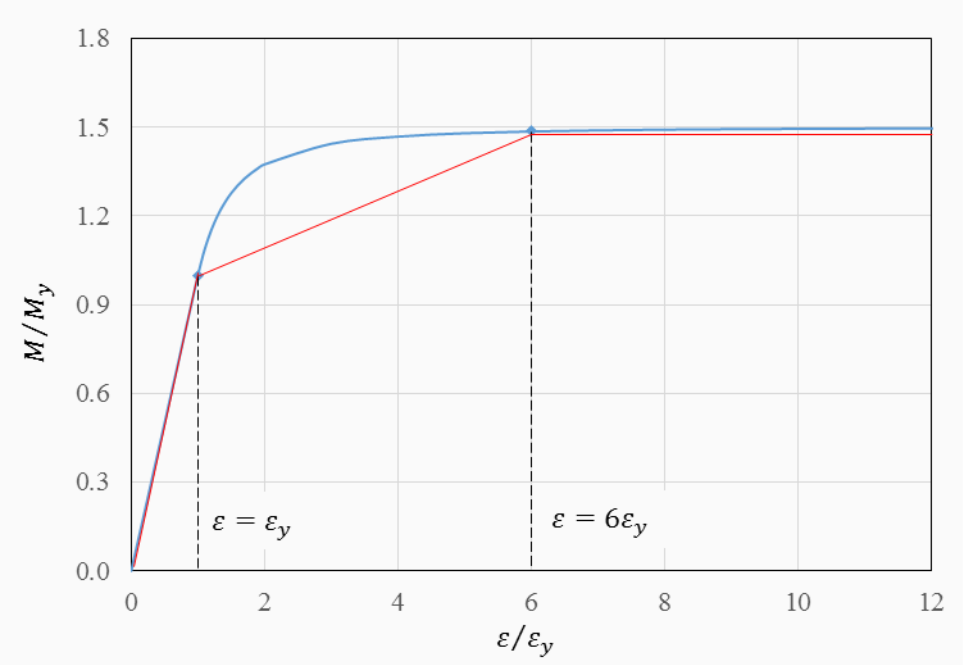

Figure 3.29 The simplified tri-linear moment-curvature relationship

The trilinear simplification of moment-curvature relation can now be used to evaluate the overall deflection. A new solution will be provided, and the failure limit can be established and related to the material rupture strain.

The whole response of the double beam set can be divided into three stages, in accordance with the behaviour of mid-span critical section. The response stages are schematically shown in Fig. 3.30, and illustrated as below:

a) Elastic stage;

b) Elasto-plastic stage, between initial yielding and the moment when full plasticity is firstly reached in the critical section;

c) Catenary stage.

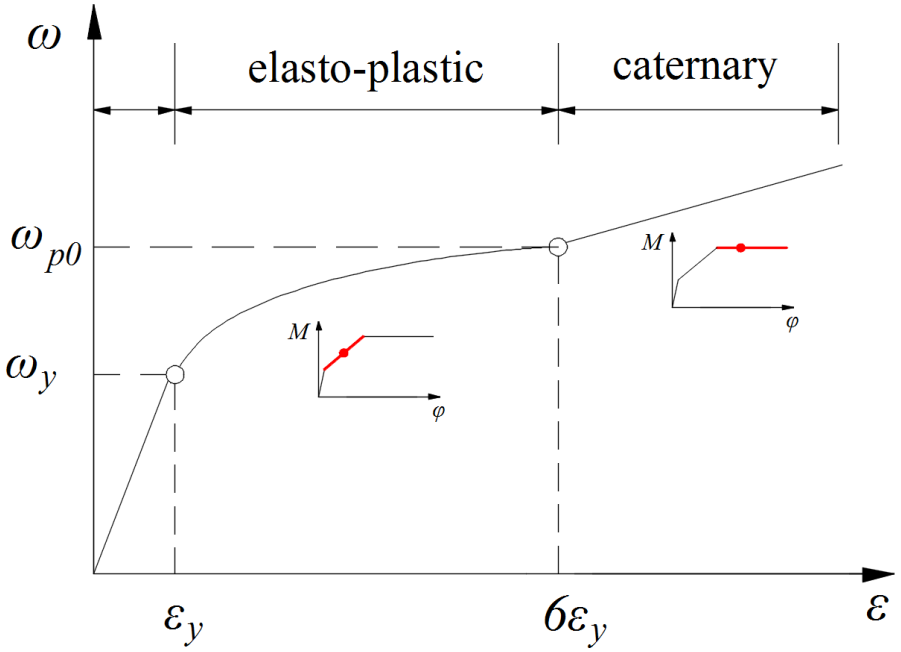

Figure 3.30 The resistance function in terms of deflection-strain relation

To shed some light on the final catenary stage, it commences immediately when the mid-span section has reached the full plastic moment. In this stage, all incremental plastic deformations are assumed to be concentrated within the equivalent plastic hinge length l_p^e. This narrow zone can be regarded as a point hinge at the beam level, providing that l_p^e is reasonably close to the beam depth. However, for the purpose of facilitating the translation between the incremental curvature and plastic rotation, we still employ the equivalent hinge length to establish the analytical formulations in the following sections.

(A) The resistance function in the elasto-plastic stage response

After the first yielding of the mid-span critical section, the simply supported double beam set is stepping into an elasto-plastic phase (Fig. 3.31). The stage will last up to the point when the critical section has reached its full plastic moment.

During the elasto-plastic response, the evolution of overall deflection is still dependent on the strain development. The associated analytical formulation can be fully resolved using the analytical solution method proposed in section 3.3.

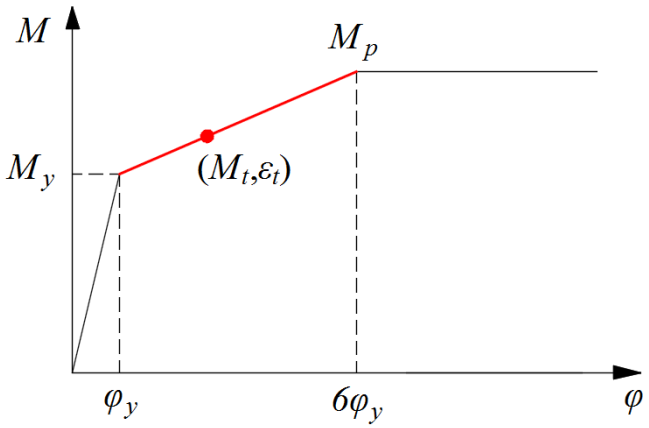

Figure 3.31 The critical section behaviour during elastoplastic state

As shown in Fig 3.29, the bending moment during the elasto-plastic stage could be given as linear interpolation, between the initial yielding and full yielding points, as follows:

$$M_t = M_y + (M_p - M_y)\frac{\varepsilon_t - \varepsilon_y}{6\varepsilon_y - \varepsilon_y} \tag{3-58}$$

For the rectangle section, the ideal full plastic moment M_p is 1.5 times of the initial yielding moment M_y, so the above interpolation becomes

$$M_t = M_y\left(1 + \frac{\varepsilon_t - \varepsilon_y}{10\varepsilon_y}\right) \tag{3-59}$$

Likewise, the bending moment diagram still takes a linear shape due to the concentrated load, as expressed by Equation (3-11). Because both the bending moment distribution and the moment-curvature relation are linear functions, the distribution of curvature along the plastic deformation zone must also follow a linear pattern as follows (Fig. 3.32):

$$\varphi(x) = \varphi_y + \frac{x}{l_p/2}(\varphi_t - \varphi_y), 0 \le x \le l_p/2 \tag{3-60}$$

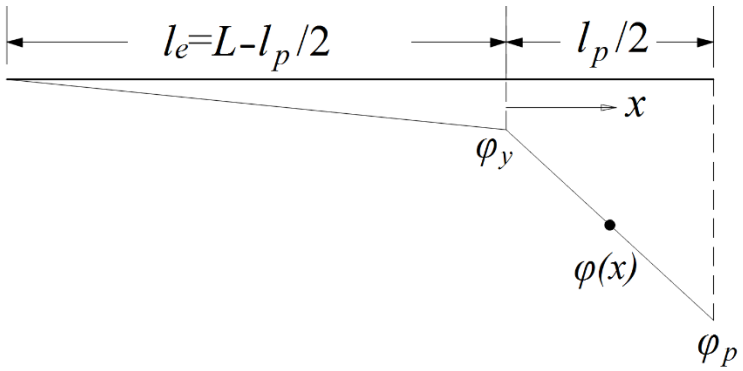

Figure 3.32 The linear curvature distribution over the plastic zone

Correspondingly, the maximum sectional strain also has the following the linear form:

$$\varepsilon(x) = \varepsilon_y + \frac{x}{l_p/2}(\varepsilon_t - \varepsilon_y), 0 \le x \le l_p/2 \tag{3-61}$$

Now that the curvature distributions along both the elastic and plastic zones are known already, the deflection shape can be obtained by integrating the curvature function twice along the whole beam. The following boundary conditions also need to be applied to solve the constants generated in the integration:

1) The deflection at the support is zero;
2) The slope angle ($d\omega/dx$) at the midspan is equal to zero;
3) The slope angle at the intersection of the elastic and plastic zones is smooth;
4) The deflection at the intersection of the elastic and plastic zones is continuous.

The derivation process is omitted here, and the deflection shape function along the plastic zone ($0 \le x \le l_p/2$) is eventually achieved as

$$\omega(x) = \frac{x^3}{l_p}(\varphi_t - \varphi_y) + \frac{\varphi_y}{2}x^2 - \frac{l_p}{4}(\varphi_t + \varphi_y)x - \frac{\varphi_y}{3}l_e^2 - \frac{l_p l_e}{4}(\varphi_t + \varphi_y) \tag{3-62}$$

Substituting $x = l_p/2$ into the formation gives the maximum deflection at the mid-span location. It varies as a function of φ_t, which is determined by the maximum strain at the critical section given from:

$$\omega_{max} = \frac{2\varphi_t + \varphi_y}{24}l_p^2 + \frac{\varphi_y}{3}l_e^2 + \frac{\varphi_t + \varphi_y}{4}l_e l_p \tag{3-63}$$

From the bending moment diagram, the length of the plastic zone length can be calculated as:

$$\frac{l_p}{2} = \frac{M_t - M_y}{M_t}L = \left(1 - \frac{1}{1 + \frac{\varepsilon_t - \varepsilon_y}{10\varepsilon_y}}\right)L = \frac{\varepsilon_t - \varepsilon_y}{\varepsilon_t + 9\varepsilon_y}L \tag{3-64}$$

Therefore, combining the above two formulations, the overall deflection against the maximum strain can be established during the elasto-plastic stage.

(B) The resistance function in the catenary stage

As soon as the full plastic moment is reached for the mid-span section, the catenary response comes into play (Fig. 3.33). Thus, it is necessary to record the overall deflection at the end of the previous elasto-plastic stage. In this way, the incremental deflection caused by further strain increase could be added on.

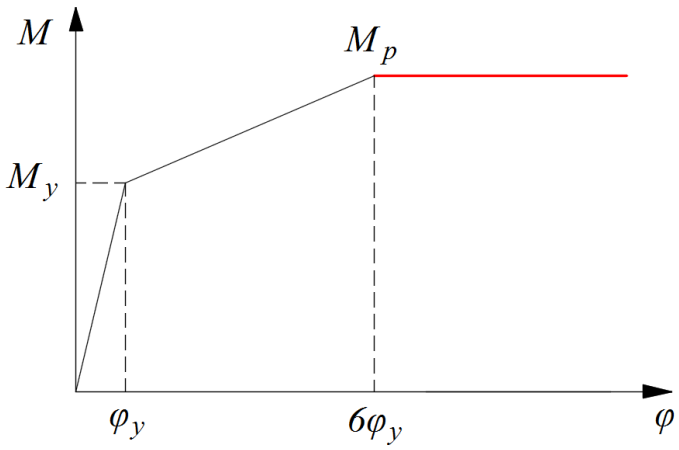

Figure 3.33 The critical section behaviour during catenary state

When the artificially designated point of full plasticity, i.e. $\varepsilon_t = 6\varepsilon_y$, is reached, the actual plastic zone has a total length of $l_p = 2L/3$. Thus, the elastic zone also has a length of $l_e = 2L/3$ on each single span.

Substituting the values of $\varphi_t = 6\varphi_y$ and $l_e = l_p = 2L/3$ into Equation (3-63), the maximum deflection, which is denoted as ω_{p0}, will be

$$\omega_{p0} = \frac{13}{24}\varphi_y l_p^2 + \frac{\varphi_y}{3} l_e^2 + \frac{7\varphi_y}{4} l_e l_p = \left(\frac{13}{24} + \frac{1}{3} + \frac{7}{4}\right)\varphi_y \left(\frac{2L}{3}\right)^2 = \frac{7}{6}\varphi_y L^2 \quad (3\text{-}65)$$

Due to the linear curvature distribution along the plastic zone, the equivalent plastic hinge length (Fig. 3.34) is calculated as

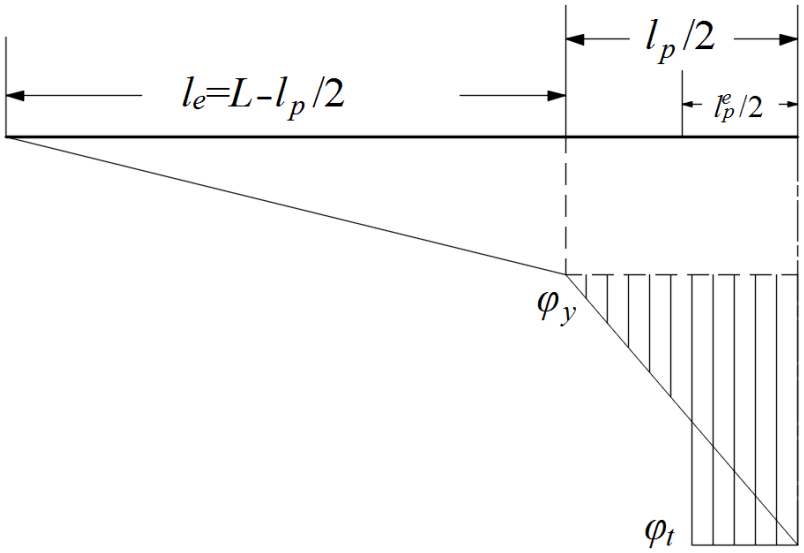

Figure 3.34 The curvature distribution after first yield of the mid-span section

$$l_p^e = \frac{\theta_p}{\varphi_p} = \frac{\frac{l_p}{2}(\varphi_t - \varphi_y)}{\varphi_t - \varphi_y} = \frac{l_p}{2} = \frac{1}{6}(2L) \tag{3-66}$$

The result shows that the equivalent plastic hinge length will be 1/6 of the beam span length. Considering that the economical beam design usually has a depth-span ratio around 1/10-1/20, it is acceptable that this hinge length can be considered to be close to the magnitude of the beam depth. In this sense, the equivalent plastic hinge could be simplified into a hinge point (Fig. 3.35). The plastic deformation will be concentrated into the hinge point from the full plastic point. Unlike the existing studies, the equivalent plastic hinge length l_p^e will still be made use of, in order to translate the strain or curvature into plastic rotations.

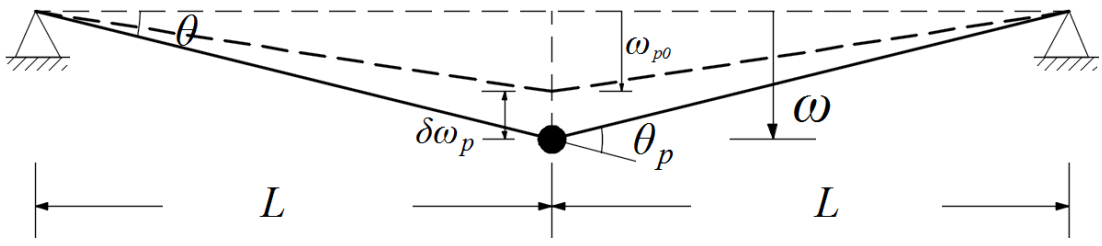

Figure 3.35 The deflection diagram after the hinge formation

Under this circumstance, the increment plastic rotation is given by means of multiplying plastic curvature by the equivalent plastic hinge length as:

$$\delta\theta_p = \delta\varphi_p \cdot l_p^e = \delta\varphi_p \cdot \frac{L}{3} \tag{3-67}$$

From the geometric kinematics, the incremental plastic deflection could be eventually achieved as

$$\delta\omega_p = \left(\delta\theta_p/2\right) \cdot L = \frac{L^2}{6} \cdot \delta\varphi_p = \frac{L^2}{3h}\delta\varepsilon \tag{3-68}$$

The total deflection and strain are simply the incremental values added on to the deflection and strain at the start point of full plastic state

$$\omega = \omega_{p0} + \delta\omega_p \tag{3-69}$$

$$\varepsilon = 6\varepsilon_y + \delta\varepsilon \tag{3-70}$$

Therefore, the overall deflection can be associated with the strain plastic strain development. More importantly, the ultimate failure deflection can be identified through the material rupture strain.

4 Experimental studies: a supplementary laboratory perspective on plastic deformation concentration and its effect on realistic resistance of double-span beam assemblies

4.1 Introduction

4.1.1 A brief overview of past experimental studies

Various research efforts have been devoted in recent years to the understanding of the damage processes and the mechanisms governing the development of the arching action and the catenary effects. For instance, Sadek et al. (2011) experimentally studied a steel beam assembly with a combined weld-bolt beam-column connection and observed steel fracture and bolt shear failure. Yang and Tan (2013) tested the behaviour of different bolted steel beam-column joints subjected to catenary action, and discussed the general response features of the typical joints. Li et al. (2013) tested two steel beam-tubular column connections, and demonstrated two flexural failure modes which determined the patterns of the resistance functions. They also examined the details of the joints and how they affected the ultimate deformability and hence the effective development of the catenary action. Taking into account the effect from the concrete slab, Guo et al. (2013) carried out a test on a one-way composite floor system under a column-missing scenario, and observed the influence of the presence of the slab on the collapse mechanism and the resistance over different stages of the response.

These experimental studies and the associated numerical verifications have provided coverage of response characteristics and potential failure modes of some typical joints. However, questions remain concerning the ultimate limit of catenary action, especially in terms of the concentration of the plastic deformations surrounding the connection regions and how fundamentally this can dictate the extent to which the catenary action could eventually develop. It is with such questions in mind that a set of scaled beam assemblies have been investigated to supplement the existing experimental literature.

4.1.2 Scope and objectives

The experimental studies presented in this chapter is in supplement to the experimental literature to provide a fuller coverage of plastic deformation patterns in the connection regions and how they affect the development of the catenary action – or indeed whether in some cases the catenary action could be developed to an effective extent at all.

Laboratory specimens at a scale of 1:2 ~ 1:3 were designed and fabricated, and they were subsequently tested under push-down loading at the middle joint position. The first group of specimens, denoted as **A1~A3,** represent square hollow section (SHS) beam-column substructures featuring three generic connection types. The second group of specimens **B1~B3** represent standard I section beam-column substructures, with the latter two of them having a one-way RC slab combined with the steel beam through shear studs. The purpose-designed connection details allow different local plastic mechanisms and local failure modes to develop, thereby enabling observation of the correlation among local failure (e.g. rupture of steel), the spread of plastic regions, the development of regional plastic deformation, and consequently the overall ultimate deformability and resistance.

As schematically shown in Fig. 4.1, the local failures are expected to be observed in the critical regions adjacent to the joint zone, with the increase of the mid-span deflection. The resistance function can be established by the load resistance (P) and the vertical displacement (Δ). Particular attention has been paid to the ultimate deformation limits, the various local failure events that are revealed, and the associated impacts on the overall load resistance function.

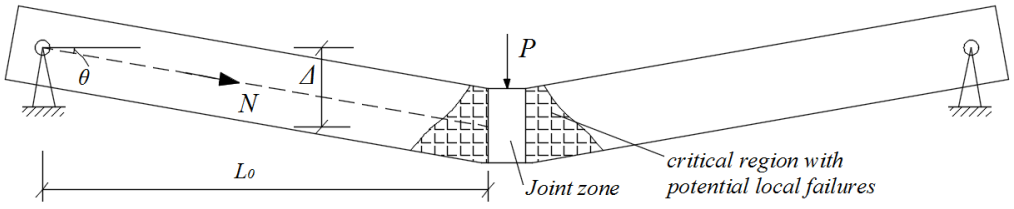

Figure 4.1 Schematic view of a deflected double beam assembly under central column loss

The implications of the results and the mechanisms to enable an effective development of the catenary action and improve deformation ductility are discussed. Compared to the existing experimental literature (e.g. Li et al. 2013, Yang and Tan 2013), the tests reported here provide further insight into the behaviour of the beam assemblies towards the smaller deformability range of the subject.

4.2 Quasi-static tests on double beam assemblies with three generic types of steel joints

The first group of three specimens **A1~A3** were designed and tested to investigate the resistance function of double beam assemblies with generic middle joints representing different possibilities of plastic deformation development around the middle joint. In particular, the first specimen **A1**, which had a purposely prepared beam-column interface resembling a welded joint, was intended to provide insight into the impact of concentrated plastic deformation on the overall behaviour in terms of the ability to develop into catenary stage, to echo the analytical conclusion for a generalised solid beam in Chapter 3. The other two tests on specimens **A2** and **A3** were aimed to show how possible premature failure at the joint region could dictate the overall deformation capacities and the ultimate resistance.

4.2.1 Specimen design and beam-to-column joint details

The overall geometrical configuration of the three specimens is shown in Fig 4.2. It actually represents a 1/4 reduced scale prototype steel frame substructure subjected to internal column removal. The double beam substructure was simply supported at both ends, with a single span of 725 mm. The beam web areas surrounding the pin holes were strengthened to prevent unwanted damage at the supports. The central column stub was pushed vertically downwards until the complete failure of the specimen. The complete failure is reached when the vertical load resistance cannot be picked up again.

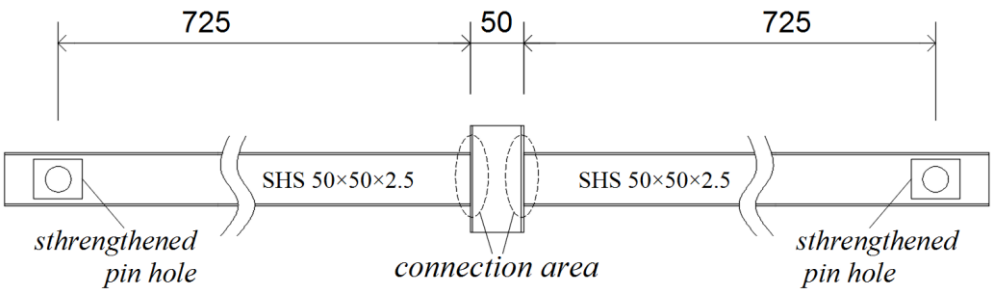

Figure 4.2 The general configuration of specimens A1~A3

The double beams and central column stub were all made from structural steel grade S235. The steel material has a yield strength of 235 MPa, elastic modulus of 206 GPa, and an ultimate strength of 360 MPa. All of the elements in the beam assemblies were made from 50 mm square hollow section (SHS) with a wall thickness of 2.5 mm.

In the design of steel structures, for instance following Eurocode 3, the steel beam-column joints are generally classified into three categories based on the rotational stiffness, namely rigid, semi-rigid and nominally pinned joints. In this group of specimens, the three joint types were designed and fabricated to resemble each of the above types, respectively. They shared the same overall configurations except for the beam-column connection details of the middle joint. The features and configurations of the middle joints are described in Table 4.1.

Table 4.1 Specimen design description

Specimen	Connection type	Features
A1	Rigid	Full weld between the beam and column
A2	Semi-rigid	Welded between the flanges and bolted between the webs
A3	Pinned	Top and seat angle and web bolted

The first specimen **A1** was designed with full welding around all the connection area between the beam and column, to represent the rigid connection. Such a connection type is widely used in steel frame constructions to ensure a sufficient stiffness at the connections. The perspective view and the connection configuration are shown in Figure 4.3.

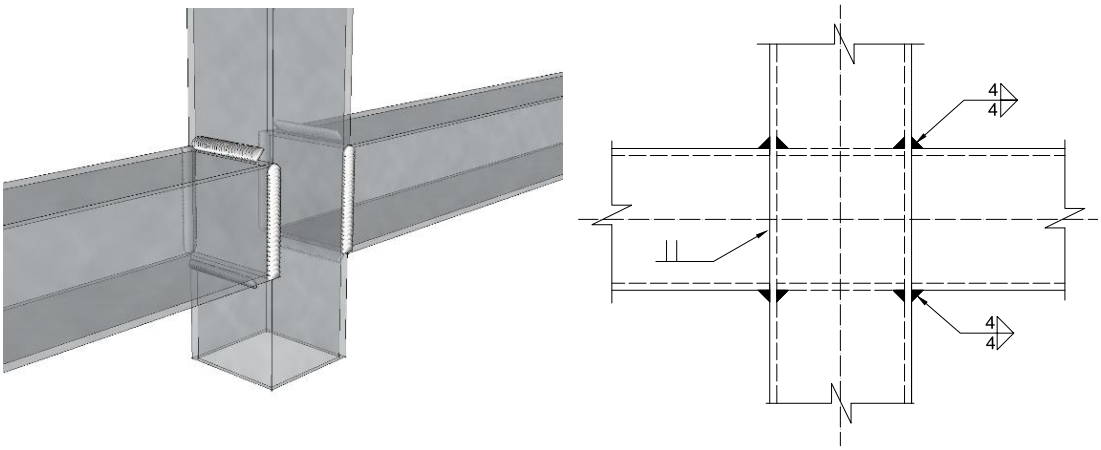

Figure 4.3 Design of Specimen A1: fully welded beam-to-column connection

Specimen **A2** was designed to have weld-bolt hybrid connections. The beam and column flanges were fully welded, while each side of the webs was connected using a 2 mm thick flat plate, and a single row of two M6 bolts, as depicted in Figure 4.4.

The web-bolted and flange-welded (often abbreviated as WBFW) hybrid connection is also one of the most commonly used types in steel frame structures. In engineering practice, the high strength bolts on the beam web are tightened before the beam flanges are welded on site. When it comes to the design resistance assessment, it is assumed that the flange welds carry the whole bending moment, while the web bolt connection part bears the shear force (Tanaka et al. 1996).

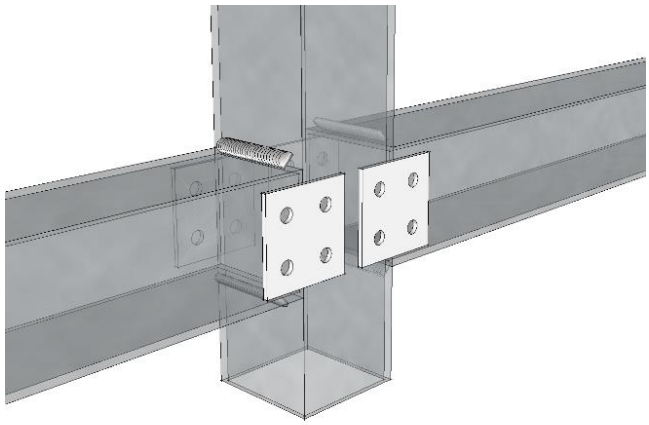

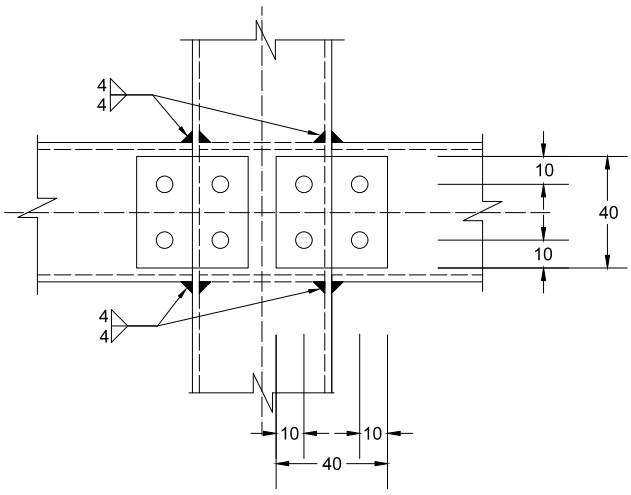

Figure 4.4 Design of Specimen A2: welded - bolted beam-to-column connection

The third specimen **A3** was fully bolted within the connection area, as shown in Fig 4.5. Top and seat angles were used for the bolt connection between the flanges, while the webs were linked using also flat plates and a single row of bolts. For this connection type, Abdalla et al. (2015) concluded that increasing the thickness of angles can effectively improve the stiffness and strength of the structure. However, when the thickness increased to a certain level, it is the bolts that will govern the joint behavior. Although this joint type is not designed for moment resistance, the top and seated angles do provide additional stiffness. However, because the initial rotational stiffness is quite low and the moment resistance is very limited, it is herein classified as nominally pinned joints.

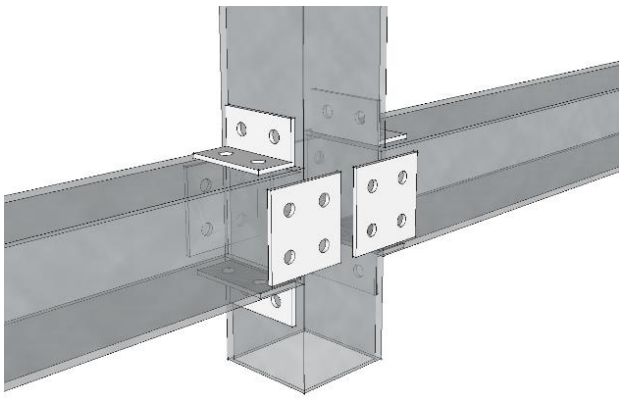

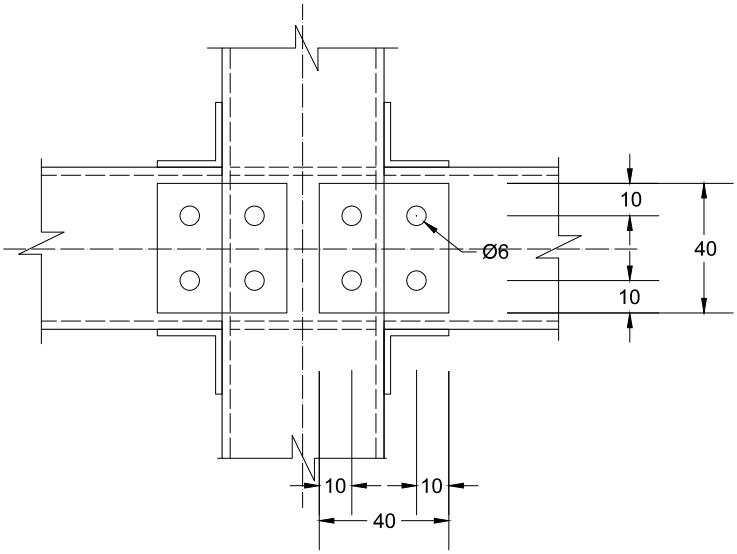

Figure 4.5 Design of Specimen A3: fully bolted beam-to-column connection

For each of the specimens, two inner stiffeners were welded inside the column stub, levelling with the top and bottom beam flanges (Fig. 4.6). This stiffening treatment can effectively maintain the joint continuity, and prevent premature local buckling of the column walls under compression.

Figure 4.6 The assembled specimens of A1~A3

4.2.2 Test set-up and loading scheme

Figure 4.7 schematically shows the test supporting system, which consists of a base beam and end support blocks. A pair of channel beams, 1.8 m long and sufficiently strong, are connected back to back by high strength bolts to provide a base platform

for the testing. There is a reserved gap of 60 mm between the backs of channels, to allow for large vertical displacement of the specimen. Any horizontal tension force produced will be transmitted from the support blocks to the base beam set.

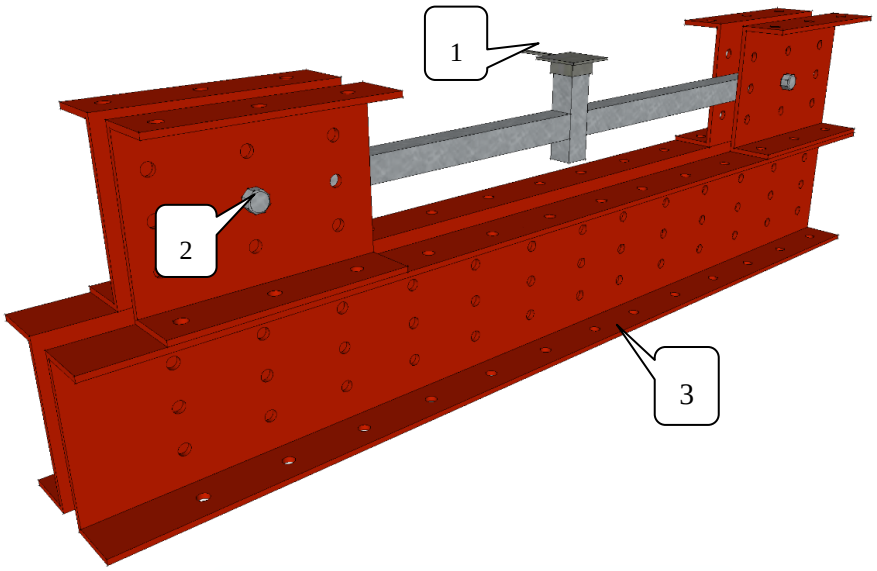

Notes: 1. Steel loading cap; 2. Pin support for the specimen; 3. Base beam block

Figure 4.7 Design of the specimen supporting system

The pin support conditions were achieved by using an M24 bolt for each end to rotate about. According to the anticipated levels of vertical displacement and axial force, the height of specimen installation was adjustable by changing the position of the pin support holes on the support blocks. A steel loading cap shown in Fig 4.6 was close-fit on top of the central column stub, and a piece of 5-mm cork layer was placed between the steel cap and the loading head. The friction between the tightly-contacted surfaces acted to prevent lateral movement of the specimen.

As shown in Fig. 4.8, a linear voltage displacement transducer (LVDT) was installed to measure the vertical displacement of the central beam-to-column joint. Besides, four strain gauges were installed on the beam web within the elastic zone of the beam, in order to measure the strain variation and then calculate the development of axial force.

The Avery loading machine with a 1000 kN capacity and a stroke of 350 mm were used to apply the vertical downwards load on top of the central column head. To prevent the inward displacement of the support blocks, additional restraints were are installed between them, as shown in Fig 4.9. After the first yielding or a local fracture, the load was applied slowly in a displacement-controlled manner at slow rates of around 5 mm/min to complete the full range of the response.

Figure 4.8 Displacement transducer setup

Figure 4.9 Enhancement of horizontal restraint to prevent the inward displacement between the end supports

4.2.3 Results of load resistance functions and failure mechanisms

For each one of the specimens **A1~A3**, the records of the loading and vertical displacement were synchronised, thus a curve representing the development of the load-deflection relationship (referred to as load resistance function) can be generated. In the meantime, local failure processes at critical deflection points during the full-range loading process were closely monitored, and these were associated with the development of the load-displacement curve.

In the following discussions, particular attention will be paid to the ultimate load and deformation limits of the double beam substructures with different middle joint

details. The modes of local failure events, and the consequent impact on the global load resistance function will be highlighted.

Another important result is the variation of axial force developed in the beam. It can be calculated by converting the strain data obtained in the elastic zone section. Subsequently, the contribution to the overall load resistance by the axial force can be evaluated at any displacement level by Equation (4-1), according to the force diagram in Fig 4.10. This evaluation can be used to aid the examination of the capability of each double beam substructure to develop into catenary stage.

$$P_N = 2Nsin\theta = 2N\omega/L \tag{4-1}$$

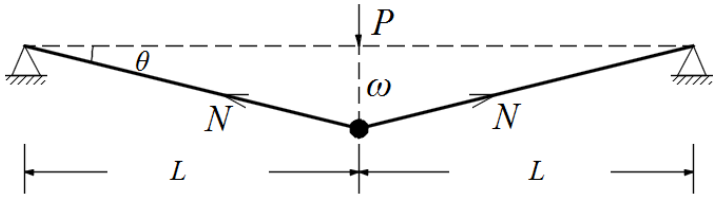

Figure 4.10 Force diagram to evaluate the axial force contribution to the load resistance

4.2.3.1 Response and failure process of specimen A1

For the loading test of specimen **A1**, the development of load resistance is plotted against the middle joint displacement in Fig 4.11. Overall, it reaches an ultimate displacement of 148 mm, which is equivalent to a beam rotation of 0.20 rad (11.3 degreeS). This level of displacement met the general rotational requirement of tie force design approach specified in DoD (2009).

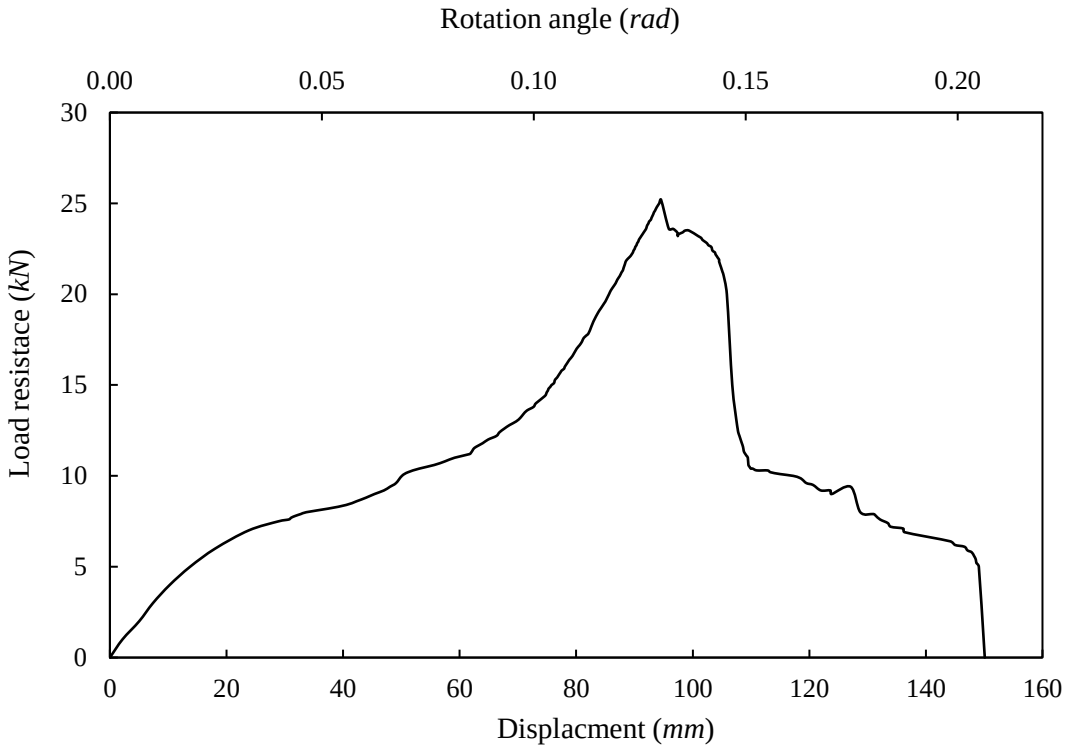

Figure 4.11 The load-displacement development of specimen A1

As can be seen, the double beam assembly underwent a stable elastic-plastic bending response, before the peak load resistance of 25.2 kN was reached at the displacement of 95 mm. At this peak point, the joint integrity was firstly reduced by the cracking and separation of the bottom stiffener plate from inside the column wall. Failure of the continuous plate resulted in the first reduction of the load resistance. Then the load was able to hold on for a short while until the second load drop occurred, due to the weld fractures between the beam and column webs on one side. This unsymmetrical connection failure is not unexpected as no perfect symmetry could be achieved in a physical specimen.

Under the combined bending moment and axial force, the weld cracks progressively extend throughout the whole connection depth, as shown in Fig. 4.12. This is accompanied by laceration of the column thin wall, resulting in a continuous degradation of overall load resistance, which appeared to be mainly contributed by the residual tying force of the damaged connection.

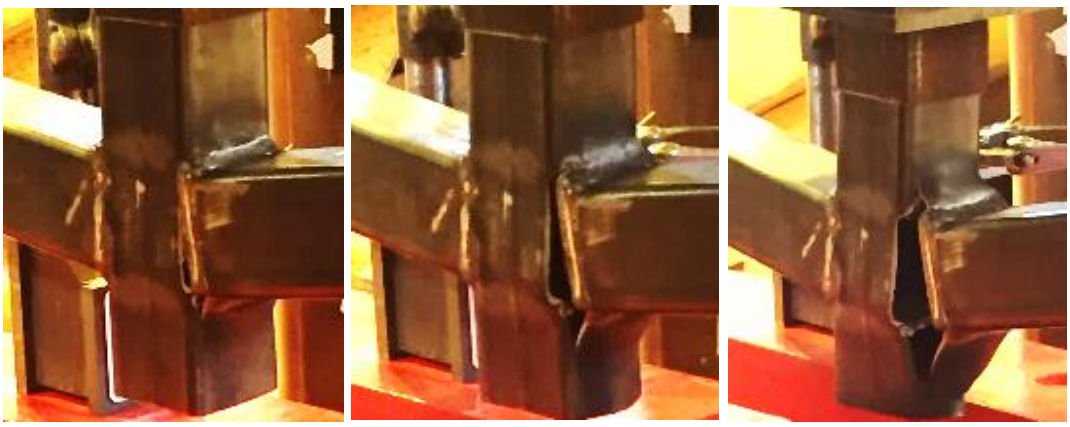

Figure 4.12 Specimen A1: The weld crack and progressive failure of the joint

In summary, for specimen **A1**, the overall resistance and deformation capacity were apparently governed by the weld cracking mechanism. Due to the brittleness of the weld cracking, the substructure could not develop into a proper catenary stage, which would otherwise recover the resistance and prolong the collapse progress.

By monitoring the axial strains of the beam section in the elastic zone, the axial force development can be calculated as shown in Fig. 4.13. Its contribution to the overall load resistance can be evaluated as shown in Fig. 4.14. It is evident that the axial force was almost negligible during the later stage of the bending phase. Afterwards, the plastic bending deformation kept increasing, until the peak load resistance was reached.

At the peak point, the maximum axial force only reached about 50% of the full plastic axial resistance of the beam section, and the axial force contribution made up about 60% of the total load resistance. Due to the brittle weld cracking, the axial force dropped abruptly, resulting in a similar drop of the overall resistance. It can also be observed from Fig. 4.14 that, at the displacement of 110 mm, the load resistance was fully provided by the axial force, indicating the start of the catenary stage. However, the axial force could not develop further beyond this point due to unsymmetrical failure of the double-side connections.

To conclude, the fully welded connection allowed the double beam substructure to develop only very limited deformation capacity after the first major weld cracking.

Consequently, the load resistance did not recover at all after the weld failure. These factors collectively resulted in the fact that the catenary action was not sufficiently mobilised to achieve a more robust post-bending behaviour.

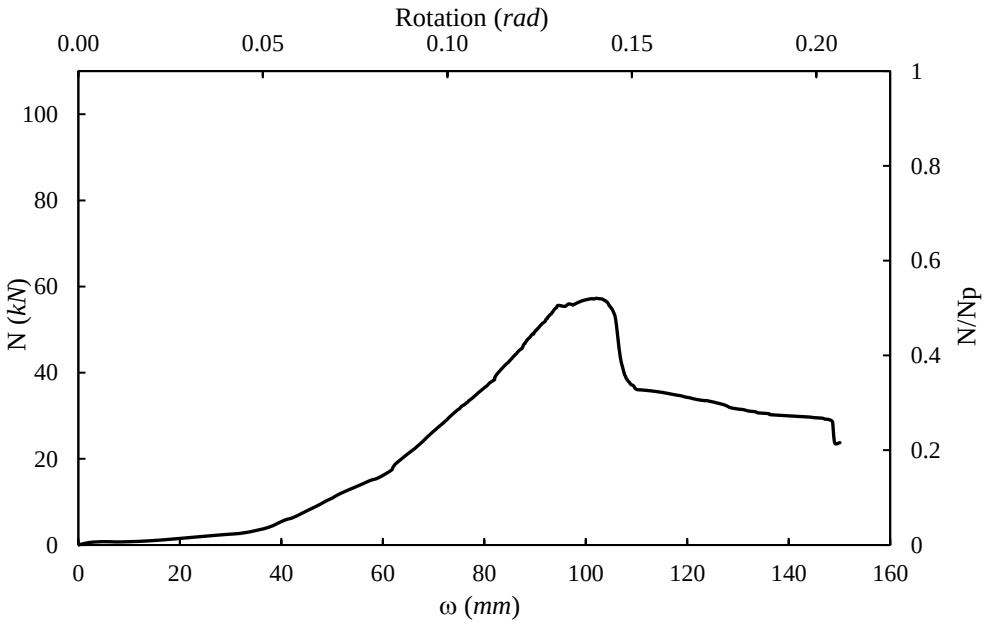

Figure 4.13 The axial force development within specimen A1

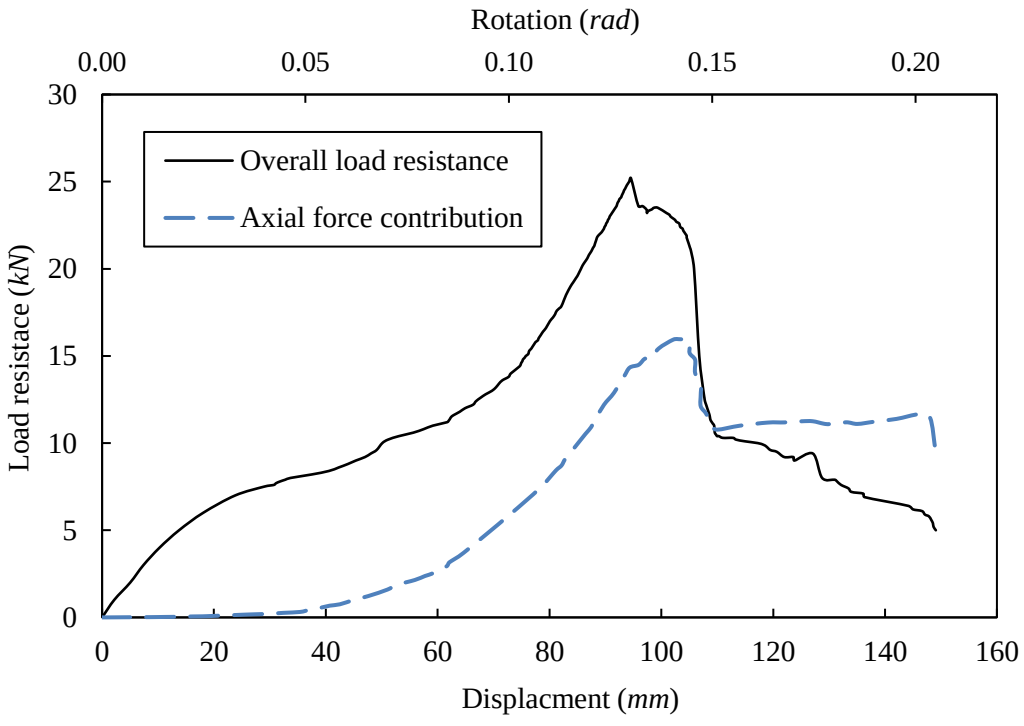

Figure 4.14 The axial force contribution to the load resistance of specimen A1

4.2.3.2 Response and failure process of specimen A2

The specimen **A2** with weld-bolt hybrid connections exhibits a load resistance function as shown in Fig. 4.15.

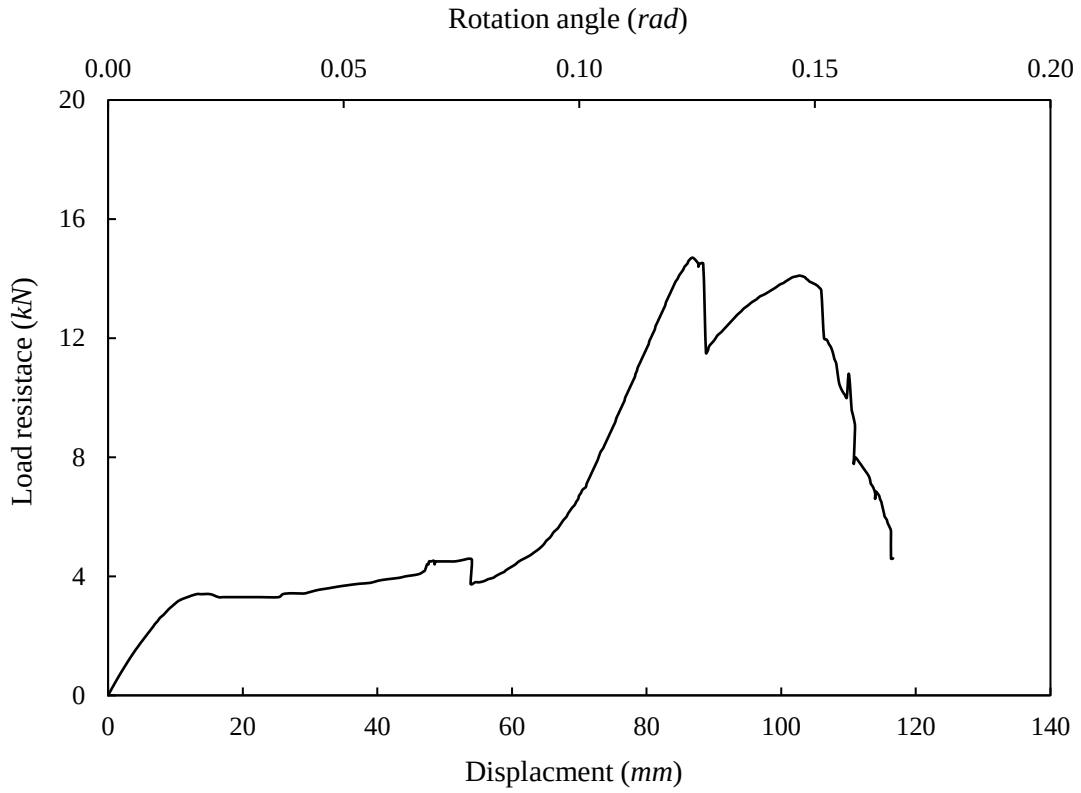

Figure 4.15 The load-displacement development of specimen A2

Similar to the specimen **A1** with the fully welded connection, the substructure experienced an elastic-plastic response stage up to the displacement of 54 mm, when the bottom stiffener cracked and separated from inside the column wall. However, the load resistance was able to continue increasing after the above local failure. The load reached a maximum value of 14.6 kN at the displacement of 86 mm. At this point, the bottom fillet weld between the beam and column flanges in tension failed suddenly (Fig 4.16(a)), leading to about 20% loss of load resistance.

After the weld fracture, the load resistance picked up again, as the web bolt connections began to carry both the bending moment and axial force. In this stage, the bolt holes near the column side exhibited marked bearing deformation while the bolts remained intact (Fig 4.16(b)). When the displacement reached 103 mm, the bolt row almost completely slid out of bearing plate. The substructure soon completely lost its resistance thereafter, and the test was ended.

(a) Bottom fillet weld cracking (b) Failure of the web bolt connection

Figure 4.16 Specimen A2: Bottom weld cracking and failure mode of bolt connection

Generally, the weld-bolt semi-rigid connection exhibited a relatively ductile performance under continuous push-down loading. Although the exact axial force development was not recorded due to unexpected issues with the strain gauges, the axial force contribution evidently extended the deformation limits, especially when the web bolt connection maintained the joint integrity after the bottom weld fracture. However, the enhancement of catenary tension force was very limited, due to the fact that the bolt connection had low axial loading and deformation capacities. This test demonstrated again that the tensional capacity of the beam-to-column joint is crucial to the ability of the beam assembly to develop an effective catenary action.

4.2.3.3 Response and failure process of specimen A3

The load resistance function of specimen **A3**, which involved a fully bolted connection, is schematically shown in Fig 4.17.

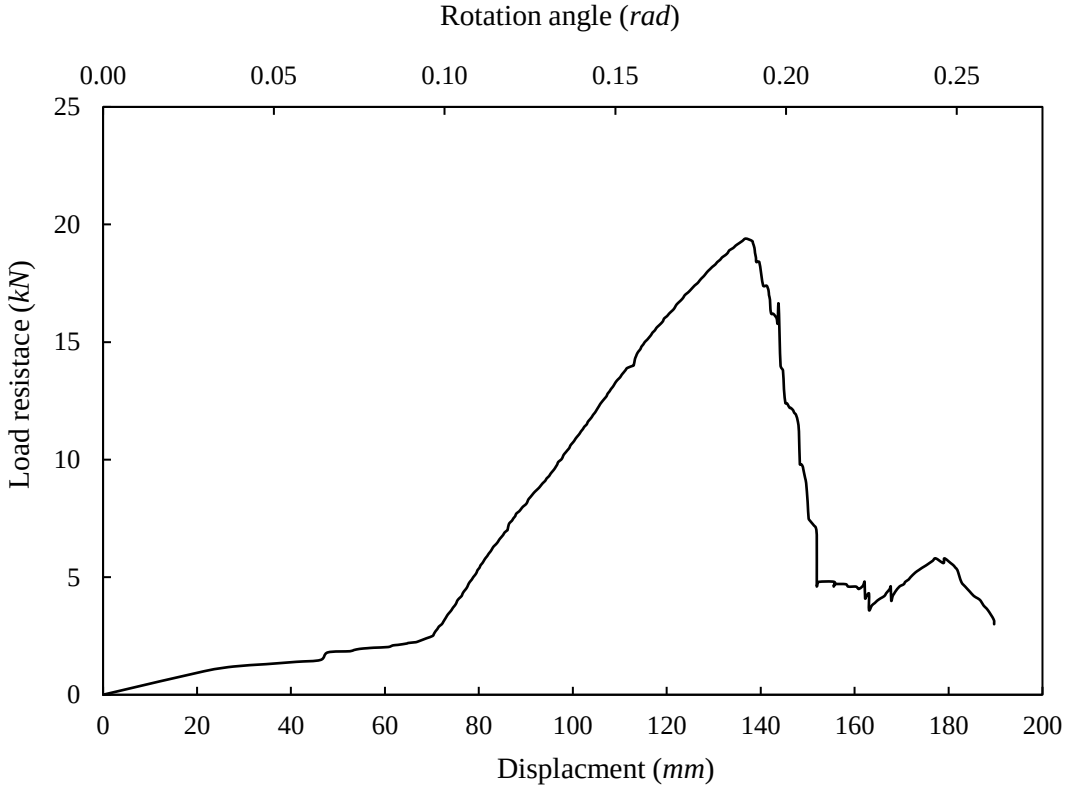

Figure 4.17 The load-displacement development of specimen A3

The beginning of the response curve shows a slow growth of the vertical load up to displacement of about 70 mm, and this is similar to the large-size specimen test in Yang and Tan (2013) with a bolted connection. During this period, the bolted connection gradually engaged, and relative slips between the bolts and connection plate occurred. With a relatively weak angle plate, the seat angle plate in tension was being pulled almost straight as shown in Fig 4.18(a).

After this stage, the whole joint started to exhibit moment resistance with the increase of displacement and joint rotation, and the overall load resistance increased linearly to its peak point of 19.4 kN, at a displacement of 137 mm. By this time the seat angle and web connection plate had been torn apart, while the bolts remained unscathed, as shown in Fig 4.18(c). Because of this severe connection failure, nearly

75% of the load resistance was lost. Then the substructure proceeded to complete collapse at the displacement limit of 190 mm.

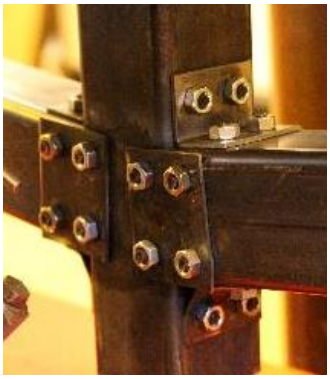

(a) Deformed seat angle plate

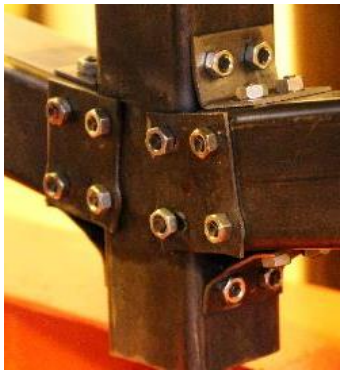

(b) Damage status at ω = 70mm

(c) Failure modes of bolt bearings

(d) Final failure mode of the connection

Figure 4.18 Specimen A3: failures of bolt connection

The axial force developed in specimen **A3** and its contribution to the overall load resistance are illustrated schematically in Fig 4.19 and Fig 4.20, respectively. The maximum axial force only reached about 20% of the section axial capacity, much lower than that of specimen **A1** with fully welded connections. At the peak point, less than half (45%) of the load resistance was attributed to the axial force. After that point, the contribution to overall resistance became more from the catenary axial force. However, the joint connections failed very quickly after the maximum resistance point, resulting in the substructure being incapable of developing an ductile behaviour after the peak load resistance.

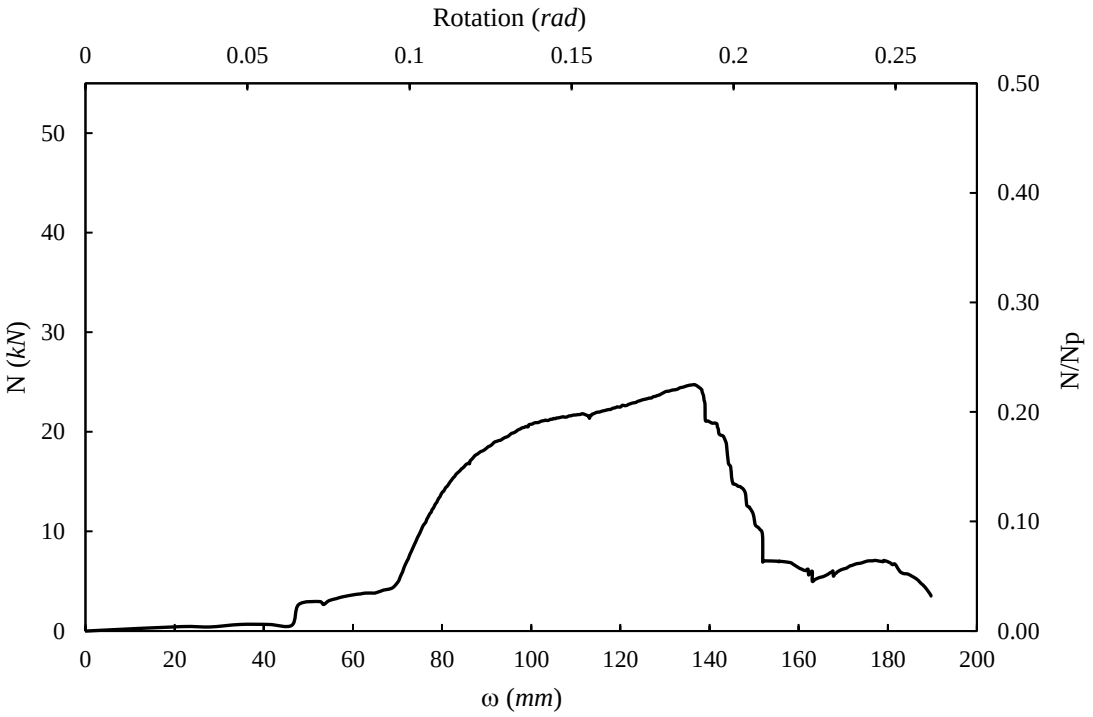

Figure 4.19 The axial force development within specimen A3

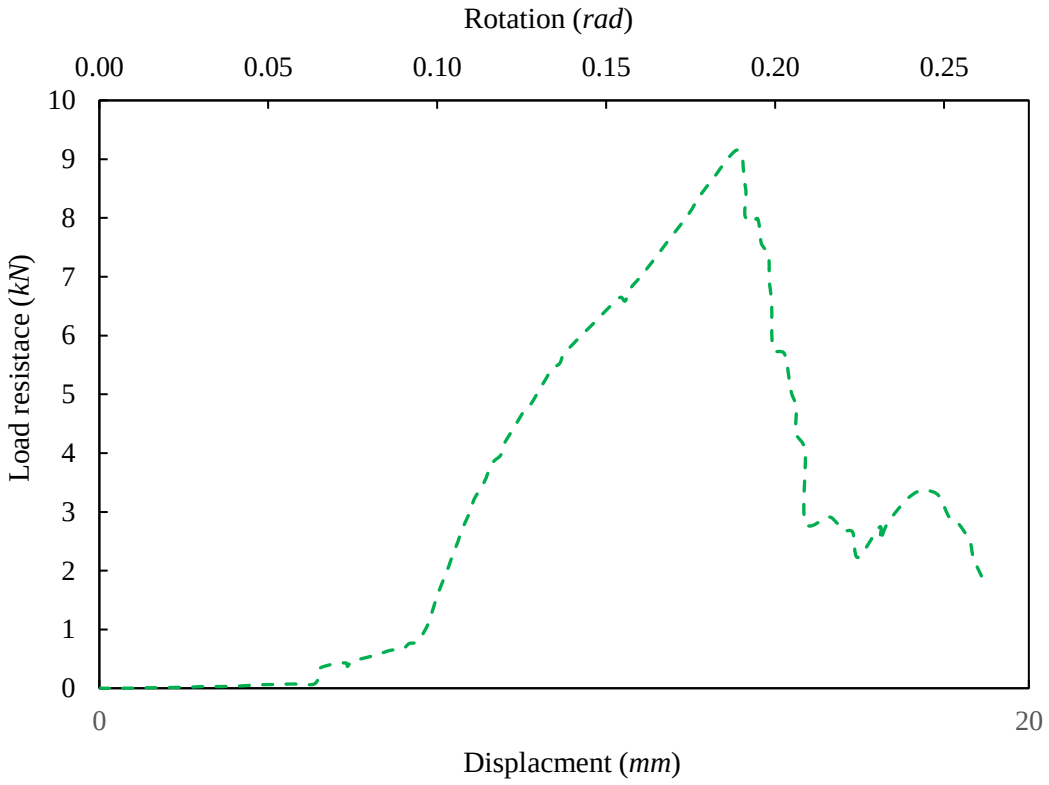

Figure 4.20 The axial force contribution to the load resistance of specimen A3

4.2.4 Comparison of the behaviour of different beam-to-column joints

The behaviour and deformation characteristics of the three different beam-to-column joints are comparatively discussed in this section.

Firstly, the classification of the joints in terms of rotational stiffness can be readily verified. The comparison can be made by a scrutiny at the load-displacement relationship at initial bending stage. As can been seen from Fig 4.21, the comparison is clearly in conformity with the steel joint classification recommended by the design guidance of Eurocode 3 (BSI 2005).

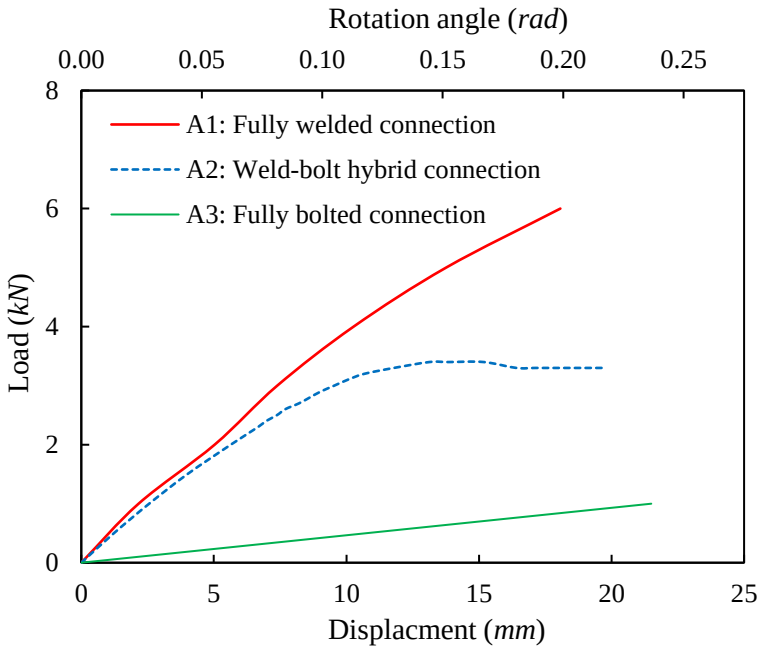

Figure 4.21 Comparison of the initial stiffness of the connections

The load resistance functions of the three reduced-scale double beam substructures are schematically shown together in Fig 4.22 for comparison. Table 4.2 summarizes the load and deformation limits of each specimen, and the local failure modes within the joint zone of the substructure are listed in Table 4.3.

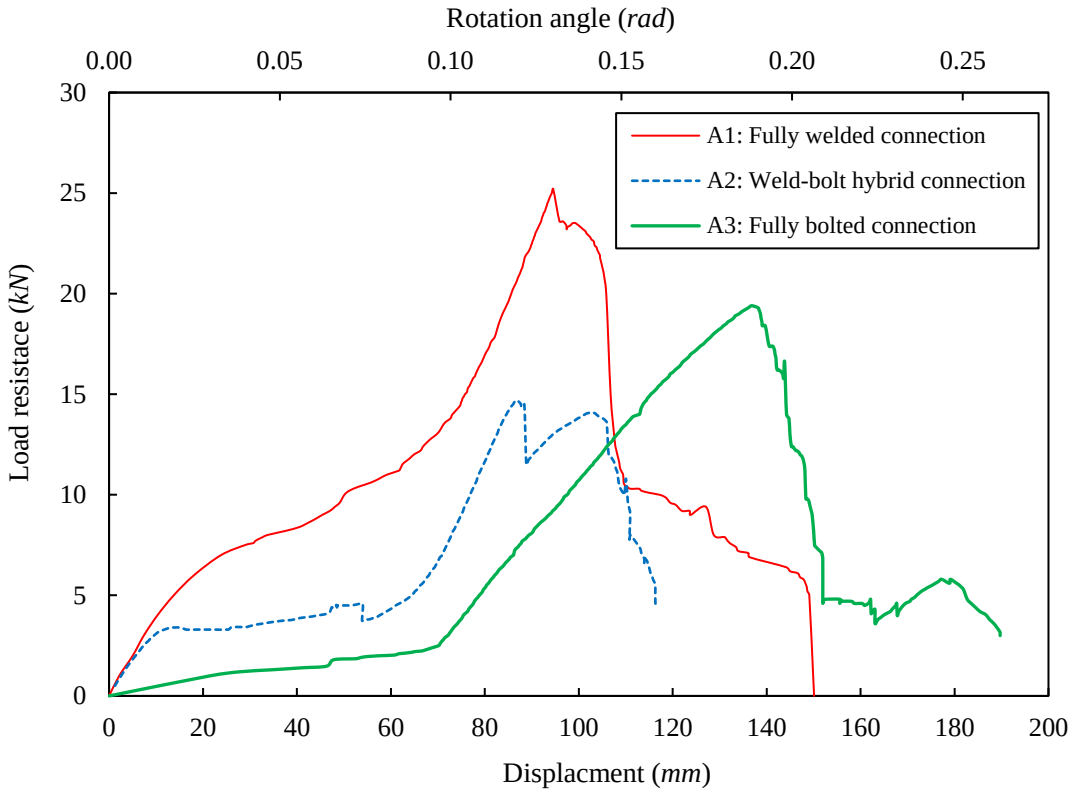

Figure 4.22 Comparison of the load resistances curves of the double beam subassemblies featuring three different connection types

Table 4.2 Summary of load and deformation capacities for specimens A1~A3

Specimen	Load capacity	Deformation limit	Rotational capacity
A1	25.0 kN	148 mm	0.20 rad (11.5°)
A2	14.5 kN	116 mm	0.16 rad (9.1°)
A3	19.2 kN	190 mm	0.26 rad (14.6°)

Table 4.3 Summary of local failure modes observed for specimens A1~A3

Specimen	Local failure modes
A1	Continuous plate cracking inside the column, weld cracking
A2	Flange fillet weld cracking, bolt bearing plate failure
A3	Angle plate yielding, bolt bearing plate failure

It is apparent that specimen **A1** achieved the highest load-carrying resistance. The full weld connections provided sufficient bending stiffness, as well as a much higher bending strength. However, these advantages eventually diminished due to the significant drawback of the fillet welds because of brittle weld cracking, which is susceptible to uncertainties due to weld quality. The brittle failure can be expected to lead to abrupt and irreversible separation between the weld-connected parts. Consequently, it is almost certain that the load resistance would not increase any further beyond the point at which weld cracking is initiated. Furthermore, the rapid propagation and expansion of weld cracks also limit the overall deformation capacity to a great extent. It can therefore be reasonably concluded that a welded connection is not a favourable design choice if sufficient robustness against collapse is required in a particular design situation.

Specimen **A2**, featuring a semi-rigid joint with double side weld-bolt hybrid connections, turned out to have the lowest load-carrying and deformation capacities. As stated before, in the flange welded - web bolted connection, the bending moment is supposed to be carried almost entirely by the top and bottom weld connections. Therefore, once the ultimate moment capacity of the weld pair is reached, cracking and separation of the bottom weld in tension will occur in a brittle manner, thereby leading to a complete loss of the bottom flange connection. As a result, the bending moment and axial tension force will be immediately transferred to the bolt connection between the beam and the column webs. However, due to the inherently limited moment resistance and the additional effect of tension force, the bolt connection can be subjected to a considerable increase of the internal forces, which can lead to a quick deterioration and hence the collapse of the substructure especially when the bolt connection is not designed with sufficient strength and the deformability.

Specimen **A3**, which contains a fully bolted beam-to-column connection, achieved what appeared to be the most desirable resistance performance under the column loss scenario. As evidenced by Fig 4.22, the double beam substructure exhibits a

sustained load resistance with the largest deformation limit among the three specimens. This is primarily attributed to the more ductile manner in which the bolt-angle flange connection fails, in contrast with the brittle fracture of fillet welding.

Based on the above observations, the following concluding remarks can be made for the weld and bolt connections:

1) Weld connections tend to exhibit limited robustness concerning the steel joints under a column removal scenario. The brittleness of the weld cracking tends to limit the ultimate load resistance in the beam assemblies despite a more desirable performance at the bending dominated stage.
2) Bolt connections tend to fail in a more ductile manner. However, the ability of the connections to enable sufficient development of the load resistance in the later stage depends closely on the strength and deformability of the angle or plain plates. Otherwise premature angle or plate bearing failure would still limit the extent to which the catenary action could develop.
3) From a further comparison of the axial force development in specimens **A1** and **A3** in Fig 4.23, it can be seen that the tensile capacity of the joint is generally must lower than that of the intact beam section, so the tensile capacity of the joint governs the overall axial force development. A further point to note is that the axial force developed in specimen **A1** with weld connection was much higher than that in specimen **A3** with a relatively weak bolt connection. However, a higher axial force does not necessarily mean a higher vertical load carrying capacity, as it also depends upon the deformation capacity (the ductility) which determines inclination angle.

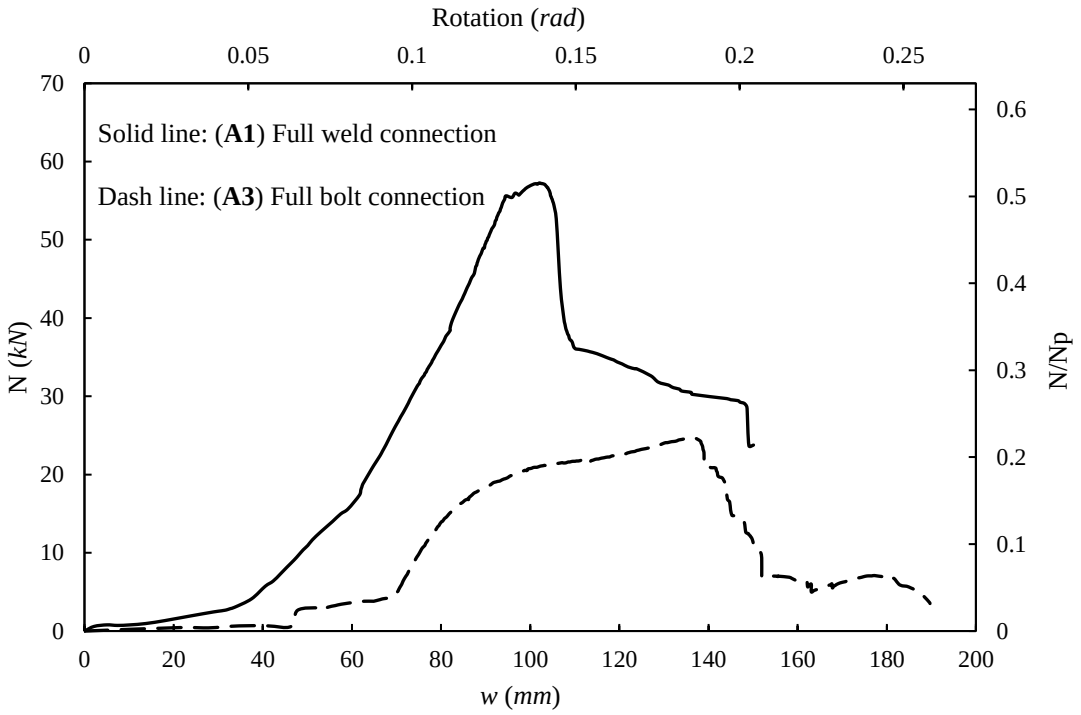

Figure 4.23 Comparison of the axial forces within specimens A1 and A3

4) It should be pointed out that the three specimens tested here all had relatively weaker connections. As shown in the literature review in Chapter 2 and the further discussion in Chapter 4, in more general situations with such joints, the overall performance into the later stage response can be expected to be better than what have been observed in the present tests. Nevertheless, these specimens can be regarded as representing lower bound cases for the respective types of the joints, and the results highlighted the critical importance of the joint details in determining the ultimate load resistance in a column removal scenario.

4.3 Experimental tests on the failure mechanisms of steel-concrete composite beam-column subassemblies

4.3.1 Introduction

The objective of this group of tests was to further demonstrate the effect of concentrated local plastic deformation around the beam-column connection on the overall resistance capacity of a double beam assembly. In addition, a composite steel beam - reinforced concrete slab configuration was also included to shed further light into other potential local failures that could limit the development of the resistance of beam assemblies into the large deformation regime.

These specimens went through elastic and plastic bending stages, as expected; however, no effective catenary action developed in most cases, due largely to premature failures in the critical regions around the joint connections in the form of steel fracture, or concrete cracking and bolt shear. The test results are presented and discussed, and possible remedies to enable an effective development of the catenary action are suggested.

4.3.2 Specimen design and experimental program

This test group consisted of three steel beam specimens, and two of them included one-way reinforced concrete slabs to represent the beam-slab composite effect. The specimens were prepared at a scale of1:2 ~ 1:3 to full-size beams, and a joint with detailed configurations was created in the middle of each beam assembly as in the specimens in Section 4.2. All the beams and column stubs features a universal joist section of U102×44×7, made from structural steel grade S355JR, as specified in British standard EN 10025:2004.

During the test, the specimens were axially constrained at both ends, and vertical load was applied on top of the middle joint until complete failure, as with the specimens described in Section 4.2. The specimens had purpose-designed beam-column connection details to allow different local plastic mechanisms and local failure modes to develop, thereby observing the correlation among local failure (e.g.

rupture of steel), the spread of plastic regions, the development of regional plastic deformation, and consequently the overall ultimate deformability and resistance.

The first specimen **B1** featured a generalised I-section beam assembly, with notch cuttings on both sides of the middle join area to represent a weakened beam-to-column connection. Spot welds were applied at the edges of the cuts to simulate possible weld failure when deflection increases. As shown in Figure 4.24, strain gauges were attached to elastic area on one side to monitor the developed axial force, and near the beam-column connection area to capture plasticity development.

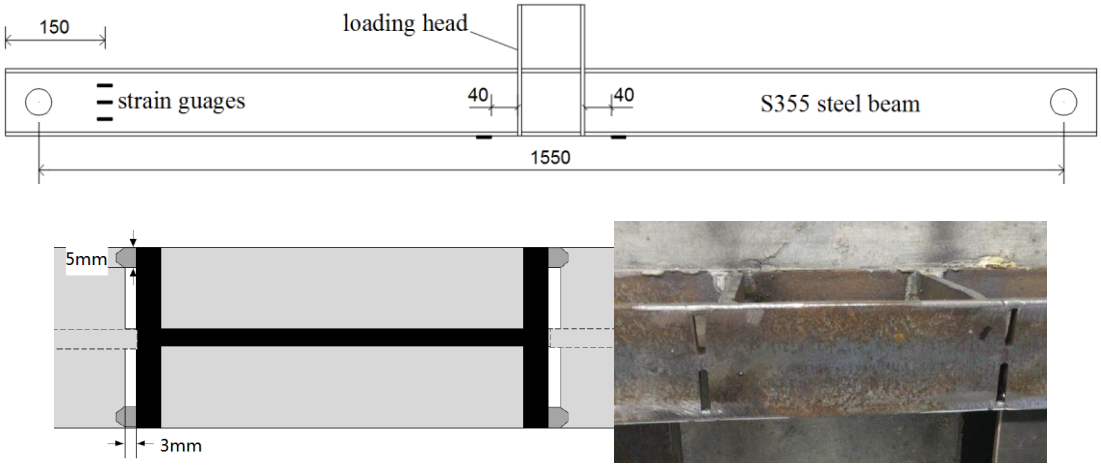

Figure 4.24 Steel double beam specimen B1, with notch cuttings spot welds

The second and third specimens had a strip of reinforced concrete slab integrated with the I-beams, denoted as specimens **B2** and **B3**, to form beam-slab composite substructure assemblies (Fig. 4.25). The layout of single-layered rebars, and the shear studs joining beams and slab together, are shown in Figure 4.26. The slab was cast on top of the I-beams in a standard way and shear studs were provided to ensure the composite effect. The shear studs were cut from the smooth rebars of 6 mm in diameter, then welded to top side of the beams, and embedded into the concrete slab.

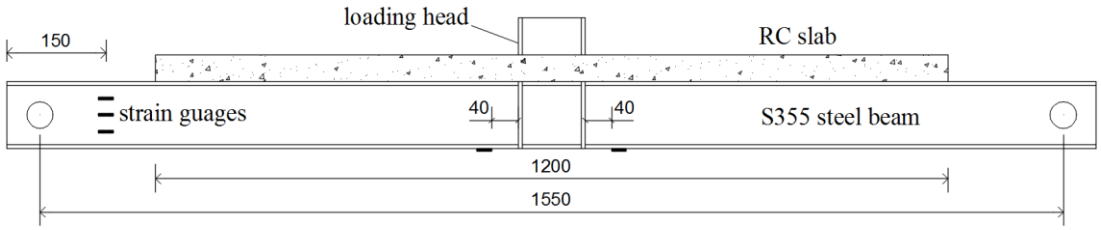

Figure 4.25 Elevation view of the beam-slab specimens B2 and B3

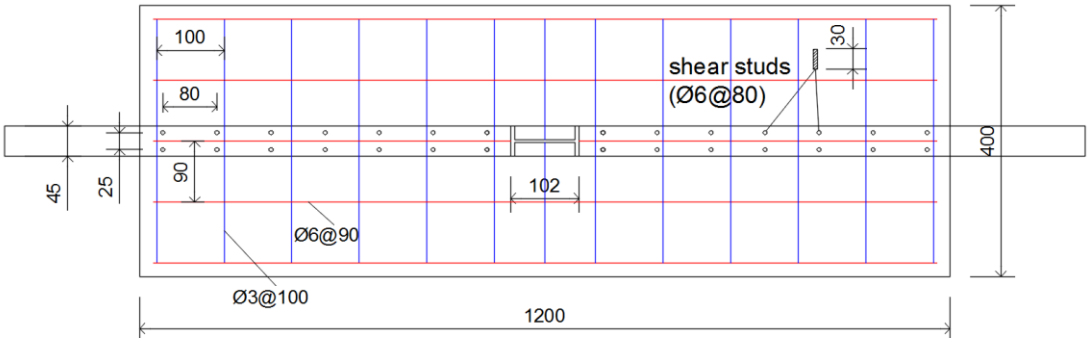

Figure 4.26 Rebars and shear studs layout of specimens B2 and B3 (Elevation view)

While specimens **B2** and **B3** shared identical configurations, they had different designs of the beam-column joint details. As illustrated in Figure 4.27, specimen **B2** included double shear bolted beam-to-column connections. As shown in Figure 4.28, specimen **B3** has weakened sections near the joint zone, by drilling circular holes. This was intended to mitigate the plastic concentration around the critical region and hence improve the overall deformation capacity.

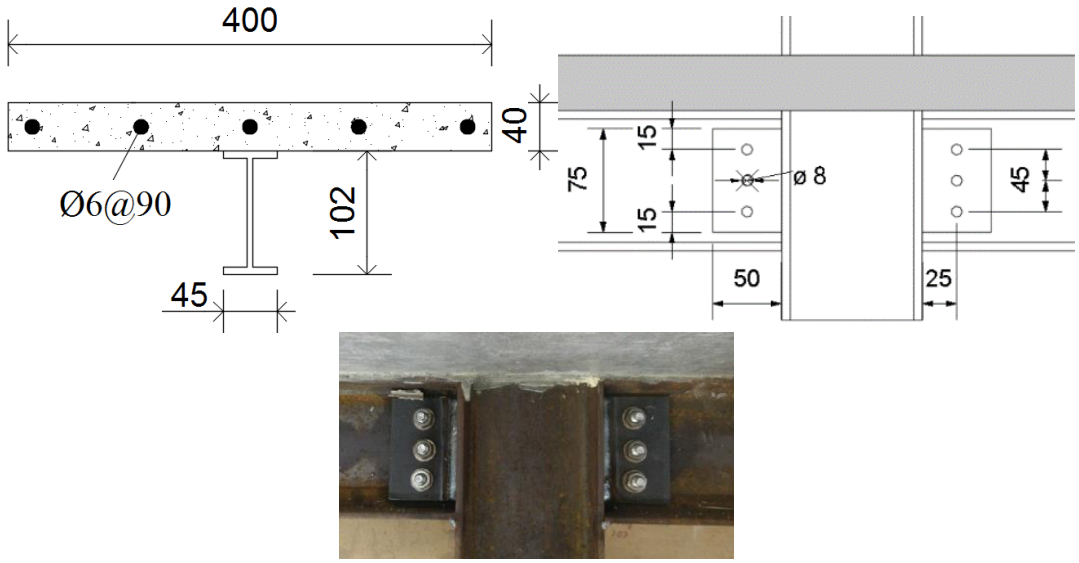

Figure 4.27 Specimen B3 with a typical bolted beam-column connection

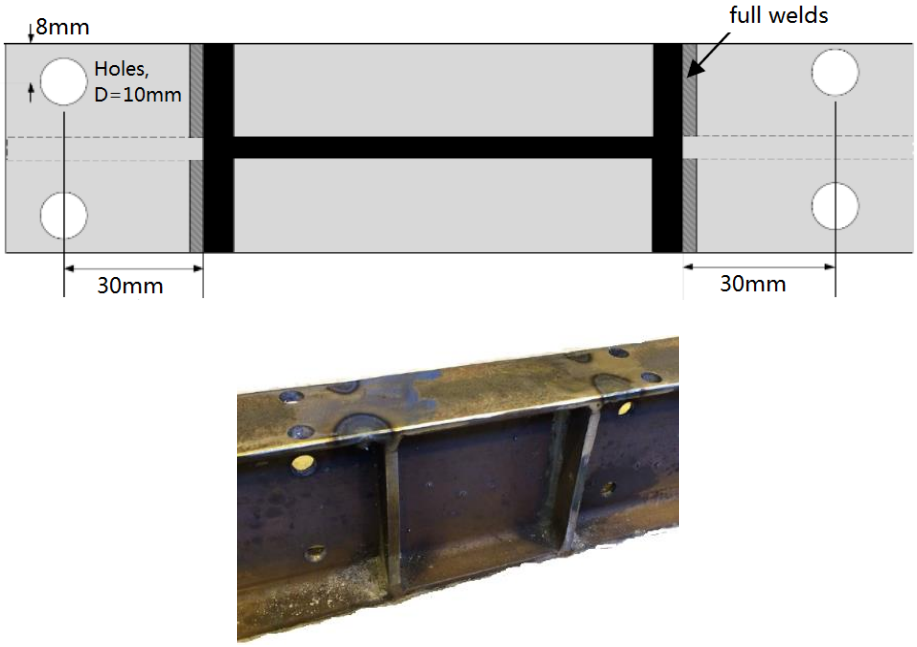

Figure 4.28 Specimen B3 with a generic "ductile" joint connection

The same experimental frame and setup were employed for the testing of the assembled specimens. The test setup of the composite beam assembly is shown in Figure 4.29. The specimens were attached to the supporting blocks (pink) by using two high strength M24 bolts, to achieve pin support conditions. Horizontal steel bars were clamped in between the two end blocks, to prevent the inward displacement of the end supports.

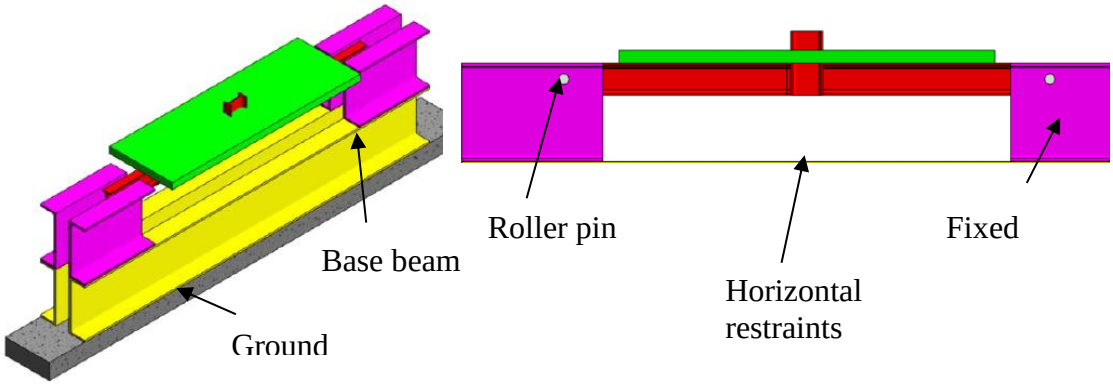

a) Overview of loading system b) Elevation of simply supported assembly

Figure 4.29 Schematic of the test setup showing the composite beam assembly

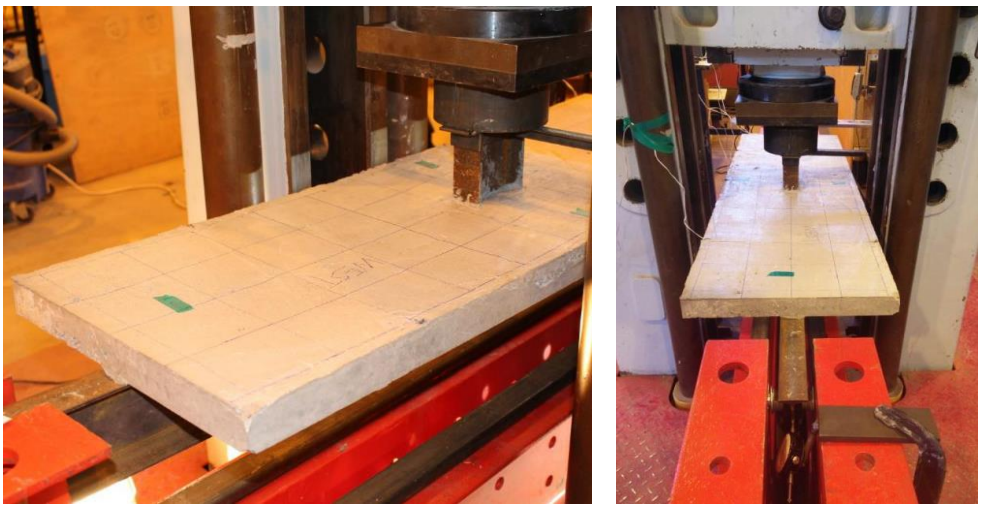

Figure 4.30 Test setup on site for the composite and RC beam assembly

The displacement-controlled loading scheme in the previous tests is also employed in this second series of tests.

4.3.3 Test results and failure mechanisms

For each of specimens **B1**~**B3**, the load-deflection responses can be established by assembling the time history of load and deflection. The local failure modes can be directly observed at critical points of the loading process.

4.3.3.1 Response and failure process of specimen B1

The generalised bare steel double beam assembly turned out to possess the ultimate resistance of 22 kN, and the deformation limit of 92 mm, which leads to a rotation of 0.13 rad upon complete failure.

Figure 4.31 shows the load-deflection relationship and associated damage process for the bare steel beam assembly. The initial elastic stage of response ended at a deflection about 7mm (point A), where the cracking of spot welds (Figure 4.32-A) occurred on one side of the joint zone. The load was still able to increase, at a lower rate though, until the spot weld fully separated and the fracture started to propagate upwards to the beam web. At this point B, the displacement reached 14 mm, and the load reached its highest value of 22 kN. Immediately after point B, the load

experienced a sudden drop of about 20% to 18 kN, and then gradually decreased with the increase of the displacement and propagation of the cracks in the web of the beam (Figure 4.32-C).

At the displacement of 45 mm, the axial force developed within the steel beam and became the dominant mechanism. The beam elongation further expedited the fracture of beam web (Figure 4.32-D, Figure 4.32-E) until the final collapse.

At the later stage (deflection 60 mm and beyond) the overall resistance appeared to start picking up; however, the specimen could not develop a meaningful catenary action as crack propagated through much of the cross-section, diminishing the axial capacity. The specimen finally collapsed due to crack cutting through the entire section.

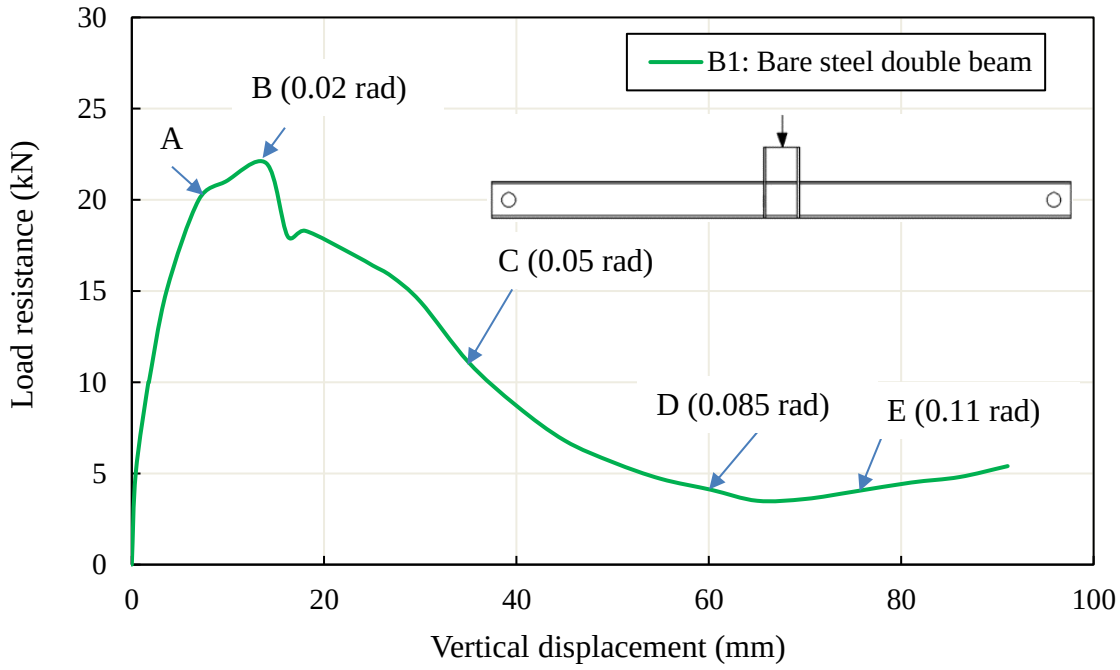

Figure 4.31 The load-displacement function of specimen B1

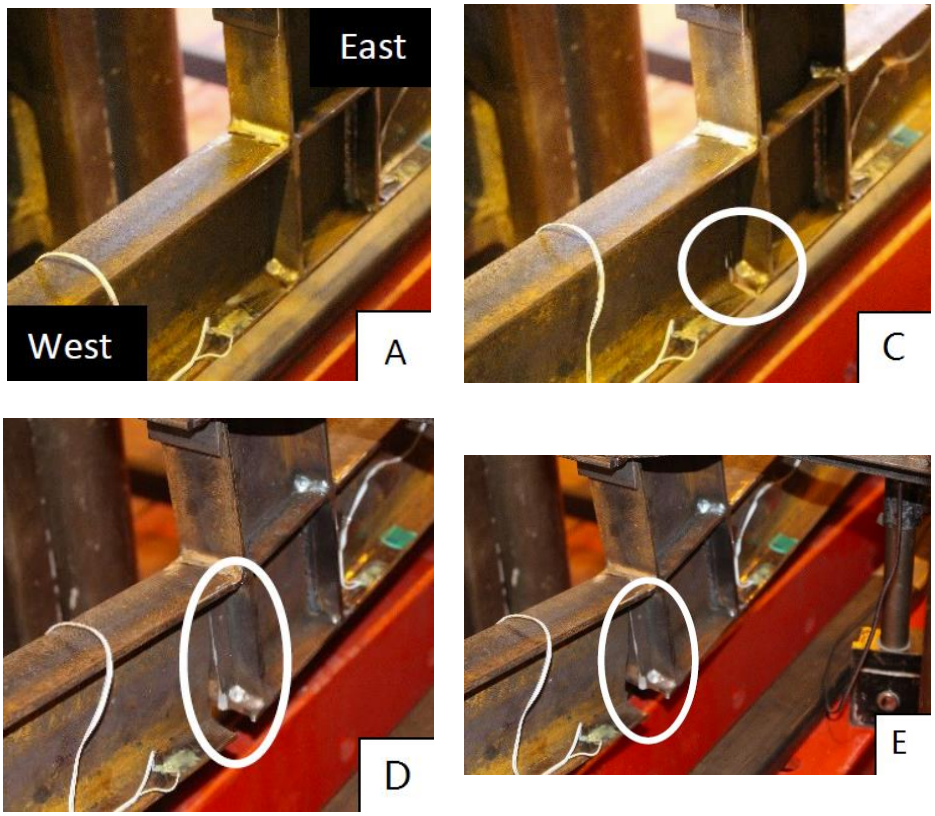

Figure 4.32 Observed response of specimen B1 at critical points (A, C, D, E)

4.3.3.2 Response and failure process of specimen B2

Figure 4.33 shows the load-deflection relationship and associated damage process for the one-way beam-slab composite assembly. The response involved more local failure events except for the material fracture, due to the complex behaviour of the bolt connection and the participation of the attached RC slab.

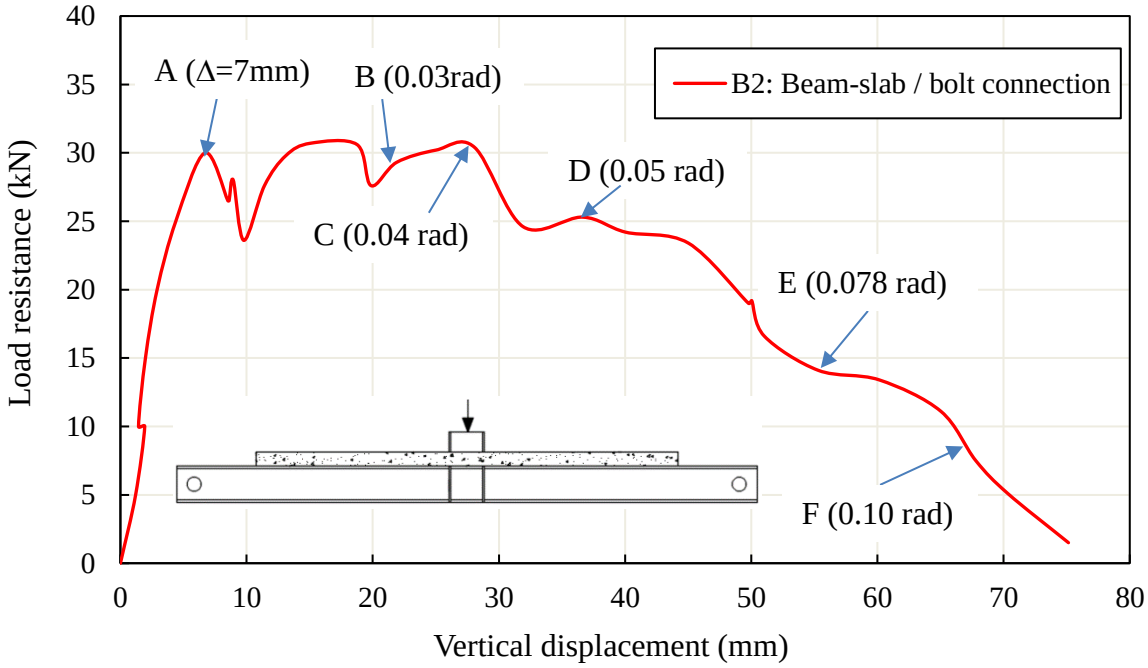

Figure 4.33 The load-displacement function of specimen B2: beam-slab with bolt connection

The assembly passed an elastic bending stage, and achieved its first peak resistance of 30 kN at the deflection of 7 mm, followed by the spot welds cracking at the beam bottom (Figure 4.34-A).

Following the fracture of the spot weld at the bottom flange, the load transfer at the joint turned to a pure bolt-connection mechanism, and with further increase of the deflection the overall resistance picked up to reach the magnitude of the first peak. The bolt mechanism allowed the specimen to develop a marked plastic deformation stage. During this stage of the plastic bending, a dip of the load appeared and this may be attributed to the deterioration of the remaining composite effect.

Subsequently, longitudinal cracks formed along the RC slab centre line (Figure 4.34-B). This is early indication of concrete crushing failure surrounding the embedded shear studs. The failure got worse when the lateral concrete cracking was observed (Figure 4.34-C), implying the flexural damage of the one-way RC slab in the mid-span. As a result, the bonding between the beam and slab was significantly damaged, leading to another 20% reduction of the load resistance.

While the slab completely split along the beam-slab interface, gradual failure of the bolt group started to occur after the deflection reached 30 mm (or 0.04 rad), and the top bolt on one side of the joint was sheared-off.

The concrete crushing near the shear studs further developed up to the overall rotation of 0.05 rad (Figures 4.34-D1, D2). This eventually resulted in the complete splitting along the beam-slab interface (Figure 4.34-E). From this point onwards, the load resistance monotonically reduced to almost zero with deformation still increasing. During the last stage, bolt shear failure was also observed (Figure 4.34-F) prior to the final collapse.

To conclude, the specimen **B2** also did not manage to enter into an effective catenary action phase. Although the bolted joint exhibited considerable rotational deformability, significant reduction of the axial strength took place before the global deflection reached a sufficient magnitude to enable an effective vertical load capacity from the axial force.

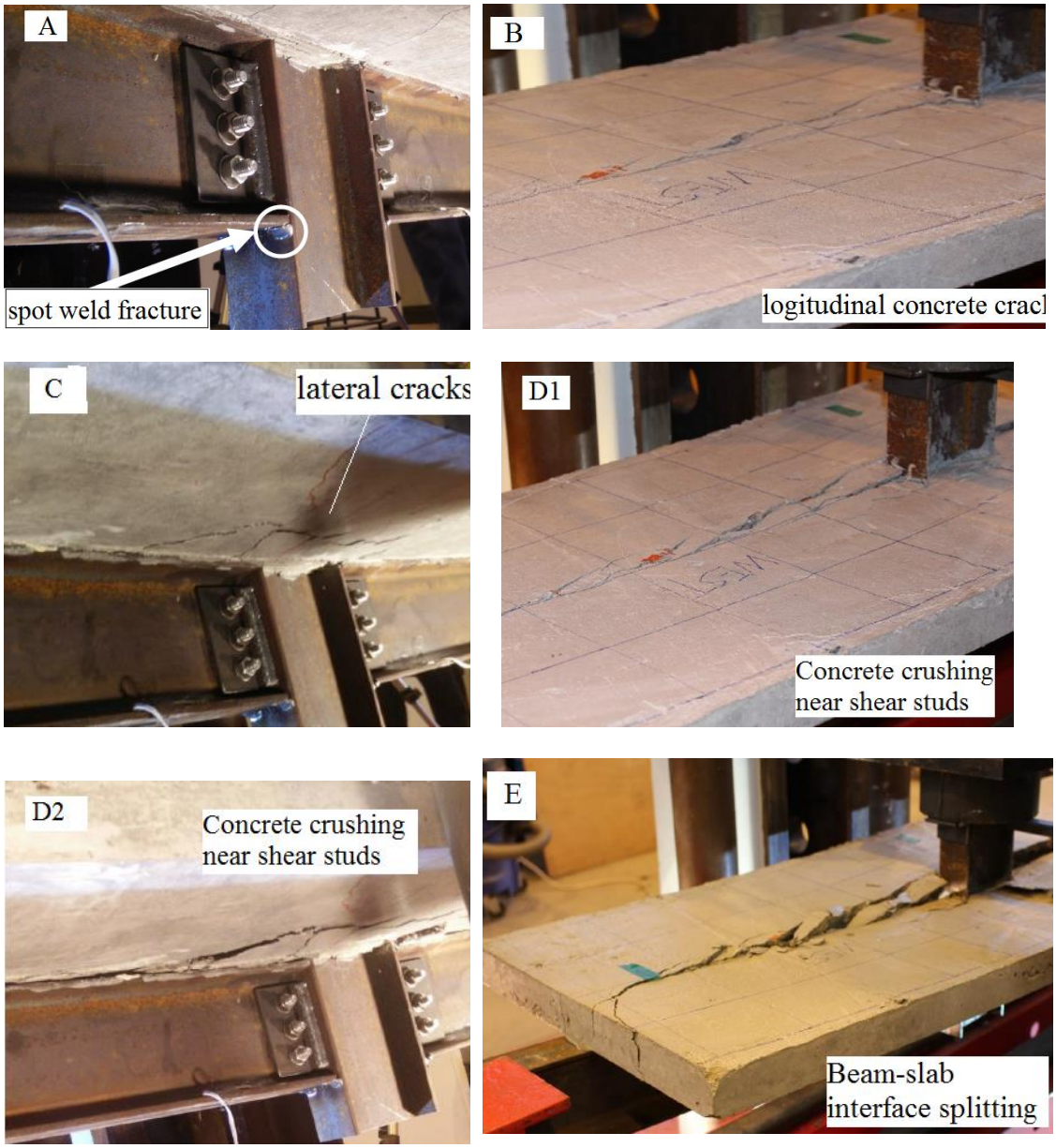

Figure 4.34 Photographic test results for specimen B2

4.3.3.3 Response and failure process of specimen B3

Figure 4.35 shows the load-deflection relationship and the associated damage process of specimen **B3**, featured with full welded connections and weakened sections nearby.

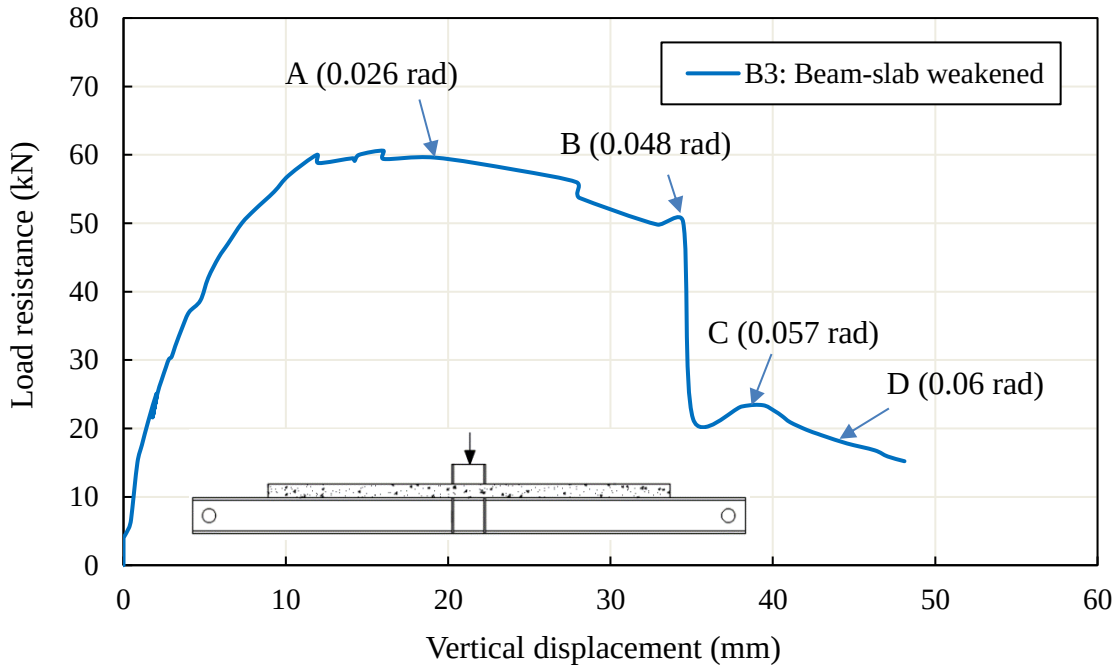

Figure 4.35 Photographic test results for specimen B3: beam-slab with weakened section

The specimen exhibited much higher peak resistance but lower deformation capacity. It underwent an elastic-plastic stage until the peak load of 60 kN was reached at the displacement of 12 mm. After a relatively stable loading stage, slight cracking at the beam-slab interface was observed, along with longitudinal concrete cracking appearing on top of the RC slab again (Point A). The continuous growth of cracks resulted in a gradual decline of load capacity up to point B, where the beam-slab interface approached complete failure (Figures 4.36-B1, B2). The loss of composite effects soon caused a significant sudden drop of the load resistance (Point B). Subsequently, the load resistance was predominantly contributed by the steel beam. The load picked up slightly until fracturing at the weakened section on one side (Figure 4.36-C). The propagation of the beam web fracture finally led to the complete failure of the assembly. The concrete crushing surrounding the shear studs also split the slab into two pieces (Figure 4.36-D).

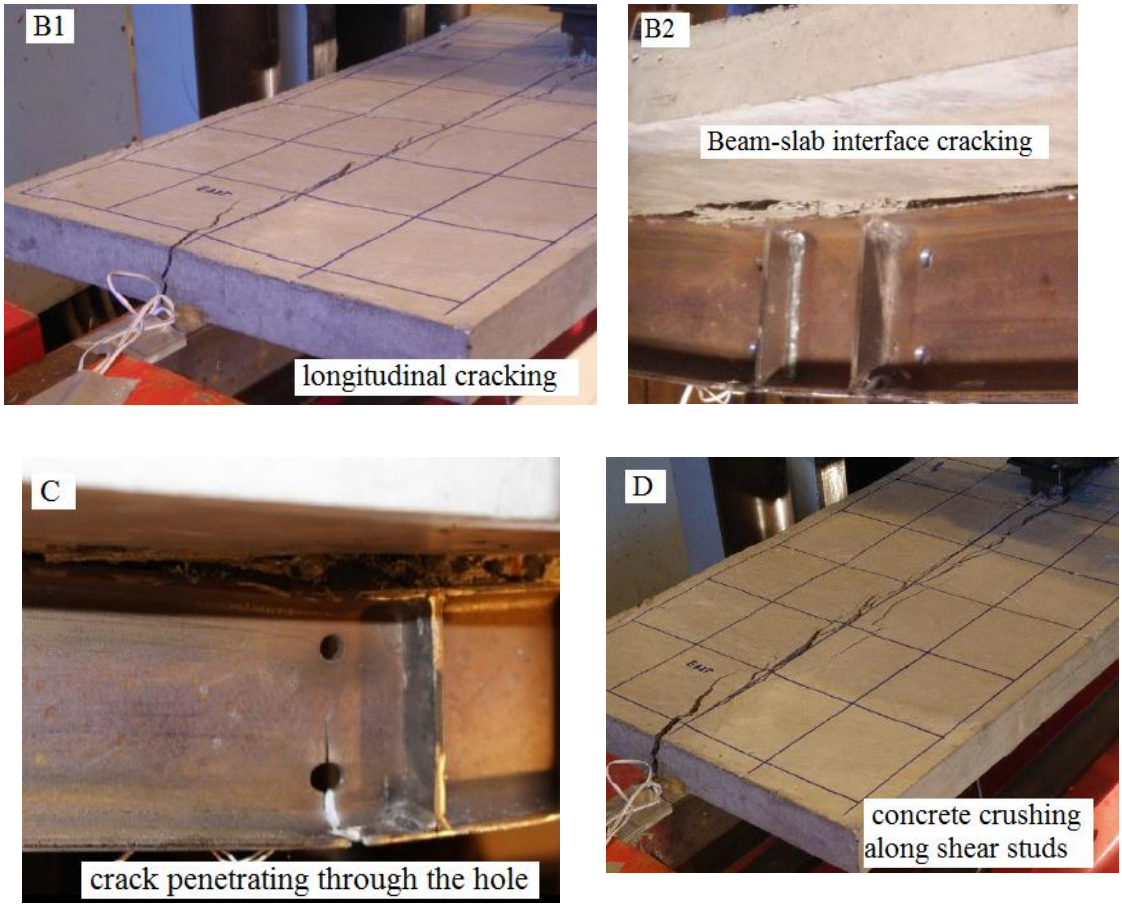

Figure 4.36 Photographic test results for specimen B3

As mentioned earlier, specimen **B3** featured a strong weld connection but with a weaker area nearby (about 40 mm away from the beam-column interface), simulating a more ductile behaviour in terms of normal flexure. As can be seen, the specimen did exhibit a marked ductile response in the bending stage, until a deflection of 34 mm (or a drift angle of 0.05). The load resistance then sharply decreased, and this was identified to be due to the rupture of the bottom flange at the supposedly ductile region with the weakened section. Rupture quickly propagated through the web, resulting in the termination of the resistance. The final stage of the response was essentially similar to specimen **B1**. However, it involved more local failure events except for the material fracture, due to the participation of bolts and the attached RC slab.

It should be noted that the peak resistance is not directly comparable with specimen **B1** because of different bending moment capacities at the critical sections. However,

comparing to a theoretical analysis of the pure bending capacity of the steel beam in **B2** without the RC slab (details not shown here), it can be understood that the RC slab contributed to more than 50% of the peak resistance in specimen **B3**.

It was also observed that during the plastic bending stage with a relatively stable loading resistance, cracking started to emerge at the beam-slab interface, along with longitudinal concrete cracking appearing on top of the RC slab. The continuous growth of cracks resulted in a gradual decline of load capacity up to point B, where the beam-slab interface approached complete failure.

4.3.4 Summary and discussion

A comparison of the responses for three specimens involving a generalised bare steel beam and beam-slab composite assemblies is summarised in Fig. 4.37.

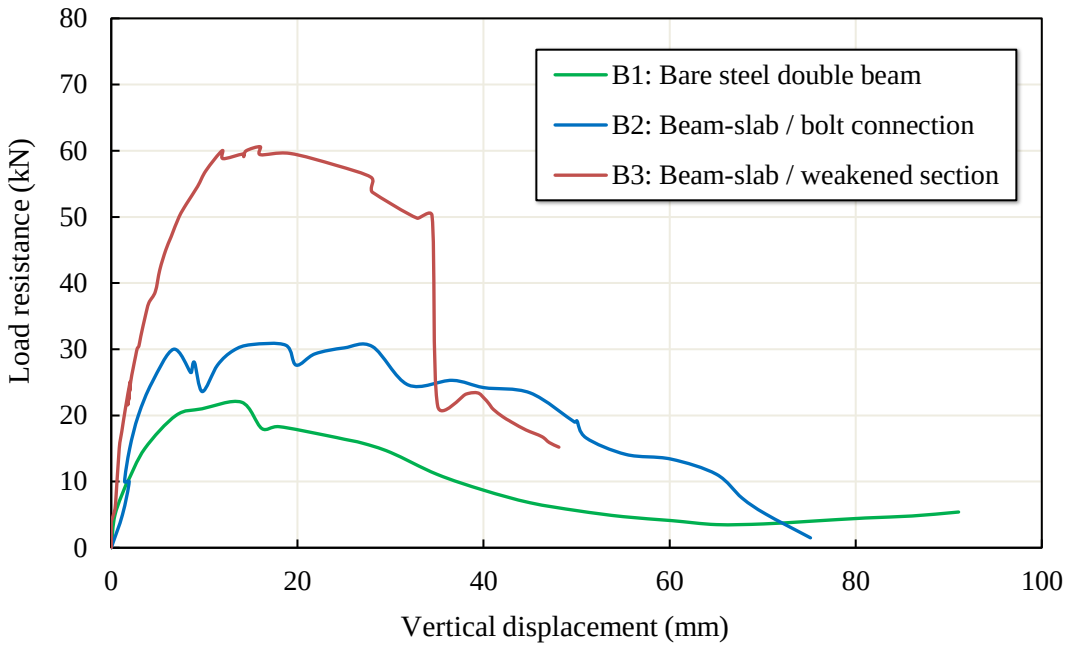

Figure 4.37 Comparison of load resistance functions for the three specimens

The three specimens involved different failure mechanisms, as had been anticipated. However, none of the specimens managed to develop meaningful catenary resistance. Although strength degradation of the critical regions was generally expected, the

degree of the plastic deformation concentration and the resulting early premature failure have been somewhat striking.

It is worth mentioning at this juncture that the plastic concentration can be strongly dependent upon the connection details, as mentioned earlier with the previous three specimens (A1-A3). Therefore caution should be exercised with regard to interpretation of the results quantitatively. Nevertheless, the results from these tests, along with those from the testing of specimens A1-A3, have clear implications on the real behaviour of beam-column assemblies in actual structures and the importance of preventing premature local failure due to high plastic deformation localisation. More specific discussion and observations are listed as follows.

1) Although not exactly comparable due to different bending moment capacities at the critical sections, the participation of the RC slabs has certainly improved the ultimate load capacities. However, adverse effects were also brought in as a result of increased local deformation (plastic strain) for the same level of global deformation, due to the increased effective depth of the section, and hence generally decreased plastic region deformation and consequently the overall deformation capacity. In addition, premature debonding of the beam-slab interface also accelerated the deterioration of the composite action.
2) As evidenced from specimens **B1** and **B2**, the post bending behaviour was dictated by the plastic deformation capacity of the critical regions, i.e. the beam-column connection and the proximity area.
3) The test specimens did not have the full details of actual beam-column joints, but the test results have demonstrated three characteristic failure modes which are representative, namely the material/weld fracture (associated in practice more with welded joint), the bolt failure, and the shear debonding of beam-slab interface.
4) The trend of the progression of the response indicated that the ultimate resistance of the beam assemblies could be improved by improving the deformability of the weld and bolt connections. However, such improvements still will not fundamentally change the fact that there will always be plastic concentration attached to the joint response. It is important therefore to

recognise that the overall deformability of the beam assembly is governed by the plastic rotation and plastic extension capacity of the plastic zone, which in turn depends on the product of the size (length) of the plastic zone and the failure strain (or its equivalent). Therefore for a given "strain" limit, boosting the plastic zone size becomes critical in increasing the overall deformability and thus enabling the development of an effective catenary action.

5) In this sense, a robust design or retrofitting for structures concerning progressive collapse resistance should look into enhancing the plastic deformation distribution in a wider or larger area, thus increasing the total deformation capacity of the critical plastic region and the overall deformation capacity of the substructure. The modification proposed for specimen **B3** may be regarded as a representation of such a concept.

4.4 Summary

Two groups of tests have been carried out on six reduced-scale double-beam assemblies to characterise the detailed local plastic deformation mechanisms and their influences on the advanced and post-bending behaviour of the substructures. The double beam assemblies were tested under vertical loading up to total failure. The first three specimens (**A1**~**A3**) were built with steel beam and typical weld and/or bolt connections. In the second group of specimens (**B1**~**B3**), the effect of the RC floor slabs have also been incorporated.

The tests were intended to represent lower bound cases with high plastic concentration at the connection regions, thus supplementing the existing experimental literature in terms of the correlation between the governing local failure mechanisms and the global deformability, and hence the potential of developing effective catenary action.

Test results revealed that the specimens went through elastic and plastic bending stages. As a matter of fact, the axial force developed in the beam contributed significantly to the global vertical resistance, and the tested assemblies exhibited quite desirable deformation capacities. However, the load resistance rarely recovered

again after a major local failure occurred, and the final collapses were following quite closely. In other words, the catenary actions were not sufficient to help recovering structural resilience after local failure events caused significant load drops.

The outcome highlighted the crucial importance of enabling the plastic deformation to “spread” in order to ensure more plastic deformation capacity in the plastic zones, and thereby a sufficient global deflection capacity for the development of an effective catenary action. The axial capacities of the connections are also important for the large deformation to develop.

In conjunction with the experimental studies available in the literature, the observations pave a way for subsequent study into quantification of the total plastic deformation capacity of typical join designs, and the incorporation of the local deformation and strength properties into the analysis of the overall resistance of the beam assemblies.

5 Component-based analytical framework for the realistic beam-column substructure with typical steel joints

5.1 Introduction

In Chapter 2 Literature review, the past research efforts to develop design-oriented component modelling methods for the framed steel joints were summarized. It is understandable that the classic component methods can be extended to the modelling of steel joint performance and the analysis of the resistance function under progressive collapse scenarios. However, considering the characteristics of large deformation response under a column loss, the classic component models and the associated analytical methods are deemed to have the following limitations.

(1) The previous component models reviewed in Chapter 2 are mostly limited to the evaluation of initial stiffness and maximum resistance under pure bending. With the initial stiffness and maximum capacity in bending, a simplified joint model can be readily established by an analytical moment-rotation relationship. Obviously, the post-bending limit behaviour is not covered, and the effects of the ultimate joint component failure are represented.

(2) Some recent studies have extended the component method to account for the axial force involvement. However, these studies focus on special design cases where a certain level of axial force needs to be considered. In reality, the developed axial force under column loss changes would contribute significantly to the load- carrying capacity with the increase of vertical deflection. At the same time, the complicated bending moment - axial force (M-N) interaction within the joint has to be properly reflected in the mechanical model.

(3) With regard to the analytical process for the component models, almost all of the past studies utilized commercial finite element software to complete the solutions. In the models composed of springs and rigid links, the component behaviour functions are prescribed in terms of the spring properties, and subsequently the analysis can be carried out in the finite element analysis. Even though, if the spring failures and disconnections are to be simulated, then the explicit analysis

would be required to overcome the convergence issues. However, an explicit analysis would be rather time-consuming.

(4) In the simplified component models, some critical components such as the equivalent T-stub and the bolted double-angle have been investigated in the past years. Yet there still exist gaps in the full description of the critical component responses under both tension and compression. These include the bolted lap-plate component and fillet/butt welds. In order to realistically model the large deformation response of the commonly-used steel joints under very large deformation, the full-range constitutive laws of the components have to be appropriately quantified, along with reasonable failure limits. This is the most crucial part of the component-based joint modelling in a progressive collapse scenario, and it is necessary to identify and close up such gaps in the existing component behaviour studies.

To address the above limitations, this chapter is firstly aimed for a direct physical mechanism based analytical procedure, which can explicitly and quickly establish the resistance function with ultimate deformation limits of a double-beam assembly featuring a typical middle joint. The development of the analytical solution is based on the governing force equilibrium and deformation compatibility, between the joint deformation zone and the steel beam segments. An iterative calculation process is carried out to solve the rotation centre of the component spring group under each incremental deflection level. By developing an in-house program using numerical platform MATLAB, the analytical procedure can be realised in a convenient manner. The program requires the input of basic structural parameters, and more importantly, is applicable to any number of components in parallel and any form of component behaviour descriptions.

The analytical framework is dependent on the simplified component models, which focus on the behaviour of critical component sets in representative typical joint types. In order to apply the analytical framework to achieve a reliable solution, the quantitative studies on the constituent joint components are reviewed and examined.

By using the developed framework, a widely-used pinned joint and a typical semi-rigid joints are selected for verification analyses, namely web cleat connection and top-and-seated and web angle (abbreviated as 'TSWA' hereafter) connection. They are both composed of the general bolted double-angle component, while the top and seat angles in the TSWA connection can be regarded essentially as one-half of the same component. The analytical solutions generated by the framework using the developed program show that the predicted load and deformation limits are in good agreement with the experimental results. This indicates the proposed analytical framework and the solution program work satisfactorily. Further discussions are focused on the discrepancies of the component failure process and critical failure points. Further research needs with regard to the current component behaviour formulations are identified through the comparisons and discussions.

The proposed analytical framework provides a much more efficient tool to evaluate the joint performance and structural behaviour under a column loss scenario. In addition, the establishment of the assembly resistance functions can be applied in engineering design practice. For instance one direct application is to employ such resistance functions in a single-degree-of-freedom (SDOF) model and hence can incorporate the dynamic process. In this way, the dynamic effects associated with a sudden removal of a column under various resistance patterns and loading magnitudes can be quantified in a straightforward manner.

5.2 The proposed analytical framework to establish the load resistance function of double-span beam substructure with realistic beam-column connections

5.2.1 General considerations of the analytical framework

The full-range resistance function (or force-deflection relation) of a double-span beam assembly under column loss is difficult to establish reliably, due to the involvement of complicated joint behaviour and evolving local failure events. As has been summarized in the literature review chapter, in the existing studies of the substructure behaviour in progressive collapse, the analysis is typically carried out by

firstly quantifying the joint rotation and axial deformation under combined bending moment and axial force (Stylianidis and Nethercot 2015). This is followed by incorporating the obtained results into a simple beam model with axial springs and joint rotational springs (Stylianidis et al. 2015). By using conventional structural or finite element analysis, the overall load-deflection relation can then be obtained.

In such an existing analysis framework, the solutions of the joint response and the resistance function of the whole assembly are separated, thus making it effectively an indirect solution. Apparently, the modelling of joint response under combined bending moment and axial force is the more crucial part, ahead of the further beam response analysis. The analytical process requires large amount of computation work, making it not very suitable for practical use. Most importantly, the solutions are derived based only on a bilinear or elastic-plastic component property. For more generalized component behavioural functions, the solutions are not applicable.

A new analytical framework is proposed here, aimed at a direct solution, which combines the solution of the evolving joint behaviour together with the overall sub-structure (beam assembly) resistance function. More importantly, the solution procedure would suit any form of constitutive properties of the joint components.

In the present analytical framework, firstly the beam assembly (central part of the double-span beam between contra-flexure locations) is divided into elastic beam zones and the middle joint zone, as shown in Fig 5.1. The beam zones are represented by one-dimensional beam element, while the middle joint is comprised of parallel component springs that are bounded by rigid bars. In reality, much of the concentrated deformations occur at beam end connection zones, especially at large deflection regimes. In this model, all the deformations are lumped into the geometric region of the joint. The beam and the boundary rigid bar are rigidly connected. Thus, all relevant deformations within and surrounding the middle joint area are considered by the spring sets.

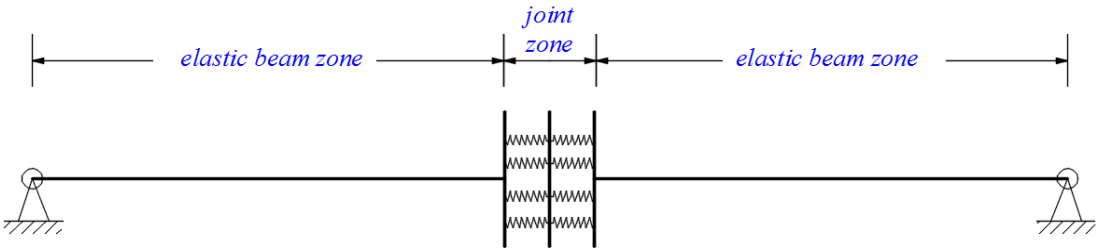

Figure 5.1 Schematic of separation of the beam and joint zones in a double-beam assembly

In the model, the ends of the beam assembly are assumed to be both pin-supported as they represent the contra-flexure points. However, if the flexibility of the axial restraint stiffness is essential to be included, it can be represented by an axial spring with a stiffness of K_s, as shown in Fig 5.2. In this case, the effect can be represented by an equivalent beam axial stiffness as:

$$K_a = \frac{1}{\frac{1}{K_s} + \frac{L_0}{EA}} \tag{5-1}$$

where L_0 and A are the beam net length and sectional area, E is the material elastic modulus.

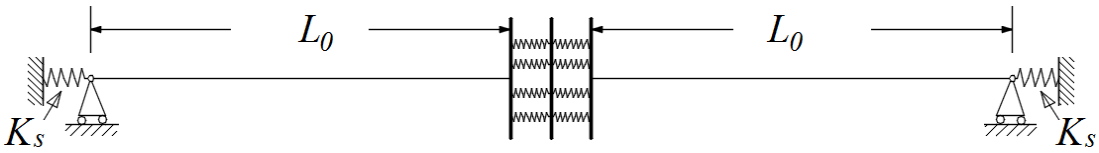

Figure 5.2 Beam assembly with axial restraint stiffness considered

When the assembly is subjected to a continuous pushdown action at the mid-span, the equilibrium condition requires that the resultant axial force of the joint and the axial force within the elastic beam zone be equal to each other, i.e.

$$F_j = F_{beam} \tag{5-2}$$

The axial deformations of the joint and the main beam section should satisfy the following compatibility condition, where Δ_{total} is the total elongation of the single span assembly, Δ_j and Δ_{beam} are the elongations of the joint and beam:

$$\Delta_{total} = \Delta_j + \Delta_{beam} \tag{5-3}$$

The above two equations form the basic governing equations of the analytical solution. The five parameters of forces and deformations in the two equations are evaluated during the analytical procedure, and then be integrated back into the equilibrium and compatibility equations.

At a particular solution step for a given joint rotation (which is related to the central deflection and will be discussed later), in the joint model, the basic unknown parameter will be the rotation centre position of the component springs group. Once the location (coordinate) of the joint rotation centre is solved, the component spring deformations can be determined, and the component forces are found according to the pre-defined constitutive properties. Figure 5.3 shows an illustrative scenario where the rotation centre (defined as y_r, which is measured from the top-most component of the connection) is lying above the top component, indicating that all components are in tension. y_i in the figure denotes the distance from component spring "*i*" to the rotation centre. This is expected to occur during the large deformation or catenary response phase. If the rotation centre lie between the springs, then the components above the rotation centre would be subjected to compression force, whereas the others would be in tension. This usually occurs during the bending and transitionary stages.

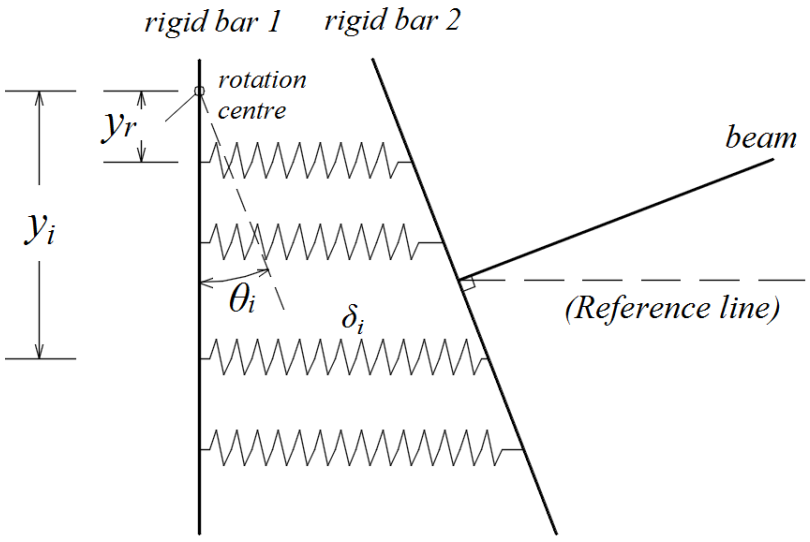

Figure 5.3 Illustrative deformation diagram of the joint component model (one side of joint considering symmetry)

In the above deformation diagram, the rotation angle θ_i is determined by the vertical deflection magnitude, assuming a triangle deflection shape which is commonly adopted in the analysis of the beam assemblies due to the predominant response in the large deformation phase. The reference line is taken as being horizontal and through the intersection point between the beam axis and the joint. With the reference line, the known rotation angle and the solved rotation centre, the total joint deformation can be evaluated. The total joint force F_j can be evaluated by simply summing up all the component forces.

The key part in the solution procedure is to solve the positon of the joint rotation centre. Once it is resolved, the individual component deformations and forces are determined. Subsequently, the bending moment and axial force of the middle joint can be calculated, and from there the total vertical load resistance can be determined. By completing the analysis in an incremental manner step by step, the entire resistance function of the beam assembly is established.

In the step-by-step analysis process, local failure events (i.e. failure occurring at any spring component) can be identified and the consequential effect on the resistance function, as well as the ultimate failure limits, can be established. The analytical framework is capable of accommodating complicated forms of component behaviour.

5.2.2 The step-wise analytical solution procedure

In order to produce the entire nonlinear resistance function and capture the evolving failure events, an incremental step-by-step solution procedure is appropriate. The main steps are detailed in the following. It is worth noting again that the analysis ignores the bending deformation of the elastic beam part.

Step-1:

Let the current middle joint vertical deflection be w_i, and the beam chord rotation θ_i is determined as (Fig. 5.4):

$$\theta_i = \arctan(w_i/L_0) \tag{5-4}$$

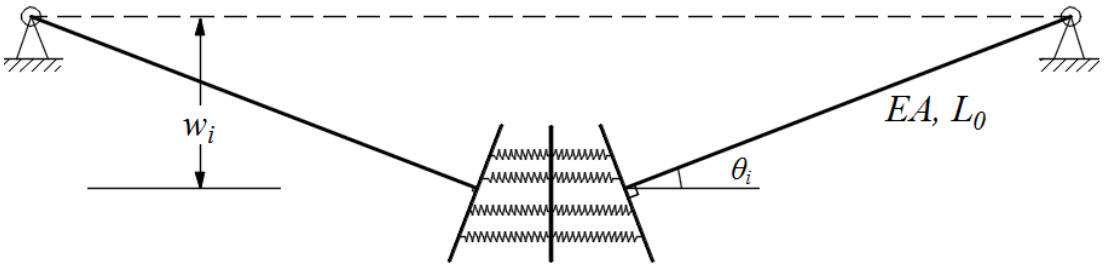

Figure 5.4 The global deformed shape of the double beam assembly

Step-2:

Assuming an initial value for the joint rotation centre coordinate y_r (see Figure 5.5). Based on the rotation angle and the assumed coordinate of the rotation centre, the tensile (positive) or compressive (negative) deformation δ_i of each individual component can be calculated through multiplying the component lever arm by the rotation angle as:

$$\delta_i = \theta_i \cdot y_i \tag{5-5}$$

Note that the level arm value y_i for each individual component could be positive or negative. Components above the rotation centre have negative value and hence sustain compressional forces, while components below the rotation centre have positive value and sustain tensional forces.

In the meantime, the overall deformation of the joint is evaluated by:

$$\Delta_j = \theta_i \cdot y_j \tag{5-6}$$

where y_j denotes the vertical distance from the rotation centre to the reference line.

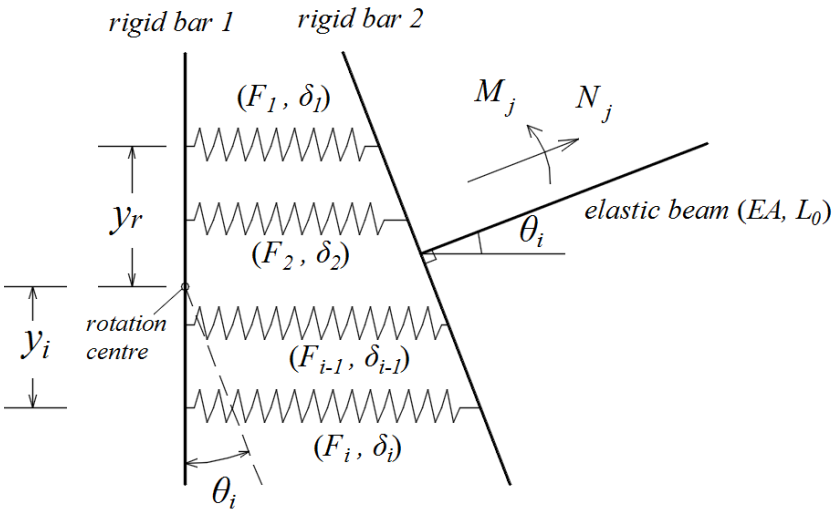

Figure 5.5 The proposed analytical method of joint response

Step-3:

For each component, as the deformation has been available from Step 2, the corresponding component forces F_i can be found from the pre-defined component force-deformation curves. Therefore, the total axial force within the joint zone can be obtained as:

$$F_j = \sum_i F_i \tag{5-7}$$

Step-4:

The total axial elongation of one side of the beam assembly can be calculated according to the geometric approximation. Subsequently, the elastic elongation along the beam outside the connection zone is obtained as:

$$\Delta_e = \Delta_{total} - \Delta_j = (\sqrt{w_i^2 + L_0^2} - L_0) - \Delta_j = \frac{w_i^2}{2L_0} - \Delta_j \tag{5-8}$$

The beam axial force F_{beam} is calculated according to the elastic deformation Δ_e and the axial stiffness of the beam EA:

$$F_{beam} = EA\frac{\Delta_e}{L_0} \tag{5-9}$$

Here L_0 is the net distance from the beam support end to the boundary of joint zone.

Step-5:

Both the axial forces in Equations (5-7) and (5-9) are actually functions of the only unknown parameter y_r. The equilibrium condition in the axial direction requires:

$$F_j(y_r) - F_{beam}(y_r) = 0 \tag{5-10}$$

From the equation, the unknown parameter y_r will be solved. In the present procedure this is done by using a numerical iterative method, which will be explained later.

Step-6:

Once the coordinate of the joint rotation centre is solved, the component forces and the total joint force can be calculated. The global vertical load resistance contributed by the catenary axial force P_N can be evaluated based on the axial force and beam rotation:

$$P_N = 2F_j \cdot \sin\theta_i \tag{5-11}$$

Since all the component spring forces are known, the bending moment of the middle joint (M_j) can also be calculated. Therefore, the contribution to the global load resistance by the flexural action can be evaluated as:

$$P_M = 2\,M_j/L_0 \tag{5-12}$$

Step-7:

The total vertical resistance P_i is the sum of the contributions of flexural action and catenary axial force,

$$P_i = P_N + P_M \tag{5-13}$$

where P_N and P_M are the load resistance contributed by axial force and bending moment, respectively. Finally, with the solution under every incremental step solved,

the whole set of load-deflection ($P_i - w_i$) results will form the resistance function curve.

The full analytical solution procedure is summarised in a flow chart, as shown in Figure 5.6.

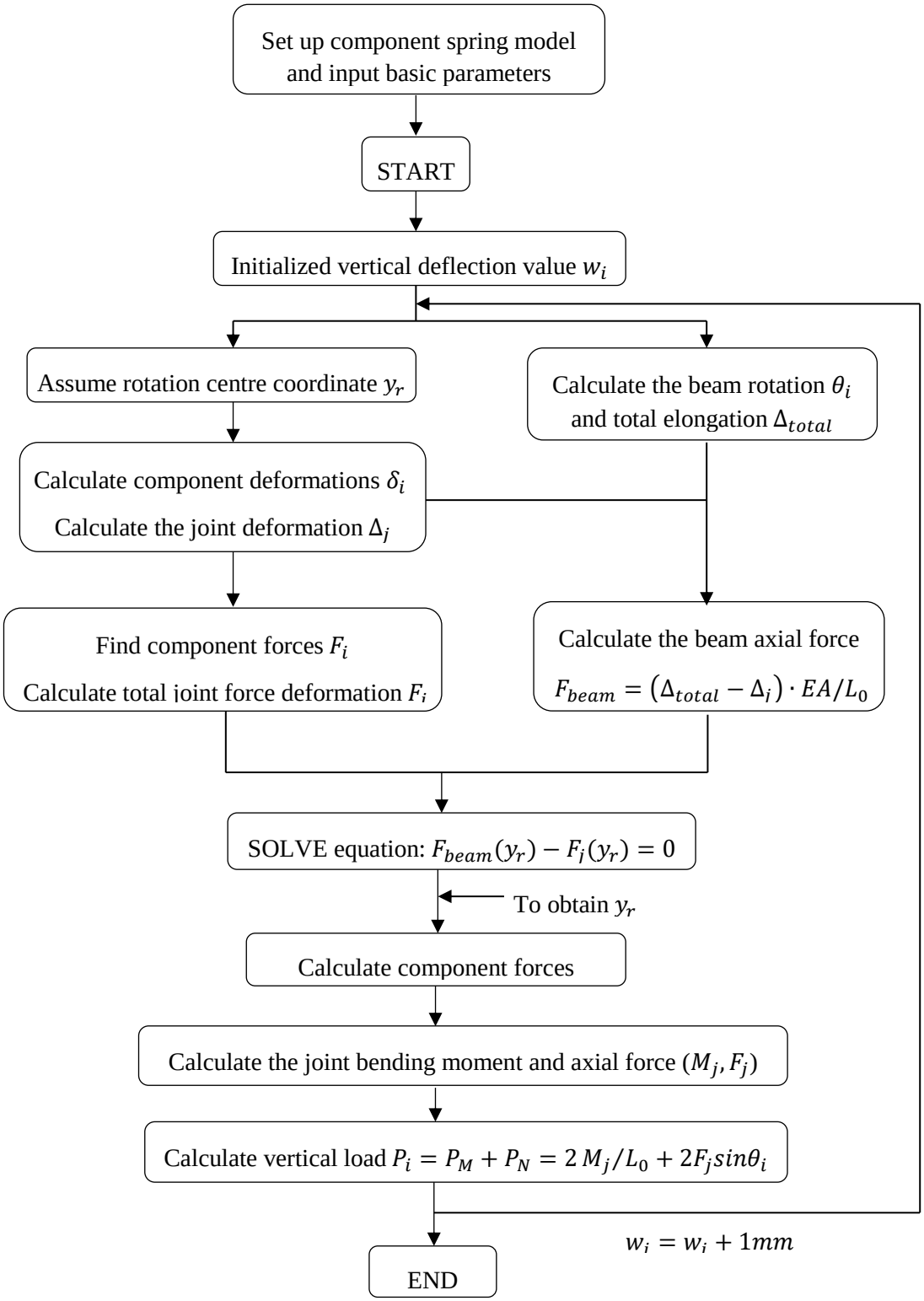

Figure 5.6 The flow-chart of the analytical procedure

5.2.3 Discussion of the proposed analytical framework

In this proposed analytical framework, there are some critical parameters and solution techniques, which need further discussion and detailed explanation.

a) The total elongation of single span beam

As shown in Figure 5.4, the axial elongation of the single span beam is firstly evaluated by the geometrical relationship as:

$$\Delta_{total} = \sqrt{w_i^2 + L_0^2} - L_0 \tag{5-14}$$

By using the Taylor series expansion, the above equation is expressed as:

$$\begin{aligned} \Delta_{total} &= L_0 \left(\sqrt{1 + \left(\frac{w_i}{L_0}\right)^2} - 1 \right) \\ &= L_0 \cdot \left[\frac{1}{2}\left(\frac{w_i}{L_0}\right)^2 - \frac{1}{8}\left(\frac{w_i}{L_0}\right)^4 + \cdots \right] \approx \frac{w_i^2}{2L_0} \end{aligned} \tag{5-15}$$

Take an example of a single span length of $L_0 = 2.0$ m and a vertical deflection w_i of up to 200 mm, the difference of the result from the above two equations is found to be less than 0.2%. So the simplified equation of axial elongation is justified to be applicable to large deflection regimes.

b) The joint rotation centre position (y_r)

When the beam assembly develops a sufficiently large deflection and beyond, all the joint components would be in tension. Consequently, the centre of the joint rotation would be outside of the set of component springs. However, at the beginning of the post-yield transition stage, the flexural action is still dominant, as a result some of the component springs are subjected to compression forces, and the centre of rotation is located somewhere between the component springs. The solution procedure accommodates both situations by a simple trial and correction routine.

c) The component force identification (F_i)

In Step 2, the component deformation δ_i is derived as a function of the unknown parameter y_r. As the actual (spring) component behaviour is generally represented by a nonlinear multi-stage curve, especially for those components which exhibit complicated behaviour with several response stages. Therefore, it is not straightforward to expressly determine the associated component force F_i, based on a component deformation which is given as a mathematical function. In the study of Stylianidis and Nethercot (2015), all of the component properties are simplified into bi-linear approximations, which however narrows the applicability of the procedure.

In the present analytical solution, the component behaviour is represented by either multi-stage mathematical formulations or in a tabulated form of data points. For the step function type constitutive law, the component force is determined by firstly identifying which interval the deformation lies in, and then calculating the force accordingly. If the component behaviour is presented by a tabulated series of data points, then the component force would be found by linear interpolation between two closest points.

d) Dealing with extra-large compressive stiffness

As mentioned before, in the post-yield response, the component springs could be subjected to tension or compression. This requires the component behaviour under compression to be properly defined. Some critical components may have quite large compressive stiffness. In this case, as shown in Figure 5.7, the rotation centre would be very close to the level of the compressive spring. For an extreme scenario, if the compressive stiffness is infinitive, then the rotation centre would be exactly coincident with the compressive spring.

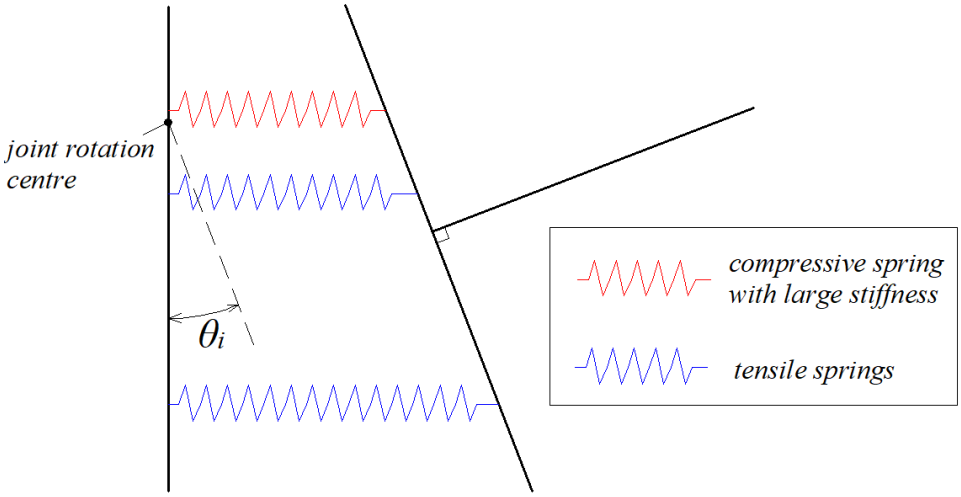

Figure 5.7 The model including compressive spring with extra-large stiffness

Obviously, the value of y_r would be very small if the compressive stiffness is extra-large. Therefore, in the iterative solution of the joint rotation centre, the incremental step size should be sufficiently small, in order that a proper solution of y_r can be mathematically found, with a reasonable tolerance.

e) Predicting the component failures and the associated effects

For each component, the ultimate deformation limit (δ_u) at failure is a critical parameter that has to be clearly quantified, in addition to the detailed force-deformation relation. Once the failure limit is reached under a certain deflection level, the component instantaneously fails and is disconnected. In the present analytical solution, the component can still develops deformation after ultimate failure, but the component force is dropped to zero at the ultimate failure, see Fig. 5.8.

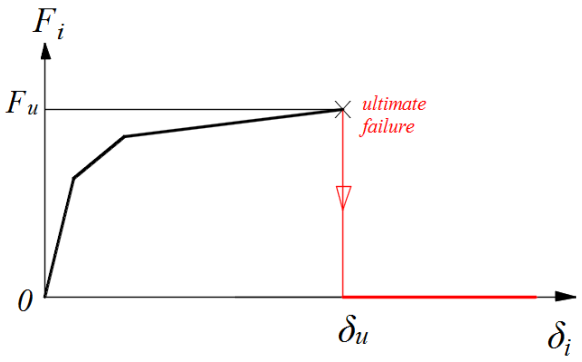

Figure 5.8 A schematic of the component function considering the ultimate failure

f) Limitations of the analytical framework

This analytical framework is only applicable to symmetrical double beam assemblies, with equal spans on either side of the column. Another limitation is that both of the beam ends are assumed to be pin supported. Although flexible axial restraints can be taken in to account by calculating an equivalent beam axial stiffness, as shown in Fig. 5.2 and Equation (5-1), the rotational restraints cannot be properly incorporated into the model.

5.2.4 Realization of the analytical framework

The core part of the solution procedure is to solve the joint rotation centre position (y_r) from a nonlinear equation, which is not straightforward, especially when the component behaviour is formulated in a nonlinear multi-stage form.

In this study, the solution process is written in a program using MATLAB to execute the analytical framework and obtain the full-range load-deflection curve of the beam assembly. A nonlinear programming solver is employed to find the accurate rotation centre coordinate for the joint components group.

The structure of the MATLAB program to carry out the analytical framework is presented below. It includes a main function, and three sub-functions, which are listed in Table 5.1.

Table 5.1 The structure of the analytical program

Function name		Function purpose
Main function		Solve the equilibrium equations and produce the full-range load-deflection curve, and also the force and deformation data in each step
Sub-function 1	ComBehaFun	Define the component behaviour function
Sub-function 2	calcFj	Calculate the component deformation and force under each deflection step w_i and assumed y_i
Sub-function 3	FindYi	Establish the axial force equilibrium equation

5.3 A survey of critical components of common steel joints and their constitutive properties

5.3.1 Summary of the critical components in the common steel joints

As has been described before, some of the key components can be identified in the typical steel beam-column joints.

For a web cleat connection, the key component is characterised by a single bolt connecting two angle legs to the beam web, and two bolts connecting another two angle legs to the column flange, which is deemed as the fixed support.

The component has an effective width, which is determined according to geometric dimensions. A visual representation and the deformed shape of the bolted double-angle component are shown in Figures 5.9 and 5.10, respectively.

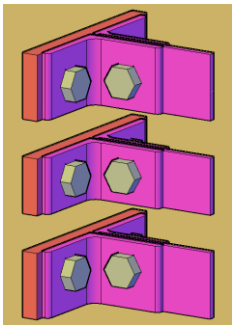

Figure 5.9 The component of double-angle-bolts set

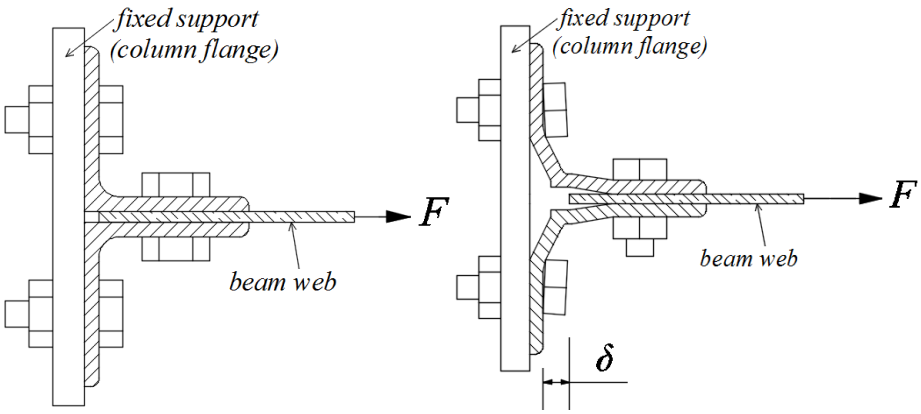

Figure 5.10 The sectional view and potential deformed shape of the bolted double-angle component

The critical component which represents the behaviour of top and seated angles is shown by Figure 5.11. It is featured with two bolts linking the angle legs to the column and beam flanges, respectively. The column flange part acts as the fixed support, while the beam flange is subjected to parallel force *F*.

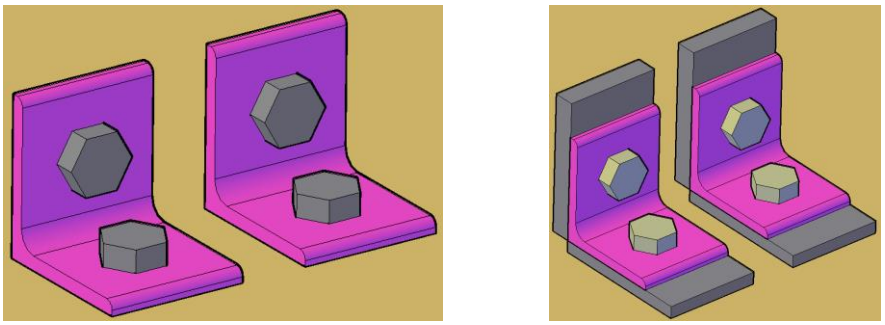

a) Bolt-angle set

b) Bolt-angle set with supporting beam and column flanges

Figure 5.11 The bolted single-angle component

The deformed shape of the bolted single-angle component is shown in Figure 5.12. Within the component, the column flange part is fixed in position, and the beam flange part can only deform in the horizontal (*x*) direction. This boundary condition feature makes it possible to consider the component as half of the bolted double-angle component. Therefore, this component is actually identical in character to (half of) the previous bolted double-angle component.

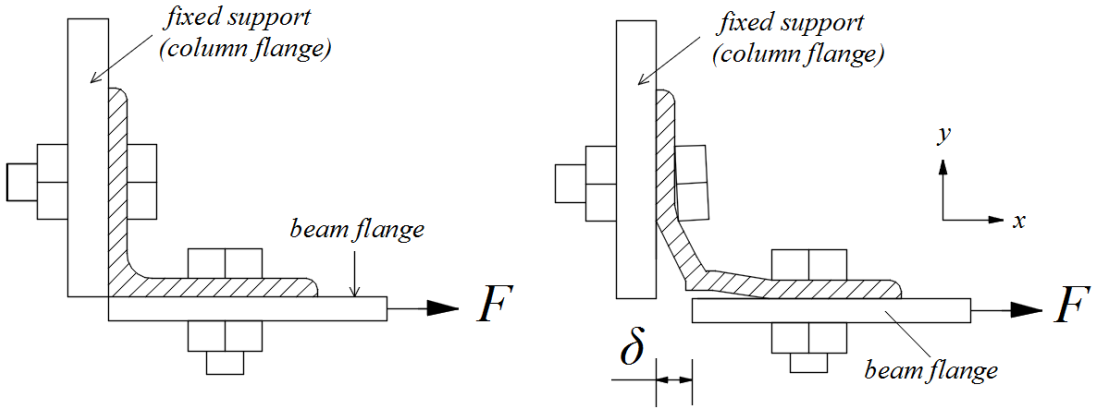

Figure 5.12 The component and its potential deformed pattern

For a fin plate connection (also referred to as “single plate shear connection”), the key component is featured by a bolt connecting a certain effective width of fin plate

and beam web, as shown in Figure 5.13. This component, termed as bolted lap-plate, will be investigated in the next chapter.

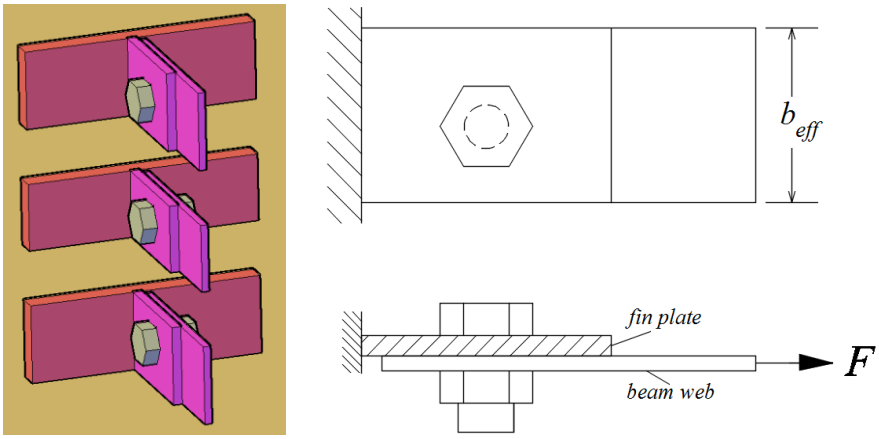

Figure 5.13 The extracted component for fin-plate connection

The components of equivalent T-stub and bolted double-angle are the most common type in steel joints. Their tensile behaviour has been investigated in the past studies. In the next two sections, the existing mechanical modelling and quantitative formulations for the two components are reviewed and discussed.

5.3.2 The equivalent T-stub component set

The T-stub analogy can be utilised to model and analyse the components for end-plate connections. Figure 5.14 shows an example of the extended end-plate connection, within which the column flange in bending and the end plate in bending can both be made equivalent to a series of T-stubs in compression or tension.

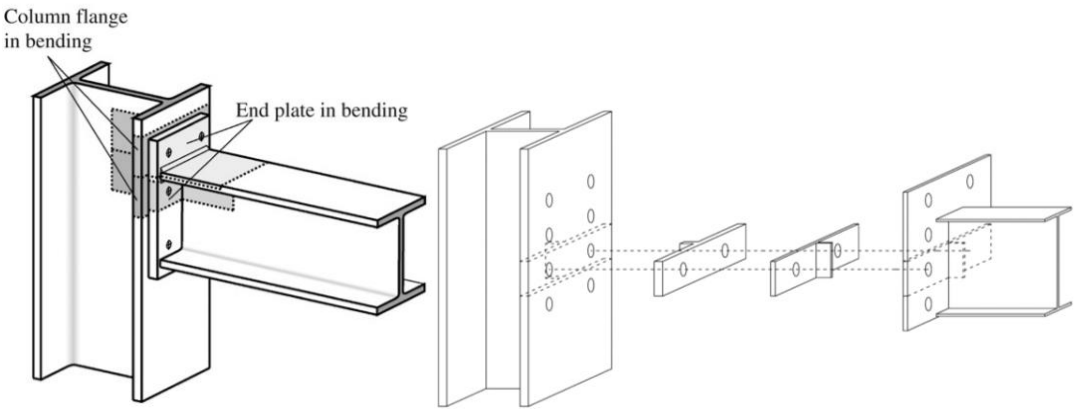

Figure 5.14 The column flange and end-plate in bending made equivalent to T-stubs

The equivalent T-stub in tension has been extensively investigated in the past years. The force-displacement formulation has been obtained. It is recognised that the controlling failure mode of the component is the fracture of the angle or bolt. The relative strength ratio between the angle and bolt will govern the final failure mode. When the angle legs are thin, the angle tends to yield and eventually fracture close to the heel, while the bolts are not yielding. This is noted as mode 1 in Table 5.2. On the contrary, if the steel angle is strong enough, the bolts would be pulled to failure, either by bolt shank necking, or by bolt threads being stripped out. It is noted as mode 2 in Table 5.2. The failure mode 3, with both the steel angle and bolts yielding, is between the previous two failure modes. The T-stub resistance can be determined as the smallest value of the force limits of the three possible failure modes. Figure 5.15 shows the three different failure modes.

Table 5.2 Three different failure modes of the T-stub

Failure mode	Description	Conditions
1	Angles yield close to heel and at bolt holes, without bolts yielding	$\frac{M_{p,tf}}{B_u} < \frac{n}{\zeta}$
2	Angle fracture close to heel, with bolts yielding	$\frac{n}{\zeta} \leq \frac{M_{p,tf}}{B_u} < m$
3	Bolts yielding, no plastic hinges formed in the angles	$\frac{M_{p,tf}}{B_u} \geq m$

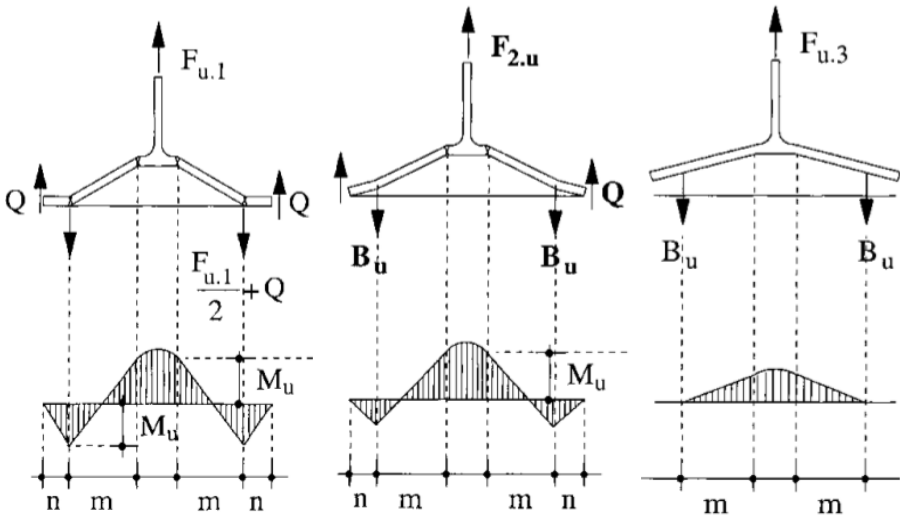

(a) Failure mode 1 (b) Failure mode 2 (c) Failure mode 3

Figure 5.15 Failure mechanisms of T-stub (Piluso et al. 2001)

Based on the material property shown in Figure 5.16(a), Piluso et al. (2001) derived a piecewise linear approximation for the force-displacement relationship. The relationship can be established by identifying four characteristic points. It is assumed that the stress-strain relation is linear from the maximum load point to the fracture load point. As schematically shown in Figure 5.16(b), the first point (F_y, δ_y) corresponds to the attainment of the first yield condition. The second point (F_h, δ_h) corresponds to the beginning of strain hardening. The third point (F_m, δ_m) corresponds to a stress level in the plastic stage and the fourth point (F_u, δ_u) corresponds to the ultimate stress and deformation.

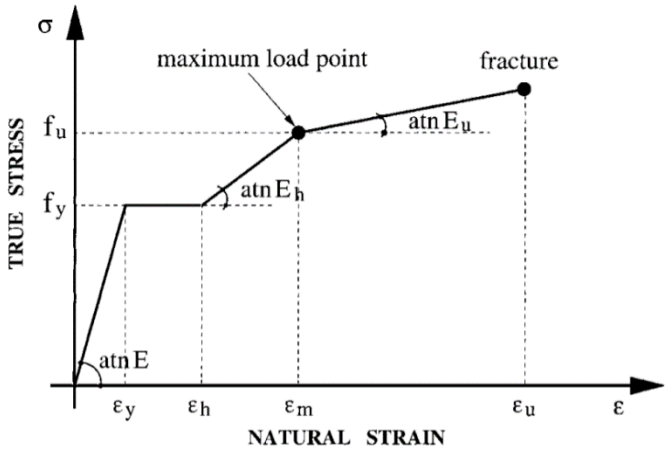

(a) Multi-linear stress-strain curve for the steel material

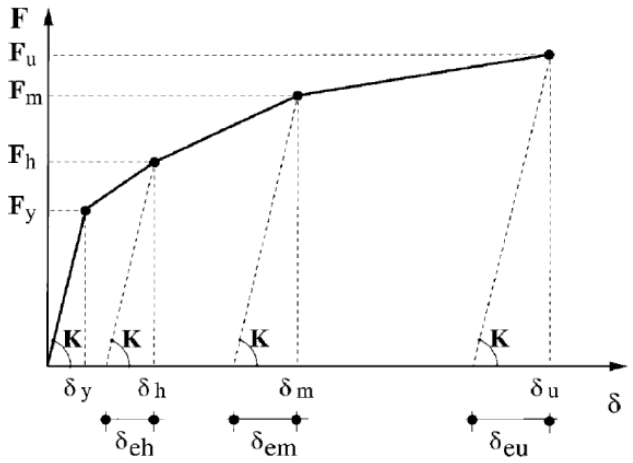

(b) Derived force-displacement relationship for the T-stub

Figure 5.16 Piluso model of T-stubs in tension (Piluso et al. 2001)

The determination of the effective width of the T-stub per bolt row can be sourced from Eurocode 3 or the work of Faella et al. (2000). According to Figure 5.17, for the typical top and seated angle connection, the component effective width is determined by:

$$b_{eff,ta} = min(d_h + 2m_a;\ \frac{d_h}{2} + 2m_a + \frac{w}{2};\ \frac{b_{ta}}{2}; e_x + \frac{d_h}{2} + m_a) \qquad (5\text{-}16)$$

For the inner bolt rows in the web angle connection, the component width is determined by

$$b_{eff,wa} = min(d_h + 2m_a;\ p) \qquad (5\text{-}17)$$

For the two outer bolt rows in the web angle, the component width is

$$b_{eff,wa2} = \min\left(d_h + 2m_a;\ \frac{d_h}{2} + 2m_a + \frac{p}{2};\ e_{xw} + \frac{p}{2};\ e_{xw} + \frac{d_h}{2} + m_a\right) \qquad (5\text{-}18)$$

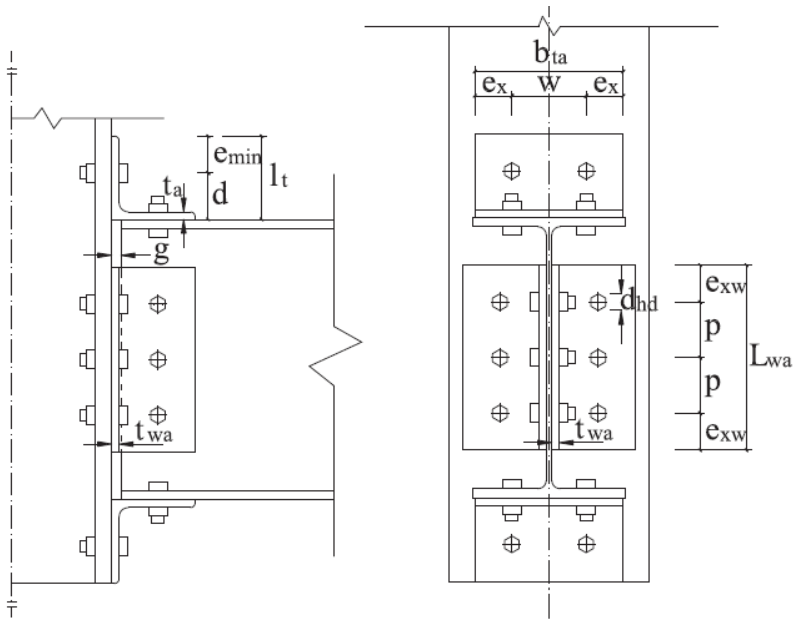

Figure 5.17 Parameters for evaluating the component effective width (Faella et al. 2000)

5.3.3 The bolted double-angle component set

As has been described before, the bolted double-angle component typically represents the web cleat connections, and some other connections in which the beam web is connected to the column flange through back-to-back steel angles. The component is schematically shown in Figure 5.18.

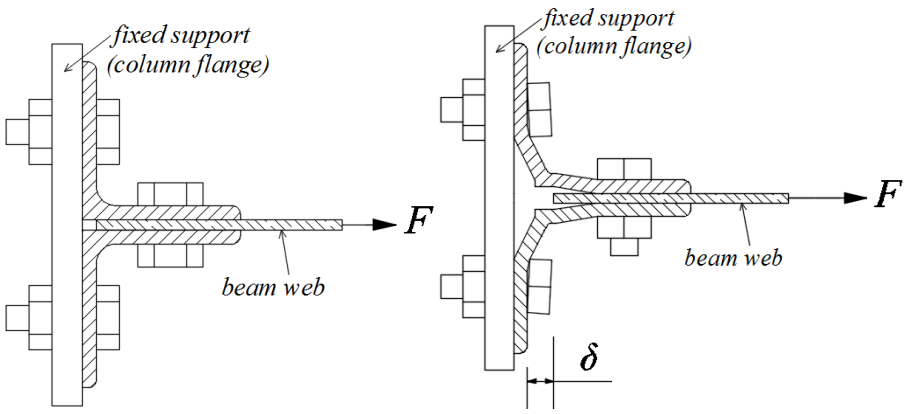

Figure 5.18 The cut view and potential deformed shape of the bolted double-angle component

Different from the T-stub, the bolted double angle have two extra features. Firstly, the beam web is connected to the angle legs via a double-shear bolt. Therefore, due to the bolt-hole clearance and the pre-tension bolt force, a frictional slipping response

stage is expected to occur before the angle develops deformation. Secondly, the corner heel of the steel angle can deform away from the beam web plane. In the T-stub component, the angle heel always deforms in the axial force direction. This characteristic can extend the ultimate deformation limit of the bolted double-angle, thus leading to a more ductile performance compared to the T-stub.

The failure mode of the bolted double-angle is still related to angle fracture and bolt yielding. It is dependent on factors such as bolt size, angle thickness, material properties, etc. A different combination of these parameters can lead to different failure mechanisms.

Shen and Astaneh-Asl (2000) proposed a tri-linear piecewise linear *F-δ* curve by simplifying the component into beam structure with reasonable boundary conditions. The tri-linear envelope of hysteresis model is full obtained as Figure 5.19. Figure 5.20 shows the configuration details of the bolted double-angle, where g_1 and g_2 are the distances from the bolt centre line to angle edges.

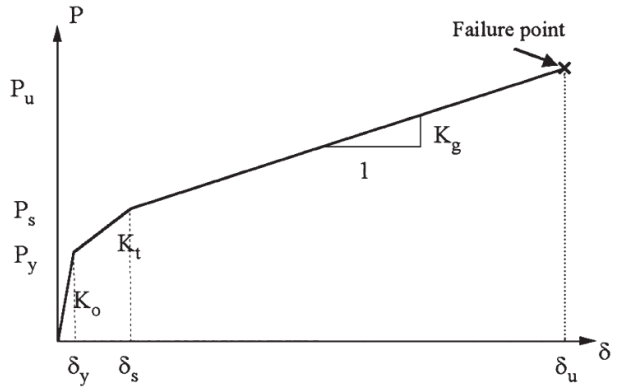

Figure 5.19 The tri-linear force-displacement curve for the bolted double-angle (Shen and Astaneh-Asl 2000)

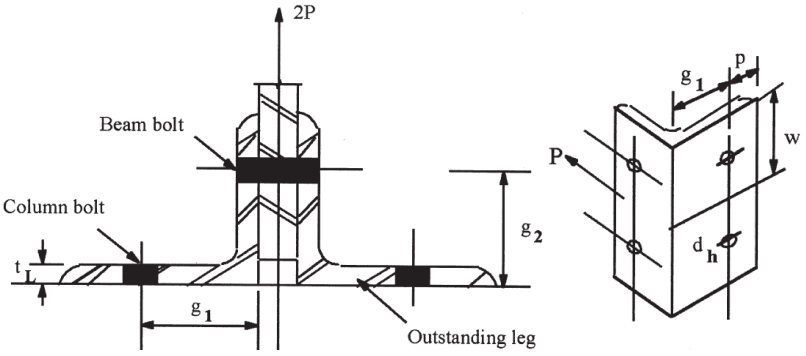

Figure 5.20 The configuration details of bolted double-angle

Figure 5.21 shows the simplified models to evaluate the initial elastic response and the tangent stiffness in the second stage. According to the models, cross-section A yields first when its bending moment reaches M_y. Thus, the initial stiffness K_0 and first yielding load P_y are formulated as:

$$K_0 = \frac{12EI}{g_1^3}\left[1 - \frac{3g_2}{4(g_1+g_2)}\right]$$
$$P_y = \frac{4g_1 + g_2}{g_1(2g_1+g_2)} M_y \tag{5-19}$$

The tangent stiffness of the second stage is obtained as:

$$K_t = \frac{3EI}{g_1^3}\left[1 - \frac{3g_2}{8g_1+6g_2}\right] \tag{5-20}$$

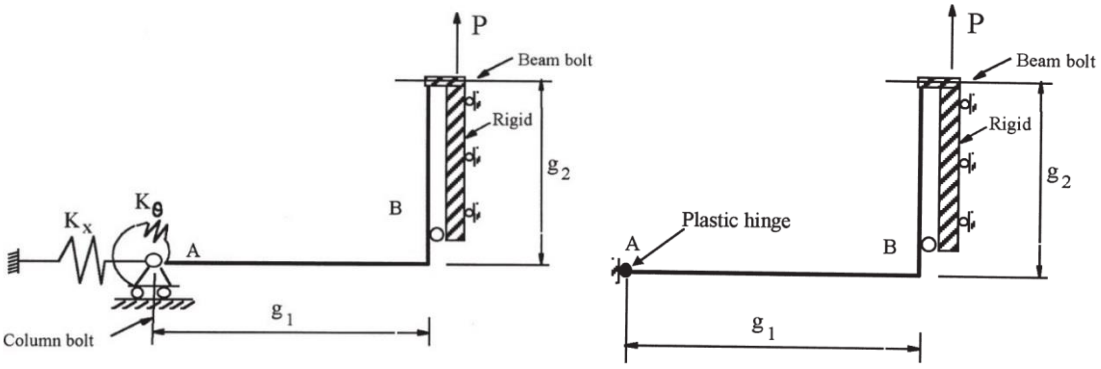

Figure 5.21 Models to evaluate the initial stiffness (left) and tangent stiffness (right) (Shen and Astaneh-Asl 2000)

In the third response stage, large plastic deformation will form close to the heel or the bolt-hole. Two different failure deformation patterns are depicted in Figure 5.22.

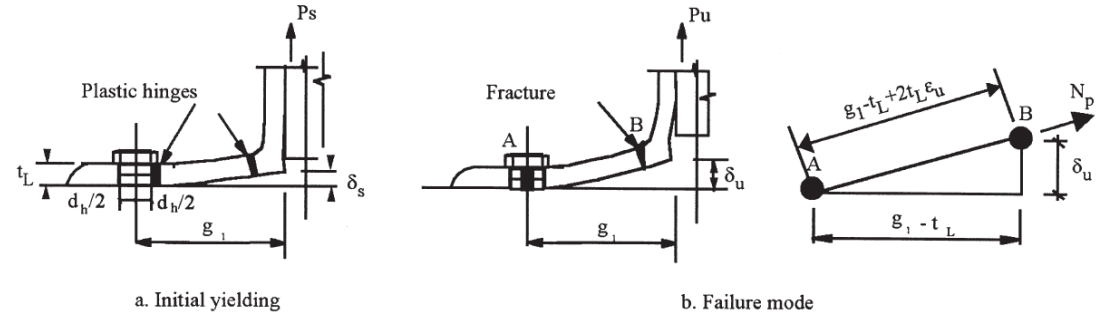

(a) Deformation pattern 1

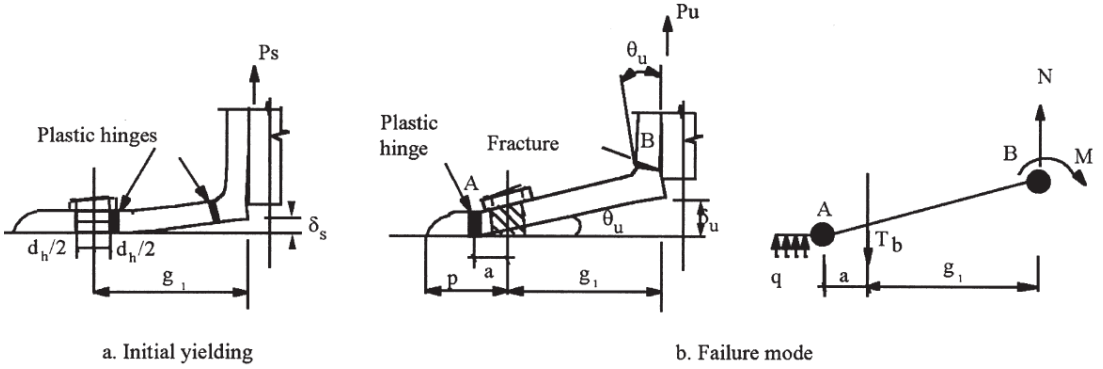

(b) Deformation pattern 2

Figure 5.22 Two different patterns in the large deformation stage (Shen and Astaneh-Asl 2000)

The transitional yielding loads corresponding to the two different deformation modes, P_{s1} and P_{s2} are derived as:

$$P_{s1} = \frac{2M_p}{g_1 - t_L - d_h/2}$$
$$P_{s2} = \frac{M_p(2 - d_h/w)}{g_1 - t_L/2} \quad (5\text{-}21)$$

Where M_p is the plastic moment capacity of the angle leg cross-section, d_h is bolt hole diameter, and t_L is the angle thickness.

When δ_u and P_u are known, the post-yielding stiffness (k_g, see Fig. 5.19) can be evaluated as

$$k_g = \frac{P_u - P_s}{\delta_u - \delta_s} \tag{5-22}$$

1) Deformation pattern 1

For the post-yielding behaviour of the first deformation pattern, assuming that the plastic hinge length of a rectangular cross-section is equal to its height, the maximum deformation and maximum strength are calculated according to Equations (5-22). Here *n* is the number of column bolts and N_p is the full plastic capacity of the angle-leg section.

$$\begin{gathered} \delta_u = 2\sqrt{(g_1 - t_L)\varepsilon_u t_L} \\ P_u = nN_p \sin\alpha \\ \alpha = tan^{-1}[\delta_u/(g_1 - t_L)] \end{gathered} \tag{5-23}$$

2) Deformation pattern 2

For the post-yielding behaviour of the second deformation pattern, the maximum deformation is reached when the maximum rotation of the hinge at section B reaches the ultimate strain value ε_u. The rotation of the angle leg, θ_u, may be considered as approximately equal to the ultimate strain ε_u. Under the assumptions, the ultimate deformation δ_u and loading capacity P_u can be derived as:

$$\begin{gathered} \delta_u = (g_1 + a)\tan(\varepsilon_u) \\ P_u = n\left[T_b - \frac{wt_L^2 f_y}{2(p-a)}\right] \end{gathered} \tag{5-24}$$

where *a* can be taken as *P*/2, as suggested by existing experiments (Shen and Astaneh-Asl 1999).

Yang and Tan (2013) carried out experimental investigations on bolted double-angle connections under pure tension, and divided the response into five characteristic stages. As can be seen from Figure 5.23, an elastic stage (O-A) and a bolt slippage stage (A-B) firstly occur before the elastic deformation stage (B-C). A transition stage (C-D) is developed up to the full yielding of the angle. Then mechanism deformation stage (D-E) comes into being before the final fracture of the whole component. During the whole response, point D marks the full yielding of the angle,

and it can be predicted by the current codified formulations (Eurocode 3). The large deformation stage, though, has not been quantified.

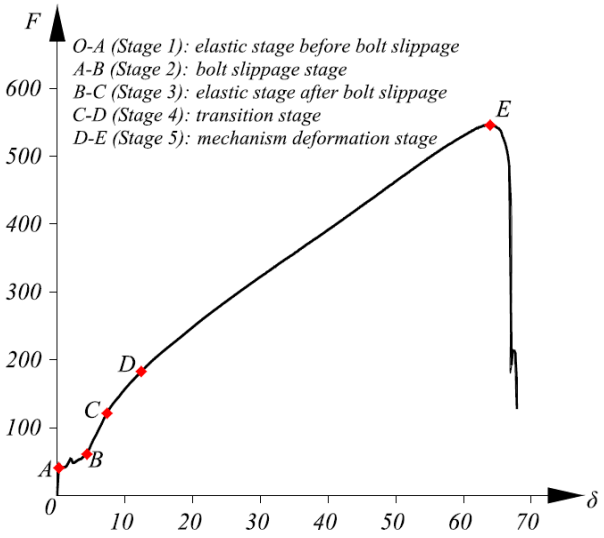

Figure 5.23 The test result of the 3-bolt row component (Yang and Tan 2013)

The parameters studied in the experiments mainly included gauges length m, angle thickness t_a, as shown in Figure 5.24, and the bolt size and material properties.

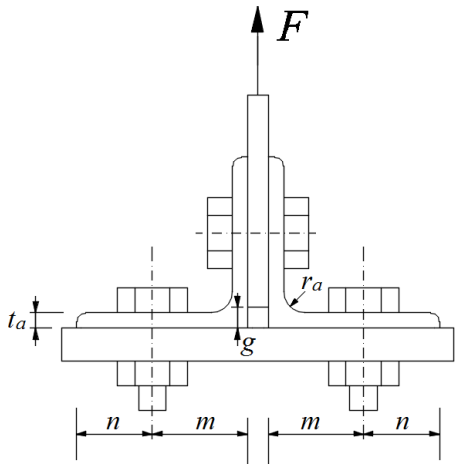

Figure 5.24 The component cut-view and key geometrical parameters

Depending on the relative strength ratio between the angles and the bolts, five different component failure modes were observed from the tests, as are shown in Figure 5.25.

(a) (**Mode 1**) Angle fracture at bolt holes

(b) (**Mode 2**) Angle fracture close to heel

(c) (**Mode 3**) Angle fracture at bolt holes with yielded bolts

(d) (**Mode 4**) Angle fracture close to heel with yielded bolts

(e) (**Mode 5**) Angle fracture at bolt holes with yielded bolts

Figure 5.25 Failure modes of the bolted double-angle component in tests

During the large deformation stages, three different mechanisms are summarized in Figure 5.26. The difference is that the plastic hinge around the bolt could be closer to the angle heel, in the bolt centre-line, or closer to the angle edge. This dependent on the relative strength between the angle and the bolt.

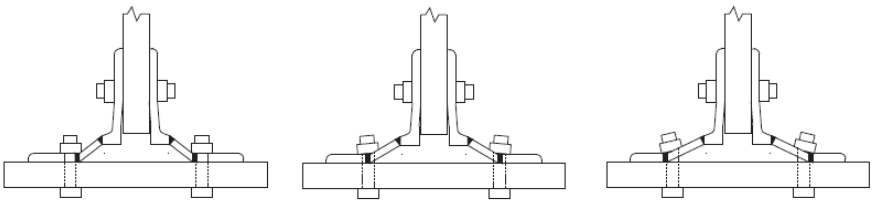

(a) Hinge close the angle heel; (b) Hinge in the bolt centre line; (c) Hinge close the angle edge

Figure 5.26 The failure modes of bolted double-angle component (Yang and Tan 2013)

Based on the experimental results, Yang and Tan (2013) developed a new mechanical model as well as mathematical formulations for the bolted double-angle connections. In their proposed model, the following issues are particularly addressed:

1) the interaction between the angles and the bolts;
2) the failure criteria to determine the ultimate deformation;
3) the load limits due to bolt tensile fracture.

The full component behaviour is schematically represented by Figure 5.27. In this model, the small deformation response, including the initial slippage phase (O-A) and the loading phase up to the angle yielding (A-B), still follow the codified formulation by Eurocode 3.

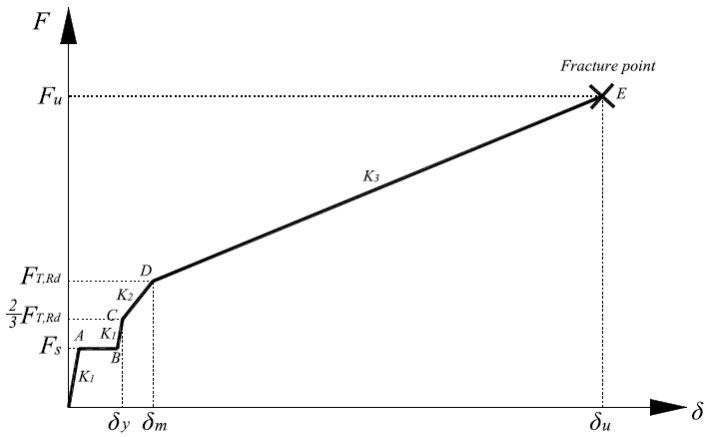

Figure 5.27 Yang's multi-stage model of bolted double angle under tension (Yang and Tan 2013)

According to Eurocode 3 (Part 1-8), the frictional force limit is calculated by:

$$F_s = nc_f p_{pf} \tag{5-25}$$

where c_f and p_{pf} are the frictional coefficient and the pretension force applied to the bolt.

The initial stiffness K_1 is calculated by the formulation proposed by Faella et al. (2000) as:

$$K_1 = E\frac{0.5b_{eff}t_a^3}{(m - t_a - 0.8r_a)^3}\left(\frac{4\gamma_a}{4\gamma_a + 3}\right)$$
$$\gamma_a = \frac{I_2/L_2}{I_1/L_1} \tag{5-26}$$

where the parameters I_1, I_2, $L_1$and L_2 are shown in Figure 5.28.

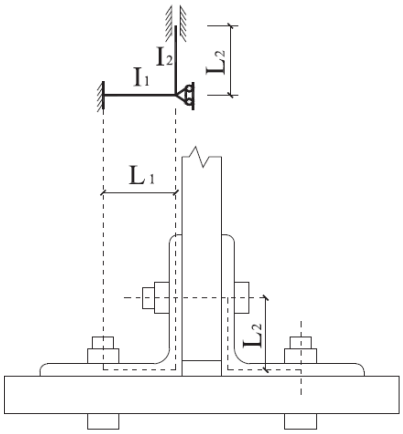

Figure 5.28 Mechanical model of the angle in bending (Yang and Tan 2013)

In the large deformation response, a constant value of the tensile force within the deformed angle was assumed. It is estimated by Equation (5-27), where *n* is the number of bolts along the effective width, d_h is the diameter of the bolt-hole:

$$N_a = \left(b_{eff} - nd_h\right)t_a f_u \tag{5-27}$$

In reality the tensile forces increase gradually rather than maintaining a constant value. Hence, the proposed tensile force will only be used to calculate the load increment to reduce the calculation error due to this assumption. Therefore, at large deformation stage, the load resistance will be calculated based on an incremental approach from:

$$\Delta F = 2N_a\left(\frac{\delta_1 + \Delta}{\sqrt{m^2 + (\delta_1 + \Delta)^2}} - \frac{\delta_1}{\sqrt{m^2 + \delta_1^2}}\right) \tag{5-28}$$

At the failure stage of the specimens, the deformation of the horizontal legs of the angle at the modified gauge length is shown in Figure 5.29. Since at this moment the angle is under very large tensile strain, the tensile elongation of the horizontal leg at the modified gauge length is assumed to be $m^* \cdot \varepsilon_u$ (Fig. 5.30). Under this assumption, the ultimate displacement δ_u can be calculated as Equation (5-29),where the angle θ is formulated according to the study of Piluso et al. (2001).

$$\delta_u = m^*(1 + \varepsilon_u)sin\theta = m^*(1 + \varepsilon_u)sin\left(\frac{m^*\varepsilon_u}{2t_a}\right) \tag{5-29}$$

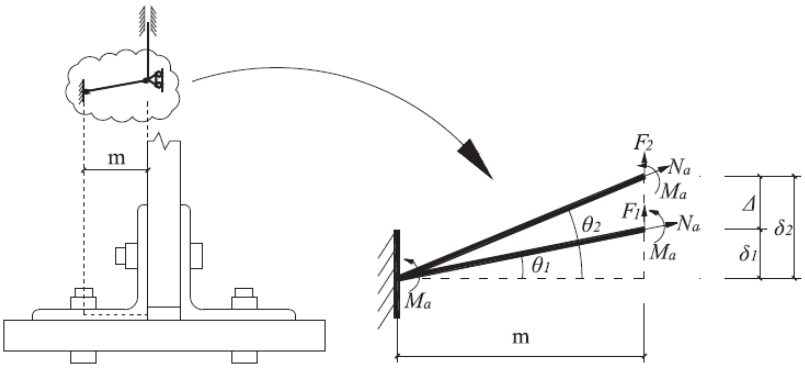

Figure 5.29 Mechanical model of the angle legs (Yang and Tan 2013)

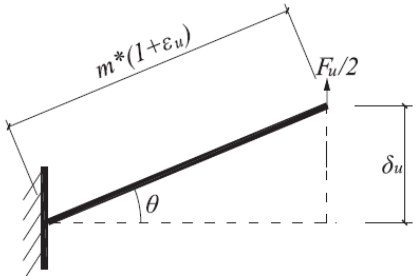

Figure 5.30 Ultimate status of the angle horizontal leg

In particular, Yang and Tan (2013) recommended a new equation to formulate the gauge length m^* (the distance between two plastic hinges at the horizontal leg). This is due to the fact that the strength ratio between angles and bolts will influence the plastic hinge locations formed in the angles, so the interaction between angles and bolts needs to be considered. Normally it is assumed that the plastic hinges of angles formed around the bolt centrelines. For more flexible angle legs, plastic hinges may be located closer to the angle heel, while for relatively stiff angles, plastic hinges tend to move closer to the angle edge. The angle-bolt interaction is considered by the following equation, proposed by Yang and Tan (2013):

$$m^* = m - t_a - 0.8r_a + \eta d_b \tag{5-30}$$

where η is a coefficient related to the strength ratio between the axial resistance of bolts, F_b, and the yield strength of angle legs, F_g. They are calculated by the following equation.

$$\eta = 1.1335 - 0.00242\frac{F_b}{F_g}$$
$$F_b = f_{yb}A_b,\ F_g = F_{T,Rd}/b_{eff} \tag{5-31}$$

The angle resistance $F_{T,Rd}$ is calculated according to Eurocode 3, as determined by the steel angle strength, angle thickness and angle gauge length.

5.4 Application of the proposed analytical framework to typical bolted connections

This section uses the proposed analytical framework with existing component behaviour formulations to investigate the resistance functions of a double beam assembly, with two typical connection types, namely the web cleat connections, and top-and-seat with web angles (TSWA) connection. The former is a representative and commonly-used simple connection, while the latter is a typical semi-rigid connection. Both of the connections consist of bolted angle components. The existing studies of the bolted double-angle behaviour, especially its large deformation behaviour and quantified load-deformation formulations up to failure have been reviewed and summarized in section 5.3.3. The recent component model proposed by Yang and Tan (2013) will be employed and fit into the present analytical framework, to investigate the joint behaviour and the global load-deflection behaviour of the double beam assembly.

The analytical results of the load resistance functions are presented and validated against the experimental results. Additionally, the failure events predicted by the analytical solution will be described, and also compared with the failure characteristics observed in the tests. Through the validation and associated discussion, the potential gap or inadequacy of the existing component behaviour quantification can be identified, and some further work will be recommended.

5.4.1 Specimen configuration details

Yang and Tan (2013) tested totally seven double beam assemblies with bolted steel joints with missing internal column. The web cleat and TSWA connections are included among the seven specimens. All of the tested assemblies are pin-supported at the two ends, and the overall geometric dimensions are shown in Figure 5.31. The Universal Column 203×203×71, with a sectional depth of 216 mm, was used for all central column stubs. The beam section was UB 305×165×40, which has a sectional area of 5130 mm^2, and the net single span was 2.33 m.

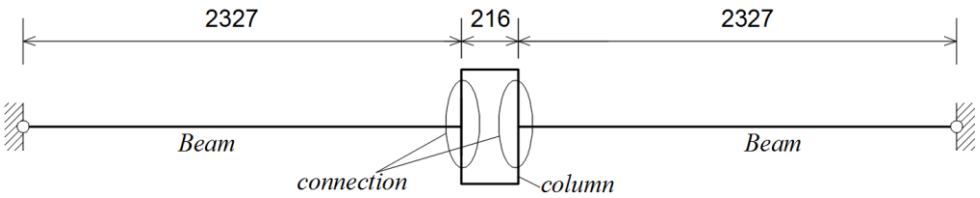

Figure 5.31 The geometric configuration of the tested specimens

The configuration and dimensions of the web cleat and TSWA connections are schematically depicted in Figure 5.32. Both connections had exactly the same details regarding the beam web connection part, with two back-to-back angles and three high strength bolts used to connect the beam web to the column flange. The only difference was that, in the TSWA connection, two extra top and seat angles were installed to connect the beam and column flanges. Therefore, it is expected that the assembly with a TSWA connection would have extended flexural bending stage, and also larger deformation limits.

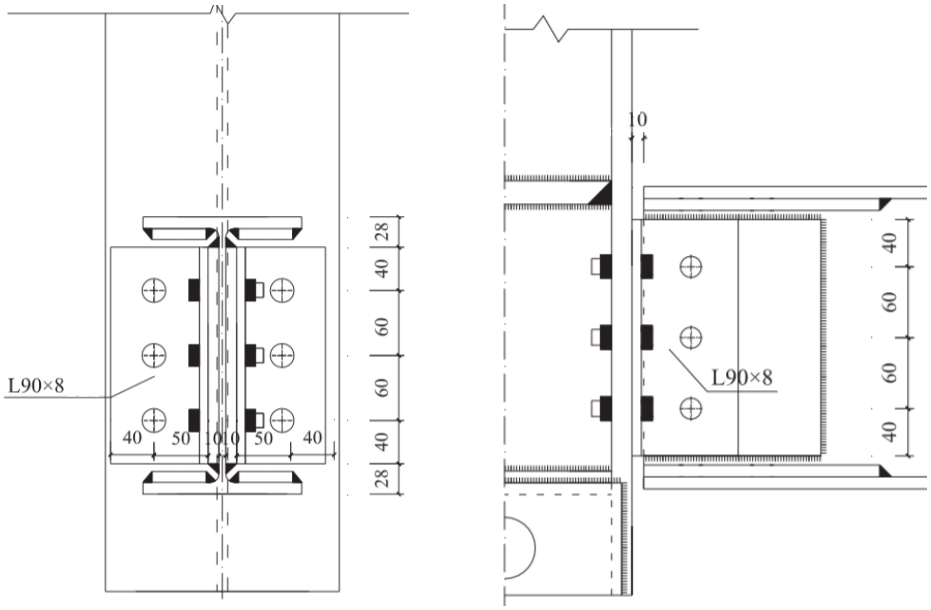

(a) Web cleat connection

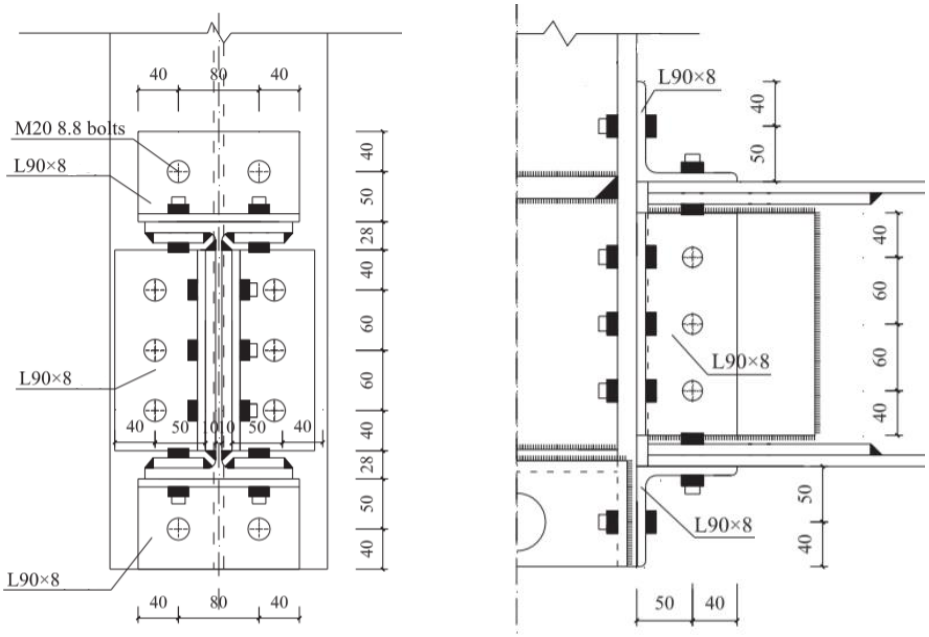

(b) Top-and-seat with web angle (TSWA) connection

Figure 5.32 The configuration details of the web cleat and TSWA connections (Yang and Tan 2013)

Noteworthy is that two extra plates were welded to beam web, and two horizontal stiffeners for the column web were installed. These treatments helped mitigate the influence of beam web and column panel deformations. Accordingly, the mechanical

models in the present analysis will not include components related to the beam web and column panel deformations.

The L shape steel angles have a thickness of 8.0 mm, and are made of steel grade S275JR. According to the coupon test conducted, the yielding and ultimate strength of the angle steel material are 331 MPa and 484 MPa, respectively. The fracture strain is 0.31, based on proportional coupon gauge length of $5.65\sqrt{S_0}$, where S_0 is the original cross-sectional area of coupons.

5.4.2 Summary of the relevant test results

The load-deflection response of the assembly with web cleat connection is shown in Figure 5.33. As can be seen from the load resistance curve, the assembly initially experienced a pin rotation stage before gaining obvious vertical resistance. As the web cleat connection has limited moment resistance, the vertical load was mostly resisted by catenary force. At the deflection of 368 mm (9 degrees rotation), one of the web angles fractured close to the heel, and was soon followed by the other angle fracture.

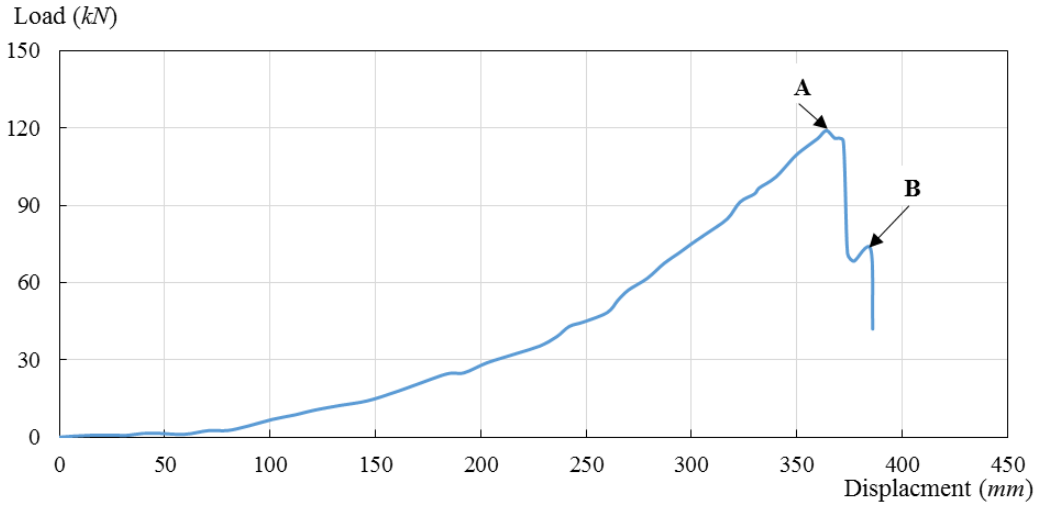

Figure 5.33 The resistance function of the assembly with web cleat connection (after Yang and Tan, 2013)

The characteristic failure points are listed in Table 5.3, along with the test photos showing the failure modes, and the corresponding deformation levels. It is shown

that the angle fractured near the heel, and the plastic hinge line also formed near the bolts.

Table 5.3 The failure points and the test observations (web cleat connection) from Yang and Tan (2013) experiment

Characteristic points	**A**	**B**
Test photo		
Failure status	Web angle 1 fractured	Web angle 2 fractured
Vertical deflection	ω = 368*mm*	ω = 385*mm*
Rotation $\theta = w/L$	θ = 0.16 *rad* (9.0 *degrees*)	θ = 0.17 *rad* (9.4 *degrees*)

The load-deflection response of the assembly with TSWA connection is shown in Figure 5.34. Clearly, the assembly possessed higher load and deformation capacities, and the connection underwent multiple failure events in the course of large vertical deflection. Points A and B represent the angle fracture at the bottom, while points C and D denote the web angle fractures on one connection side. The fractures of two bottom angles marked the end of the bending stage and the onset of the catenary action stage.

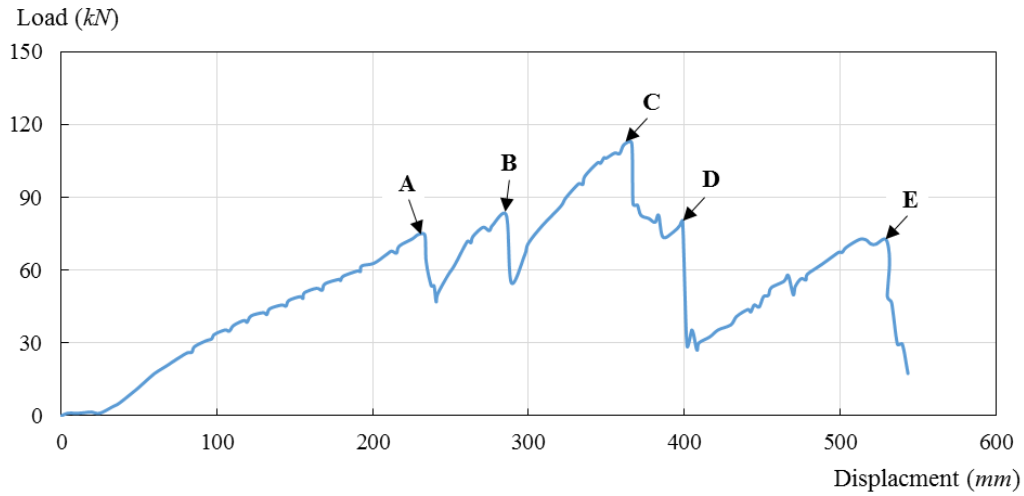

Figure 5.34 The resistance function of the assembly with TSWA connection (after Yang and Tan, 2013)

The fracture of the angles on another side (point E) forced the test to terminate, and it was considered to be the ultimate state of the assembly. Actually, the joint was still held by two top angles, yet the load and deformation after this point would be very limited.

Figure 5.35 The failed TSWA connection sustained by top angles

The characteristic failure points are listed in Table 5.4, with the photos showing the failure modes and the corresponding deflection/rotation magnitudes. The angle fracture modes are identical to that of the web cleat connection.

Table 5.4 The failure points and the test observations (TSWA connection)

Failure points	**A**	**B**	**C**	**D**	**E**
Test photo					
Failure status	Left bottom angle fractured	Right bottom angle fractured	Right web angle 2 fractured	Right web angle 1 fractured	Left web angle 2 fractured
Vertical deflection	ω = 233*mm*	ω = 286*mm*	ω = 366*mm*	ω = 399*mm*	ω = **530*mm***
Rotation $\theta = w/L$	0.10 *rad* (5.7 *degrees*)	0.12 *rad* (7.0 *degrees*)	0.16 *rad* (8.9 *degrees*)	0.17 *rad* (9.7 *degrees*)	**0.23 *rad*** (**12.8 *degrees***)

5.4.3 Component models and determination of quantitative component properties

Firstly, the web cleat connection can be divided into three bolted double-angle components, each representing one bolt row and an effective width of steel angles, as shown in Figures 5.36 and 5.37. Components 1 and 3 have the same properties due to symmetry, while component 2 representing the inner bolt row may have different properties.

Secondly, for TSWA connection, the web angle connection is discretised in the same way. With regard to the top or seat angle connection, there are two bolt rows, and one bolted single-angle can be considered as half of a bolted double-angle. Therefore, the top or seated angle connection can be made equivalent to a bolted double-angle component. They are denoted as components 4 and 5, which have the same properties. The models for the TSWA connection are shown in Figures 5.39 and 5.40.

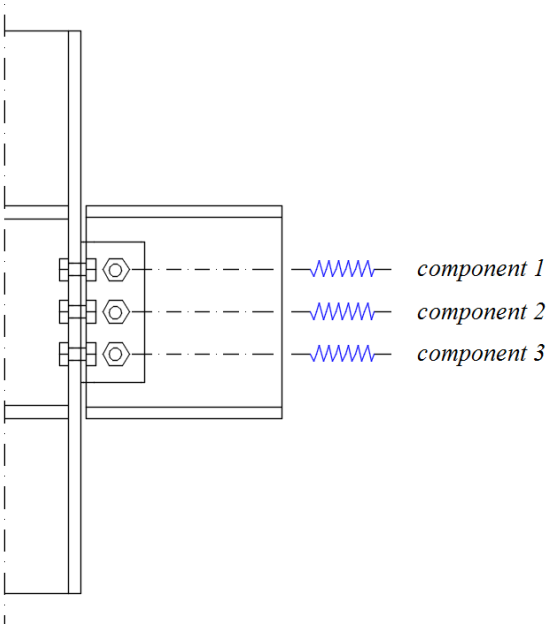

Figure 5.36 The component discretization of the web cleat connection

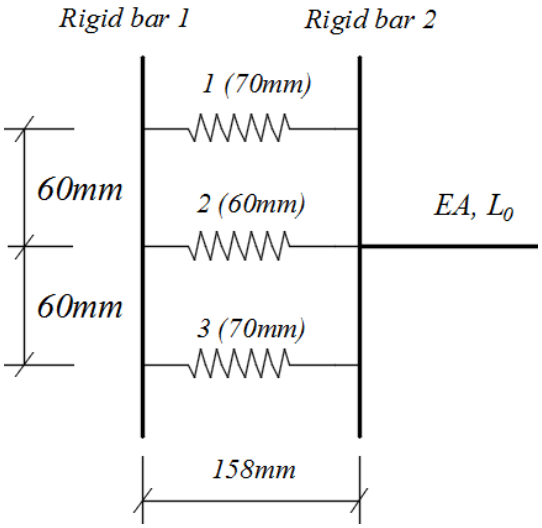

Figure 5.37 The component model for the web cleat connection on one side (symmetric)

As recommended by Eurocode 3, the lever arm of the top and seated angle is calculated between the bolt rows in tension and compression. When it is in tension, the force line is parallel to the bolt centre line. When the component is in compression, the force line is parallel to the mid-thickness of the horizontal angle leg. Hence, the locations for components 4 and 5 are determined accordingly.

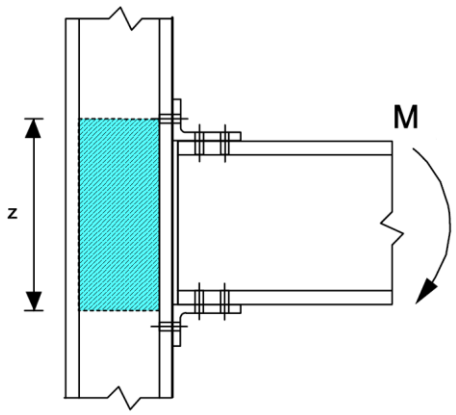

Figure 5.38 Lever arm of the top and seated angle connection recommended by Eurocode 3

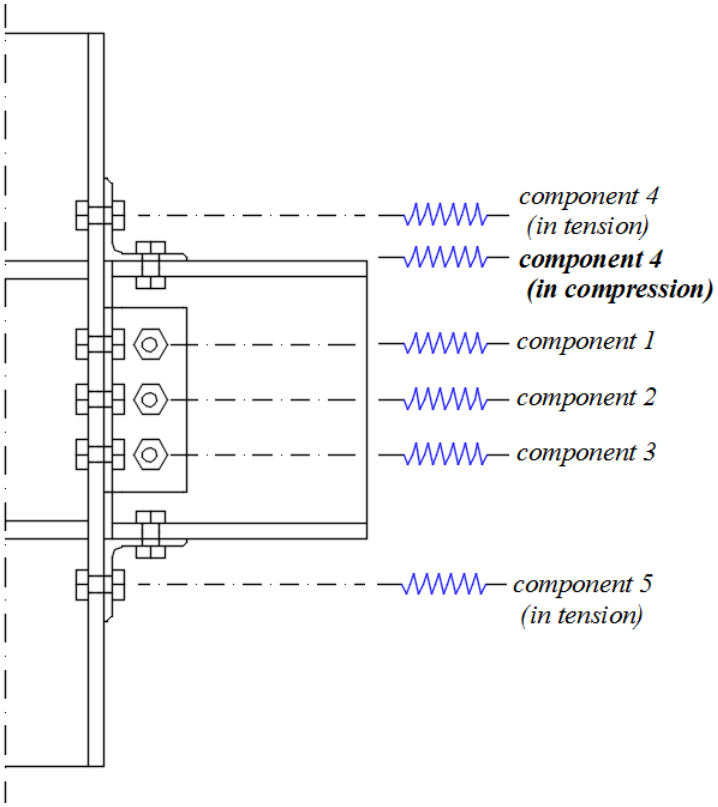

Figure 5.39 The component discretization of the TSWA connection

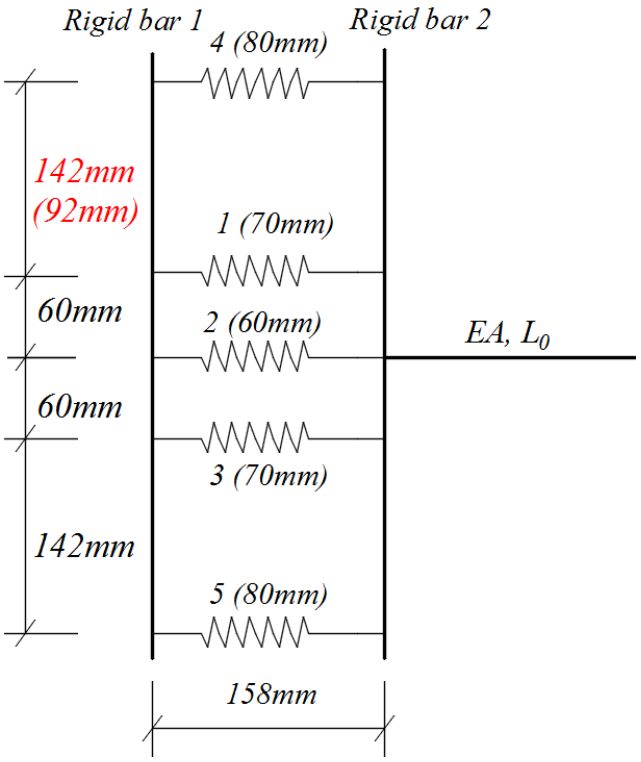

Figure 5.40 The component model for the web cleat connection on one side (symmetric)

For the web angle connection, the effective widths for components 1 and 3 (outer bolt row) and component 2 (inner bolt row) are calculated to be 70 mm and 60 mm, respectively. The effective width for components 4 and 5 in the top and seated angles is calculated to be 80 mm.

The parameters of the bolted double-angle component section are shown in Figure 5.41. The multi-stage model proposed by Yang and Tan (2013) is used to formulate the component behaviour functions. The associated parameters are calculated and listed in Table 5.5.

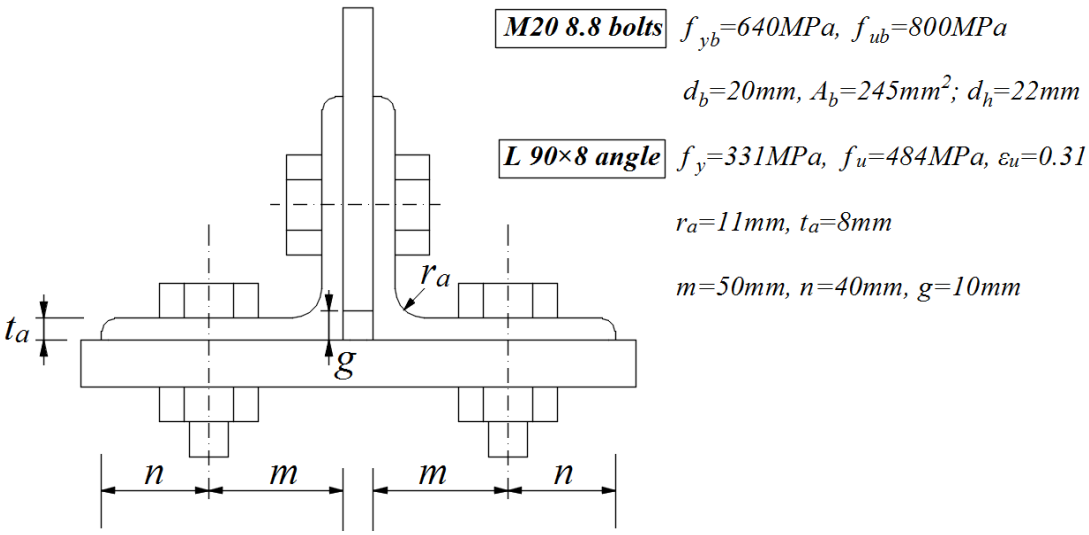

Figure 5.41 The parameters of the bolted double-angle component section

Table 5.5 The calculated properties for the bolted double-angle components

Component property	Results (1 and 3)	Results (2)	Results (4 and 5)
Frictional force limit (F_s)	16.0 kN	16.0 kN	16.0 kN
Initial stiffness (K_i)	57.4 kN/mm	49.2 kN/mm	65.6 kN/mm
Gauge length (m_a)	28.8 mm	28.8 mm	28.8 mm
Angle-bolt strength ratio (η)	0.08	0.08	0.08
Plastic hinges distance (m^*)	33.7 mm	33.7 mm	33.7 mm
Angle yielding strength (F_T)	51.5 kN	44.1 kN	58.8 kN
Angle yielding deformation (δ_m)	4.7 mm	4.7 mm	4.7 mm
Ultimate deformation (δ_u)	24.3 mm	24.3 mm	24.3 mm
Ultimate load (F_u)	178.7 kN	144.8 kN	212.4 kN
Load limit due to bolt fracture (F_u')	213 kN	213 kN	213 kN

5.4.4 Analytical results and discussion

The effective elastic beam length, measured from the vertical bolt-row centre line to the pin-support end, is calculated as 2327 – 50 = 2277 mm. Consequently, the steel beam has an axial stiffness of EA/L = 205 MPa × 5130/2277 = 461.8 kN/mm.

The component properties are plotted below. Figure 5.42 represents the constitutive properties of components 1to 3 in the web angle connection. Figure 5.43 shows the constitutive properties of components 4 and 5, for the top and seated angle connections, respectively.

As can be seen from the curves, the frictional slipping stages under tension and compression are symmetrical. For the compressive behaviour, the stiffness is very large. As has been discussed before, the solution step size will need be greatly reduced to achieve a desirable result.

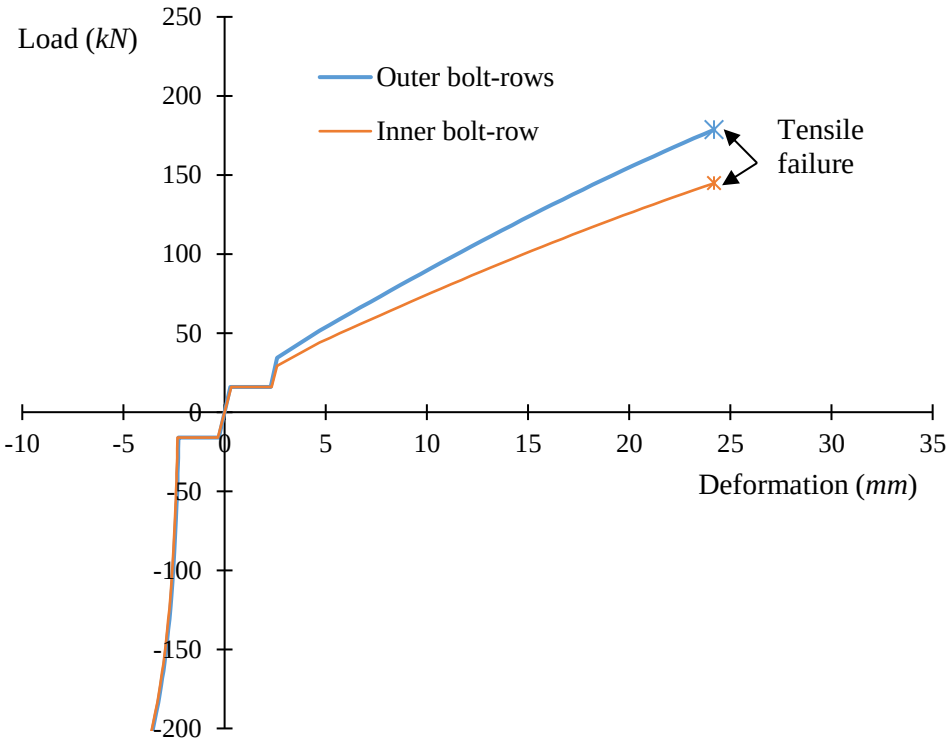

Figure 5.42 The calculated behaviour of the components in the web angle connection

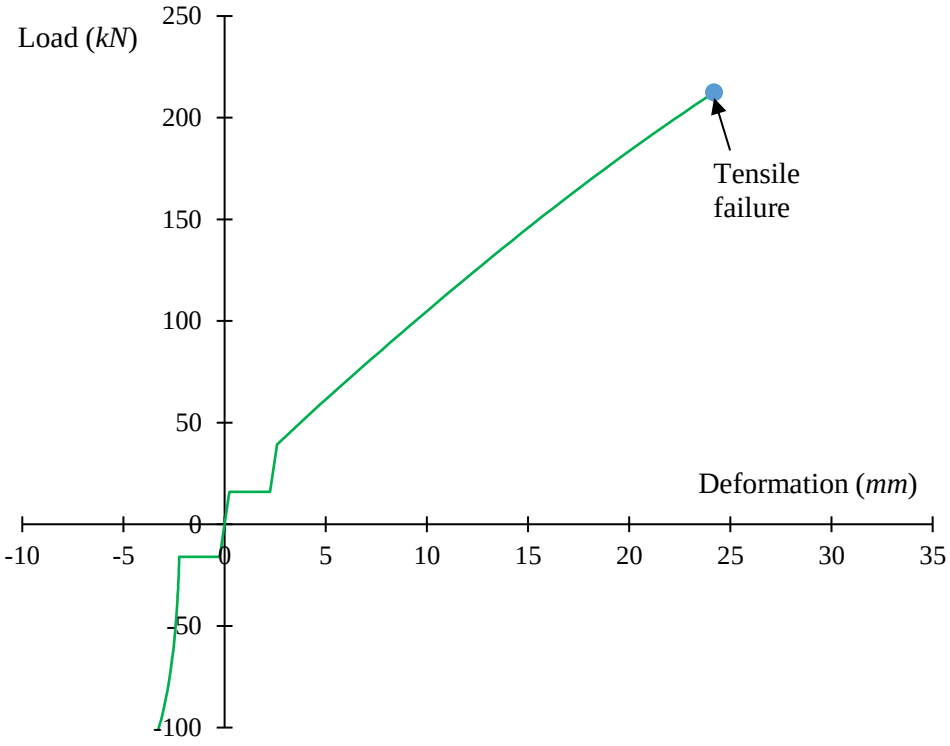

Figure 5.43 The calculated behaviour of the equivalent components of the top/seat angle connection

Using the programmed analytical framework, the full resistance function for the double-beam assembly with web cleat connections is obtained as plotted in Figure 5.44. The test results are also shown for comparison. As can be seen, the ultimate load resistance and deformation limit predicted by the analytical framework are generally in good agreement with the test results.

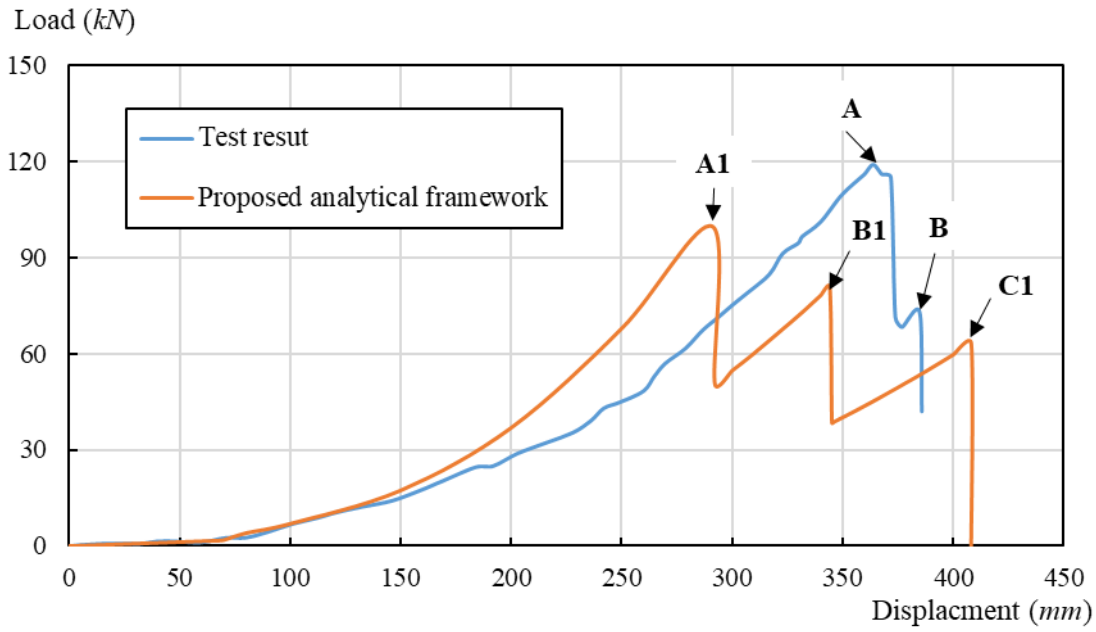

Figure 5.44 The analytical solution of the assembly with web cleat connection

The sequential failure of the three components and the associated effects on the resistance function have been successfully predicted. The failures occur at points A1, B1 and C1, as shown in Figure 5.44. It is clear that there are notable discrepancies between the predicted failure points and the experimentally obtained points (A and B). This can be explained by the inherent difference between the component model and the realistic structure. In the component model, the three springs are separated and parallel with each other. They will fail one by one, from the bottom to the top. However, in the realistic connection, the three bolt-rows with angle parts work more collectively during the whole loading response. As has been observed in the experimental test (Table 5.3), the web angle fracture propagation is in a progressive manner, making the tested curve smoother, up to the final failure.

Despite of the above differences between the predicted failure points and the tested ones, the analytical framework works generally well for the double-beam assembly featuring the web cleat connections.

As the component forces under each deflection level are available from the solution, the load resistance contributed by the bending moment and axial force are calculated and plotted against the deflection in Figure 5.45.

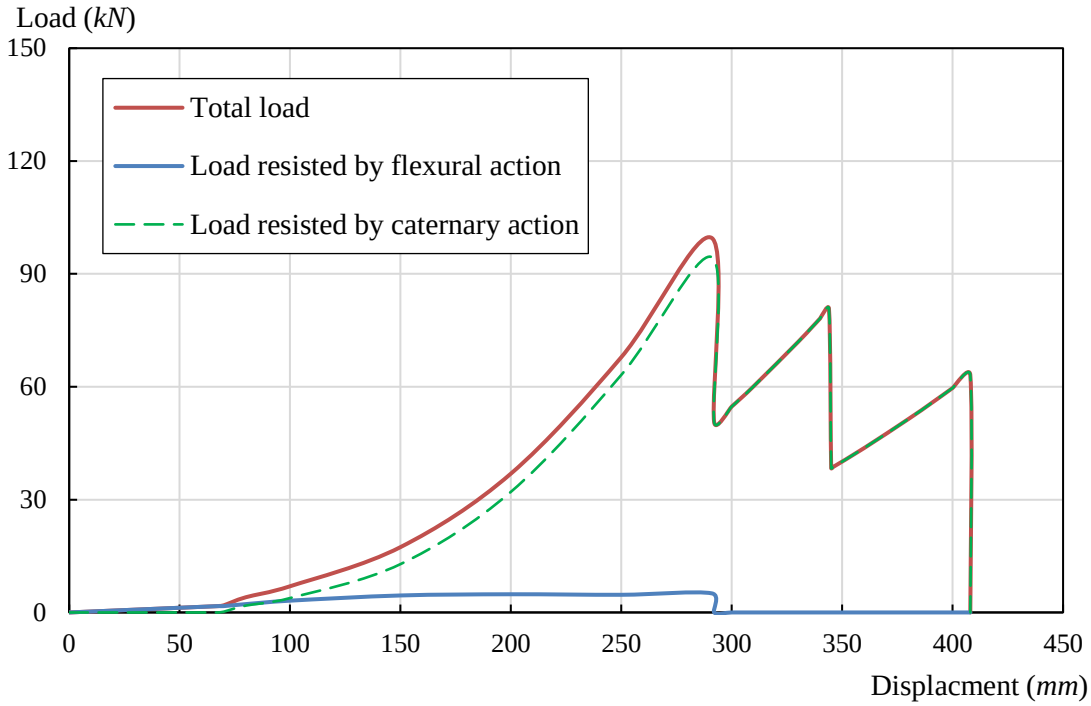

Figure 5.45 The analytical solution of loads resisted by flexural and catenary actions in the beam assembly with web cleat connection

It is apparent that for the double-beam assembly with web cleat connection, the majority of the vertical load resistance is contributed by the axial force. Before the first component failure, the flexural action has a constant and limited participation in the vertical load resistance. After the bottom component fails, the vertical load is solely resisted by the catenary axial force. The predicted characteristics are in line with the test observations.

With regard to the double beam assembly featuring TSWA connection, the analytical solution of the resistance function is obtained and plotted in Figure 5.46. The corresponding test result is also shown in the same graph for comparison.

As can be clearly seen, the peak load resistance has been generally well predicted by the proposed analytical framework. However, the calculated ultimate deformation limit (point E1) is far larger than the experimentally obtained deformation limit (point D). This is because in the real test, the pushdown loading process was terminated at point D where the web angle connections had completely failed.

Actually, the top angle connections were still holding the assembly, as shown in the test photo (Figure 5.35). The loading did not continue for a reason not mentioned by the authors, but actually the top angle connections could have still sustained the development of vertical deflection, as reflected by the analytical solutions (D1-E1).

Another important note is that only one side or half of middle joint is modelled and analysed in the analytical solution, assuming the connection on the other side has exactly the same response due to the symmetry. However, perfect symmetry is not possible in the realistic assembly, due to either manufacturing process or the materials themselves. Therefore, it was observed in the test that the seated angles on the two joint sides failed at different points (points A and B). While in the analytical solution, the two seated angles are assumed to fail simultaneously (point A1). Such differences are understandable and could be interpreted in an explicit way. Hence, it would not affect the validity of the analytical solution.

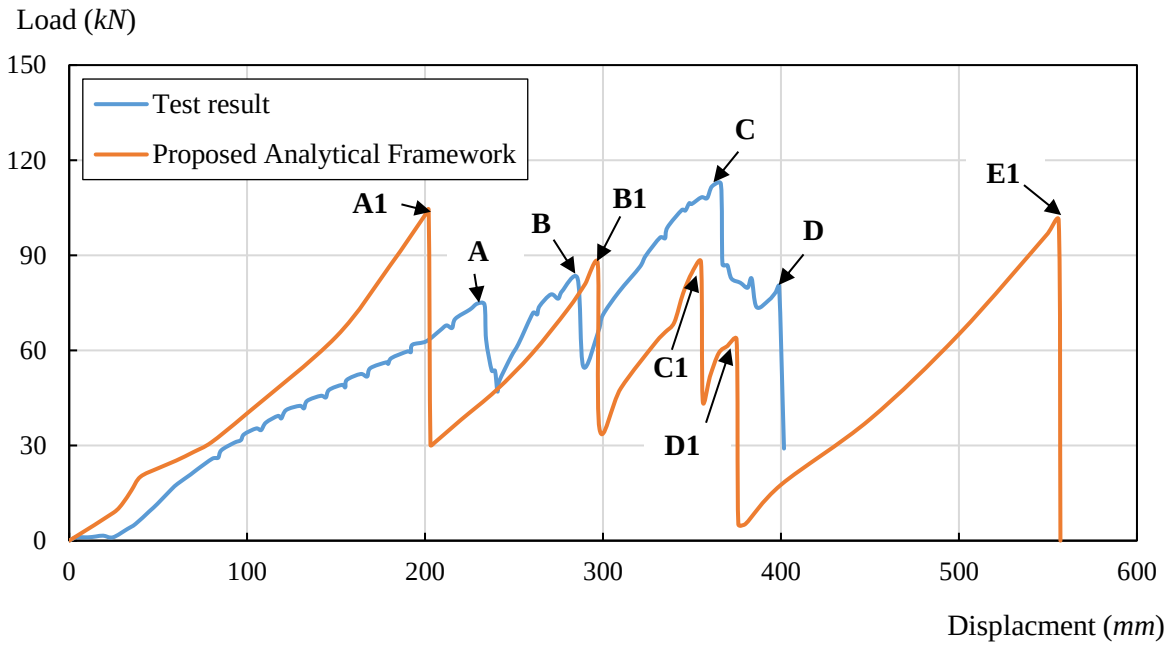

Figure 5.46 The analytical solution of the assembly with TSWA connection

The load resistances contributed by the bending moment and axial force are calculated and plotted against the deflection as shown in Figure 5.47. Likewise, after the bottom component in the web angle connection failed, the vertical load was

essentially wholly resisted by the catenary axial force. This is also in line with the experimental observation.

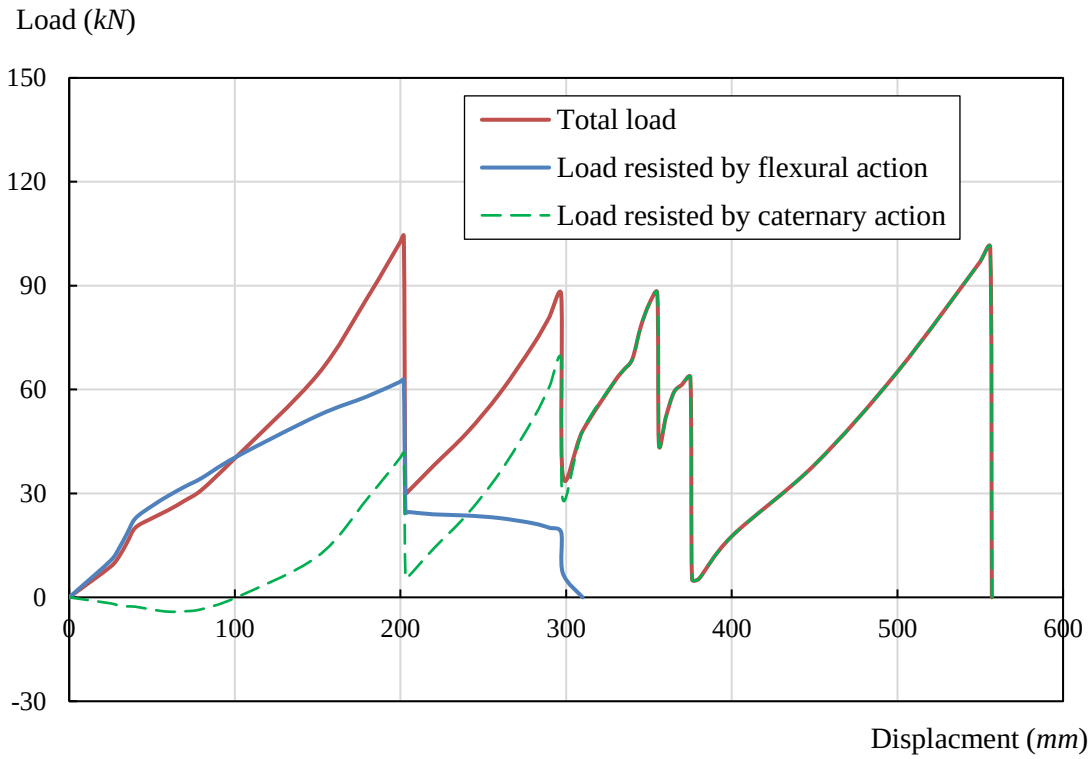

Figure 5.47 The analytical solution of loads resisted by flexural and catenary action in the beam assembly with TSWA connection

To conclude, the analytical solutions for the double-beam assembly including typical web cleat connections and TSWA connections are in generally good agreement with the test results, especially in terms of the peak load resistance and ultimate deformation limits. This indicate that the proposed analytical framework is effective for the analysis of the beam assemblies and the generation of the resistance functions. The results also indicate that the current formulations of bolted double-angle component is suitable for the application in the component-based modelling analysis; nevertheless further improvement in the accuracy of the component deformation limits will be beneficial.

5.5 Summary

In this chapter, a simplified and explicit analytical framework has been developed to predict the full-range load-deflection characteristics of a double-span beam assembly with typical steel joints. The analytical solution procedure is carried out on the basis of the constitutive component models, and satisfies the force equilibrium and deformation compatibility conditions.

The proposed analytical framework provides an effective and executable approach for establishing the full-range resistance function of a double-span beam assembly under internal column loss. The solution process also enables further interpretation of results, in terms of the contributions of the flexural action and catenary axial force to the vertical load resistance.

The analytical framework has been verified on the beam assembles with web cleat connections and TSWA connections using experimental data from the literature. The existing models for the bolted double-angle component are examined and employed to establish the constitutive properties of the discretised components. The analytical results show good agreement with the test results, especially in terms of the peak load resistance and ultimate deformation limits. The scope for further improvement in terms of the predicted failure points and the reasons at the joint component level is discussed.

The outcome of this chapter will lay a foundation and platform for future analysis of the behaviour of the steel joints and the overall response of the beam-assembly substructures in a progressive collapse scenario. Additional features of the components, representing the reinforced concrete flanges (slab), profiled steel decking and fillet/butt welds, can be readily integrated into the component model and analysed using the proposed solution framework.

With the availability of the analytical solution, the key to the reliability and soundness in the analysis of the resistance function lies upon the adequacy and accuracy of the description of the joint components. Although a range of the joint components is generally available from the literature, some are still not properly formulated. One of such examples is with a fin-plate joint. The next chapter will discuss the formulation and implementation of components for beam assemblies involving fin-plate joints.

6 Analytical modelling of fin-plate connection for the resistance function evaluation of double beam assembly in a progressive collapse scenario

6.1 Introduction

The previous chapter has proposed an analytical solution framework for the calculation of the resistance function of steel beam assemblies using component-based joint models. The complete analysis is implemented using a numerical procedure. Using this procedure, representative beam assemblies with joints involving typical connection components have been analysed to demonstrate the ability and limitation of the existing methods for the establishment of property parameters of these components.

This chapter focuses on the component-based modelling of fin-plate connections in a double beam assembly subjected to central column loss. As mentioned in Chapter 5, the constitutive parameters for defining a fin-plate component are less well developed.

Thus the primary objectives are to:

1) Provide an overview of the fin-plate connection failure modes and the associated influence factors;
2) Formulate the basic force-displacement relationship of the bolted lap-plate component;
3) Incorporate the formulated component properties into the analytical framework, provide solutions of resistance functions, and predict key failure events;
4) Compare the results with the available experimental test data, and identify any discrepancies and needs for modification of the basic component properties;
5) Modify the formulation for the bolted lap-plate component, by employing the finite element analysis, and examine the improvement of the modifications by comparing again to the experimental test.

The development presented in this chapter allows for a complete analytical evaluation of the resistance functions of beam assemblies involving fin-plate connections. The fin-plate component model also enables the analysis for beam connections using fin-plate in combination with other components.

6.1.1 Overview of fin-plate connections

Fin-plate connection (Figure 6.1) is the most widely used beam-column joints in gravity-designed (i.e. non-seismic) frame structures. In a fin-plate connection, a rectangular fin-plate (also termed as "shear tab" in design practice) with pre-drilled bolt-holes is welded to the column flange using complete-joint-penetration (CJP) groove welds. At the construction site, beams are connected to the fin plate simply by installing the bolts. Therefore, this connection type is very economical to manufacture. More importantly, they are the quickest to erect on site, as they do not have the problem of shared bolts in two-sided connections.

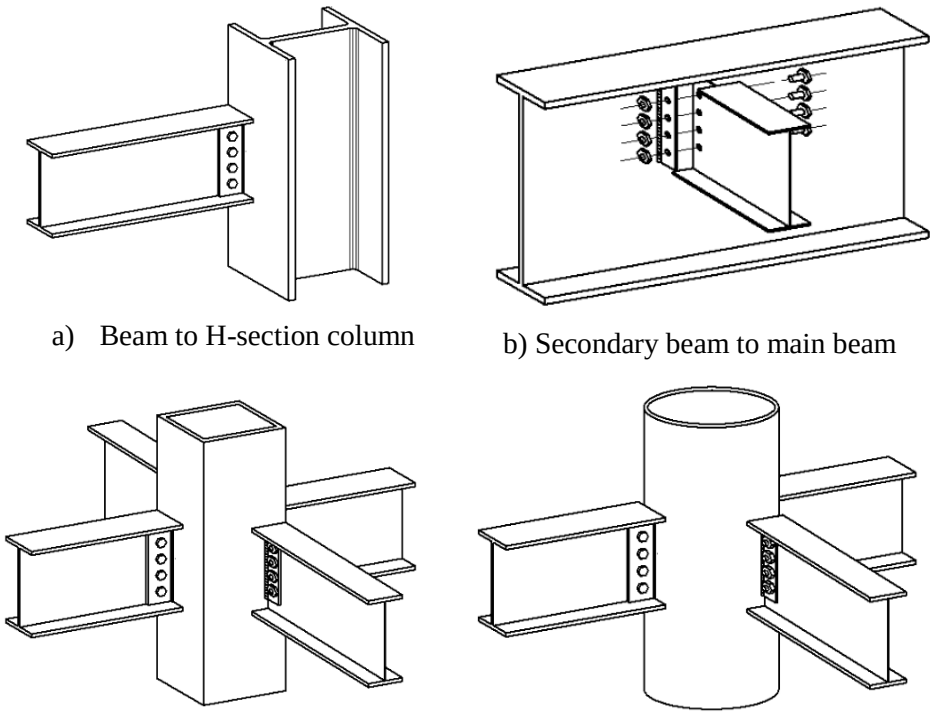

a) Beam to H-section column

b) Secondary beam to main beam

c) Beam to rectangular column

d) Beam to circular column

Figure 6.1 Fin-plate connections used in various scenarios (www.steelconstruction.info)

Similar connection can be seen in beam-to-beam connections, as shown in the experimental specimen featuring the connections between the beam and the outer-diaphragm of a tubular column (Li et al. 2013). As shown in Figure 6.2, a lap-plate was bolted to the two beam webs in the connection area. It is not a fin-plate connection, but the loading conditions and mechanisms in the web connection are quite similar.

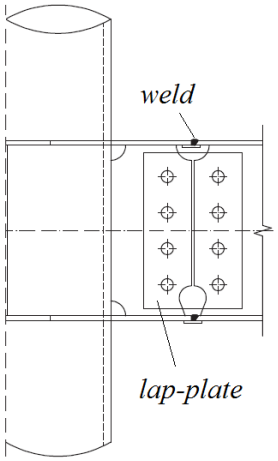

Figure 6.2 Bolted lap-plate connection in beam-tubular column connection (Li et al. 2013)

Figure 6.3 schematically illustrates the geometric configurations and key parameters which will potentially govern the connection performance and failure modes.

1) Edge distance (e): The edge distance should be sufficient so that the plate section is not excessively weakened, and the net section failure can be avoided.
2) End distance (L_e): This is important as it determines the behaviour of the bearing region and possible failure modes. It will be discussed later in detail.

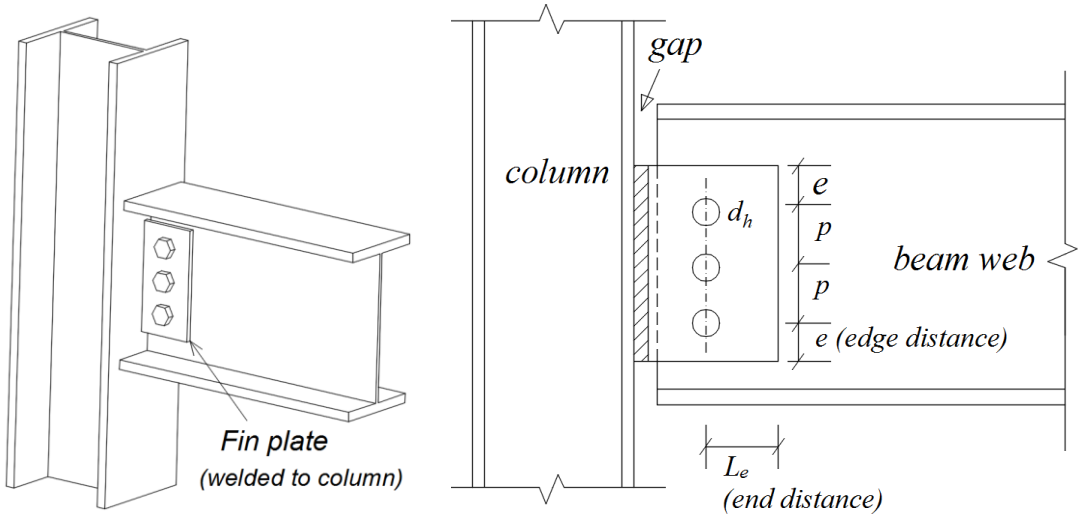

Figure 6.3 Configurations of a typical fin-plate connection

As shown in Figure 6.3, in design practice, there is usually a gap between beam flange and column flange. It is prescribed to avoid hard contact and large prying force, which may expedite the failure process.

For the above parameters, the minimum design requirements of the parameters in Eurocode and Chinese code are summarized in Table 6.1, in which d_h is the bolt-hole diameter. Eurocode apparently has lower limits for the bolt layout on the fin-plate.

Table 6.1 Summary of design requirements in different codes

		Minimum distance (Eurocode 1993, part 1-8)	Minimum distance (GB 50017-2003)
Edge distance	e	$1.2d_h$	$1.5d_h$
End distance	L_e	$1.2d_h$	$2.0d_h$
Spacing	p	$2.4d_h$	$3.0d_h$

The clearance holes are pre-drilled in the fin plate and beam web, for the ease of installation. According to Konkong and Phuvoravan (2017), the clearance bolt-hole sizes are listed in Table 6.2.

Table 6.2 Bolt-hole sizes with different bolt diameters

Bolt diameter, d_b (mm)	Hole diameter, d_h (mm)
$d_b \leq 12.7$	$d_h = d_b + 0.8$
$d_b \geq 12.7$	$d_h = d_b + 1.6$

6.1.2 Experimental observations of beam-assembly with a fin-plate connection under column loss scenario

Weigand and Berman (2014) experimentally evaluated the resistance of steel subassemblies with fin-plate connections subjected to the interior column removal. The connection assembly specimen shown in Figure 6.4 was subjected to axial extension force and shear force in a displacement-controlled manner. For the tested subassemblies, failure typically originated because of a bolt fracture or the plate tear-out of the horizontal end distances.

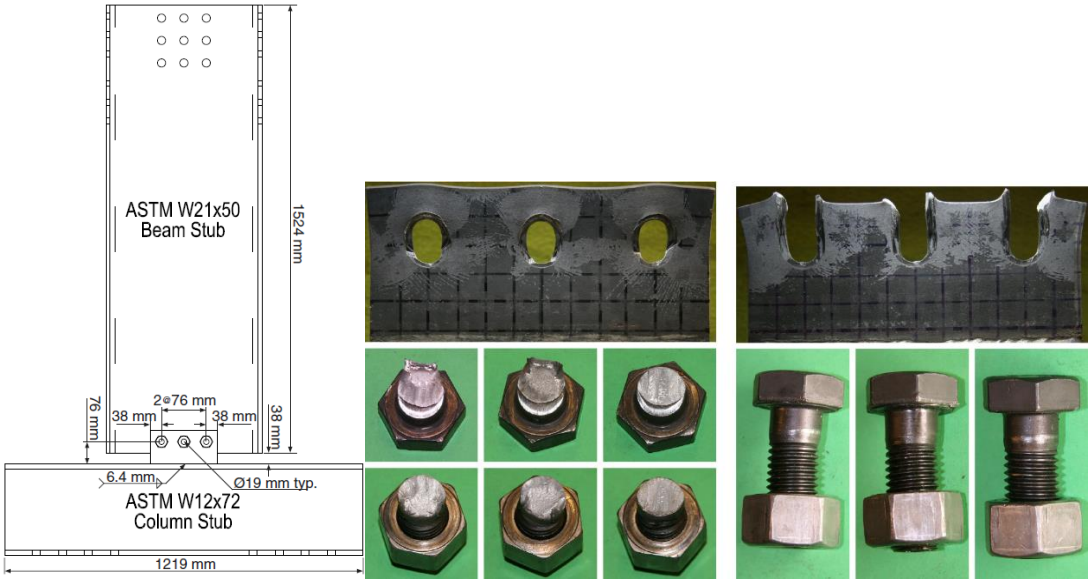

Figure 6.4 Test observations of two different failure modes: bolt shearing and plate bearing tearout (Weigand and Berman 2014)

For most of the specimens, bolt shear fracture controlled the ultimate failure. When the bolt fracture occurred, significant bearing deformations were also observed at the bolt-holes in both the beam web and fin plate. As can be seen from Figure 6.5, the global resistance exhibited a significant drop when the first bolt row failed (end of stage III), either by bolt fracture or plate tearout. The beam assembly continued to deform at a reduced load, until the outermost intact bolt row developed the largest deformation and failed next. With further deformation, the other bolt rows failed in sequence until the substructures finally collapsed.

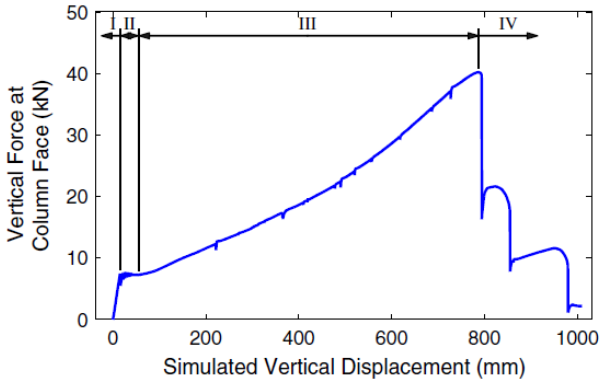

Figure 6.5 Typical resistance function from test (Weigand and Berman 2014)

In the experimental tests by Yang and Tan (2013), a beam assembly involving two-side fin-plate connections was tested. It was found that the bolt fracture controlled the ultimate failure, and the effects on the global resistance function was similar to that described above. This experimental case will be used later in Section 6.4 as an example to investigate the component behaviour functions. Therefore, the details will be accordingly given later in Section 6.4.

6.2 Component modelling of the fin-plate connection: basic considerations

Following the proposed framework of modelling the beam-column joint with spring components in Chapter 5, a component-based model for a 3 bolt-row fin-plate connection is depicted by Figure 6.6.

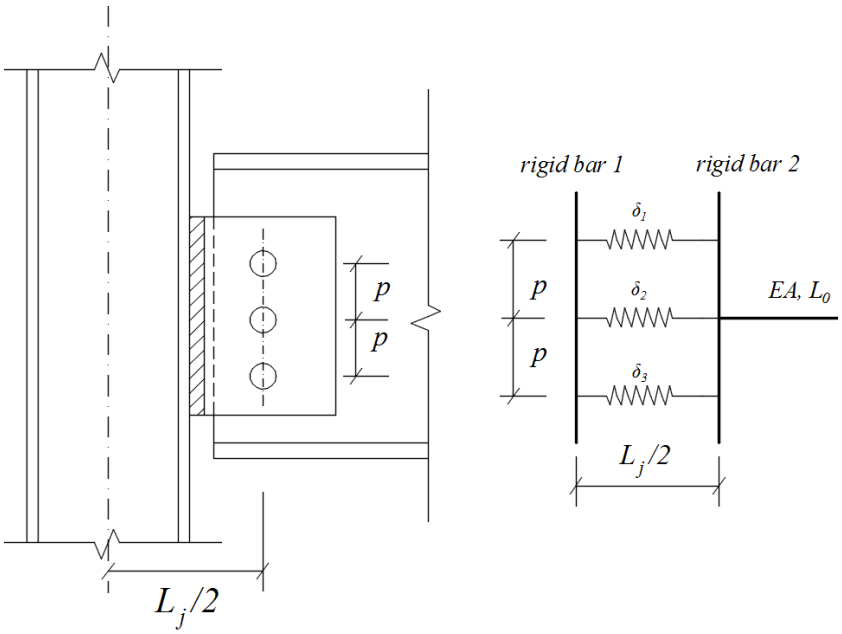

Figure 6.6 The component spring model for the fin-plate connection

For each bolted lap-plate component, i.e. each macro spring shown in Figure 6.6, it usually needs to be further divided into a group of constituient sub-components. Figure 6.7 illustrates an example of the breakdown for the bolted lap-plate component (Taib and Burgess 2013). However, it suffers a critical shortcoming that the solution of such a non-aligned model could only be be achieved by utilizing the finite element analysis.

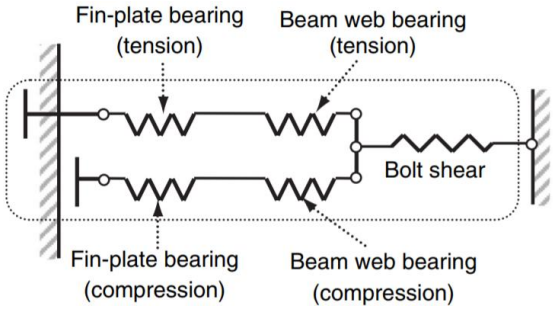

Figure 6.7 Component model of a bolt row in the fin-plate connection (Taib and Burgess 2013)

6.2.1 Basic considerations of the bolted lap-plate component

Figure 6.8 shows a representative bolted lap-plate component. As has been discussed in Chapter 5 about the component-based analytical modelling, the deformation in the column panel is negligible, especially during the large deflection regime. Therefore,

the fin-plate connection can be discretized as a group of bolted lap-plate components, as has been shown in Figure 6.6.

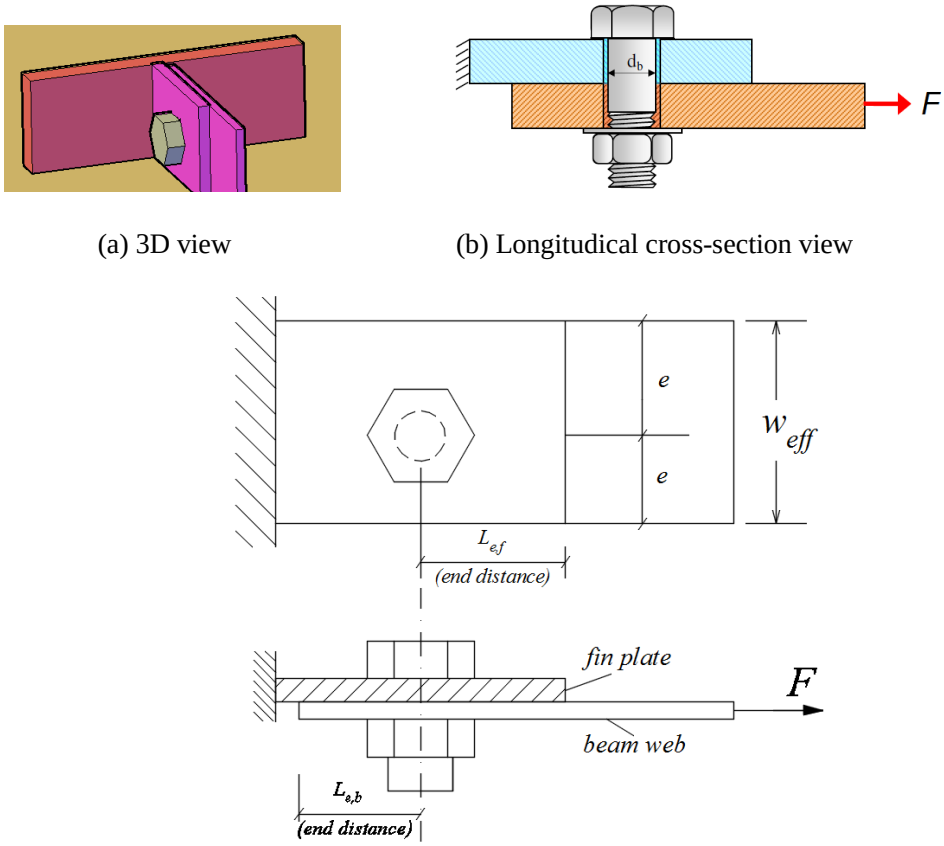

(a) 3D view (b) Longitudical cross-section view

(c) Key defining parameters

Figure 6.8 A discretised bolted lap-plate component for the fin-plate connection

An individual bolted lap-plate component is featured by a bolt connecting an effective width of the fin plate and the beam web. Each bolted lap-plate component is modelled by a spring with a force-displacement constitutive relationship.

As is shown in Figure 6.9, the component spring groups are connected by two rigid bars on the boundaries. The original distance between the rigid bar 1 and bar 2 is equal to the distance from the column centre line to the bolt row centre line. In particular, the rigid bar 1 is not allowed to rotate, due to the symmetry. It can only move in the vertical direction. The rigid bar 2 can have both rotation and horizontal displacement.

In this chapter, a new integrated component model is proposed for the bolted lap-plate component. It follows the convential component concept but with a simplified

form to allow for a complete analytical solution for a beam assembly with a fin-plate connection. As is shown in Figure 6.9, each component further consists of four basic sub-components in a serial arrangement. The rigid bars 1 and 2 represent the boundary of the joint deformation zone. The sub-components and the associated deformations are:

1) Fin plate in bearing ($\delta_{b,f}$);
2) Beam web in bearing ($\delta_{b,w}$);
3) Bolt in shear (δ_v);
4) Frictional slip (δ_s).

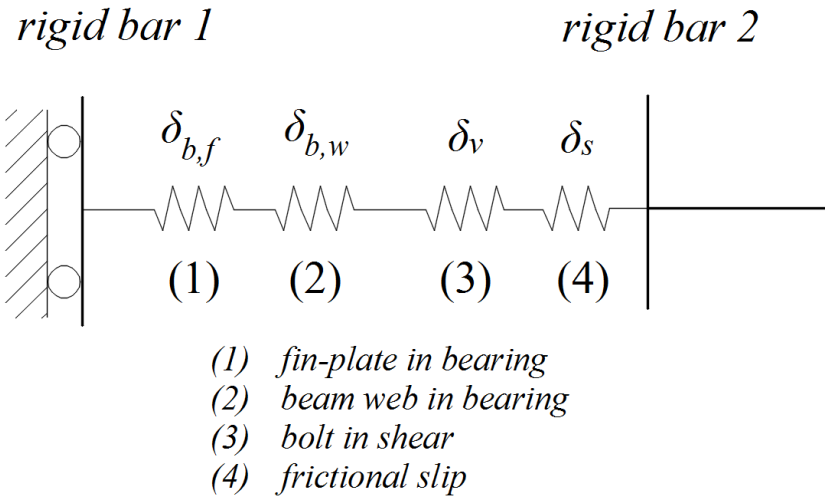

Figure 6.9 The sub-components of the bolted lap-plate component

Among the sub-components, the frictional slip (δ_s) deformation can be set as a constant value, which is equal to the geometrical displacement before the full bearing contact takes place, thus:

$$\delta_s = d_h - d_b \tag{6-1}$$

where d_h is the bolt-hole diameter and d_b is the bolt diameter.

The total deformation of the bolted lap-plate component (δ_j) is the sum of the four independent component deformations.

Therefore, to establish the integrated force-deformation relationship of the component, it is necessary to formulate the deformations of all sub-components under the same loading level.

6.2.2 Failure modes of the bolted lap-plate component

In the formulation of the above integrated force-deformation relationship for the component, it is also necessary to identify the governing component failure mode. Generally speaking, two failure modes may be involved, namely the bolt shearing fracture and the plate tear-out failure, and these have been clearly observed in existing experiments. A global tension failure of the plate may be excluded, provided that the relevant code requirements to avoid plate tension failure is satisfied.

For the plate in bearing, the major influence factor is the end distance (L_e), see Figure 6.8. If the bolt is located too close to the plate edge, and the bolt itself is strong enough, the tear-out failure of the bearing plate is very likely to occur. This phenomenon has been observed in the previous experimental tests (Li et al. 2015), numerical simulations (Sadek et al. 2008), and the experimental tests presented in Chapter 4. Keeping the bolt at a sufficient distance away from the plate edge can avoid the undesirable tear-out failure. With increase of the load capacity, large bearing deformation of in the bearing region will be induced.

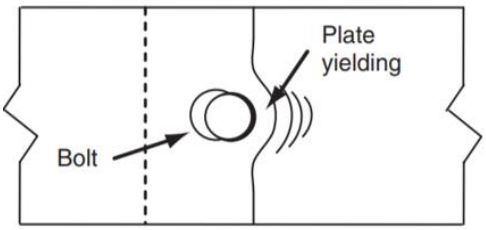

Figure 6.10 Bearing deformations against the bolt

Clearly the relative strength between the plate in bearing and the bolt in shear will determine the eventual failure mode. If the bolt shearing capacity is lower than the ultimate plate tear-out capacity, the bolt will fail first, as is shown in Figure 6.11.

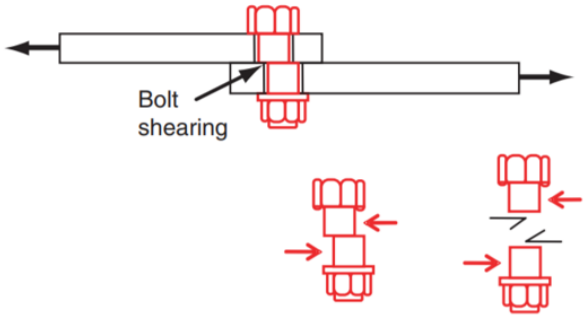

Figure 6.11 The bolt in shearing

6.3 Formulation of the bolted lap-plate component constitutive behaviour

This section presents detailed formulation for the bolted lap-plate component to establish its complete force-displacement relationship in tension, including the ultimate deformation and failure mode. The behaviour of the component under compression is assumed to be the same as that in tension, as has been assumed in other studies by Yu et al. (2009), Taib and Burgess (2013), and Liu et al. (2015).

The existing formulations for the stiffness and loading capacity of the two dominant failure modes are firstly reviewed and summarized. The method to integrate them to achieve a unified component set function is presented. In addition, the ultimate deformation limits are discussed and defined.

6.3.1 The plate in bearing against the bolt shank

The plate bearing deformation is a result of concentrated in-plane deformation around the bolt-hole. After slip has occurred in the bolt connection, the bolt will be in bearing against the side of the hole. In general, considerable plastic deformation of the bearing plate in front of the bolt could be expected. The ultimate state could be due to the occurrence of bolt tear-out through the material. Therefore, aside from the tensile failure of the net section and the bolt shear fracture, the bearing failure or tear-out is also a critical limit state, which needs to be quantified.

a) Bearing capacity

The bolt bearing strength has been extensively investigated in the past, and formulations have been proposed and some are adopted in design guidance. These formulations mostly concern the ultimate load capacity based on a tear-out failure mode. Below a brief review of the existing formulations is presented first.

Generally, the bearing stress is developed in the plate material adjacent to the bolt hole. Initially, this stress is concentrated at the point of contact. An increase in load causes yielding and the embedment of the bolt on a larger contact area, and this results in a more uniform stress distribution. When the bolt shank is in full contact with the bolt hole, the average stress can be expressed as Equation (6-2), in which d_b denotes the nominal bolt diameter, and *t* the plate thickness:

$$f_b = \frac{F_b}{d_b t} \tag{6-2}$$

Assuming that the edge distance is sufficient to avoid the failure of the critical net section, the actual failure mode in bearing depends on such geometrical factors as the end distance, the bolt diameter, and the plate thickness. The bolt tears out through the plate due to insufficient end distance, or excessive deformation is developed in the material adjacent to the bolt hole.

Fisher and Struik (1974) originally proposed a simple and useful failure model for the evaluation of the maximum bearing load capacity. The tearout is considered to be a result of the shear failure of the material along specific shear planes.

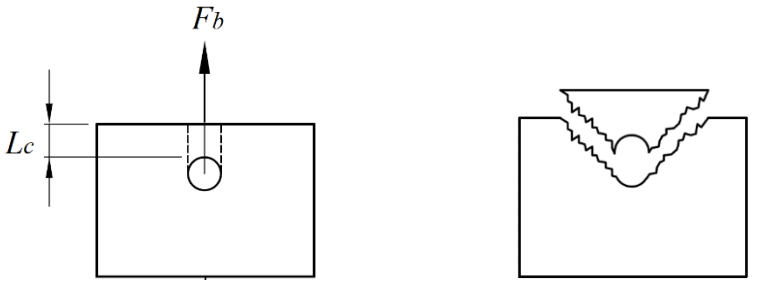

(a) Straight shear planes (b) Diagonal shear planes

Figure 6.12 The shear planes of the potential tearout failure.

According to this model, a lower bound of bearing capacity can be expressed as the shearing resistance developed along the dashed lines shown in Figure 6.12:

$$F_b = 2 \cdot L_c t \cdot \tau_u \tag{6-3}$$

where τ_u is the shear strength of the plate material. For most commonly used steels, it is about 70% of the tensile strength f_u. L_c is the clear distance from the bolt-hole edge to the bearing plate edge, and L_e is the distance from the bolt centre to the plate edge. Therefore, Equation (6-3) can be transformed into:

$$F_b = 2 \cdot L_c t \cdot (0.7 f_u) = 1.4 f_u (L_e - \frac{d_b}{2}) t \leq 3.0 f_u d_b t \tag{6-4}$$

An upper bearing stress limit of $3.0f_u$ (Fisher and Struik 1974) is applied to the tearout capacity, in order to limit the bolt-hole deformation.

The AISC specification (LFRD 1993) adopted the same model by Fisher and Struik (1974), but recommended a simpler formulation for the plate bearing capacity, based on the shear strength of the two straight shear planes as shown in Figure 6.12.

$$F_b = f_u L_e t \ \leq 2.4 f_u d_b t \tag{6-5}$$

The reduced upper limit was adopted to limit the bearing deformations. The specification also states that an upper bearing stress limit of $3.0f_u$ can be used instead for situations where excessive bolt-hole deformation is not a concern.

The updated AISC specification (LFRD 1999) has recommended a similar but relatively conservative estimation of the bearing capacity, which is 14% lower than the original prediction suggested by Fisher and Struik (1974). The formulation is expressed as:

$$F_b = 2 \cdot L_c t \cdot (0.6 f_u) = 1.2 f_u (L_e / d_b - 0.5) d_b t \tag{6-6}$$

Eurocode 3 (1993) has suggested the Equation (6-7) to evaluate the bearing capacity of the plate. The two coefficients are dependent on the multiple key parameters mentioned before.

$$\begin{gathered} F_b = \alpha_b k_1 f_u d_b t \leq 2.5 f_u d_b t \\ \alpha_b = \min(\frac{L_e}{3 d_h};\ \frac{f_{ub}}{f_u};\ 1) \\ k_1 = \min(2.8 \frac{w_e}{d_h} - 1.7;\ 2.5) \end{gathered} \tag{6-7}$$

Assuming that the bolt steel tensile strength is greater than the plate steel tensile strength ($f_{ub} \geq f_u$), and that the edge distance (w_e) is large enough, the above equations can be simplified and rewritten as:

$$F_b = \frac{2.5}{3} \cdot \frac{L_e}{d_h} f_u d_b t \leq 2.5 f_u d_b t \tag{6-8}$$

It is also worth noting that providing a tightening force in the bolt leads to an increase in the ultimate bearing resistance. This is because the load is partially transmitted by the frictional resistance on the faying surfaces. For simplicity the pre-tightening force is not considered in this Chapter.

Various formulations for the bolt bearing strength reviewed above are listed in Table 6.3.

Table 6.3 Representative bearing capacity formulations

Reference source	Proposed formulation
Fisher and Struik (1974)	$F_b = 1.4 f_u \left(\frac{L_e}{d_b} - 0.5\right) d_b t_p \leq 3.0 f_u d_b t_p$
AISC Specification (LRFD 1993)	$F_b = f_u L_e t_p \leq 2.4 f_u d_b t_p$
AISC Specification (LRFD 1999)	$F_b = 1.2 f_u (L_e/d_b - 0.5) d_b t_p \leq 2.4 f_u d_b t_p$
Eurocode 3 (2005)	$F_b = \alpha_b k_1 f_u d_b t_p \leq 2.5 f_u d_b t_p$ For edge bolts: $\alpha_b = min(\frac{L_e}{3d_h};\ \frac{f_{ub}}{f_u};\ 1);\ k_1 = min(2.8\frac{w_e}{d_h} - 1.7;\ 2.5)$
AISC 360-10 (2010)	$F_b = 1.5 f_u (L_e/d_b - 0.5) d_b t_p \leq 3.0 f_u d_b t_p$ if bolt hole deformation is not a design consideration; $F_b = 1.2 f_u (L_e/d_b - 0.5) d_b t_p \leq 2.4 f_u d_b t_p$ if excessive deformation of the connection is limited.
Wang et al. (2007)	$F_b = (1.039 L_e/d_b + 0.183) f_u d_b t_p$

Noteworthy is that the bearing capacity here is independent on the effective width of the component. This implies an underlying assumption that the effective plate width, or the bolt edge distance, is sufficiently large to eliminate the possibility of net section failure.

Rex and Easterling (2003) carried out a series of experimental tests on a single bolt bearing against a single plate, and showed that the formulation recommended by ASIC specification (LFRD 1993) best fits the test results. Therefore, this formulation will be employed in the analysis model in this study.

b) Bearing stiffness

In order to establish the bearing force-deformation (*F-δ)* curve for the bolted lap-plate component, the bearing stiffness in the initial loading stage is another critical parameter to be quantified.

Rex and Easterling (2003) proposed a simplified method to determine the bearing stiffness in the initial bearing stage. In this model, two assumptions were made to simplify the problem into a basic problem of geometry.

1) The problem is assumed to be two-dimensional;
2) The plate steel in the overlapping area with the bolt is assumed to be at the yielding stress f_y of the plate material.

Under these two assumptions, for a given displacement the bearing force can be estimated by

$$F_b = f_y \cdot w_b \cdot t_p \tag{6-9}$$

where w_b denotes the effective bearing width, and t_p is the plate thickness.

The geometrical model is shown in the following figure, where R_1 and R_2 are the radii of the bolt and hole, respectively.

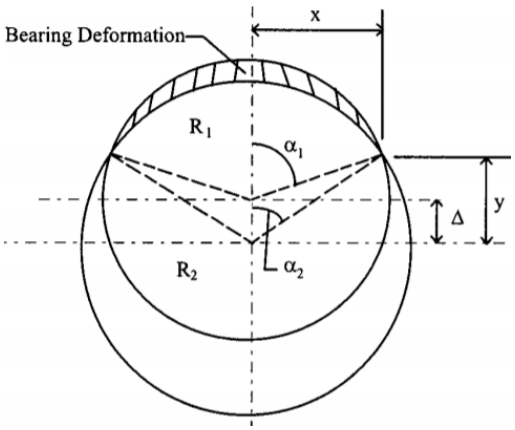

Figure 6.13 Bearing stiffness model (Rex and Easterling 2003)

According to the law of cosines, the following relationships are obtained:

$$cos(\alpha_2) = (\Delta^2 + R_2^2 - R_1^2)/(2R_2\Delta)$$
$$cos(\alpha_1) = -(\Delta^2 + R_1^2 - R_2^2)/(2R_1\Delta) \quad (6\text{-}10)$$

Hence the effective bearing width, which is perpendicular to the bearing load direction, can be calculated as:

$$w_b = 2x = 2R_2 \cdot sin(\alpha_2) \quad (6\text{-}11)$$

Regarding bearing deformation, there are two ways to quantify it. The first one is to directly use the bolt bearing depth into the plate along the bearing load direction. It can be simply put as:

$$\delta_b = \Delta - (R_2 - R_1) \quad (6\text{-}12)$$

The second measure is to evaluate the average nominal deformation along the overall bearing width. It is the total bearing deformed area divided by the bearing width. In the study of Rex and Easterling (2003), they made a further simplification that the total bearing deformed area is equal to the geometric overlapping area between the bolt shank and the plate. Therefore, the resulting average bearing deformation can be obtained as:

$$\delta_b' = A_{lap}/w_b = \frac{\frac{1}{2}\alpha_1 R_1^2 + \frac{1}{2}R_2\Delta\sin(\alpha_2) - \frac{1}{2}\alpha_2 R_2^2}{2R_2 \cdot sin(\alpha_2)} \quad (6\text{-}13)$$

However, this assumption seems to be inappropriate, as the bearing deformed zone tends to expand outside the geometric overlapping area.

Therefore, in the present study the first method of defining the component displacement is used. It also allows a more convenient relationship with the overall deformation of the component set. Hence, the bearing stiffness is calculated to be

$$K_{b,i} = \frac{F_b}{\delta_b} = \frac{f_y t_p \cdot 2R_2 sin(\alpha_2)}{\Delta - (R_2 - R_1)} \tag{6-14}$$

As can be judged from the above equations, the secant bearing stiffness varies with different bearing deformations. Therefore, it is necessary to define a reasonable point to calculate the secant stiffness, which can represent the bearing stiffness in the initial loading stage.

Rex and Easterling (2003) chose δ = 0.102mm (0.004 inch) and standard bolt-hole sizes to calculate the initial bearing stiffness. This choice was based on comparisons between the best fit value of K_i through the initial experimental data and finite element models. In the present study the same choice is adopted.

Using the above defining point and after mathematical derivation, the initial bearing stiffness is suggested to be:

$$K_{br} = 120 f_y t_p (d_b/25.4)^{0.8} \tag{6-15}$$

The above formulation implies that the initial bearing stiffness is only dependent on the bolt diameter, once the plate material and thickness are given. The following figure schematically shows the variation of the calculated secant stiffness at varying bearing deformations, for different common bolt sizes. It can be seen that at the deformation of 0.102 mm, the calculated secant stiffness is becoming steady. In this sense, selecting the secant stiffness at this particular point is reasonable to represent the initial bearing stiffness.

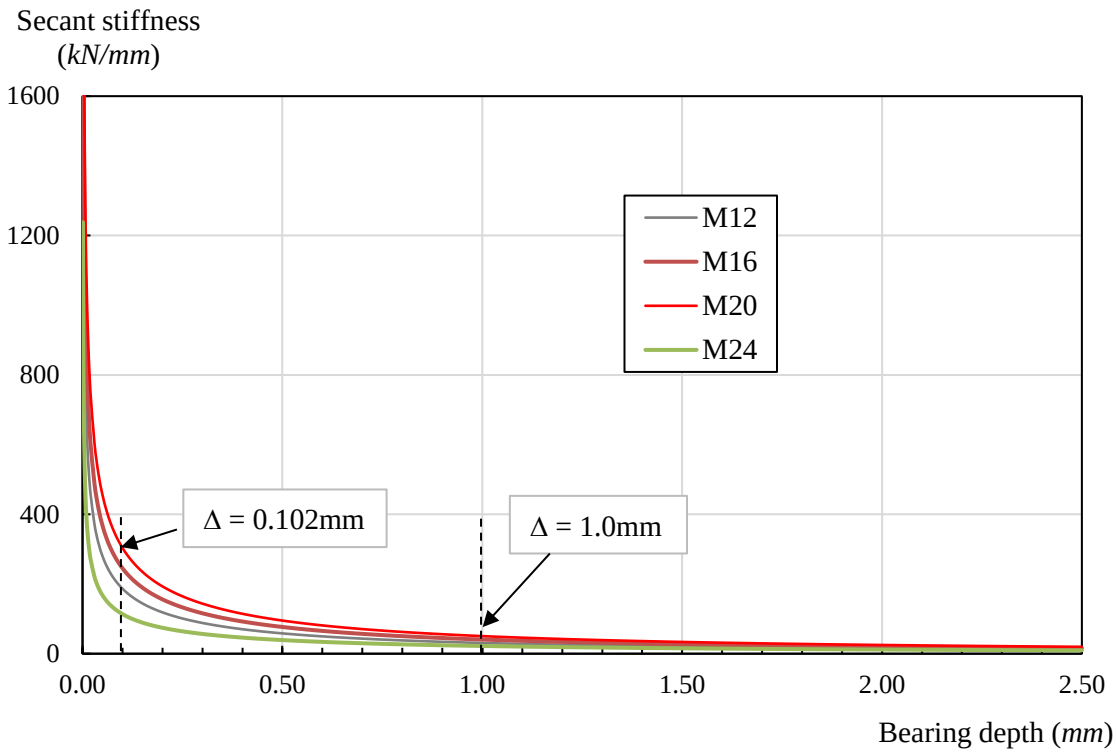

Figure 6.14 The calculated secant bearing stiffness vs. bearing depth (S275, *t* = 8mm plate) for common bolt sizes

c) Establishment of the full bearing force-displacement relationship

So far, there has been very little research on the quantitative formulations for the complete bearing resistance function.

Rex and Easterling (2003) proposed a semi-empirical formulation to describe the relation between normalized bearing force and deformation. It was obtained using statistical regression on the experimental data for single bolt lap-plate components. The function is expressed as:

$$\frac{F}{F_{b,u}} = \frac{1.74\bar{\delta}}{\left(1+\bar{\delta}^{0.5}\right)^2} - 0.009\bar{\delta} \qquad (6\text{-}16)$$

$$\bar{\delta} = K_{e,i}(\delta / F_{b,u})$$

In the function, the bearing capacity $F_{b,u}$ has been discussed in the previous section and the formula recommended by AISC (LFRD 1993) is adopted.

The equivalent stiffness ($K_{e,i}$) is evaluated based on the combination of the bearing, bending and shearing stiffness of the end plate material between the hole edge and the plate edge. By simply assuming the three springs in series, the overall stiffness can be expressed as:

$$K_{e,i} = 1/\left(\frac{1}{K_{br}} + \frac{1}{K_b} + \frac{1}{K_v}\right) \tag{6-17}$$

where K_{br} is the bearing stiffness.

As shown in Figure 6.15, the bending and shearing stiffnesses are derived by assuming a rectangular elastic fixed end beam (grey area) between the bolt and the plate end (Rex and Easterling 2003). They are expressed as:

$$K_b = 32Et_p(L_e/d_b - 0.5)^3$$
$$K_v = 6.67Gt_p(L_e/d_b - 0.5) \tag{6-18}$$

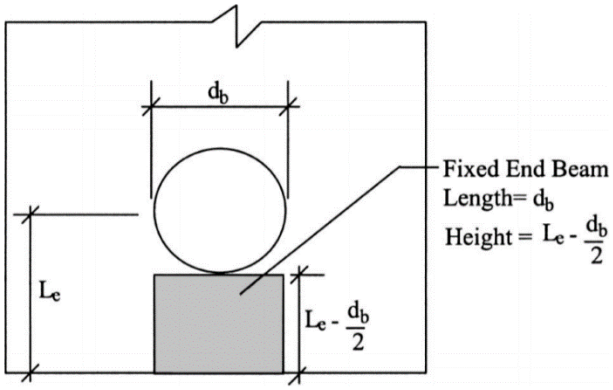

Figure 6.15 The bending and shearing stiffness model

However, as will be shown later the bending and shearing stiffnesses calculated according to the above equations are both much larger than the bearing stiffness. In other words, the bearing stiffness itself dominates the bearing deformation. In this sense, the calculation of combined stiffness may not be necessary.

6.3.2 The bolt shearing deformation and ultimate deformation

The bolt shearing deformation is the second critical parameter in the bolted lap-plate component set. However, there has been very limited research on the quantification of bolt shearing deformation.

Sarraj (2007) made use of curve-fitting on the FE modelling results, based on the standardized Ramberg-Osgood function (Ramberg and Osgood 1943) to obtain an empirical formula as:

$$\delta_v = \frac{F_v}{K_{v,b}} + 2.5\left(\frac{F_v}{F_{v,Rd}}\right)^6 \tag{6-19}$$

where δ_v is the bolt shearing deformation, K_{vb} and F_{vb} are bolt shearing stiffness and resistance, respectively.

As adopted by Sarraj (2007), typically the bolt shear failure is assumed to occur immediately when the shear resistance F_{vb} is reached. However, in the tests conducted by Yu et al. (2009) under elevated temperature, the shear load was observed to decrease gradually after the peak shear resistance was reached. It is not clear whether the bolt shear fracture under ambient temperature will indeed occur in a brittle manner or it has a certain level of ductility. In the present study, the shearing failure mechanisms and the associate deformation will be investigated further using finite element method and this will be presented later in Section 6.7.

In Eurocode 3 (2005), the bolt shear capacity is simply given as:

$$F_{v,Rd} = 0.6 n_b f_{ub} A_b \tag{6-20}$$

where $n_b = 1$ if the bolt is in single shear, A_b is the effective cross-sectional area of the bolt shank and f_{ub} is the ultimate strength of the bolt material.

In the present model, for the bolt shearing stiffness the equation proposed by Sarraj (2007) is adopted (Equation 6-21). A correction factor of 0.15 is introduced to account for the error in shear strain energy caused by assuming constant strain through the bolt section, instead of realistic parabolic strain distribution.

$$K_{v,b} = \frac{0.15 G A_b}{d_b} \tag{6-21}$$

6.3.3 Complete force-deformation relationship for the bolted lap-plate component and the failure criteria

As has already been explained in the component model description in Section 6.2, the total deformation of the bolted lap-plate component (δ_j) is actually comprised of four independent deformation components. Except for the frictional slip (δ_s) which is a constant value ($\delta_s = d_h - d_b$), the other three deformations can be determined using the previously summarized formulations. Because the sub-component behaviour functions are monotonically increasing, for each certain loading magnitude *F*, the corresponding sub-component deformations can be obtained. Then they are summed up as the deformation of the bolted lap-plate component (δ_j). Therefore, the full force-deformation relationship of the bolted lap-plate can be established.

In reality, the relative loading capacity of plate bearing and bolt shearing has already determined the failure modes of the bolted component set. Therefore, the ultimate deformation of the component set can be determined at the failure of either plate bearing or bolt shear, whichever happens first. At the first failure point, the sum of the plate bearing and bolt shearing deformations is the ultimate deformation limit of the component set.

For the bolt shearing, it is assumed that the ultimate deformation is reached when the shearing capacity is reached. In the study of Sarraj (2007), the bearing failure is considered to occur when the bearing depth reaches the value of bolt shank radius (i.e. $0.5d_b$). However, no information of the background or justification was given.

In the later finite element investigation, it will be shown that for a typical fin-plate in the steel structure, the bearing deformation when the force reaches the bolt shearing capacity is well below d_b. Hence the tearout failure may not be expected to happen in a practical fin-plate connection, as the end distance is always beyond this value.

Additionally, as has been mentioned by Weigand and Berman (2014) and Yu et al. (2009), the bolt shearing fails first in most cases of structural fin-plate connections. The plate bearing tearout would mostly happen in thin-wall structures and cold-formed steel bolt connections (Konkong and Phuvoravan 2017).

Therefore for simplicity the bolt fracture is the primary concerned failure mode of the bolted component set, and the combined deformation when the force reaches the bolt shearing capacity is calculated to be ultimate deformation of the component set (δ_u).

6.4 Application of the fin-plate component model and assessment of adequacy

6.4.1 Description of the experimental case

Yang and Tan (2013) tested a series of bare steel double beam assemblies, each with a representative beam-column connection type. The general configuration of the specimen is schematically illustrated in Figure 6.16. The specimen represents a double-span beam assembly with a lost middle column, extracted between two contra-flexure points, hence it is pin supported at both ends.

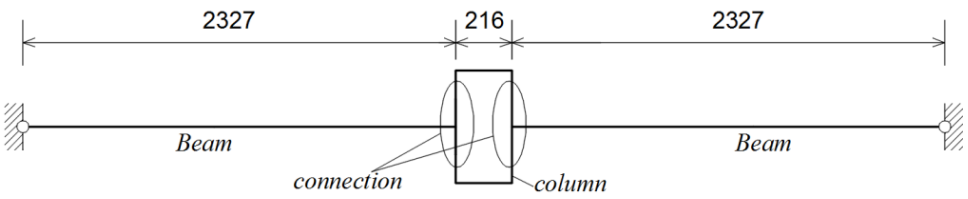

Figure 6.16 Overall geometric dimensions of the double-span beam assembly

The fin plate connection details are shown in detail in Fig. 6.17. It should be noted that an enhancement steel plate of 10 mm thickness was welded to the beam web in the connection area. Thus the effective thickness of the beam web is 16 mm in the fin-plate connection zone. The purpose of attaching the plate was to limit the beam web deformation and focus on the fin-plate and bolt row performances. Nevertheless, the deformation of the strengthened beam web is still considered in the following modelling and analytical procedures.

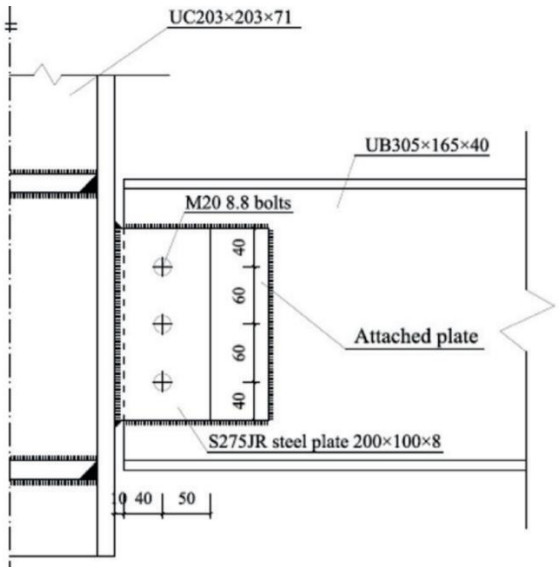

Figure 6.17 The configurations of the fin-plate connection specimen (Yang and Tan 2003)

Table 6.4 The connection details and members sectional dimensions (in *mm*)

	Depth	Width	Flange thickness	Web thickness
Beam	303.4	165.0	10.2	6.0
Column	215.8	206.4	17.3	10.0

Based on the test results, the vertical load-deflection curve is plotted in Figure 6.18, up to the ultimate failure of the beam assembly. Points A, B and C typically refer to the changing points where significant local failure events occur in the connection zone and drops of the load resistance are induced.

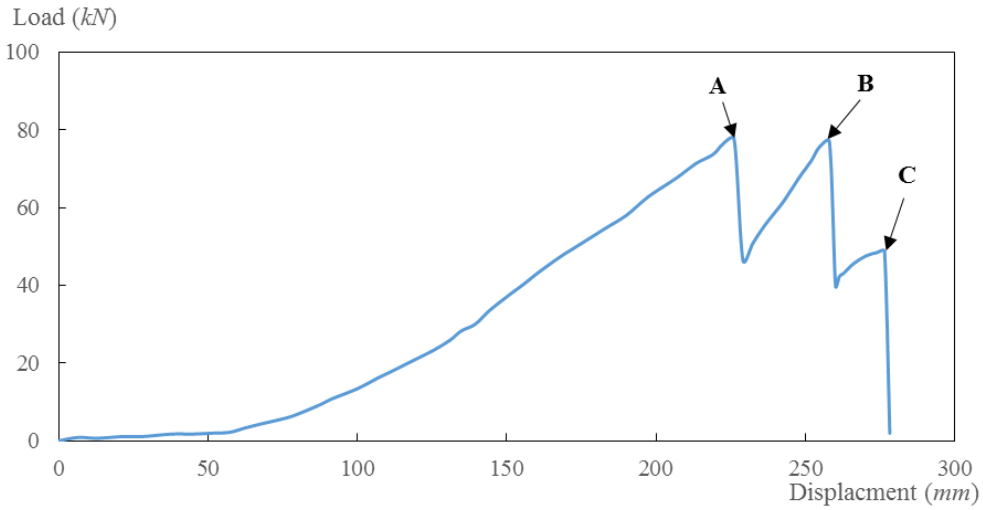

Figure 6.18 The measured resistance function of the fin-plate jointed beam assembly

Table 6.5 summarizes the failure points, along with the associated failure events description and deformatiom levels. It is clear that the fin plate connection failed due to bolts shearing fractures, as can be prediceted due to relatively lower shearing capacity than the plate bearing capacity. The three bolts on one side of the middle joint failed one by one from the bottom to the top. At the failure points, it was observed that the fin plate itself has undergone significant bearing deformations around the bolt holes.

Table 6.5 The characteristic points and corresponding test observations

Characteristic point	**A**	**B**	**C**
Test photos			
Failure status	left bottom bolt shear fracture	left middle bolt shear fracture	left top bolt shear fracture
Vertical deflection	w = 226mm	w = 258mm	w = 276mm
Rotation $\theta = w/L$	θ = 0.10rad (5.5 *degrees*)	θ = 0.11rad (6.3 *degrees*)	θ = 0.12rad (6.8 *degrees*)

The observations at the end of the test, as shown in Figure 6.19, exhibit significant bearing deformations and the bolt shearing failure at the location of fin-plate and beam web interface.

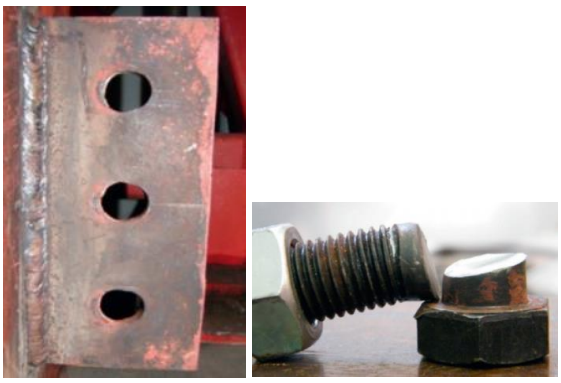

Figure 6.19 The fin-plate bearing deformation and bolt shear fracture at the end of the test

Additionally, it was found that the beam assembly was almost not able to resist any load in the initial loading stage. This phenomenon was also observed in the specimen test featuring the web cleat connection as discussed in Chapter 2. This is presumably due to the following two reasons.

1) First, at the two end supports, the pin holes that were pre-drilled for the latch-type rollers had gaps of approximately 1-2 mm to allow for easier set-up installation. These gaps would close up with the increase of vertical deflection from zero to a certain level. In this test case, it is estimated that an initial deflection of 67.5 mm would be required to close up a gap of 1.0 mm in the clearance hole at the pin supports. Consequently, an initial tightening stage needs to be taken into consideration. It should be noted that in a general case bending resistance would develop while any axial clearance at the support settles, so there is not a simple way to eliminate the influence of the initial gaps. Instead, it will need to be incorporated into the analysis procedure in the calculation of the evolving axial force and catenary effect. This has been covered in the analytical framework and program in the last chapter.
2) Secondly, the bolts in the fin-plate connection are usually not torque-tightened after installation. When the shear force progressively develops in the bolt-lap plate components, the force transfer would be initially by friction. Once the shear force exceeds the frictional capacity, relative slips will occur between the fin plate and the beam web, owing to the fact that the bolt diameter is mostly smaller than the bolt-hole diameter. The relative slips will

continue until the shear force is transferred by the bolt bearing against the edge of the bolt-hole. Therefore, some vertical deflection would also be necessary to fully engage the fin plate connection.

6.4.2 Determination of the component parameters

The geometric parameters for the fin plate and beam web plate in bearing are listed in Table 6.6.

Table 6.6 The geometric parameters of the fin plate and the beam web plate in bearing

	Fin plate		**Beam web**	
Parameter	Notation	Value (mm)	Notation	Value (mm)
End distance	L_{e1}	50	L_{e2}	40
Edge distance	w_{e1}	40	w_{e2}	40
Plate thickness	t_{p1}	8	t_{p2}	16
Bolt diameter	d_b	20	d_b	20
Bolt hole diameter	d_h	21.6	d_h	21.6

For the component joint model, the effective width is 70 mm for the top and bottom components, 60 mm for the middle component, leading to an edge distance of the bolt to be 30 mm. The M20 bolt usually has a corresponding clearance hole of 21.6 mm, as per Table 6.2.

According to the formulation presented in Section 6.3, the nominal bearing capacity is calculated using Equation (6-5). In this case, the bearing capacities of the fin plate and beam web are calculated as:

$$F_{bf} = \min(L_{e1}, 2.4d_b) \cdot t_{p1} f_{u1} = 48 \times 8 \times 445 = 170.88\ kN$$

$$F_{bw} = \min(L_{e2}, 2.4d_b) \cdot t_{p2} f_{u2} = 40 \times 16 \times 550 = 352.0\ kN$$

The equivalent stiffness is evaluated based on the combination of the bearing, bending and shearing stiffnesses of the end plate material between the bolt-hole edge and the plate edge.

The bearing, bending, shearing and resultant equivalent stiffnesses are calculated using Equations (6-15), (6-17) and (6-18) as:

$$K_{br} = 120 f_y t_p (d_b/25.4)^{0.8} = 120 \times 275 \times 8 \times (20/25.4)^{0.8}$$
$$= 218.1\ kN/mm$$

$$K_b = 32 E t_p (L_e/d_b - 0.5)^3 = 32 \times 210000 \times 8 \times (50/20 - 0.5)^3$$
$$= 4.3 \times 10^5\ kN/mm$$

$$K_v = 6.67 G t_p (L_e/d_b - 0.5) = 6.67 \times 81000 \times 8 \times (50/20 - 0.5)$$
$$= 8644\ kN/mm$$

$$K_i = 1/\left(\frac{1}{K_{br}} + \frac{1}{K_b} + \frac{1}{K_v}\right) = 212.6\ kN/mm$$

As can be seen, the bending and shearing stiffness is much higher than the bearing stiffness, so the equivalent stiffness is dominated by the bearing stiffness.

The normalized displacement of the component is expressed as

$$\bar{\delta} = K_i \delta / F_{bf} = 1.0 \times \frac{212.7kN}{mm} \times \frac{\delta}{170.9kN} = \frac{\delta}{0.8mm}$$

By using Equation (6-16), the bearing force-deformation curve can be generated and this is plotted in Figure 6.20.

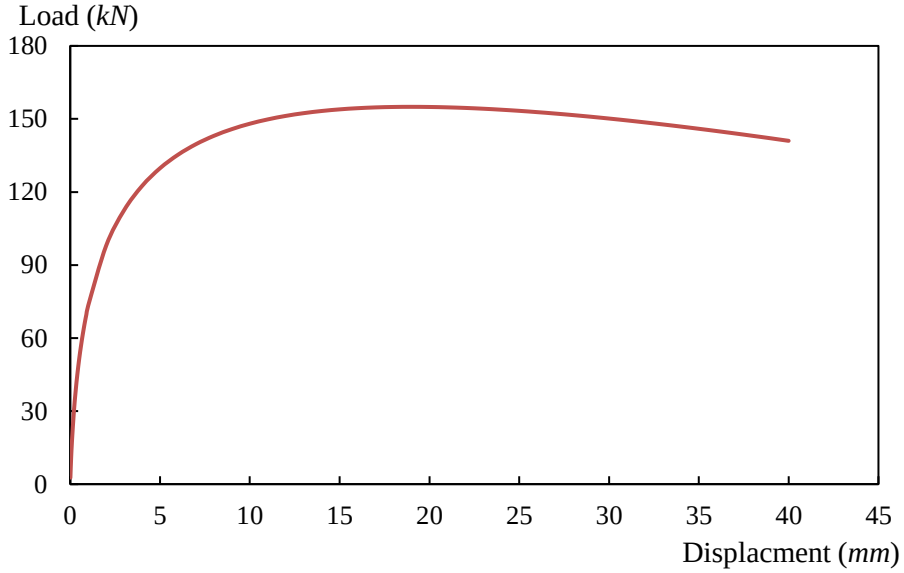

Figure 6.20 Force-displacement curve of the example plate in bearing

The beam web plate in bearing can be calculated exactly in the same way, with different parameter values.

For the Grade 8.8 M20 bolt, the single shear capacity and shearing stiffness are calculates using Equations (6-20) and (6-21) as:

$$F_{v,Rd} = \alpha_v f_{ub} A_b = 0.6 \times 800 \times 245 = 117.6\ kN$$

$$K_{v,b} = \frac{0.15 G A_b}{d_b} = 0.15 \times 81000 \times \frac{245}{20} = 148.8\ kN/mm$$

Using Equation (6-19), the shearing force-deformation can be generated and it is plotted in Figure 6.21.

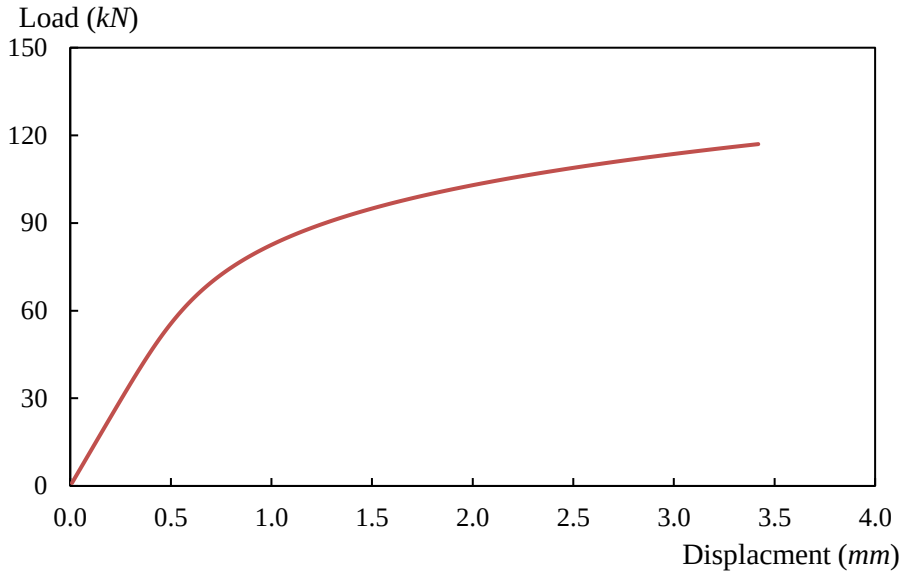

Figure 6.21 Shearing force-deformation curve of the M20 Grade 8.8 bolt

Finally, using the combined deformation, the force-deformation curve for the bolted lap-plate component set can be established, as shown in Figure 6.22.

The comparison shows that the bolt shear capacity is lower than the plate bearing capacity ($F_{v,Rd} < F_{bp}$). Therefore, the bolt shear is the defined failure mode in this fin plate connection. This results is in good agreement with the experimental observations as described earlier in Section 6.4.1.

Therefore, the bolt shearing capacity (marked by the horizontal dashed line in Figure 6.22) determines the ultimate deformation of the component set. This is found to be at $\delta_u = 6.3\ mm$.

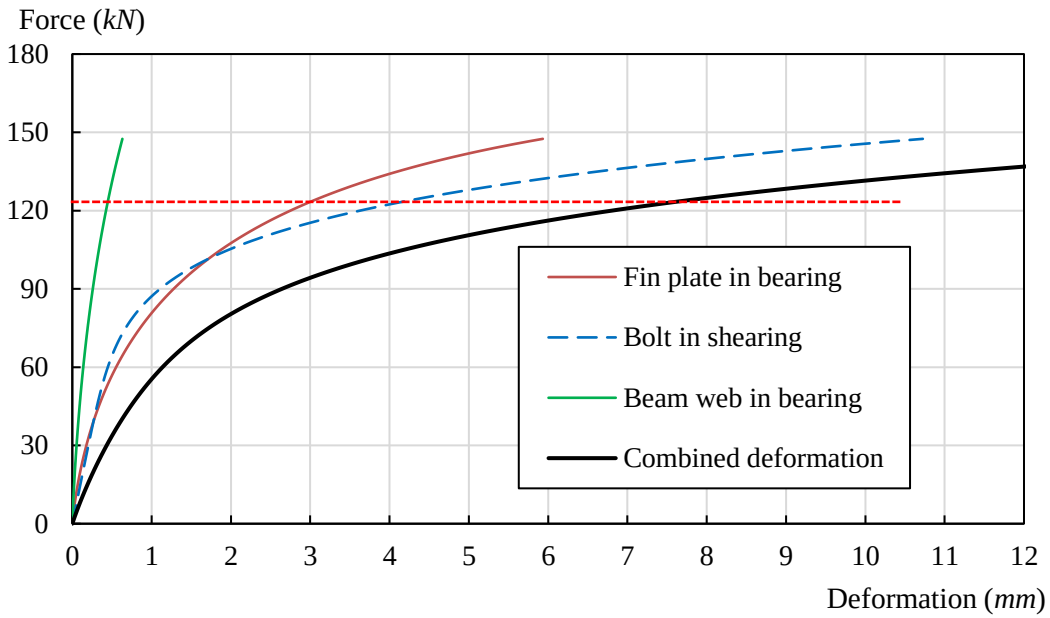

Figure 6.22 The combined force-deformation relation for the example component set

6.4.3 Analytical results of the overall resistance function and comparison with the experiment

The analytical solution of the global resistance function can now be obtained, by incorporating the above-determined bolted lap-plate component properties into the programmed analytical framework. It takes less than 30 seconds for the Matlab program to complete the iterative solution process, with the vertical deflection increasing from 0 to 300 mm, at an incremental step of 1 mm.

a) The overall resistance function

The global load resistance development with the increase of the middle-joint vertical deflection is plotted by the program at the end of the solution procedure, as shown in Figure 6.23.

The analytical solution predicts an initial stage, in which almost no load resistance is developed. This is because each individual component will have a slipping phase, in which the total slippage deformation is 1.6 mm. Thereafter, the bolt shank comes in contact with the bolt-hole circumferences, and force starts to develop with further deformation due to plate bearing and bolt shearing effects.

The fracture failures of the three bolts are captured to occur in sequence, the load drops and the subsequent recovering of the resistance are successfully simulated. The third (top) bolt failure indicates the final collapse of the assembly, and the solution procedure terminates at this point.

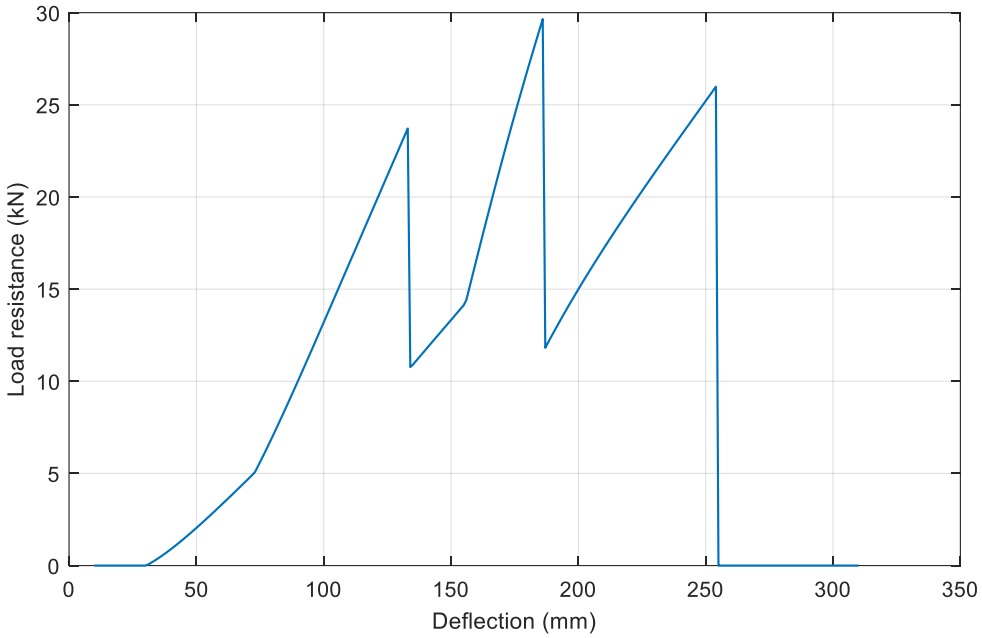

Figure 6.23 The analytical solution using the assembled component behaviour function

Apart from the load-deflection curve, the force and deformation in each individual component and at each incremental solution step can also be examined from the analysis program. Thus, the contributions by bending moment and catenary axial force are separately worked out. These results, along with the test result of the resistance function, are collectively shown in Figure 6.24.

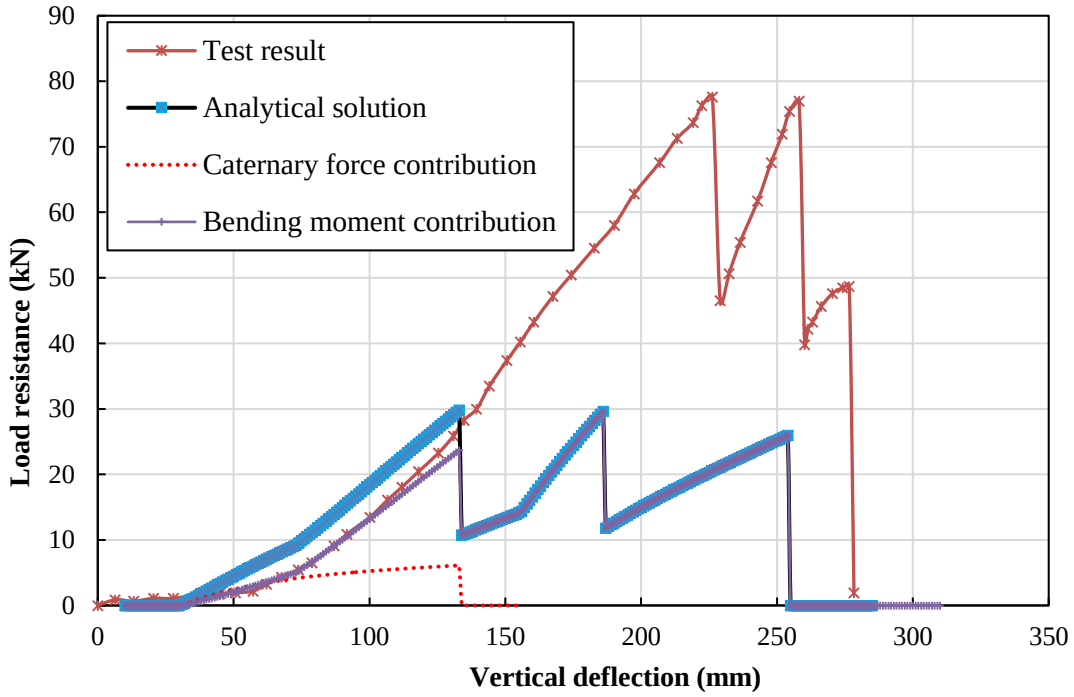

Figure 6.24 The analytical results of flexural and catenary contribution, and comparison with test results

In the original test study, the authors also calculated the contribution of catenary axial force, as shown in Fig. 6.25. The flexural action contributed a nearly constant part of the vertical load resistance before the occurrence of first bolt shearing failure. Afterwards, the load resistance is dictated by the catenary axial force. It can be judged that the analytical results are consistent with the test observations. However, quantitatively the analytical results significantly underestimate the global strength of the beam assembly, and this will be discussed further in Section 6.5.

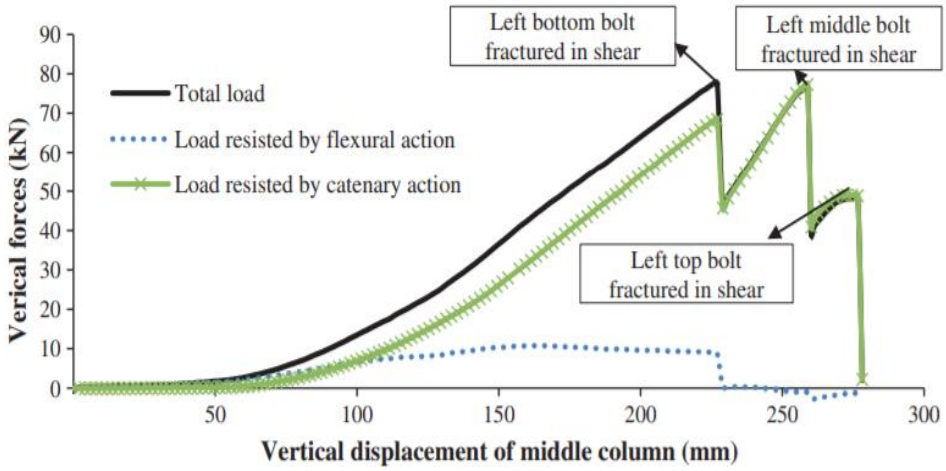

Figure 6.25 The resistance contribution of flexural and catenary action from test result (Yang and Tan 2013)

b) Key events from the analysis and comparison with experiment

The key failure events, which are due to bolt shearing fracture, are analytically predicted. The corresponding deflection levels and the states of the components are extracted and tabulated in Table 6.7.

Table 6.7 The analytical results of the component failure points

Characteristic failure points	**1**	**2**	**3**
Deflection	$\omega = 133mm$	$\omega = 186mm$	$\omega = 276mm$
Rotation $\theta = w/L$	$\theta = 0.06rad$ (3.3 *degrees*)	$\theta = 0.08rad$ (4.7 *degrees*)	$\theta = 0.12rad$ (6.8 *degrees*)
Component 1 **(top)**	$F_1 = 0\ kN$ $\delta_1 = -0.05\ mm$	$F_1 = 65.0\ kN$ $\delta_1 = 2.3\ mm$	$F_1 = 117.2\ kN$ $\delta_1 = 7.9\ mm$
Component 2 (middle)	$F_2 = 87.5\ kN$ $\delta_2 = 3.5\ mm$	$F_2 = 117.1\ kN$ $\delta_2 = 7.9\ mm$	
Component 3 (bottom)	$F_3 = 115.9\ kN$ $\delta_3 = 7.7\ mm$		

It can be seen that at the first failure point, the bottom bolt reaches its ultimate shearing capacity, while the top bolt is still in the slipping stage and is stress-free.

After this point, the components are all in tension and bolt shearing fracture controls the component failure.

c) Discussion on the significant discrepancies

From the comparison, the following two conclusions can be drawn.

1) The load resistance are seriously underestimated. This implies the component behaviour properties have inherently lower estimate of the component loading capacity, especially for the bolt in shearing, which controls the component failure in this case.
2) The predictions of the vertical deflection and the ultimate deflection capacity are within the acceptable range, compared with the experimental results.

To better understand the plate bearing and bolt shearing behaviour in an actual fin-plate connection, finite element simulations are carried out. On this basis, necessary modifications are then proposed to represent the bolted lap-plate component behaviour function more accurately.

6.5 Finite element modelling of the behaviour of a bolted lap-plate component set

The numerical modelling study starts from the full component set of a bolted lap-plate using a detailed finite element model. The objective is to produce the simulation result of force-deformation curve for the component set, so as to compare with the analytical component force-deformation relationship as shown in the example application in the previous section. The discrepancies between the two results will be examined to identify the areas of problems in the existing formulations of the plate bearing and bolt shearing properties. On this basis, further numerical modelling studies are carried out to ultimately improve the component formulations and achieve more realistic analytical solutions in the subsequent two sub-sections (6.8 and 6.9).

6.5.1 Overview of finite element modelling and simulation method

A detailed three-dimensional model of the bolted lap-plate component is established, using the general finite element platform ABAQUS. Figure 6.26 shows the configuration and FE mesh for the component.

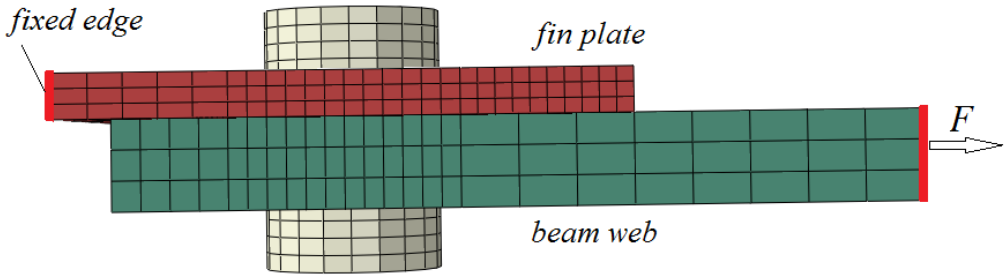

Figure 6.26 The solid brick element model of the bolted lap-plate component set

In the geometric model, the bolt head and nut sizes are specified in accordance with the British standard BS 3692:2001 (ISO metric precision hexagon bolts, screws and nuts). The washers are not modelled for simplicity, and the bolt threads are also ignored. According to the aforementioned standard, the thread length is 38-60 mm for M12-M24 bolts if the total shank length is less than 125 mm. Since the fin-plate and beam web usually have a thickness around 8-16 mm, it is considered that for the chosen bolts used in the fin-plate connections, the major part of the bolt shank in contact with the plate bearing is unthreaded.

The fin plate is fully fixed at one end, and a displacement-controlled loading is applied to the opposite end of the beam web plate. As can be seen from the experimental set-ups, e.g. Yang and Tan (2013) and Li et al. (2013), the double-span beam assembly specimens are generally restrained in the out-of-plane direction. Accordingly, the end of the beam web plate, on which the force F is applied, is assigned a symmetric boundary condition ($U_z = U_{xx} = U_{yy} = 0$).

The pre-tension of the bolts are not modelled, as the plate bearing and bolt shearing behaviour are the simulation focus. Once the pretension force is overcome in the frictional slip phase, it does not have much impact on the subsequent component behaviour.

6.5.2 The elements and contact algorithm

Due to abrupt failure events and load fluctuations, the analysis is carried out using the explicit solver. The solid element choices for an explicit analysis in ABAQUS are limited only to C3D8R and C3D8I, both with eight nodes at the brick corners. The C3D8R element uses a reduced integration with only one integration point in the middle of the brick. This reduces the computation time but at the same time could lead to inaccurate results in large deformation and high stress-gradient areas.

The incompatible mode brick element C3D8I is an improved version of the C3D8-element. It uses full integration with eight integration points (one for each node). In addition, it introduces incompatible deformation modes, which will improve the element behaviour under bending and large deformations. Bursi and Jaspart (1998) investigated the basic issues in the finite element simulations of bolted connections, and compared three different brick elements in ABAQUS. They concluded that C3D8I elements, being purposely designed for bending-dominated problems, behave particularly well in the inelastic regimes. On the other hand, C3D8R elements will underestimate the plastic failure load, because of the stiffness degradation caused by self-locking of the elements.

Therefore, in this study the C3D8I solid element is used to model the plate as well as the bolt to better capture the bearing contact behaviour with considerable material nonlinearity.

The finite element meshes of the plates and bolt are shown in Figures 6.27 and 6.28. In particular, the potential bearing contact areas are mesh-refined to sizes of approximately 1.5 mm. Likewise, the mesh in the bolt shank is also refined, aiming to capture the bolt fracture more precisely.

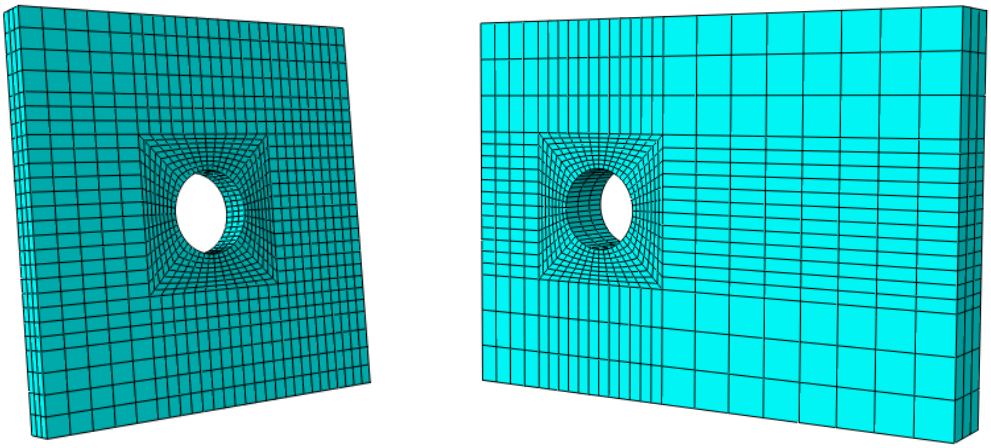

(a) Fin plate (S275 steel, t = 8mm) (b) Beam web plate (S355 steel, t = 16mm)

Figure 6.27 The meshed model of the plates with bolt-holes

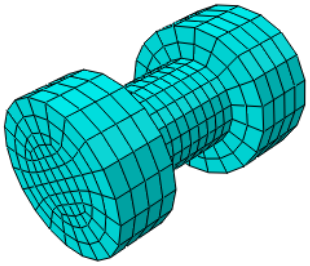

Figure 6.28 The solid element model of the M20 high-strength bolt

The contact properties are assigned for the surface contacts between the following various contact pairs:

1) The fin plate and the beam web plates;
2) The plate surface and the bolt head/nut surfaces;
3) The bolt shank and the bolt-hole circumferences.

In the contact pairs, the surfaces belonging to the bolt are always defined as master surfaces, as they possess finer meshes and stronger material.

For the tangential contact behaviour, the “penalty” friction formulation is used, and a friction coefficient of 0.25 is defined for all the surfaces in contact. For the normal contact behaviour, hard contact is defined, so that the penetration between different contact parts can be avoided, but the separation is allowed after contact.

6.5.3 Material properties

a) <u>The stress-strain curves for the steel plate and bolt material</u>

The mechanical properties of common structural steel grades S275 and S355, with isotropic plasticity, are applied to the steel members. Elastoplastic and plastic hardening properties are considered separately, with initial elasticity E_0 = 205 GPa, and Poisson's ratio ν = 0.3.

The mechanical properties of the materials specified in the British standard EN 10025 are adopted, as listed in Table 6.8.

Table 6.8 The material properties for the members and bolts

Material	Yield strength (f_y) for thickness $t \leq 16$mm	Tensile strength (f_u)	Elastic modulus (E)	Shear modulus (G)
S275 Steel	275 MPa	445 MPa	205 GPa	81 GPa
S355 Steel	355 MPa	550 MPa		
Grade 8.8 Bolt	640 MPa	800 MPa	205 GPa	81 GPa

According to Sarraj (2007), the stress-strain curves are plotted in Figures 6.29 and 6.30. They are actually the engineering stress-strain relations, obtained experimentally using standard coupon tests. Each curve includes a clear elastic stage, a plastic plateau up to the strain of 0.02, a curved hardening stage till the nominal maximum strain of 0.12-0.15, and finally a plateau afterwards.

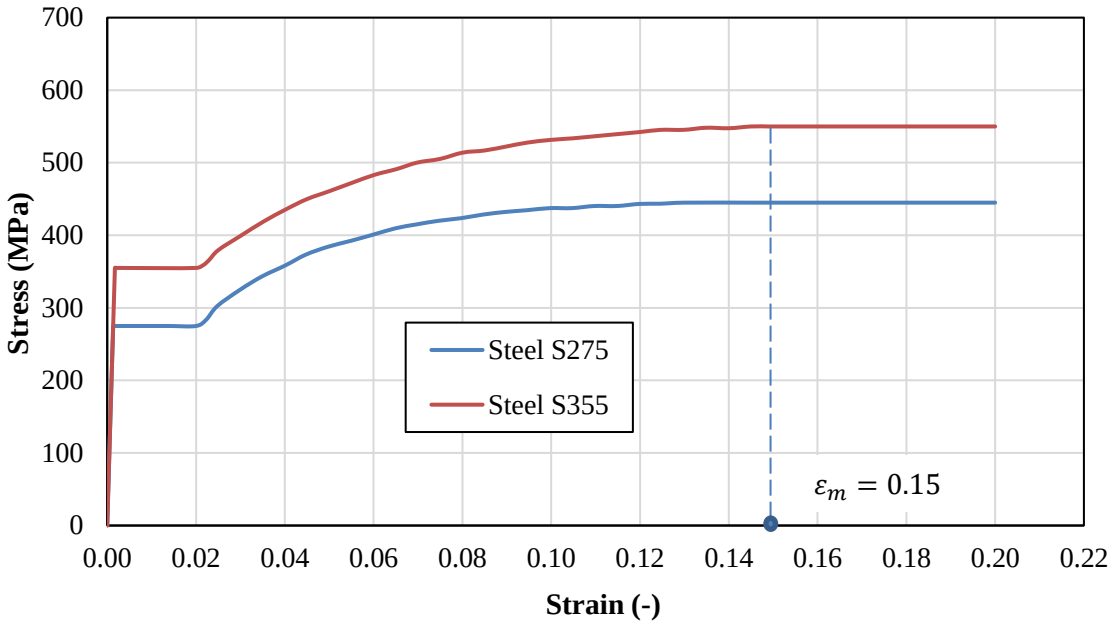

Figure 6.29 The engineering stress-strain curve of the steel grades S275 and S355

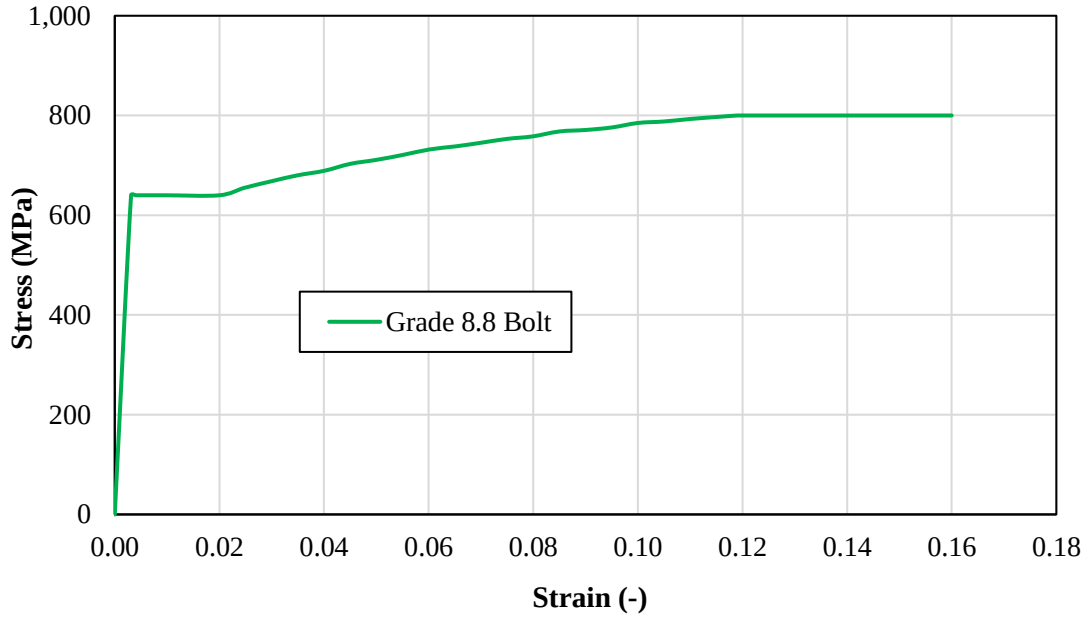

Figure 6.30 The material property of the Grade 8.8 bolt

As the simulation study involves large deformation of the elements in the bearing zone, true strain-true stress relations are required for the proper definition of the uniaxial material response (Bathe 1982). The true stress and strain are defined on the basis of current elongation value and reduced cross-sectional area. They can be calculated from engineering stress and strain using the following equations:

$$\varepsilon_{true} = \ln(1 + \varepsilon_{eng})$$
$$\sigma_{true} = \sigma_{eng}(1 + \varepsilon_{eng}) \quad (6\text{-}22)$$

where ε_{eng} and σ_{eng} are the nominal strain and stress, respectively.

The true stress-plastic strain relations are defined in the material properties of the component-set model.

b) <u>The material damage and failure criteria</u>

The Ductile Damage Model in ABAQUS is employed to simulate the material fracture and the consequent element removal. This model has been widely used to simulate the damage caused by formation and propagation of cracks in ductile metals. Figure 6.13 schematically shows the stress-strain behaviour with damage, which leads to both strength reduction and stiffness degradation.

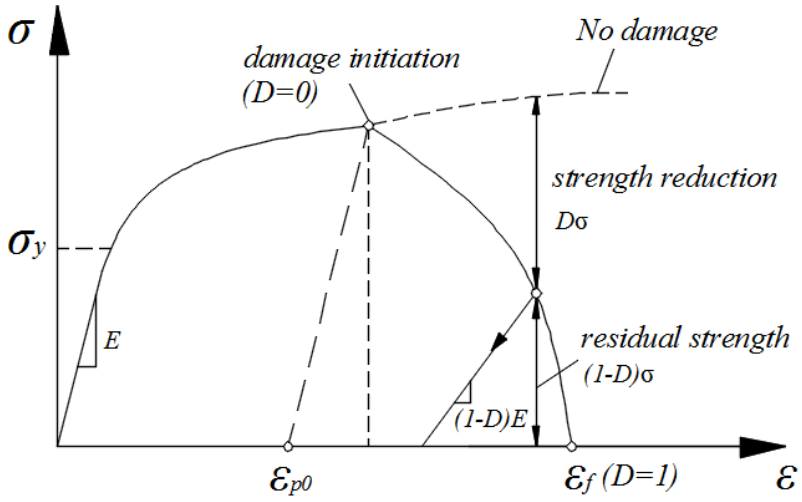

Figure 6.31 The ductile damage model to simulate the element removal

In this figure, ε_{p0} and ε_f are the equivalent plastic strains at damage initiation and failure, respectively. The equivalent plastic strain at the onset of damage is a function of stress triaxiality (strain rate is ruled out). On the basis of previous experimental and theoretical findings, Pavlović et al. (2013) derived and proposed exponential dependency of the equivalent plastic strain at damage initiation to be a function of stress triaxiality η, as given by Equation (6.24) and shown in Figure 6.32, where ε_n^{pl}

is the uniaxial plastic strain at onset of necking in a standard tensile test. The stress triaxiality η is defined as the ratio of hydrostatic stress to von Mises equivalent stress.

$$\varepsilon_{p0}(\eta) = \varepsilon_n^{pl} \cdot exp[-1.5(\eta - 1/3)] \tag{6-23}$$

$$\eta = \frac{\sigma_m}{\sigma_e} = \frac{(\sigma_1 + \sigma_2 + \sigma_3)/3}{\sqrt{(\sigma_1 - \sigma_2)^2 + (\sigma_2 - \sigma_3)^2 + (\sigma_3 - \sigma_1)^2}/\sqrt{2}} \tag{6-24}$$

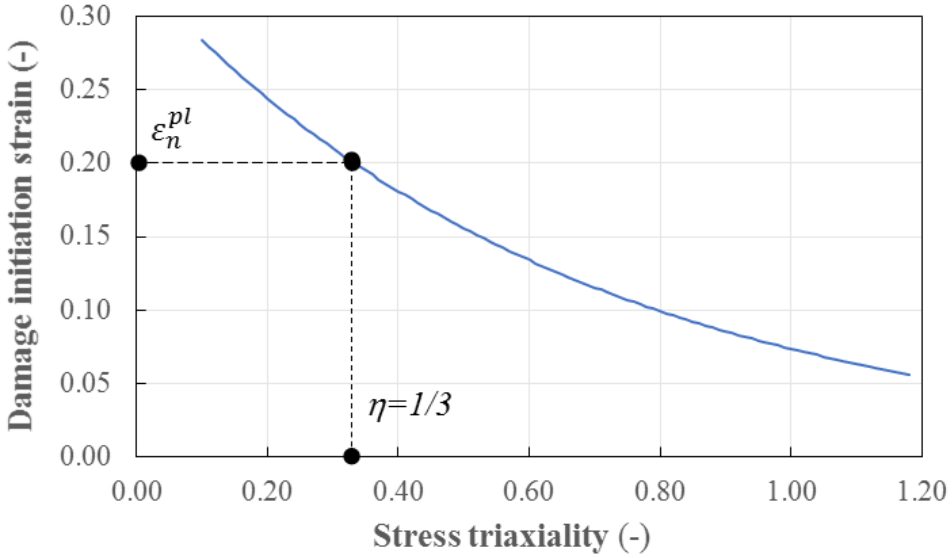

Figure 6.32 Damage ignition strain vs. stress triaxiality (Bases on Pavlović et al. (2013))

Following the initiation of damage, the damage will be accumulated until eventual fracture, which indicates the complete loss of strength and stiffness. One problem with the stress-strain relation after damage is that it does not appropriately represent the material behaviour. The strain localization will lead to strong mesh dependency. Therefore, the material strain cannot be used as a parameter to define the damage evolution. In order to alleviate the mesh size dependency of the results, Hillerborg et al. (1976) proposed the fracture energy (G_f) which is required to open a unit area of crack, or the plastic displacement at fracture (u_f), as the parameter for damage evolution and fracture criterion. They are computed by the following equations:

$$G_f = \int_{\varepsilon_{p0}}^{\varepsilon_f} \sigma \cdot du_p = \int_{\varepsilon_{p0}}^{\varepsilon_f} \sigma L d\varepsilon_p \tag{6-25}$$

$$u_f = L \cdot (\varepsilon_f - \varepsilon_{p0}) \tag{6-26}$$

In the above expressions, $u_p = L\varepsilon_p$ refers to the equivalent plastic displacement, where L is the characteristic length of elements. By this way, the material degradation can be reasonably characterised by the stress-displacement relation.

In the following presented modelling studies, the first fracture energy parameter is used for the material failure simulation, especially for the bolt shank failure under tension and shearing.

Technically speaking, if the fracture energy G_f is specified as zero or very small value, failure will follow immediately after the damage initiation point. However, the sudden drop of stress could possibly cause dynamic instabilities during analysis. Therefore, G_f is set to be sufficiently small in the present studies, to approximate the immediate removal of elements once the fracture strain is reached.

For elements in the bolt model, the fracture is activated when the element strain reaches a specified rupture strain, and the elements are consequently eliminated from the whole model. According to the coupon tests by Zhong et al. (2017) on various steel components, the rupture strains turned out to be around 0.30, based on a gauge length of $5.65\sqrt{S_0}$, where S_0 is the cross-sectional area of the coupon specimens. Hence, the fracture strain of 0.30 is defined in the current models. The fracture energy will be assigned as different values, and it will be later proved that it does not have much influence when modelling the bolt shearing failure.

c) <u>Loading scheme and analysis technique</u>

A loading reference point is created adjacent to the end of the beam web plate, and is coupled with the end surface. In this way, the load can be applied directly on the reference point. The reaction force and displacement can represent the force-deformation relationship of the component set.

In order to simulate the quasi-static behaviour, and overcome the potential convergence problems at large deformation, the tensile force is applied in a displacement-controlled manner. To further ensure steady analysis steps and avoid undulations in the initial bearing stage, the displacement is made to increase very gradually at the beginning. This is realized by applying a stable velocity to the loading point. The resultant displacement time history is shown in Figure 6.33.

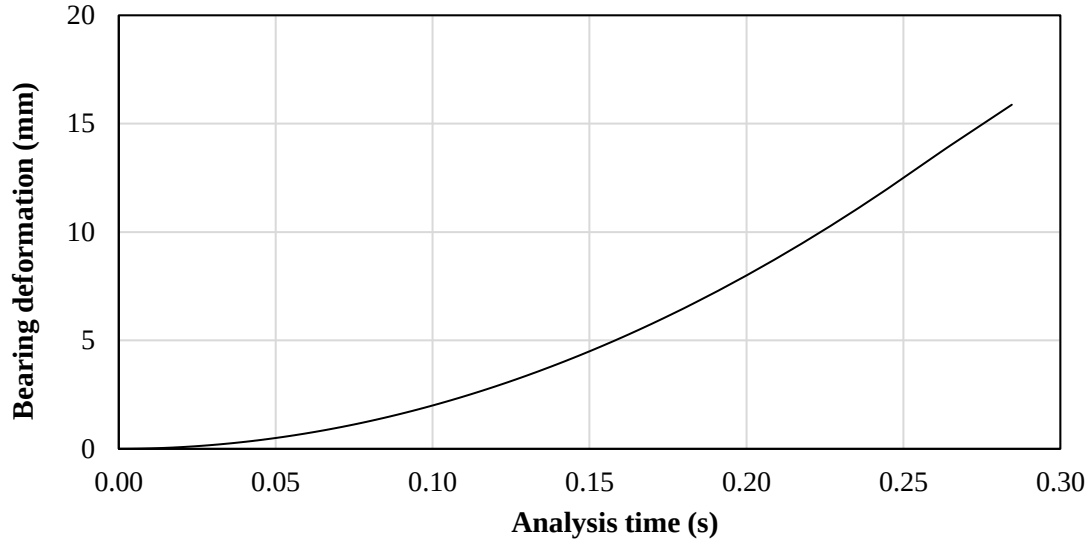

Figure 6.33 The displacement history of the loading point

The explicit analysis will be carried out, both with and without the introduction of material damage. When the material damage properties are introduced with the aforementioned fracture strain and fracture energy criteria, the bolt shear fracture or the bearing failure point can be properly captured. Then the ultimate deformation limit (δ_u) can be determined.

6.5.4 Finite Element Modelling results and comparison with analytical predictions

Firstly, the force-deformation relationship is obtained, without material damage introduced into the component set model. Figure 6.34 shows the results with two different effective widths of the component.

Some preliminary discussions can be made on the results:

1) It is shown that there is not much difference between the two results. In other words, the plate width does not have much influence on the behaviour of the component set.
2) The component behaviour curve is more like a bi-linear shape, with an "elastic" stage up to deformation of 0.7 mm, and a "hardening" stage.
3) If the calculated bolted shearing capacity of 117 kN is applied to the curve, the ultimate deformation will only be 0.7 mm, which is not realistic. It is

indicating that the existing formulations may have underestimated the bolt shearing capacity in the component.

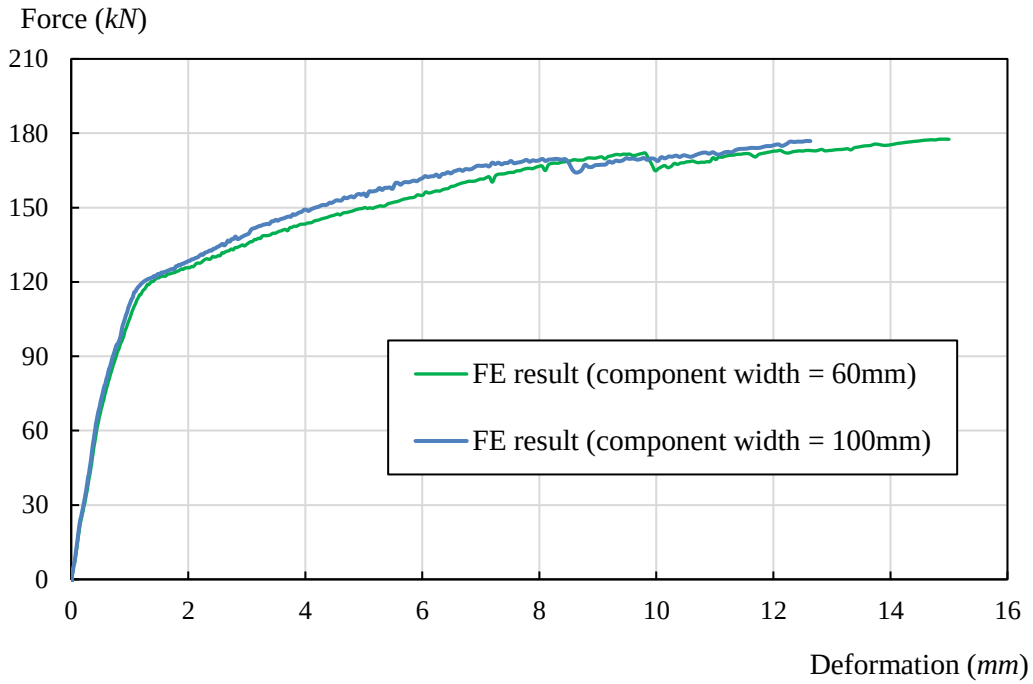

Figure 6.34 The FE result of component behaviour without material damage

The finite element modelling results are compared with the function curve, which was predicted using the existing formulation for plate bearing and bolt shearing. It confirms that the loading capacity is largely underestimated, with a gap around 30%, see Fig. 6.35.

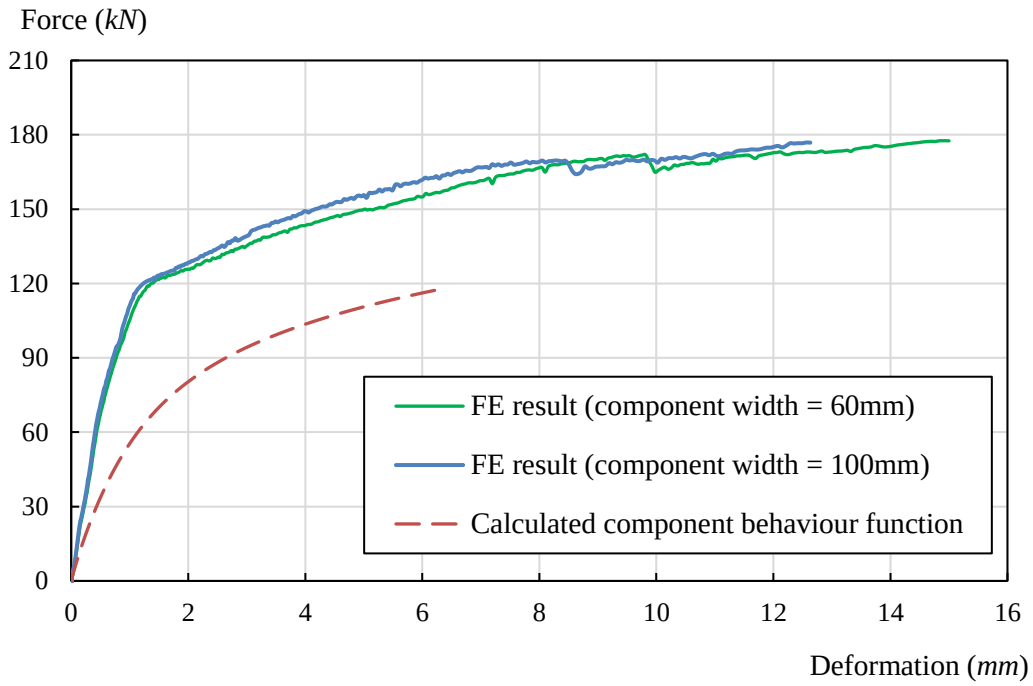

Figure 6.35 The FE result of component behaviour compared with prediction of existing formulations

The deformed shape and equivalent Von-Mises stress distributions are plotted in Figures 6.36 and 6.37.

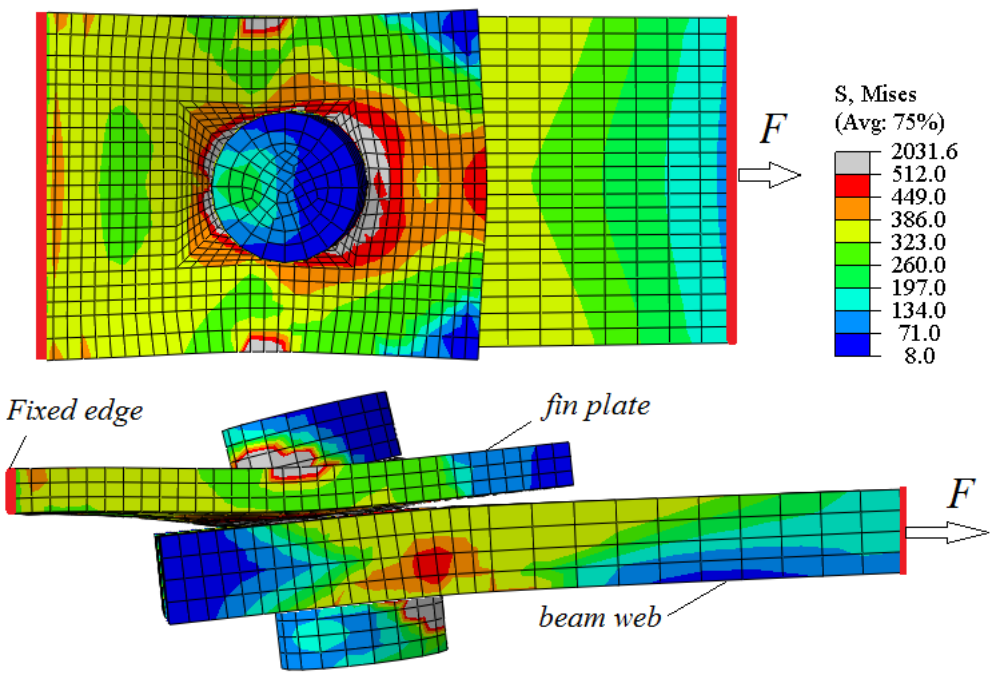

Figure 6.36 The deformed shape and stress distribution of the bolted lap-plate component

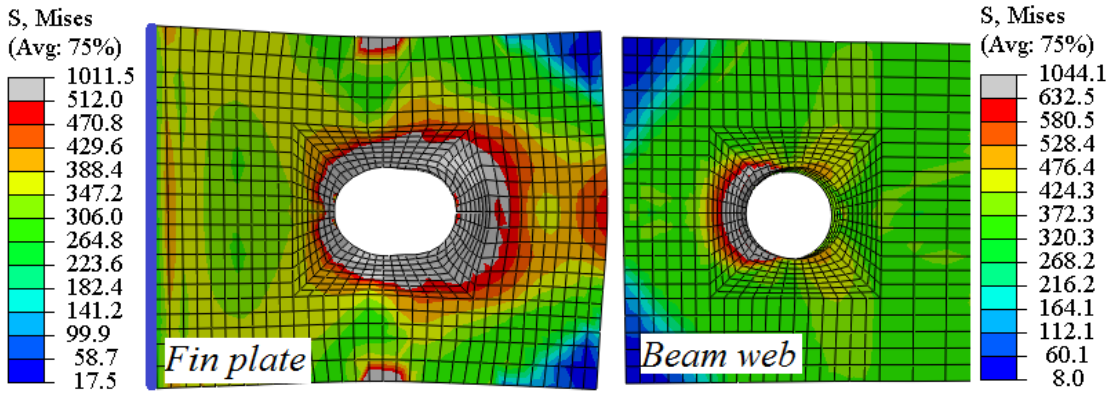

Figure 6.37 The bearing deformation of the connected fin plate and beam web

One important observation from the above deformed shape is that the bolt is not only subjected to pure shearing. As can be seen, the bolt shank has significant inclination at large deformation of the component set. This implies that the clamping effect of the bolt head and nut, together with the bearing deformation, causes a marked level of tension and bending in the bolt.

Therefore, the bolt in this particular component is actually subjected to complicated loading conditions. This may be the underlying reason why the bolt shearing capacity is underestimated using the pure shearing equation. In these regards, a modified force-deformation relation for the shearing in a bolted lap-plate component is required, and to assist in establishing the modification, a more accurate finite element modelling of bolt deformation needs to be considered.

Figure 6.38 shows the simulated ultimate failure point, by introducing the material damages which would lead ultimately to material failure or fracture. As it is shown, the bolt fracture happen in a very brittle manner, the component set immediately loses its loading capacity, once the ultimate shearing strain of the bolt (0.30) is reached.

A parametric study of the fracture energy (G_f) shows that it does not have any significant influence on the failure point prediction nor on the brittle fracture mode.

From Figure 6.39, it can be seen that the overall ultimate deformation is well predicted by using the theoretical formulations. The loading resistance capacity, though, is considerably underestimated.

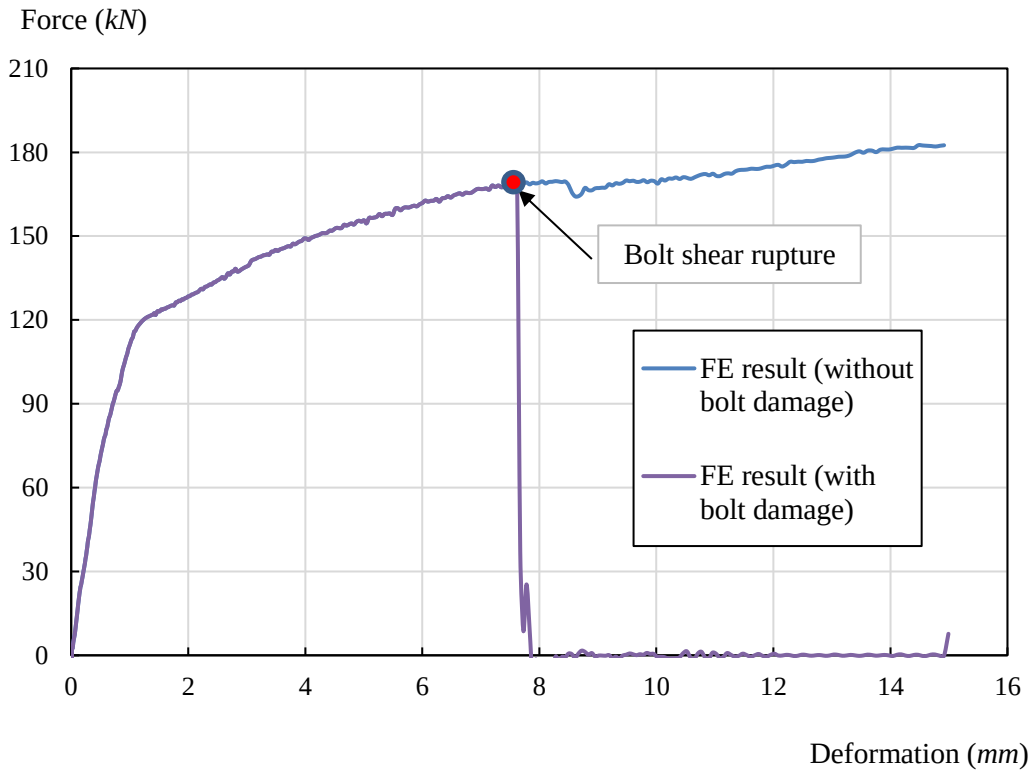

Figure 6.38 The simulation result with bolt shear damage introduced

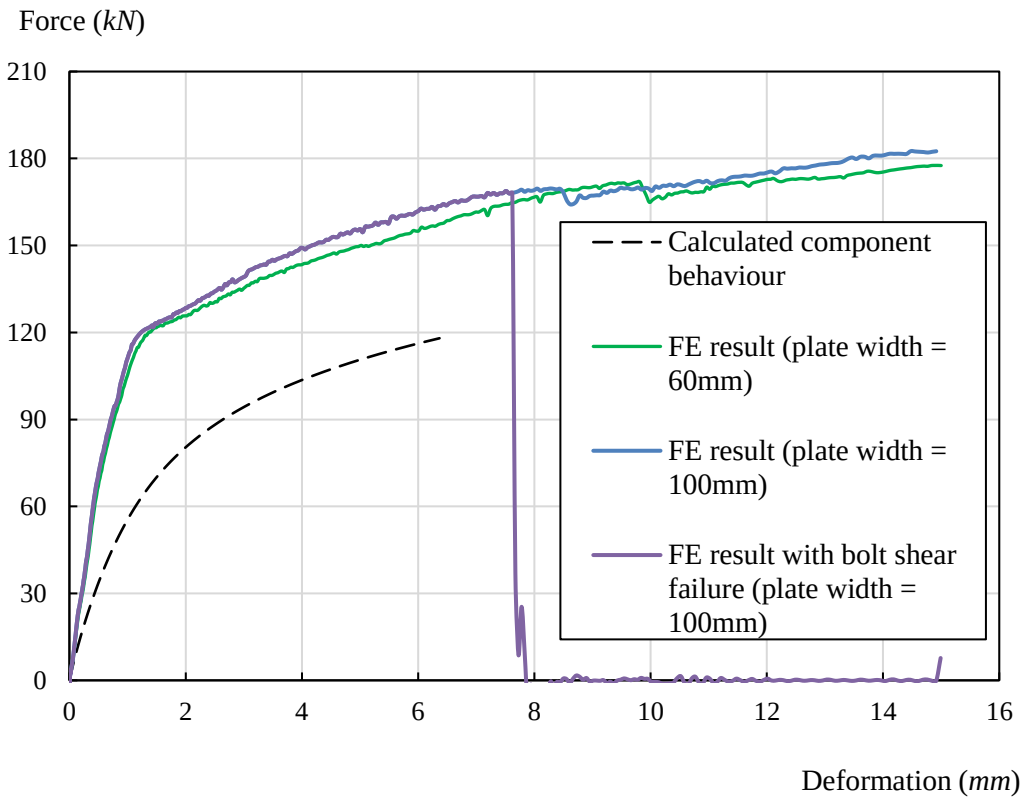

Figure 6.39 The modelling result against the prediction using existing formulations

The equivalent plastic strain (PEEQ) distribution of the bolt shank right before shearing fracture, and the bolt shearing shape are shown in Figures 6.40 and 6.41. It agrees very well with the observation of the bolt failure mode in realistic test.

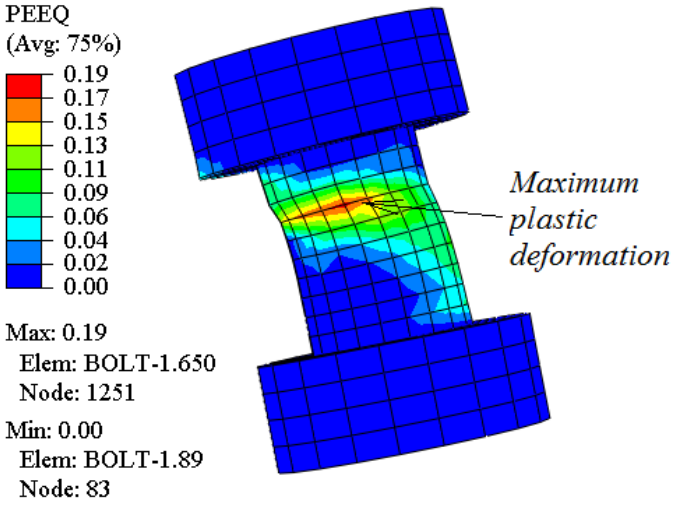

Figure 6.40 The equivalent plastic strain (PEEQ) distribution of the bolt shank right before shearing fracture

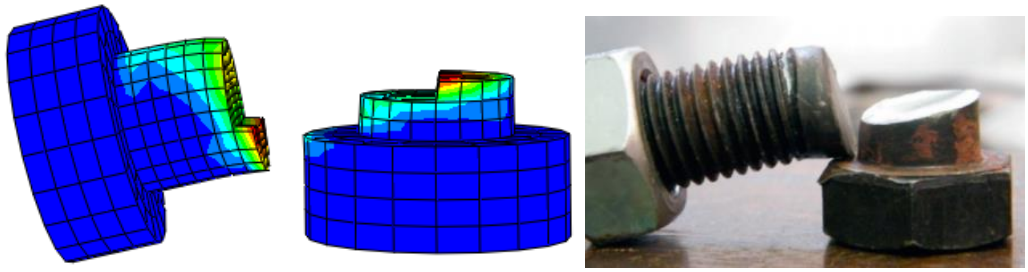

Figure 6.41 The simulated shear fracture and the test photo of bolt failure

In the component model without material damage introduced, the bolt shearing deformation can be extracted, as shown in Figure 6.42. It is represented by the relative displacement of the bolt head and nut along the load application line.

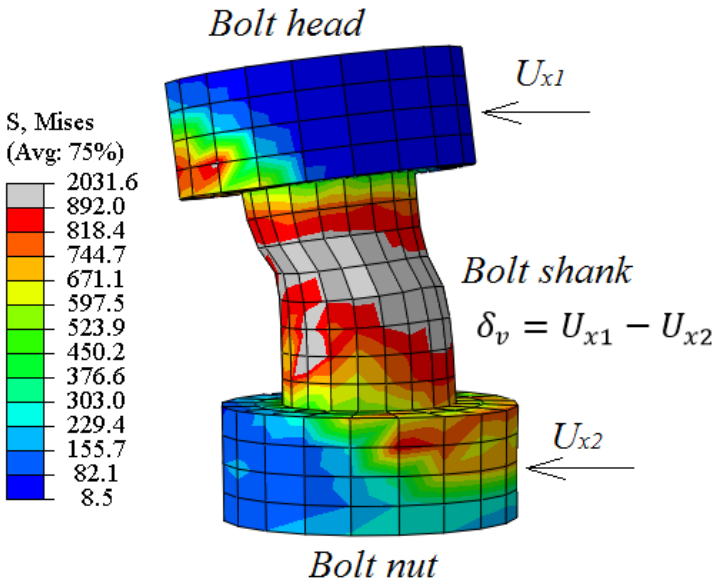

Figure 6.42 The deformation shape and stress distribution of the bolt

The time history of the shearing deformation can be plotted, as shown in Figure 6.43.

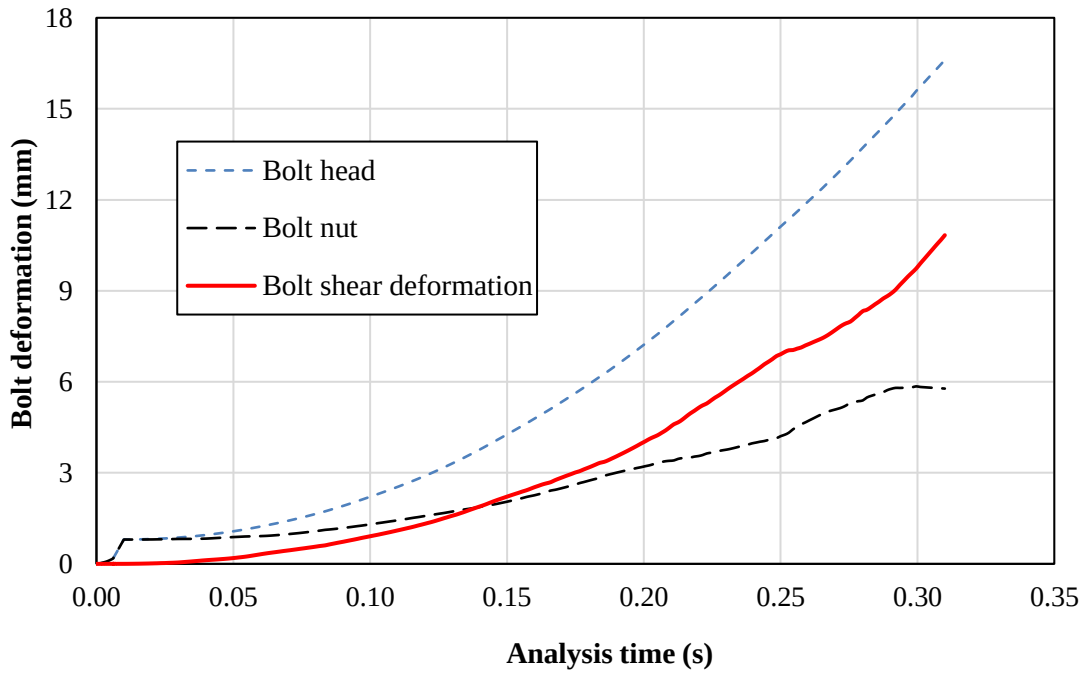

Figure 6.43 The development of bolt shear deformation

Thus, the shearing force-deformation curve can be generated for the bolt. The result can compared with the formulation of Sarraj (2007), as shown in Figure 6.44. The comparison clearly shows the discrepancy, and this needs to be rectified by modification of the formulation, as will be discussed later.

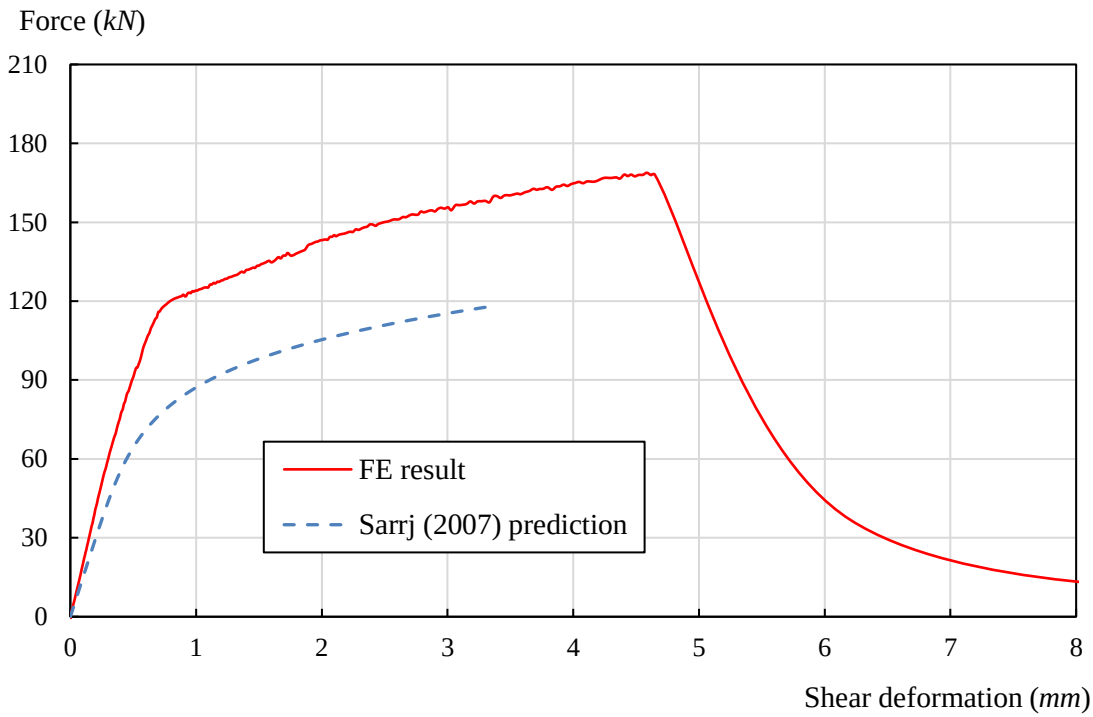

Figure 6.44 The comparison of the bolt shear shearing behaviour between FE result and existing formulation

6.6 Finite element modelling of plate in bearing and modified force-deformation

In order to examine the two main mechanisms contributing to the bolted lap-plate component behaviour more directly, the plate bearing and bolt shearing are investigated using two specially designed FE models. This subsection deals with the plate bearing mechanism.

6.6.1 Finite modelling cases and results

A model of single bolt bearing against single plate is created and analysed. To focus only on the bearing deformation, the M20 bolt shank is replaced by a rigid cylindrical body. In the ABAQUS model, an analytical rigid cylindrical surface (diameter = 20 mm) is created, which is bearing against the bolt-hole (diameter = 21.6 mm). The C3DI8 brick elements are used to model the steel plate. The material

failure is not included in the material properties. The plate is fixed on the left end side.

The displacement-controlled load is applied gradually to the rigid bolt in the horizontal direction. Explicit analysis is carried out to obtain the quasi-static behaviour. The rigid body displacement of the "bolt" and its reaction force are considered as the bearing deformation and bearing force, respectively.

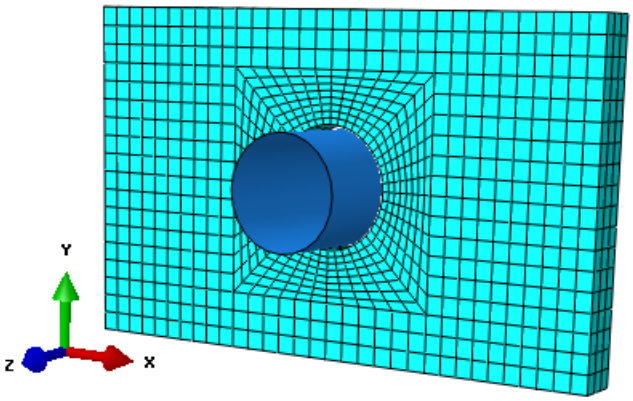

Figure 6.45 The finite element model of rigid bolt shank bearing against the plate

Two different edge distances (e = 1.5d_b, e = 2.5d_b) are considered for the plate, and the simulation results are illustrated in Figures 6.46-6.50. The edge distance e is measured from the bolt-hole centre to the top or bottom side of the bearing plate.

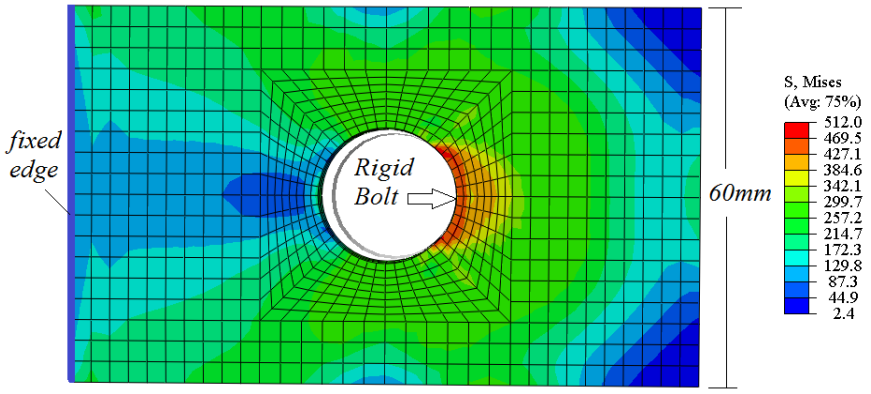

Figure 6.46 The yielding point of the plate and the start of necking deformation, at δ = 0.65 mm (plate width 60mm, e= 1.5d_b)

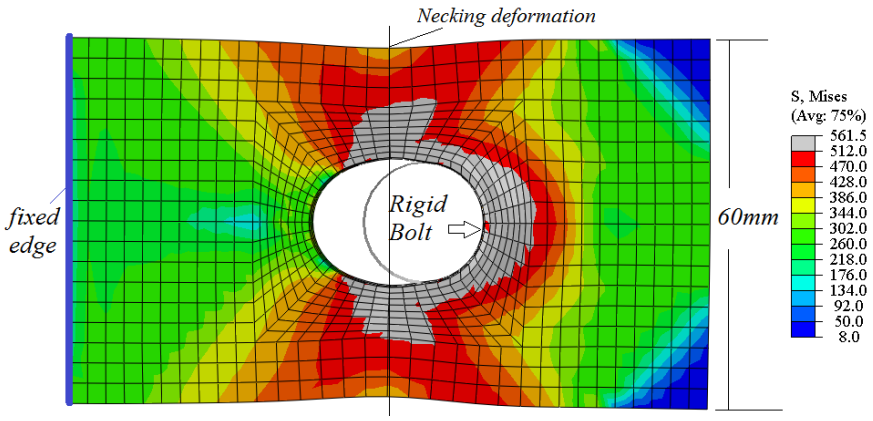

Figure 6.47 The necking deformation along the vertical bolt-hole centre line, at δ = 7mm (plate width 60mm, $e = 1.5d_b$)

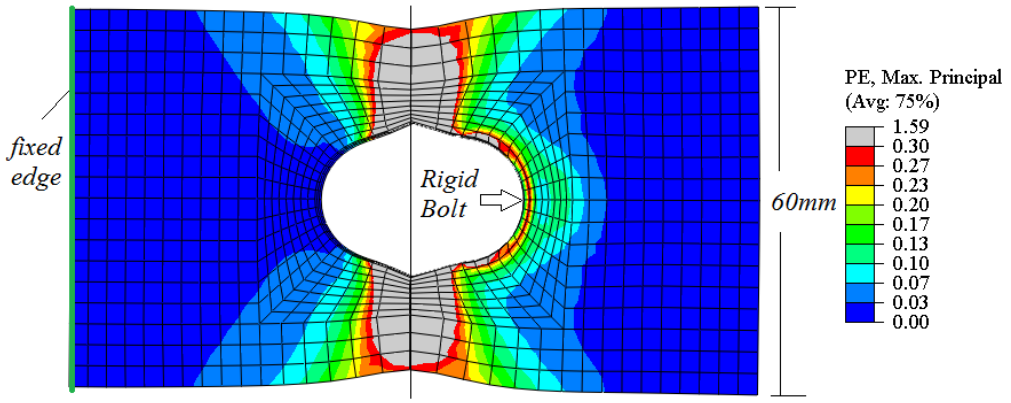

Figure 6.48 The plastic strain distribution and final failure of the plate in bearing, at δ = 11.5mm (plate width 60mm, $e = 1.5d_b$)

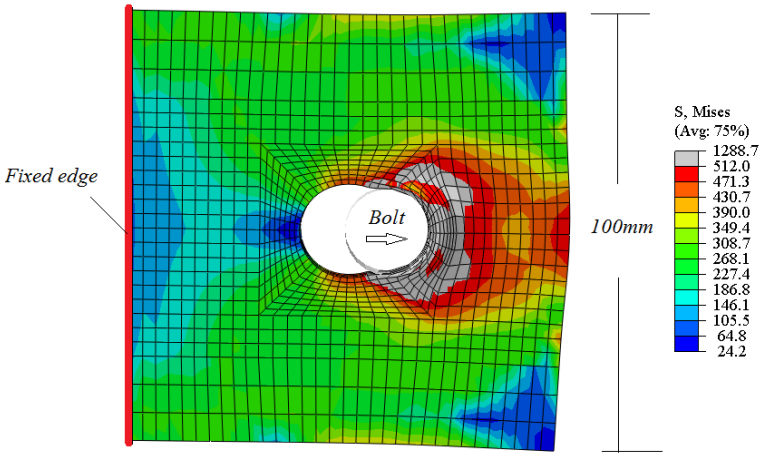

(a) The Von-Mises stress distribution

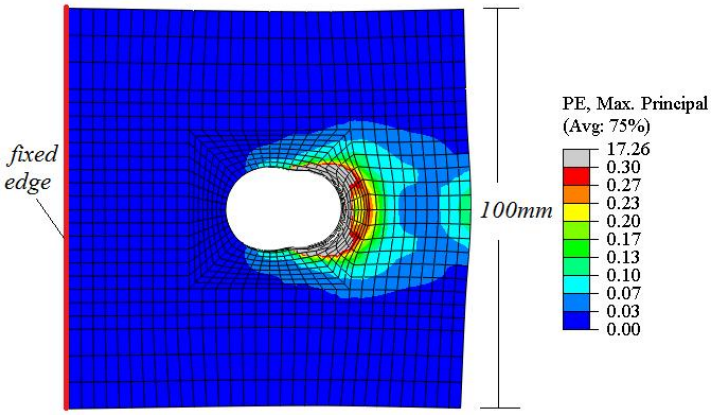

(b) The plastic strain stress distribution

Figure 6.49 The final deformation status of the plate in bearing, at δ = 9mm (plate width 100mm, $e = 2.5d_b$)

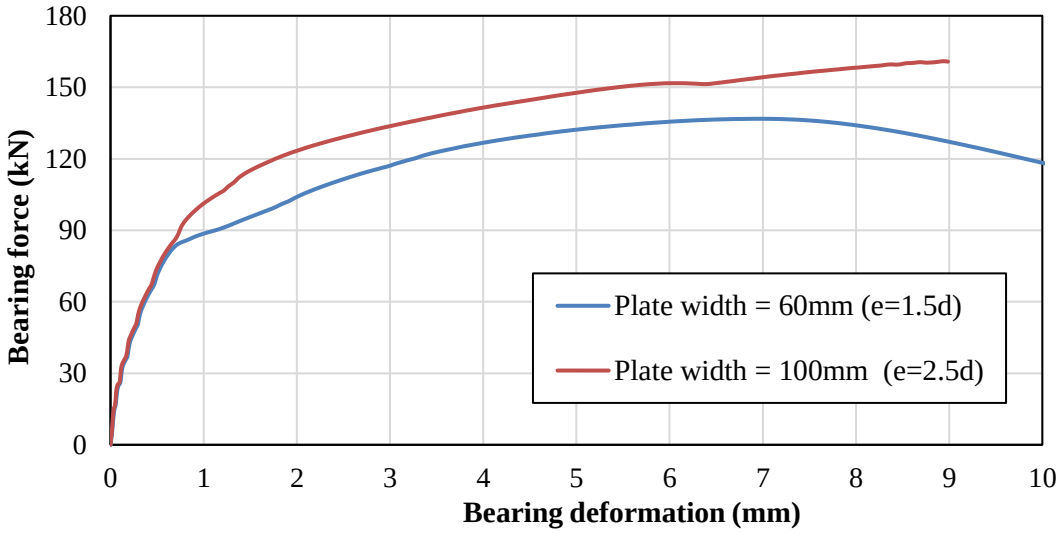

Figure 6.50 The bearing force-deformation relation for different plate widths

The modelling results shows that the plate width affects the bearing characteristics, including failure modes and the force-deformation relationship. For the edge distance of $e = 1.5d_b$, marked necking deformation near the bolt-hole comes into play, and a net section failure occurs. This phenomenon was not observed in the component set modelling result.

It should be noted that a net section failure is an unfavourable failure mode, as the bearing capacity of the plate is not utilized to prevent catastrophic failure. Such a

failure mode is not allowed under design codes. The result here for e = 1.5db tends to suggest that the British standard specification (Table 6.2) on the minimum design edge distance of e=1.2d_h may not be sufficient in preventing a net section failure.

Considering a standard situation where the edge distance is sufficient to avoid the occurrence of necking failure, the FE simulation result from the 100 mm plate width case, in which no necking failure occurred, is compared with the prediction by the formulation proposed by Rex and Easterling (2003) in Figure 6.51. As can be seen, the existing formulation underestimates the bearing force by 10-20% at a bearing deformation level up to 2.0 mm, whereas it overestimates the bearing deformation by as much as 40% under a given bearing force level. The discrepancy of deformations under a higher bearing force is even larger.

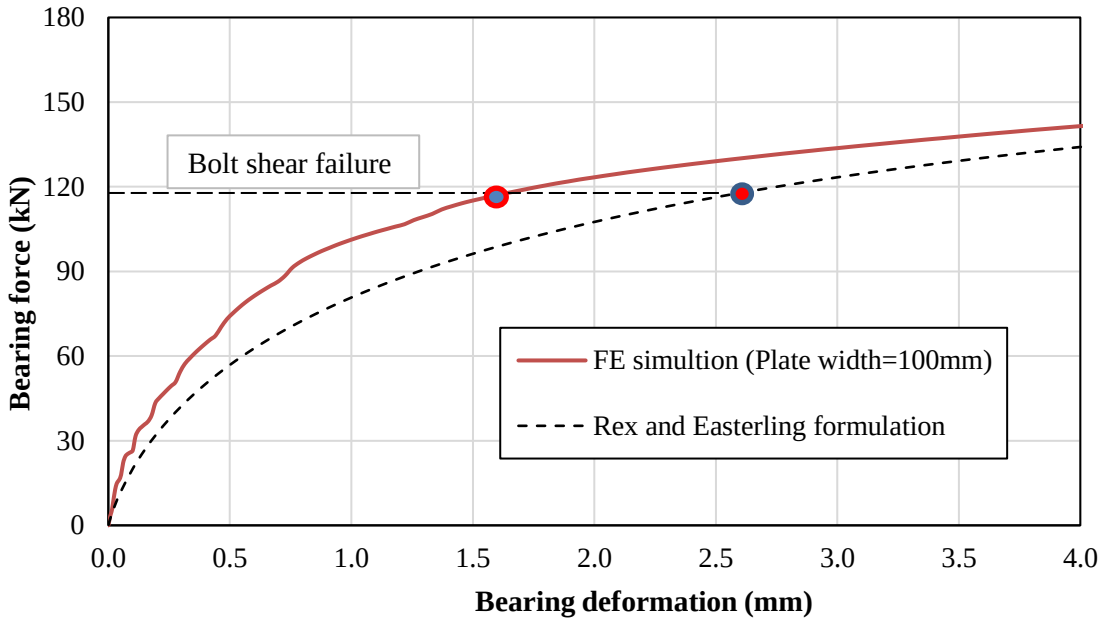

Figure 6.51 The FE analysis result of plate bearing compared with existing formulation

6.6.2 Modified bearing force-deformation formulation

First for the bearing capacity, as can be seen from Fig. 6.52, the difference towards the later stage of deformations or maximum bearing force is relatively small, so the current formulation using AISC (LRFD 1993) can still be used without modification.

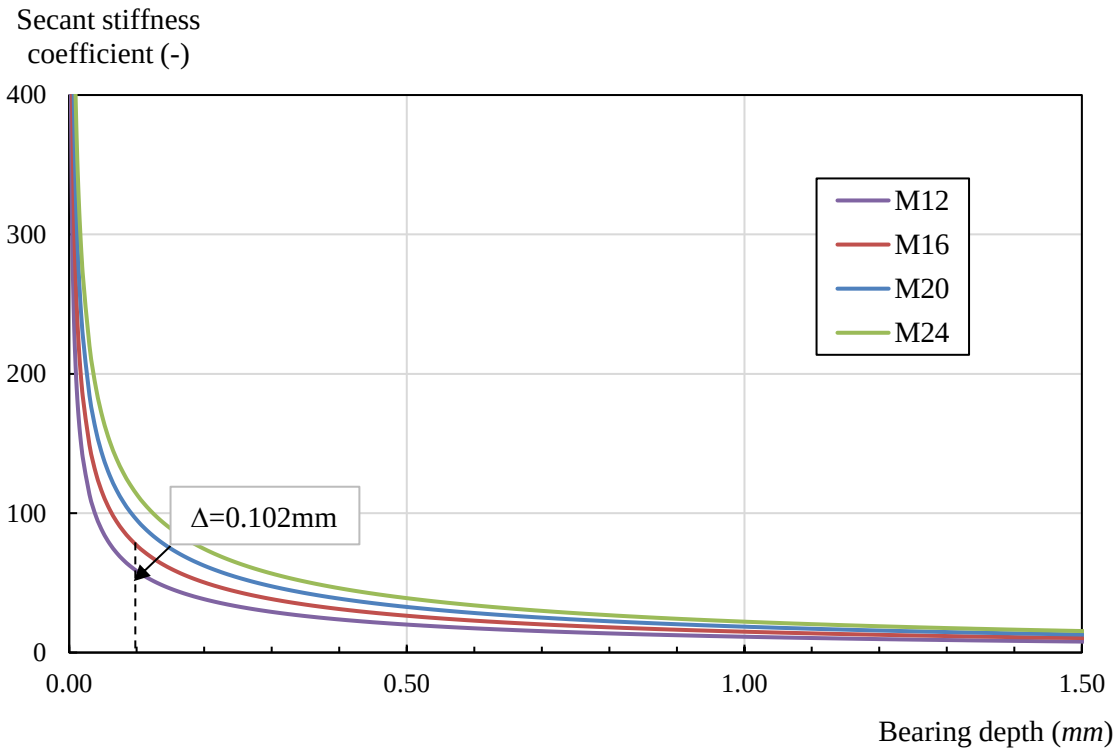

Figure 6.52 The calculated bearing stiffness coefficient under different bolts sizes

For the initial bearing stiffness, the existing formulation also appears to be acceptable. However, through calculation of the initial stiffness for various bolt sizes (Fig. 6.53), it is found that the relation between the stiffness coefficient ($\eta = K_{b,i}/(f_y t_p)$) and bolt diameter is generally proportional. This is shown in Figure 6.53, along with a linear curve-fit equation.

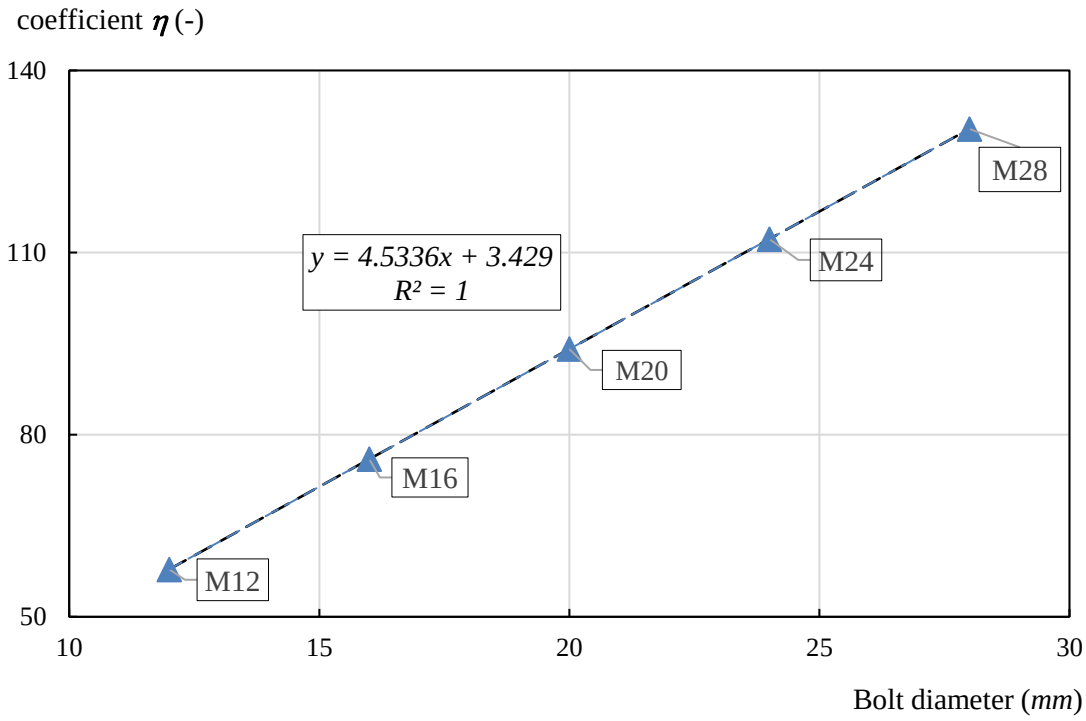

Figure 6.53 The proposed bearing stiffness coefficient with different bolt sizes

Therefore, the bearing stiffness coefficient is proposed to be a linear function of bolt diameter:

$$\eta = 4.6d_b + 3.5 \tag{6-27}$$

The newly proposed formulation of the initial bearing stiffness can be expressed as:

$$K_{b.i} = \eta f_y t_p = (4.6d_b + 3.5) f_y t_p \tag{6-28}$$

In terms of the mathematical expression for the bearing force – bearing displacement relationship, although the existing formulation by Rex and Easterling (2003) covers the entire bearing resistance function, it has two major shortcomings:

1) The calculation process is cumbersome. As has been discussed earlier, the initial bearing deformation alone dictates the overall deformation, so the bending and shearing stiffnesses of the plate do not need to be involved. The existing formulation for the initial stiffness is not explicit and straightforward to calculate.

2) The existing model is not explicit, and most importantly, it does not indicate reasonable physical meaning. For instance, the calculated bearing capacity $F_{b,u}$ is not consistent with the peak point in the curve produced by the equation.

Herein, a new formulation is proposed taking into account the bearing capacity and stiffness as discussed earlier. The expression is based on a simplified Richard equation, which has clear physical meaning.

The Richard equation is an effective function to represent any bi-linear behaviour. It was proposed by Richard and Abbott (1975), initially aimed to express the elastic-plastic stress-strain formula. It was later applied by Attiogbe and Morris (1991) to approximate the nonlinear behaviour of the moment-rotation curves for partially restrained connections, by curve-fitting the function to experimental moment-rotation data.

The Richard equation requires four parameters, as shown in Equation (6-29) and Figure 6.54. Parameters K, K_p and R_0 represent elastic and plastic stiffnesses and a transitionary force limit, respectively, while n is a shape parameter to better approximate the transition from elastic to plastic responses.

$$R(\Delta) = \frac{(K - K_p)\Delta}{\left[1 + \left|\frac{(K - K_p)\Delta}{R_0}\right|^N\right]^{\frac{1}{N}}} + K_p\Delta \tag{6-29}$$

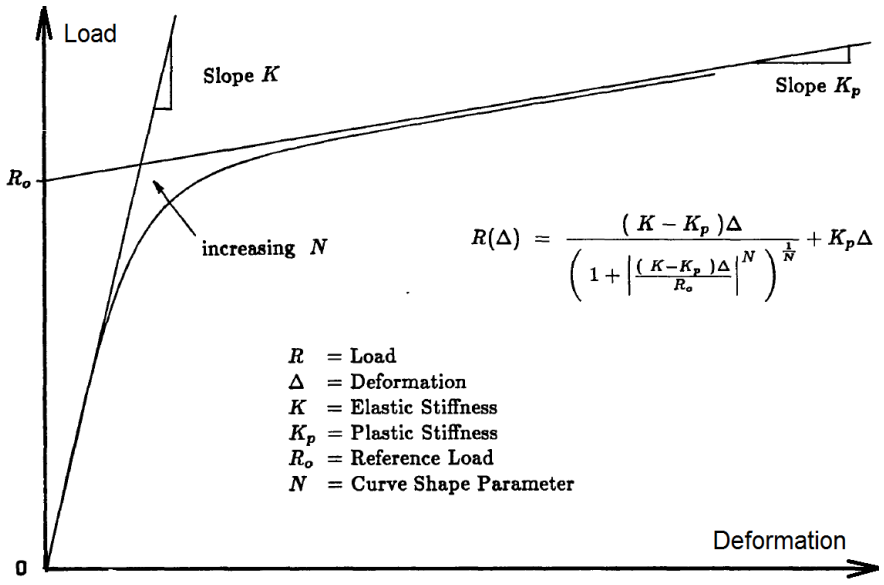

Figure 6.54 The Richard equation to formulate load-deformation (Richard and Abbott 1975)

Notably, for the increasing *n* value, the Richard equation gradually approaches a bilinear elastic-plastic function. Thus all three types of elastic-plastic component behaviour can be effectively covered.

1) When $K_p = 0$, the equation can represent the elastic-perfectly plastic behaviour;
2) When $K_p > 0$, the function can represent the elastic-plastic softening behaviour;
3) When $K_p < 0$, the function can represent the elastic-plastic degradation behaviour.

In order to use the equation to describe the bearing force-deformation function, the parameters are defined as follows, considering both representativeness and simplicity (Fig. 6.55):

1) $K = K_{b,i}$, i.e. the initial stiffness is equal to the initial bearing stiffness itself.
2) $K_p = 0$. The curve is made to be similar to the type of elastic-perfect plastic pattern with an asymptotic strength line.
3) $F_0 = F_{b,u}$. The curve is made to approach the maximum value of the bearing capacity.
4) The curve parameter *n* is set to be equal to 1.

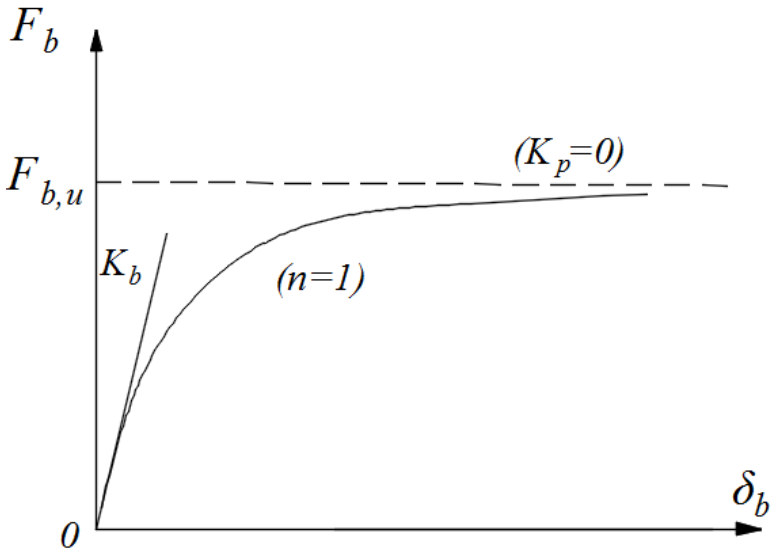

Figure 6.55 The proposed bearing force-deformation function using modified Richard equation

The equation is thus written in a simple form as:

$$F_b = \frac{K_{b,i}\delta_b}{1 + K_{b,i}\delta_b / F_{b,u}} \tag{6-30}$$

It can also be re-written as a more explicit formulation:

$$\frac{1}{F_b} = \frac{1}{K_{b,i}\delta_b} + \frac{1}{F_{b,u}} \tag{6-31}$$

The above proposed equation is applied to the fin plate bearing in the example application, and the generated bearing force – bearing deformation curve is compared against the FE simulation result in Figure 6.56. As can be observed, they are in very good agreement.

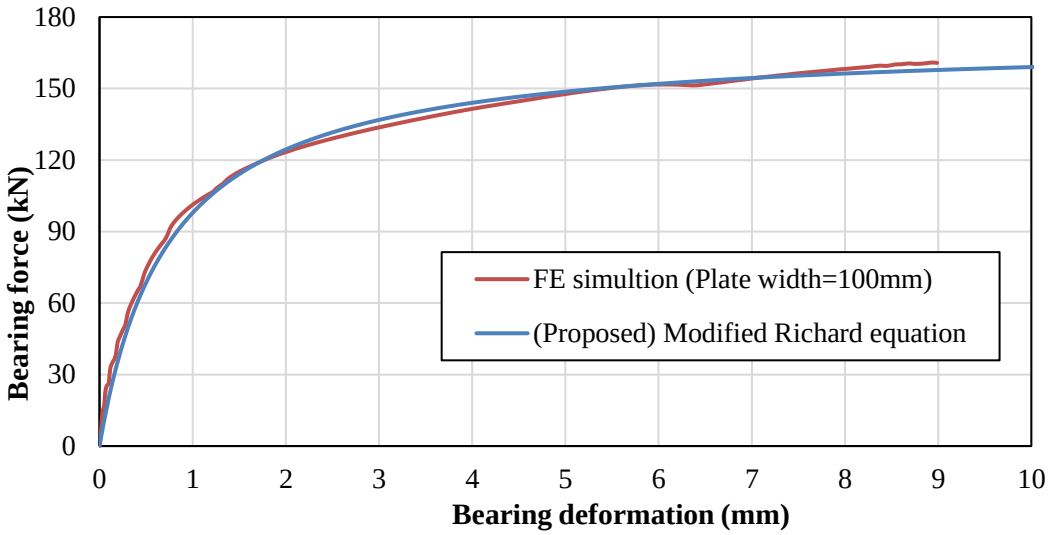

Figure 6.56 The proposed bearing formulation validated against FE modelling result

6.7 Finite element modelling of the bolt shearing and modified force-deformation formulation

6.7.1 Finite element modelling cases and results

As has been discussed, the bolt-inclination deformation is prevented in a double shear test or modelling, due to symmetry. However, as can be expected and also shown in the previous numerical modelling of the component set in Section 6.7, the bolt-inclination and the associated tension and bending deformations can significantly affect the bolt shearing capacity and the total "shearing" deformation.

Therefore, the single shear behaviour of Grade 8.8 M20 bolt is investigated within the component set. The two connected plate are assumed to be purely elastic, with a large elastic modulus. Thus, the bolt shearing deformation can be effectively investigated. Fig. 6.57 shows a finite element model to investigate the bolt shearing deformation.

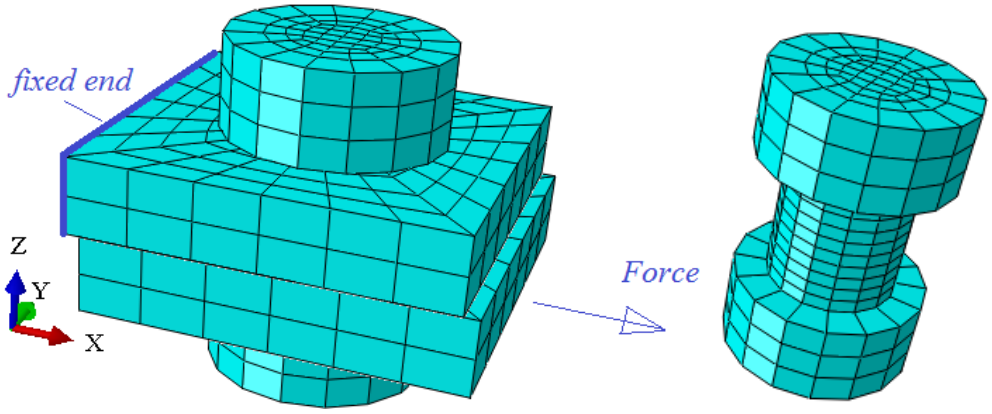

Figure 6.57 The finite element model to investigate the bolt shear deformation

With a fracture strain of 0.30 defined for the bolt material, different fracture strains (G_f) are assumed, and the results demonstrate again that G_f has insignificant effect on the bolt shearing resistance function, as shown in Figure 6.58. The bolt shear failure is also consistent with the brittle manner (Figure 6.59).

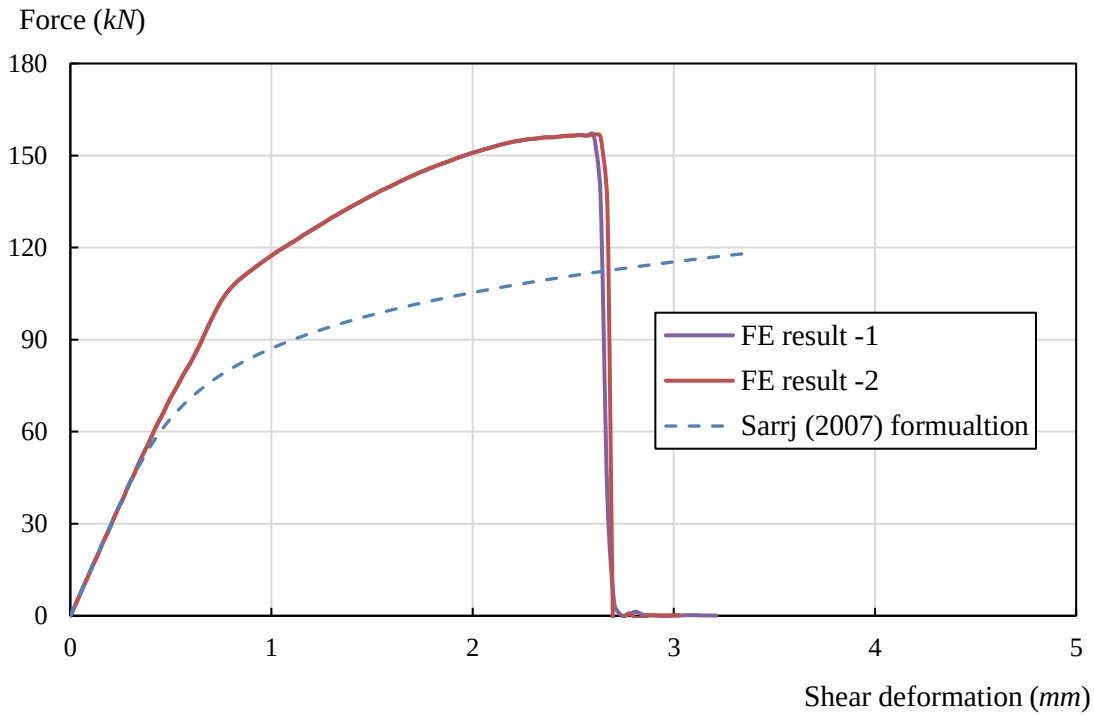

Figure 6.58 The modelling result of bolt shearing behaviour compared with the prediction of existing formulation

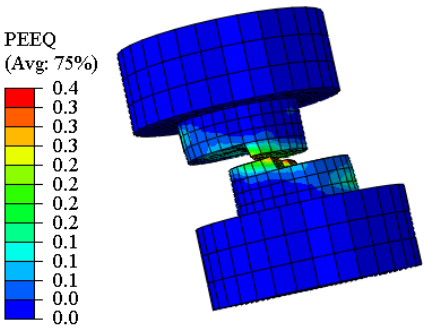

Figure 6.59 The shear fracture of the bolt in the component assembly

It is clear that the loading resistance is significantly underestimated by the existing formulation. The ultimate shearing deformation is consistent between the simulation result and the calculated values.

6.7.2 Modified shearing force-deformation formulation

It is obvious that, in the component set, the bolt shearing force calculated according to the pure shear assumption should be enhanced to better present the stress condition in the component set condition due to the combined deformations. Through the curve-fitting technique based on the Ramberg-Osgood function, the modified formulation is proposed as expressed in Equation (6-32). The modified equation is compared with the FE results in Figure 6.60, which shows good agreement.

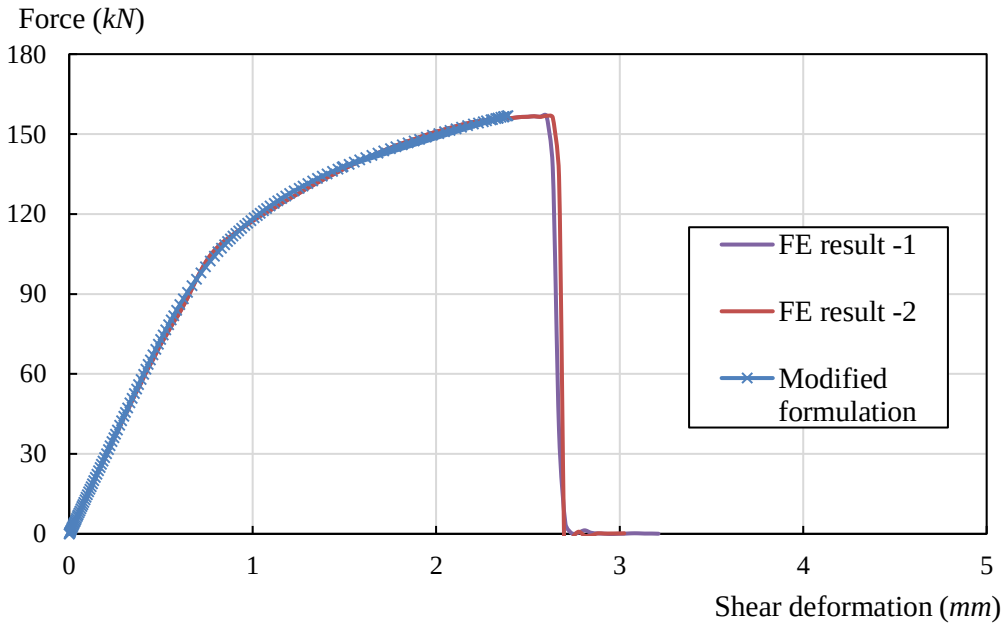

Figure 6.60 The modified bolt shearing formulation and validation against FE results

$$\delta_v = \frac{F_v}{k_{vb}} + 0.2\left(\frac{F_v}{F_{vb}}\right)^{6.6} \quad (6\text{-}32)$$

where F_{vb} is the design shearing capacity, k_{vb} is the shearing stiffness.

Another commonly used high-strength bolt M16 is further modelled in the corresponding component set. For the Grade 8.8 M16 bolt, the calculated shearing resistance and stiffness are:

$$F_{v,Rd} = 0.6 n_b f_{ub} A_b = 0.6 \times 1 \times 800 \times 157 = 75.36kN$$

$$K_{v,b} = \frac{0.15GA_b}{d_b} = 0.15 \times 81000 \times \frac{157}{16} = 106.0kN/mm$$

The modelling shearing force and deformation are extracted and plotted in Figure 6.61. The shearing resistance function calculated using the modified equation (6-32) is also presented in the same figure. It can be observed that the modified equation also works well for the Grade 8.8 M16 high strength bolt in the single shear component.

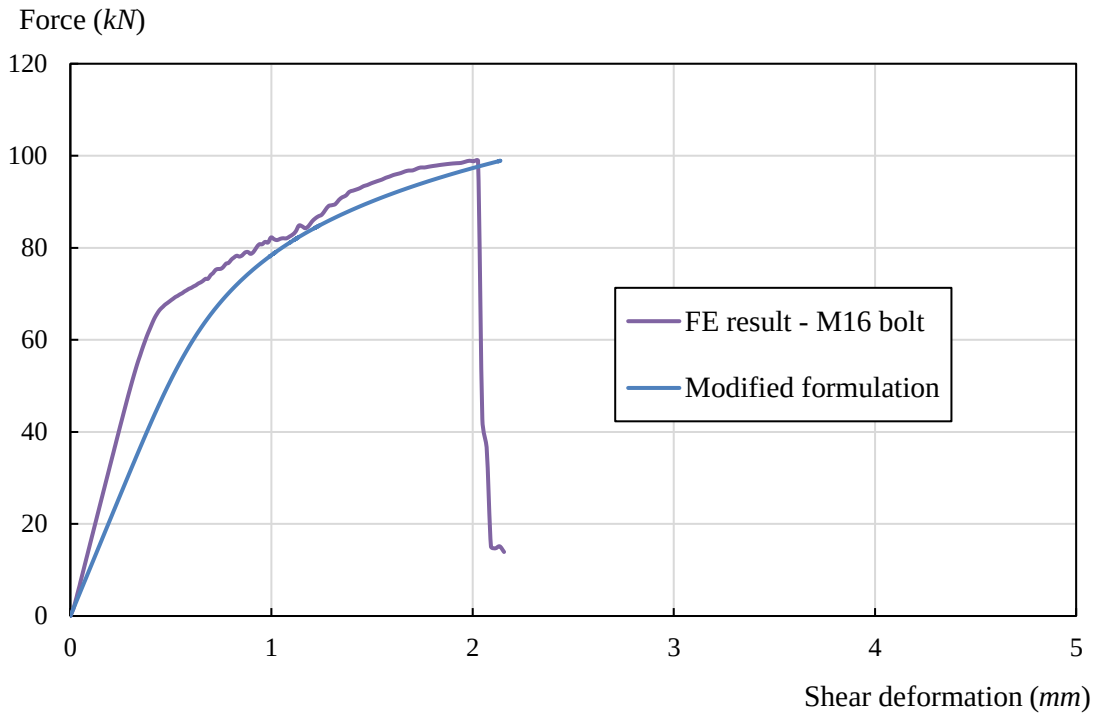

Figure 6.61 Validation of the modified bolt shearing function against modelling result of Grade 8.8 M16 bolt in single shear

6.8 The updated analytical solutions using modified component properties

The modified formulations for the bearing and bolt shearing properties are applied to the same previous example. As shown in Figure 6.62, the updated component behaviour function has good agreement with the FE modelling result. The new ultimate deformation is still determined when the bolt shearing fracture occurs at a bolt shearing deformation of 2.5 mm, and accordingly the ultimate deformation for the example component set is found to be $\delta_u = 8.9\ mm$.

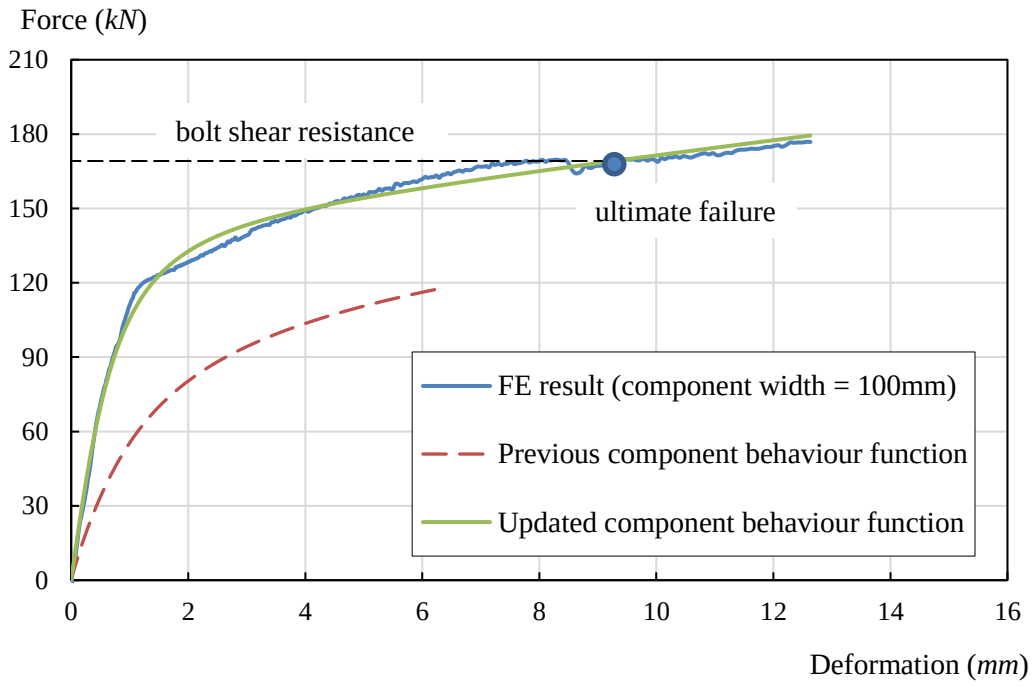

Figure 6.62 The updated component behaviour function and comparison with the FE result

The component behaviour function is implemented in the analytical framework to re-calculate the resistance function for the beam assembly, and the produced results are presented in Figure 6.63. The contributions from flexural and catenary force are also included. As is shown, the updated solution improves significantly and compares reasonably with the test result, including both the ultimate loading resistance and

ultimate deformation limit. The remaining difference in the ultimate loading capacity may be partly caused by neglecting the frictional force during the initial stage.

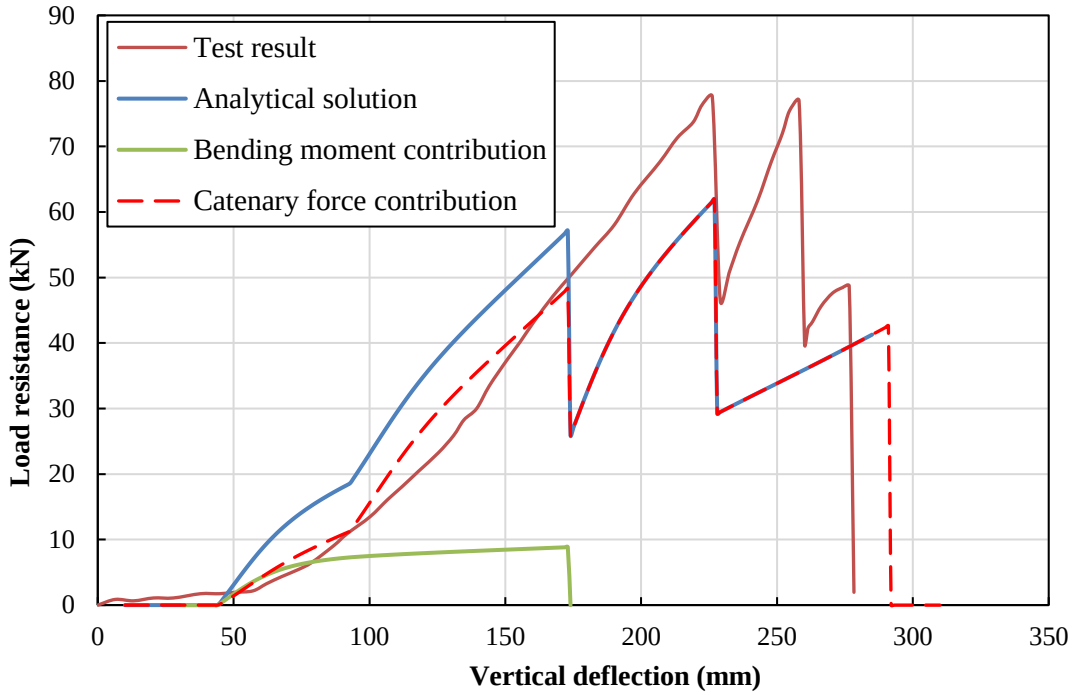

Figure 6.63 The updated analytical result of global resistance function of the double beam assembly

The key failure events, which is still due to bolt shearing fracture, are analytically predicted. The corresponding deflection levels and other details of the component are extracted and tabulated in Table 6.9.

Table 6.9 The analytical results of the component failure points

Characteristic failure points	**1**	**2**	**3**
Deflection	ω = 173mm	ω = 186mm	ω = 276mm
Rotation $\theta = w/L$	θ = 0.08rad (4.3 *degrees*)	θ = 0.08rad (4.7 *degrees*)	θ = 0.12rad (6.8 *degrees*)
Component 1 **(top)**	$F_1 = 0\ kN$ $\delta_1 = 1.6\ mm$	$F_1 = 143.8\ kN$ $\delta_1 = 5.0\ mm$	$F_1 = 168.1\ kN$ $\delta_1 = 10.9\ mm$
Component 2 (middle)	$F_2 = 151.0\ kN$ $\delta_2 = 6.2\ mm$	$F_2 = 168.4\ kN$ $\delta_2 = 10.9\ mm$	
Component 3 (bottom)	$F_3 = 167.8\ kN$ $\delta_3 = 10.7\ mm$		

It can be seen that the first failure point corresponds to the bottom bolt reaching the ultimate shearing capacity, while the top bolt ($\delta_1 = 1.6\ mm$) just passes the slippage phase and come into contact with fin-plate. After this point, all the components are in tension and the bolt shearing fracture controls the component failures.

6.9 Summary

This chapter presents the analytical modelling of fin-plate connections, especially the modelling and formulations for the bolt lap-plate component.

Existing formulations describing the plate bearing and bolt shearing behaviour are integrated to establish a complete description of the constitutive properties of the bolted lap-plate component set. These critical component properties are implemented into the developed analytical framework to construct the resistance functions and predict the key failure events.

The analytical results are compared against the available experimental test data to assess the soundness of the component formulations. Based on the comparison, it was found that both the load resistance and the ultimate deflection of the beam assembly tend to be significantly underestimated using the integrated model formulations.

To assist in the modification of the model, high-fidelity finite element analysis has been carried out for the whole bolted lap-plate component set, as well as specially configured scenarios for the plate bearing and bolt shearing mechanisms, respectively. Based on the finite element results and basic mechanics analysis, proposals for the modification of the plate bearing and bolt shearing behaviour functions are put forward.

The modifications are then implemented back into the component set model, and the case examples are re-analysed using the modified component set properties. The results confirm that the modifications are reasonable and effective.

From a generality perspective, the modelling study presented in this chapter provides an effective approach to establishing a reliable component behaviour function, from which the analytical framework as developed in Chapter 5 can be employed to quickly assess the ultimate load and deformation capacities of the critical double-span beam assembly.

It should be mentioned that the quantitative modifications proposed in this chapter are applicable for fin plate connections with typical bolt and plate properties. For more general applications, further parametric studies to cover a wider range of bolt and plate selections would need to be conducted, in a similar procedure as presented in this chapter.

7 Conclusions and prospect of future work

This thesis is devoted to investigating realistic full-range behaviour of and ultimate failure criteria of the double beam assembly under column loss. The primary conclusions are summarized as below.

7.1 Experimental findings

Two groups of tests have been carried out on six reduced-scale double-beam assemblies to characterise the detailed local plastic deformation mechanisms and their influences on the advanced and post-bending behaviour of the substructures. The tests presented have been exploratory with a particular interest in examining the correlation between the governing local failure mechanism and the global deformability, and hence the potential of developing effective catenary action.

The test results revealed that the double beam assemblies went through elastic and plastic bending stages. The axial force developed in the beam contributed significantly to the global vertical resistance, and the tested assemblies exhibited quite desirable deformation capacities. However, the load resistance rarely recovered again after a major local failure occurred, and the final collapses were following quite closely.

The outcome highlighted the crucial importance of enabling the plastic deformation to “spread” in order to ensure more plastic deformation capacity in the plastic zones, and thereby a sufficient global deflection capacity for the development of an effective catenary action. The axial capacities of the connections are also important for the large deformation to develop. The observations pave a way for subsequent study into quantification of the total plastic deformation capacity of typical join designs and the corresponding prediction methods.

In addition to the general observations, the experimental exploration also paves a way for the future experimental and numerical studies to focus on the design details in typical connection types and how they transpire into the actual development of the plastic regions and effective catenary action.

7.2 Analytical and modelling studies

7.2.1 Simplified solid beam

A generic beam under axial constraint has been investigated to allow theoretical derivation and quantitative examination into the plastic deformation concentration and how it affects the resistance function for a double beam.

Through the derivation, a theoretical relationship between the material strain and the global deformation capacity is formulated, and from there, the importance of plasticity spread over a sizable plastic region is clearly shown.

This part of the work also helped the identification of the focuses in an investigation into a realistic beam-column substructure in a progressive collapse scenario, namely plastic deformation concentration, local failure limits, and the governing role these play in determining the overall behaviour and ultimate resistance in the large deformation regime.

7.2.2 Double beam assembly with realistic steel joints

A simplified and explicit analytical framework has been developed to predict the full-range load-deflection response of a double-span beam assembly with typical steel joints. The analytical solution is carried out based on parallel component spring modelling, and the force equilibrium and deformation compatibility conditions.

The proposed analytical framework provides an effective and executable approach to establish the full-range resistance function of a double-span beam assembly under internal column loss. The solution process also enables further interpretation of results, in terms of the contributions of the flexural action and catenary axial force to the vertical load resistance.

The analytical framework has been verified on the double beam assembles with web cleat and TSWA joints using experimental data from the literature. The existing formulations for the bolted double-angle component are summarized and employed

to establish the constitutive properties of the discretised components. The analytical results show good agreement with the test results, especially in terms of the peak load resistance and ultimate deformation limits.

Furthermore, the double beam assembly with fin-plate connections is investigated using the proposed analytical framework. The existing models and formulations to describe the plate bearing and bolt shearing behaviour are integrated to establish the constitutive properties of the bolted lap-plate component set. The critical component properties are then implemented into the developed analytical framework, to work out the solutions of resistance functions and predict the key failure events. Verification of the lap-plate component model using the analytical framework with relevant experimental data show generally favourable agreement; however, deficiencies in the definition of the lap-plate component properties were also exposed.

Through high-fidelity finite element analysis, modifications to the plate bearing and bolt shearing behaviour functions are proposed, leading to improved formulations to the lap-plate component properties. The analytical results using the modified formulations for the fin-plate connections show good results with the experimental data.

7.3 Proposed future work

The outcome of analytical studies in this thesis has laid a basis and platform for future analysis of the realistic behaviour of the structural joints and the overall response of the beam-assembly substructures in a progressive collapse scenario. With the availability of the analytical solution, the key to the reliability and soundness in the analysis of the resistance function lies upon the adequacy and accuracy of the description of the joint components.

Although a range of joint components is generally available from the literature, some are still not properly formulated or validated especially for applications in the large deformation regime. Some other steel frame variants, such as composite beams with reinforced concrete flanges (slab), profiled steel decking, fillet/butt welds, etc., require detailed investigation for the establishment of the corresponding component

properties. When the component properties are available, they can be readily implemented into the component joint model and the beam assembly can then be analysed using the proposed analytical framework.

Therefore, future work should be extended with the objective to cover more joint types, so that the component-based analytical framework can be applied for general progressive collapse analysis in engineering practice.

References

Abaqus Analysis User's Manual, version 6.12, ABAQUS Inc.

Antolovich SD and Armstrong RW (2014). "Plastic strain localization in metals: origins and consequences." Progress in Materials Science; 59(Supplement C): 1-160.

European Commitee for Standardisation (1993), ENV 1993-1-1, Eurocode 3: Design of steel structures - General rules and rules for buildings, Brussel.

American Institute of Steel Construction (1993), Load and Resistance Factor Design Specification for Structural Steel Building, Chicago, IL

American Institute of Steel Construction (1999), Load and Resistance Factor Design Specification for Structural Steel Building, Chicago, IL

Attiogbe E and Morris G (1991). "Moment-rotation functions for steel connections." Journal of Structural Engineering; 117(6): 1703-1718.

Bathe K-J (1982). Finite Element Procedures in Engineering Analysis. Englewood Cliffs, New Jersey, Prentice Hall, Inc.

Bradford MA, Nethercot DA, Gardner L (2008). The behaviour and design of steel structures to EC3, Fourth Edition, Published by: Taylor & Francis.

Bursi OS and Jaspart JP (1998). "Basic issues in the finite element simulation of extended end plate connections." Computers & Structures; 69(3): 361-382.

Buick Davison, Graham W. Owens (2011). Steel Designers' Manual, 7th Edition, The Steel Construction Institute.

Dat PX, Tan KH and Yu J (2015). "A simplified approach to assess progressive collapse resistance of reinforced concrete framed structures." Engineering Structures; 101: 45-57.

Davison B and Owens GW (2011). Steel Designers' Manual, 7th Edition, The Steel Construction Institute.

Del Savio AA, Nethercot DA, Vellasco P, Andrade S and Marth LF (2009). "Generalised component-based model for beam-to-column connections including axial versus moment interaction." Journal of Constructional Steel Research; 65(8): 1876-1895.

DoD (2009). UFC 4-023-3: Design of Buildings to Resist Progressive Collapse, U. S. Department of Defence.

Faella C, Piluso V and Rizzano G (2000). Structural steel semirigid connections: theory, design, and software. Boca Raton, Florida, United States, CRC Press, LLC.

Fisher JW and Struik JHA (1974). Guide to Design Criteria for Bolted and Riveted Joints. New York, Wiley.

Fahim Sadek, Joseph A. Main, H. S. Lew and Yihai Bao (2011). "Testing and analysis of steel and concrete beam-column assemblies under a column removal scenario." Journal of Structural Engineering; 137(9): 881-892.

Guo LH, Gao S, Fu F and Wang YY (2013). "Experimental study and numerical analysis of progressive collapse resistance of composite frames." Journal of Constructional Steel Research; 89(0): 236-251.

Hou Jian and Yang Zheng (2014). "Simplified models of progressive collapse response and progressive collapse-resisting capacity curve of rc beam-column substructures." Journal of Performance of Constructed Facilities; 28(4): 04014008.

Huber G and Tschemmernegg F (1998). "Modelling of beam-to-column joints: Test evaluation and practical application." Journal of Constructional Steel Research; 45(2): 199-216.

Hillerborg A, Modeer M and Petersson PE (1976). "Analysis of crack formation and crack growth in concrete by means of fracture mechanics and finite elements." Cement and Concrete Research; 6(6): 773-781.

Izzuddin BA (2005). "A simplified model for axially restrained beams subject to extreme loading." International Journal of Steel Structures; 5(5): 421-429.

Konkong N and Phuvoravan K (2017). "An analytical method for determining the load distribution of single-column multibolt connection." Advances in Civil Engineering; 2017: 19 pages.

Khandelwal K and El-Tawil S (2007). "Collapse behavior of steel special moment resisting frame connections." Journal of Structural Engineering; 133(5): 646-655.

Kapil Khandelwal, Sherif El-Tawil, Sashi K. Kunnath and H. S. Lew (2008). "Macromodel-based simulation of progressive collapse: steel frame structures." Journal of Structural Engineering; 134(7): 1070-1078.

Lemonis ME and Gantes CJ (2009). "Mechanical modeling of the nonlinear response of beam-to-column joints." Journal of Constructional Steel Research; 65(4): 879-890.

Liu C, Tan KH and Fung TC (2015). "Component-based steel beam–column connections modelling for dynamic progressive collapse analysis." Journal of Constructional Steel Research; 107: 24-36.

Lemonis ME and Gantes CJ (2009). "Mechanical modeling of the nonlinear response of beam-to-column joints." Journal of Constructional Steel Research; 65(4): 879-890.

Ling Li, Wei Wang, Yiyi Chen, Yong Lu (2013). "Experimental investigation of beam-to-tubular column moment connections under column removal scenario." Journal of Constructional Steel Research; 88(0): 244-255.

Ling Li, Wei Wang, Yiyi Chen, Yong Lu (2015). "Effect of beam web bolt arrangement on catenary behaviour of moment connections." Journal of Constructional Steel Research; 104(0): 22-36.

Li GQ, Wang KQ, Liu YS and Chen SW (2012). "Catenary action of restrained steel beam against progressive collapse of steel frameworks." Journal of Central South University; 19(2): 537-546.

Martin LH and Purkiss JA (1992). Structural Design of Steelwork to BS 5950, Published by: Edward Arnold.

Mosalam KM and Paulino GH (1997). "Evolutionary characteristic length method for smeared cracking finite element models." Finite Elements in Analysis and Design; 27(1): 99-108.

Mariati Taib and Ian Burgess (2013). "A component-based model for fin-plate connections in fire." Journal of Structural Fire Engineering Mechanics; 4(2): 113-122.

Paulay T and Priestly MJN (1992). Principles of Member Design. Seismic Design of Reinforced Concrete and Masonry Buildings, John Wiley & Sons.

Paulay T and Priestly MJN (1992). Principles of member design. seismic design of reinforced concrete and masonry buildings, John Wiley & Sons.

Pavlović M Marković Z, Veljković M and Buđevac D (2013). "Bolted shear connectors vs. headed studs behaviour in push-out tests." Journal of Constructional Steel Research; 88: 134-149.

Piluso V, Faella C and Rizaano G (2001). "Ultimate behavior of bolted T-stubs. I: theoretical model." Journal of Structural Engineering; 127(6): 686-693.

Ramberg W and Osgood WR (1943). Description of stress–strain curves by three parameters. Technical Note No. 902. National Advisory Committee For Aeronautics, Washington DC.

Rex CO and Easterling WS (2003). "Behavior and Modeling of a Bolt Bearing on a Single Plate." Journal of Structural Engineering; 129(6): 792-800.

Richard RM and Abbott BJ (1975). "Versatile elastic-plastic stress-strain formula." Journal of Engineering Mechanics; 101(4): 511-515.

Shi Gang and Chen Xuesen (2017). "Moment-rotation curves of ultra-large capacity end-plate joints based on component method." Journal of Constructional Steel Research; 128: 451-461.

Stylianidis PM and Nethercot DA (2015). "Modelling of connection behaviour for progressive collapse analysis." Journal of Constructional Steel Research; 113: 169-184.

Stylianidis PM, Nethercot DA, Izzuddin BA and Elghazouli AY (2015). "Modelling of beam response for progressive collapse analysis." Structures; 3: 137-152.

Sadek F, El-Tawil S and Lew HS (2008). "Robustness of composite floor systems with shear connections: modeling, simulation, and evaluation." Journal of Structural Engineering; 134(11): 1717-1725.

Sarraj M (2007). The behaviour of steel fin plate connections in fire. PhD thesis. University of Sheffield.

Shen J and Astaneh-Asl A (1999). "Hysteretic behavior of bolted-angle connections." Journal of Constructional Steel Research; 51(3): 201-218.

Shen J and Astaneh-Asl A (2000). "Hysteresis model of bolted-angle connections." Journal of Constructional Steel Research; 54(3): 317-343.

Stylianidis PM, Nethercot DA, Izzuddin BA and Elghazouli AY (2016). "Robustness assessment of frame structures using simplified beam and grillage models." Engineering Structures; 115: 78-95.

Tanaka A, Masuda H, Takagi M and Hisada T (1996). "Experimental study on the static characteristics of the WBFW type beam-to-column connections." Journal of Structural and Construction Engineering (Transactions of AIJ); 61(484): 121-130.

Weigand JM and Berman JW (2014). "Integrity of Steel Single Plate Shear Connections Subjected to Simulated Column Removal." Journal of Structural Engineering; 140(5): 04013114.

Yang B and Tan KH (2012). "Numerical analyses of steel beam–column joints subjected to catenary action." Journal of Constructional Steel Research; 70(0): 1-11.

Yang B and Tan KH (2013). "Experimental tests of different types of bolted steel beam–column joints under a central-column-removal scenario." Engineering Structures; 54(0): 112-130.

Yang B, Tan KH and Xiong G (2015). "Behaviour of composite beam–column joints under a middle-column-removal scenario: component-based modelling." Journal of Constructional Steel Research; 104(0): 137-154.

Yin YZ and Wang YC (2005). "Analysis of catenary action in steel beams using a simplified hand calculation method, Part 1: theory and validation for uniform temperature distribution." Journal of Constructional Steel Research; 61(2): 183-211.

Yang B and Tan KH (2012). "Numerical analyses of steel beam–column joints subjected to catenary action." Journal of Constructional Steel Research; 70(0): 1-11.

Yang B and Tan KH (2013). "Experimental tests of different types of bolted steel beam–column joints under a central-column-removal scenario." Engineering Structures; 54(0): 112-130.

Yang B and Tan KH (2013). "Robustness of bolted-angle connections against progressive collapse: Mechanical modelling of bolted-angle connections under tension." Engineering Structures; 57(0): 153-168.

Yu HX, Burgess IW, Davison JB and Plank RJ (2009). "Experimental investigation of the behaviour of fin plate connections in fire." Journal of Constructional Steel Research; 65(3): 723-736.

Zhao XM, Wu YF, Leung AY, Lam HF(2011). "Plastic Hinge Length in Reinforced Concrete Flexural Members." Procedia Engineering; 14(Supplement C): 1266-1274.

Zhong WH, Meng B and Hao JP (2017). "Performance of different stiffness connections against progressive collapse." Journal of Constructional Steel Research; 135: 162-175.

Appendix: List of publications

Xiaobo Cheng, Yong Lu. Composite Beam-Slab Floor System against Progressive Collapse. International Conference on Structural Faults and Repair, Edinburgh, May 2016.

Xiaobo Cheng, Ofonime Harry, Mikael Irvine, Pieter Jacobs, Yong Lu. Progressive Collapse – A Laboratory Perspective of Beam Assemblies in a Column Loss Scenario. International Conference on Structural Safety under Fire and Blast, London, 2017.

Cheng, X., Lu, Y. "Steel beam-column connections in a progressive collapse scenario", Ninth International Conference on Advances in Steel Structures (ICASS'2018), 5-7 December 2018, Hong Kong.

Cheng, X., Lu, Y. "An analytical approach to evaluation of the resistance function of fin-plate jointed beam assemblies under a column removal scenario" Advances in Structural Engineering (tentative); In preparation.